Laser powder bed fusion of Cu alloys:

From process parameter optimization to oxidation analysis

by

Nadia Azizi

A thesis
presented to the University Of Waterloo
in fulfillment of the
thesis requirement for the degree of
Doctor of Philosophy
in
Mechanical and Mechatronics Engineering

Waterloo, Ontario, Canada, 2025

© Nadia Azizi 2025

Examining Committee Membership

The following served on the Examining Committee for thesis. The decision of the Examining Committee is by majority vote.

External Examiner:	Hani Naguib, Ph.D. Professor Department of Materials Science and Engineering University of Toronto
Supervisor:	Ehsan Toyserkani, Ph.D. Professor Department of Mechanical and Mechatronics Engineering University of Waterloo
Internal Member:	Hamid Jahed, Ph.D. Professor Department of Mechanical and Mechatronics Engineering University of Waterloo
Internal Member:	Adrian Gerlich, Ph.D. Professor Department of Mechanical and Mechatronics Engineering University of Waterloo
Internal-External Member:	Hamed Shahsavan, Ph.D. Assistant Professor Department of Chemical Engineering University of Waterloo

Author's Declaration

This thesis consists of material all of which I authored or co-authored: see Statement of Contributions included in the thesis. This is a true copy of the thesis, including any required final revisions, as accepted by my examiners.

I understand that my thesis may be made electronically available to the public.

Statement of Contribution

I would like to acknowledge my co-authors who contributed to the research described in this thesis:

- Prof. Ehsan Toyserkani: Supervising the research, providing the original idea for the current thesis, editing and reviewing papers, and providing experimental facilities.
- Prof. Hamed Asgari: Guiding the research work in the area of oxidation behavior of Cu alloys
- Prof. Elahe Jabari: Guiding the research work in the area of LPBF process optimization
- Prof. Akindele Odeshi: Helping in running dynamic impact testing of Cu alloys
- Dr. Mahyar Hasanabadi: Helping in LPBF process optimization

Abstract

This dissertation investigates two Cu-based alloy systems, Cu–Cr–Zr and Cu–Ag, with distinct research focuses for each alloy. The first part focuses on Cu–Cr–Zr, aiming to optimize laser powder bed fusion (LPBF) processing conditions and evaluate mechanical performances of the alloy under high strain rate loading. The second part focuses on Cu–Ag, with the goal of understanding its oxidation behavior at high temperatures, particularly when processed by LPBF. Through a systematic approach, this work establishes direct links between processing parameters, microstructural evolution, and functional properties, providing critical insights into tailoring these alloys for advanced structural and functional applications.

In the first part, a comprehensive multi-stage statistical optimization is applied to identify the optimal LPBF process parameters to maximize relative density and minimize surface roughness of Cu–Cr–Zr. A Plackett-Burman design (PBD) is first employed to screen 23 process parameters and identify the most influential factors. The key parameters, including laser power, scanning speed, hatch spacing, and layer thickness, are then fine-tuned using a central composite design (CCD) to develop predictive models for both relative density and surface roughness. The optimized process achieves near-full densification, with relative density exceeding 99.5% and surface roughness below 15 μm.

To evaluate dynamic mechanical behavior, the optimized Cu–Cr–Zr samples are subjected to high strain rate loading using a split Hopkinson pressure bar (SHPB), with strain rates ranging from 4400 s^{-1} to 11300 s^{-1}. The alloy demonstrates significant strain hardening, followed by thermal softening and adiabatic shear band (ASB) formation. At the highest strain rate of 11300 s^{-1}, the flow stress exceeds 450 MPa, while the alloy maintains considerable strain accommodation due to the dynamic activation of slip systems and localized deformation within ASBs.

In the second part, the feasibility of in-situ alloying of Cu–Ag using LPBF is systematically investigated. Single-track experiments show that increasing scanning speed reduces melt pool size, limiting Ag dissolution, while higher laser power promotes homogeneity at the cost of increased keyhole porosity. Through process optimization, the study achieves a high relative density exceeding 99.2%, along with a uniform distribution of Ag throughout the matrix.

The high-temperature oxidation behavior of optimized thin-walled and triply periodic minimal surface (TPMS) Cu–Ag components is then examined across temperatures ranging from 300 °C to 800 °C. Thermogravimetric analysis (TGA) reveals a clear transition from sub-parabolic to parabolic oxidation behavior as temperature increases. At lower temperatures (300 °C to 600 °C), Cu–2Ag initially oxidizes faster than pure Cu; however, its oxidation rate decreases significantly over time, ultimately resulting in lower total mass gain than pure Cu. At higher temperatures (700 °C to 800 °C), Cu–2Ag exhibits superior oxidation resistance from the outset, with a slower and more stable oxidation rate throughout the exposure period. The presence of Ag shifts the oxidation mechanism toward a more protective parabolic regime, indicating the formation of a stable, adherent, and refined oxide scale. Together, these findings confirm the viability of in-situ alloying via LPBF and highlight the potential of Cu–Ag alloys for high-performance applications, particularly in environments where thermal stability and oxidation resistance are essential.

Acknowledgements

The successful completion of this research would not have been possible without the support, guidance, and encouragement of many individuals, to whom I would like to express my sincere gratitude.

First and foremost, I would like to sincerely express my deepest appreciation to my supervisor, Prof. Ehsan Toyserkani, for his unwavering support, insightful guidance, invaluable advice, and continuous encouragement throughout every stage of this work. It has been a true privilege to work under his supervision, an experience that has profoundly shaped both my academic development and personal growth. His mentorship provided not only a strong foundation for this research but also a source of motivation and confidence during challenging moments.

I would also like to extend my gratitude to the members of my thesis examining committee, Prof. Hani Naguib from the University of Toronto, and Prof. Hamid Jahed, Prof. Adrian Gerlich, and Prof. Hamed Shahsavan from the University of Waterloo. I appreciate their time and effort in reviewing my thesis and providing valuable feedback and suggestions.

I would like to thank Dr. Hamed Asgari, Dr. Elahe Jabari, and Prof. Akindele Odeshi for their valuable guidance and support, as well as Dr. Ehsan Marzbanrad and Dr. Mohsen Keshavarz for their helpful advice and technical assistance throughout this research.

I would like to thank my colleagues and friends at the Multi-Scale Additive Manufacturing (MSAM) Lab, especially Dr. Tatevik Minasyan, Dr. Sahar Toorandaz, Dr. Farima Liravi, Dr. Mahyar Hassanabadi, Mingzhang Yang, and Sebastian Soo, as well as my friend Dr. Shima Akbarian. Their friendship, support, and collaboration made this journey more meaningful both academically and personally.

I would like to extend my appreciation to the technical staff at MSAM, Francis Dibia, Jerry Ratthapakdee, and Grace Kurosad, for their exceptional technical support and assistance during my experimental work.

I would also like to express my sincere appreciation to my Master's supervisor, Prof. Reza Mahmudi, whose mentorship and generous support played an important role in shaping my academic path and nurturing my passion for research. His encouragement and guidance during the early stages of my academic journey laid the foundation for my graduate studies and inspired me to pursue a Ph.D.

Finally, my deepest gratitude goes to my parents and my sisters for their endless love, patience, and unwavering support. Their faith in me never wavered, even in the most challenging moments, and their constant encouragement has been the greatest source of strength and comfort throughout this long and rewarding journey. I truly owe this achievement to their sacrifices, kindness, and unconditional belief in me.

Dedication

To my beloved parents

Table of Contents

Examining Committee Membership ii

Author's Declaration iii

Statement of Contribution iv

Abstract v

Acknowledgements vii

Dedication ix

List of Figures xiv

List of Tables xxiv

List of Abbreviations xxv

List of Symbols xxvii

Chapter 1. Introduction 1

1.1. Research motivation 1

1.2. Objectives 3

1.3. Dissertation outline 5

Chapter 2. Background and literature review 6

2.1. Introduction 6

2.2. Additive manufacturing of Cu and Cu alloys 6

2.2.1. Overview of LPBF 6

2.2.2. Challenges in LPBF of Cu 7

2.2.3. Advancements in LPBF of Cu 9

2.3. LPBF process optimization 10

2.4. Overview of Cu–Cr–Zr alloy 12

2.5. LPBF processing of Cu–Cr–Zr 14

2.5.1. Microstructure evolution in LPBF-made Cu–Cr–Zr 15

2.5.2. Mechanical behavior of LPBF-made Cu–Cr–Zr 17
2.6. Overview of Cu–Ag alloy 18
2.7. LPBF processing of Cu–Ag 19
2.8. Oxidation behavior of Cu alloys 20
2.9. Summary and research gap 22
Chapter 3. High-power laser powder bed fusion of Cu–Cr–Zr alloy: A comprehensive study on statistical process optimization, microstructure, and mechanical properties 24
3.1. Overview 24
3.2. Introduction 24
3.3. Materials and methods 26
3.3.1. Material 26
3.3.2. LPBF fabrication and methodology 27
3.3.3. Characterization 33
3.4. Results and discussion 34
3.4.1. Statistical LPBF process parameter optimization 34
3.4.2. Enhancing process efficiency by increasing layer thickness 50
3.4.3. Evaluation of the printed part properties 53
3.5. Summary 67
Chapter 4. On the microstructure and dynamic mechanical behavior of Cu–Cr–Zr alloy manufactured by high-power laser powder bed fusion 69
4.1. Overview 69
4.2. Introduction 69
4.3. Materials and methods 72
4.3.1. Material 72
4.3.2. LPBF process 73
4.3.3. Dynamic mechanical testing 73
4.3.4. Microstructural characterization 76

4.4. Results and discussion 77
4.4.1. Microstructural observation before deformation 77
4.4.2. Dynamic mechanical response 84
4.4.3. Work hardening behavior 89
4.4.4. Microstructural evolution after dynamic deformation 90
4.4.5. Damage evolution during dynamic deformation 98
4.4.6. EBSD analysis after dynamic deformation 99
4.4.7. Macrotextural analysis after dynamic deformation 104
4.5. Summary 107
Chapter 5. In-Situ alloying of Cu–Ag using high-power laser powder bed fusion: From melt pool analysis to bulk microstructure 109
5.1. Overview 109
5.2. Introduction 109
5.3. Materials and methods 111
5.3.1. Material 111
5.3.2. LPBF process 112
5.3.3. Microstructural characterization 114
5.4. Results and discussion 115
5.4.1. Cu–Ag single track analysis 115
5.4.2. Marangoni number analysis and its implications for LPBF of Cu–Ag 120
5.4.3. Experimental analysis of in-situ alloyed Cu–Ag bulks 125
5.5. Summary 133
Chapter 6. High-temperature oxidation behavior of thin-walled Cu–Ag in-situ manufactured via laser powder bed fusion: Analysis from 300°C to 800°C 134
6.1. Overview 134
6.2. Introduction 134
6.3. Materials and methods 136
6.4. Results and discussion 137

6.4.1. Characteristics of as-printed Cu and Cu–Ag 137
6.4.2. Oxidation resistance of LPBF-made Cu and Cu–Ag 141
6.4.3. Oxidation kinetics of LPBF-made Cu and Cu–Ag 144
6.4.4. Oxidation mechanism of LPBF-made Cu and Cu–Ag 149
6.4.5. Microstructure analysis of oxidized Cu and Cu–Ag 152
6.5. Summary 163
Chapter 7. Oxidation behavior of Cu–Ag alloy in-situ manufactured via laser powder bed fusion 164
7.1. Overview 164
7.2. Introduction 164
7.3. Materials and methods 166
7.4. Results and discussion 168
7.5. Summary 180
Chapter 8. Conclusions and future work 182
8.1. Conclusions 182
8.2. Future work 183
Letter of Copyright Permission 185
References 192
Appendices 214
Appendix A 214
Appendix B 215
Appendix C 216

List of Figures

Figure 1-1 Graphical illustration of the objectives for the present thesis. 4
Figure 2-1 Schematic of a typical LPBF process: (a) front view with its main constituting parts [7] and (b) side view with its main parameters [8]. 7
Figure 2-2 The defects caused in LPBF of pure Cu: (a) balling, (b) and (c) delamination [5]. 9
Figure 2-3 The effects of various laser powers and scan speeds on relative density of pure Cu in the LPBF processing at the fixed layer thickness of 0.03 mm and hatch distance of 0.09 mm [11]. 11
Figure 2-4 Relative density maps of Cu–Cr–Zr alloy showing interaction of different process parameters [52]. 15
Figure 2-5 Microstructure of LPBF-made Cu–Cr–Zr sample: SEM images in (a) ⊙BD and (d) ↑ BD planes, quality pattern images of (b) ⊙BD and (e) ↑ BD superimposed with grain and sub-grain boundaries, (c) KAM map of ⊙BD, and (f) TEM image of the solidification cells [53]..... 16
Figure 2-6 Stress–strain curves of LPBF-made Cu–Cr–Zr alloys in different states at room temperature, 204 °C and 427 °C, respectively. (a) the as-built states, (b) aging at 500 °C, (c) aging at 575 °C and (b) aging at 650 °C, respectively [54]. 18
Figure 2-7 SEM images of as-cast (a) Cu–2Ag [56], (b) Cu–4.5Ag [57], and (c) Cu–6Ag [58]. 19
Figure 2-8 X-ray computed tomography 3D visualization of as build Cu–Ag samples under different compositions [42]. 20
Figure 2-9 (a) Cross-sectional microstructure of the oxide scale formed on high-purity Cu oxidized at 673 K and 1073 K, showing the development of an inner Cu2O layer and an outer CuO layer, with the lower-temperature sample exhibiting a whisker-like CuO structure [66]. 21
Figure 2-10 (a) oxidation rate of pure Cu and Cu–5Ag powders at 250°C and (b) their electrical conductivity [64]. 22
Figure 3-1 (a) SEM image of the virgin pre-alloyed powder of Cu–Cr–Zr, showcasing its morphology, alongside (b) the corresponding particle size distribution (PSD) analysis. 27
Figure 3-2 Schematic representation of the LPBF process parameters used in the Plackett-Burman design (PBD). These visualizations align with the process parameters listed in Table 3-1. 31

Figure 3-3 Pareto chart of the standardized effects and residual for (a,c) *RD* and (b,d) S_a in the PBD analysis. These charts identify the most significant process parameters influencing *RD* and S_a in the LPBF process of Cu–Cr–Zr alloy. 36
Figure 3-4 Results of CCD for optimizing *RD* and S_a in LPBF-made Cu–Cr–Zr alloy. (a) 3D colormap showing *RD* across combinations of *LT*, skin, and core parameters: (b) 2D colormap for *LT* of 60 μm with an example of (c) high *RD* (99.34%); and (d) 2D colormap for *LT* of 20 μm with an example of (e) high *RD* (99.31%). (f) 3D colormap showing S_a across combinations of *LT*, skin, and core parameters: (g) 2D colormap for *LT* of 60 μm with examples of (h) minimum S_a (18.9 μm) and (i) maximum S_a (45.6 μm); and (j) 2D colormap for *LT* of 20 μm with examples of (k) minimum S_a (13.5 μm) and (l) maximum S_a (35.1 μm). Each point on the colormaps corresponds to a unique parameter set, identified by a_i–p_i (row #i = 1–16), with details provided in Table B1. 40
Figure 3-5 Results of CCD showing (a) *RD* changes in terms of *VED* for core exposure and (b) S_a changes in terms of *VED* for skin exposure at different *LT*s of 20 μm, 40 μm, and 60 μm. 42
Figure 3-6 Pareto chart of the standardized effects in the full quadratic model: (a) *RD* and (b) S_a, along with standardized effects and residual plots for the modified model: (c,e) *RD* and (d,f) S_a in the CCD analysis. These charts highlight the most significant factors influencing the responses in CCD, both before and after model refinement, offering insights into the optimization of LPBF process parameters for Cu–Cr–Zr alloy. 43
Figure 3-7 Response optimization plot for LPBF process parameters of Cu–Cr–Zr alloy, showing how each parameter (A–J) affects (a) *RD* and (b) S_a, while (c) representing composite desirability. The optimizer identifies an optimal parameter set with a predicted *RD* of 98.67 % and a S_a of 14.21 μm, achieving a high overall desirability (d = 0.93). 48
Figure 3-8 Computed tomography (CT) analysis and laser profilometry results of the optimized sample. (a) 3D volume and (b) a 2D cross-sectional view of pore distribution, with pores color-coded by volume as indicated in the legend, highlighting minimal and evenly distributed porosity achieved through optimized process parameters. (c) 3D surface view from multiple angles and (d) 2D front-side view of the S_a, as measured by laser profilometry. 50
Figure 3-9 Contour plots showing the relationship between laser power and scanning speed of core exposure for *RD* at different *LT*s: (a) 20 μm, (b) 40 μm, and (c) 60 μm. The results are derived from the CCD analysis with other parameters held constant at their midpoint values. Higher

relative densities are achieved at lower scanning speeds and higher laser powers, particularly for thinner layers. 52
Figure 3-10 *RD* and microhardness (HV) maps of LPBF-made Cu–Cr–Zr alloy processed at different *VED*s. (a_1–f_1) Cross-sectional optical micrographs showing *RD* values ranging from 98.75% to 99.97%. (a_2–f_2) microardness maps showing the HV change across each sample. Representative hardness indents correspond to the (e_3,f_3) highest and (e_4,f_4) lowest measured values. 55
Figure 3-11 3D surface topography maps showing the S_a of LPBF-made Cu–Cr–Zr parts fabricated with different process parameters. The color scale represents height variations, with red indicating elevated regions and blue representing lower valleys. (a, c, d) correspond to parts printed with 20 μm and 40 μm *LT*, exhibiting relatively smoother surfaces. In contrast, (b, e, f) represent parts with 60 μm *LT*, showing increased surface irregularities. 58
Figure 3-12 (a_1–f_1) Grain maps of LPBF-made Cu–Cr–Zr alloy processed at different *VED*s, showing the morphology of grains along the BD. (a_2–f_2) Corresponding histograms of grain size distribution, highlighting variations in grain size influenced by process parameters. Grains intersecting the field of view boundaries are excluded from the distribution. 62
Figure 3-13 (a_1–f_1) Inverse pole figure (IPF-Z) maps of LPBF-made Cu–Cr–Zr alloy processed at different *VED*s, illustrating the grain orientation along the BD and highlighting the elongated columnar grain structures typical of LPBF. (a_2–f_2) Corresponding grain average misorientation (GAM) maps, visualizing local misorientation within grains, with higher values indicating potential residual stress or subgrain formation. 64
Figure 3-14 (a_1–f_1) Image quality (IQ) maps and (a_2–f_2) corresponding grain boundary maps of LPBF-made Cu–Cr–Zr alloy processed at different *VED*s. The maps illustrate subgrain evolution, highlighting low-angle grain boundaries (LAGBs, $5° < \theta < 15°$, red) and high-angle grain boundaries (HAGBs, $\theta > 15°$, blue). 67
Figure 4-1 Comprehensive characterization of virgin pre-alloyed Cu–Cr–Zr powder: (a) SEM micrograph reveals the spherical morphology of the powder particles with smooth surfaces. (b) PSD graph shows D_{10}, D_{50}, and D_{90} values of 16.8 μm, 37.6 μm, and 64.7 μm, respectively. (c) Cross-sectional SEM image, with EDS elemental maps displaying the uniform distribution of (d) Cu, (e) Cr, and (f) Zr within the powder particles, confirming homogeneity. 72

Figure 4-2 (a) Schematic of the split Hopkinson pressure bar (SHPB) setup used for dynamic impact loading of the Cu–Cr–Zr samples, with the impact direction (ID) aligned parallel to the building direction (BD). (b) Magnified view showing the area subjected to EBSD analysis after testing at various firing pressures, ranging from 100 kPa to 250 kPa. 75
Figure 4-3 The overall quality of the as-built Cu–Cr–Zr cylindrical coupon produced via LPBF: (a) The CT scan result reveals a high relative density (RD) of 99.97%, indicating minimal internal porosity. (b) The laser profilometer analysis shows the surface roughness (S_a) of 11.9 ± 2.3 μm, underscoring the smooth and consistent surface finish achieved. 78
Figure 4-4 OM images of the as-built sample under (a) full and (b) partial coaxial lighting, showing the overall grain structure and layered microstructure typical of the LPBF process, including visible melt pool boundaries (MPBs) and columnar grains aligned along the BD. SEM micrographs provide a closer view of detailed features, revealing (c,d) the cellular structure within the grains and (e,f) pores formed during solidification due to gas entrapment. EDS maps of the region around the pores in (e_1,f_1,g_1) show the elemental distribution of (e_2,f_2,g_2) Cu, (e_3,f_3,g_3) Cr, and (e_4,f_4,g_4) Zr. (**GB:** grain boundary)..... 80
Figure 4-5 XRD pattern of the as-built LPBF-made Cu–Cr–Zr alloy, showing prominent diffraction peaks corresponding to the α-Cu phase, along with low-intensity peaks at $2\theta \sim 41°$ and 53°, attributed to Zr and Cr phases. Moreover, a small peak at $2\theta \sim 46°$ suggests the possible presence of Cu_xZr_y compounds, which may have formed during LPBF. 82
Figure 4-6 EBSD analysis of the as-built Cu–Cr–Zr sample showing microstructural and crystallographic characteristics: (a) The IQ map displays grain quality across the sample, with HAGBs superimposed as black lines. (b) The IPF-Z map reveals the alignment of columnar grains along the BD, with a color gradient within individual grains indicating LAGBs and suggesting the presence of defects. (c) The KAM map highlights regions of local strain, reflecting higher dislocation densities. (d) Pole figures for (111), (200), and (220) planes illustrate the microtexture, with the highest texture intensity observed in the (200) and (220) planes. 84
Figure 4-7 True stress–true strain curves showing dynamic mechanical response of LPBF-made Cu–Cr–Zr samples at varying firing pressures (100 kPa, 150 kPa, 200 kPa, and 250 kPa) during SHPB test. The corresponding maximum strain rates for each pressure are 4400 s^{-1}, 6100 s^{-1}, 8000 s^{-1}, and 11300 s^{-1}. 85

Figure 4-8 (a) The increasing trend of YS and UCS with strain rates for dynamically deformed LPBF-made Cu–Cr–Zr alloy. As strain rates increase, both YS and UCS show significant improvement due to strain rate hardening. (b) The relation between $\log\sigma_t$ and $\log\varepsilon t$. The slope (m) of linear fit highlights the material's sensitivity to strain rate, where flow stress rises substantially with increasing strain rates..... 88
Figure 4-9 (a) Work hardening rate curves of the dynamically deformed LPBF-made Cu–Cr–Zr samples at various strain rates of 4400 s^{-1}, 6100 s^{-1}, 8000 s^{-1}, and 11300 s^{-1}, demonstrating how increasing strain rate moderates the work hardening progression. (b) Schematic representation of four distinct stages of work hardening rate: (I) initial drop, (II) reduced slope, (III) increase in hardening rate, and (IV) final decrease due to strain localization and adiabatic shear band (ASB) formation..... 90
Figure 4-10 Microstructural analysis of the LPBF-made Cu–Cr–Zr samples deformed at strain rates of (a–f) 4400 s^{-1} and (g–l) 6100 s^{-1}: (a,b) OM and (c,d) SEM images at 4400 s^{-1} showing underdeveloped ASBs. (e,f) SEM images of deformed gas pores with corresponding EDS maps. (g,h) OM and (i,j) SEM images at 6100 s^{-1} revealing denser, interconnected ASBs. (k) SEM image with corresponding EDS maps showing deformed pores. (l) SEM image showing micro-voids (MVs) within the ASBs. 93
Figure 4-11 Microstructural analysis of the LPBF-made Cu–Cr–Zr samples deformed at the strain rate of 8000 s^{-1}: (a) Reconstructed OM images revealing inhomogeneous deformation within the sample, showing regions of intense strain localization. (b,c) OM images highlighting the formation of ASBs, which demonstrate severe localized plastic deformation, indicating significant strain accumulation. (d,e) SEM micrographs providing a closer examination of ASBs, revealing a more pronounced and interconnected ASB network, consistent with high strain rate conditions. (f) The presence of MVs within the ASBs, which serve as indicators of damage and potential sites for material failure. (g) SEM image showing elongated and irregularly shaped gas pores, acting as weak points for crack initiation. EDS maps confirm the elemental composition surrounding these pores, identifying (g_1) Cu, (g_2) Cr, and (g_3) Zr, confirming their origin from the LPBF process. 96
Figure 4-12 Microstructural analysis of the LPBF-made Cu–Cr–Zr samples deformed at the strain rate of 11300 s^{-1}: (a) Reconstructed OM images showing inhomogeneous deformation within the sample, with (b,c) regions of intense strain localization. (d,e) SEM micrographs indicating the intersection of ASBs, reflecting severe localized plastic deformation and complex strain

accommodation. The presence of (f) crack and (g,h) MVs within the ASBs, serving as indicators of damage and potential sites for material failure. (i–k) SEM images showing deformed pores, acting as weak points for crack initiation. EDS maps confirm the elemental composition surrounding these pores, identifying (j_1,k_1) Cu, (j_2,k_2) Cr, and (j_3,k_3) Zr. 97
Figure 4-13 (a) Schematic representation of deformed zones in dynamic tests, illustrating strain localization in distinct regions under high strain rates, alongside actual images of the deformed samples. (b) Schematic of ASB formation at varying strain rates, with corresponding SEM images for each strain rate. As strain rates increase, ASBs become more pronounced and localized, leading to intensified plastic deformation. MVs nucleate within the ASBs, serving as precursors to crack initiation. At higher strain rates, these MVs coalesce, contributing to material softening and ultimately resulting in crack formation and propagation, marking the progression toward material failure under extreme conditions. 99
Figure 4-14 EBSD results of LPBF-made Cu–Cr–Zr alloy deformed at various strain rates of: (a_1–a_4) 4400 s^{-1}, (b_1–b_4) 6100 s^{-1}, (c_1–c_4) 8000 s^{-1}, and (d_1–d_4) 11300 s^{-1}. The data includes (a_1,b_1,c_1,d_1) IQ map, (a_2,b_2,c_2,d_2) IPFZ map, (a_3,b_3,c_3,d_3) KAM map, and (a_4,b_4,c_4,d_4) pole figures of (111), (200), and (220) planes, corresponding with the analyzed region. 102
Figure 4-15 Comparison of KAM distributions between deformed LPBF-made Cu–Cr–Zr samples at various strain rates and the as-built sample. 103
Figure 4-16 Distribution of dislocation density across the microstructure of (a) undeformed as-built LPBF-made Cu–Cr–Zr sample and deformed samples at strain rates of (b) 4400 s^{-1} and (c) 11300 s^{-1}, with values ranging from 10^{12} m^{-2} to 10^{15} m^{-2} (red regions). The red zones indicate areas of extreme dislocation accumulation, while the blue zones represent areas with lower dislocation density, corresponding to areas with less strain accumulation. White areas denote regions that were not indexed during the EBSD scan. 104
Figure 4-17 Macrotexture analysis of LPBF-made Cu–Cr–Zr samples, including (a) undeformed (as-built) and deformed at strain rates of (b) 4400 s^{-1}, (c) 6100 s^{-1}, (d) 8000 s^{-1}, and (e) 11300 $s^{-1,}$ highlighting how increasing strain rates impact the material's overall texture. 107
Figure 5-1 SEM images of the virgin elemental powders of (a) Cu, (b) Ag, and (c) Cu–2Ag and corresponding particle size distributions. 112
Figure 5-2 Schematic representation of the in-situ alloying process in LPBF of Cu–Ag. (a) illustration of laser interaction with the powder bed and (b) cross-sectional view of the melt pool,

highlighting the Marangoni-driven convection within the melt pool, which influences melt pool depth and promotes element mixing. 113
Figure 5-3 Top view of LPBF-processed single tracks of in-situ alloyed Cu–Ag under varying laser power and scanning speed. Lower speeds produce continuous and stable tracks, while higher speeds lead to instability, discontinuities, and balling defects. Excessive spreading occurs at high power and low speed, whereas high-speed conditions exacerbate track irregularities. 117
Figure 5-4 Optical micrographs of single-track cross-sections for laser powers of 600 W and 900 W, processed at different scanning speeds (500 mm/s, 600 mm/s, and 1000 mm/s). (a) and (c) captured under full coaxial lighting, outlining melt pool boundaries to highlight variations in melt pool depth and width. (b) and (d) captured under partial coaxial lighting, enhancing the visibility of melt pool boundaries 119
Figure 5-5 Measured melt pool geometry of LPBF-made Cu–Ag single tracks at different laser powers and scanning speeds. (a) Melt pool depth decreases with increasing scanning speed due to reduced laser-material interaction time. (b) Melt pool width follows a similar trend, with higher power levels producing wider melt pools. 120
Figure 5-6 Variation of Ma with scanning speed for Cu–2Ag single tracks at different laser power levels. A decreasing trend in Ma is observed with increasing scanning speed, while higher power enhances Ma, indicating stronger thermo-capillary flow. 125
Figure 5-7 Relative density of LPBF-made Cu–Ag bulk samples at different laser powers and scanning speeds. At 600 mm/s, samples exhibit high relative densities, with the highest densification (RD ~99.49%) observed at 900 W. In contrast, at 800 mm/s, increased porosity leads to lower densities, indicating lack-of-fusion defects due to insufficient energy input. These results confirm that lower scanning speeds combined with higher power levels promote better fusion and densification. 126
Figure 5-8 SEM and EDS elemental maps of Cu–Ag bulk samples processed at 800 mm/s, showing non-uniform Ag distribution. The SEM images reveal Ag segregation, with Cu (red) and Ag (blue) maps confirming poor mixing. High scanning speed results in limited melt pool residence time, restricting Marangoni flow-driven mixing and leading to localized Ag-rich regions. 128
Figure 5-9 SEM and EDS elemental maps of Cu–Ag bulk samples processed at 600 mm/s, showing improved Ag uniformity. The SEM images indicate better in-situ alloying, with Cu (red) and Ag (blue) maps confirming a more homogeneous elemental distribution. The analysis points marked

by stars highlight regions where Ag is well-dispersed, demonstrating the positive effect of lower scanning speed on mixing efficiency. 129
Figure 5-10 XRD patterns of pure Cu and in-situ alloyed Cu–2Ag. (a) Both materials exhibit three main Cu diffraction peaks, but Cu–2Ag shows a shift towards lower angles. (b–d) Magnified views highlight this peak shift, which results from Ag incorporation into the Cu matrix, causing lattice expansion. This confirms the successful formation of an in-situ alloyed solid solution during LPBF processing. With alloying validated, these samples are now prepared for the next stage: oxidation evaluation to assess high-temperature performance. 132
Figure 6-1 3D view of surface profile measurements and X-Ray CT images of LPBF-made thin-walled samples: (a,c) pure Cu and (b,d) Cu–2Ag. 137
Figure 6-2 (a) SEM micrograph and EDS elemental maps of LPBF-made Cu–2Ag thin-walled sample, showing the distribution of (b) Cu and (c) Ag. The blue stars in (a) indicate the locations of point analyses used to determine the local chemical composition, with measured Ag contents provided. 138
Figure 6-3 EBSD results of as-printed pure Cu and Cu–2Ag thin-walled samples. (a) Grain map of pure Cu, showing an average grain size of 77.3 ± 8.9 μm, and (b) corresponding IPF-Z map. (d) Grain map of Cu–2Ag, with an average grain size of 64.1 ± 8.1 μm, and (e) corresponding IPF-Z map. The (200) pole figures, obtained from XRD, are shown for (c) pure Cu and (f) Cu–2Ag. Both materials exhibit random texture, while the addition of Ag results in slight grain refinement and a shift in the maximum texture intensity to lower angles with reduced overall intensity. 141
Figure 6-4 Mass gain of LPBF-made Cu and Cu–2Ag thin-walled samples after 24 hours of oxidation in air at different temperatures. 142
Figure 6-5 Oxidation rate of Cu and Cu–2Ag at different temperatures, showing mass gain as a function of time. At temperatures below 700 °C, Cu–2Ag initially oxidizes at a faster rate than pure Cu but later exhibits a lower oxidation rate. 144
Figure 6-6 Parabolic analysis of oxidation kinetics in LPBF-made Cu and Cu–2Ag thin-walled samples, showing squared mass gain (Δm^2) as a function of time. Cu follows a parabolic oxidation law at all temperatures, indicating diffusion-controlled oxidation. In contrast, Cu–2Ag exhibits sub-parabolic behavior at 300–600 °C, where the oxidation rate slows more significantly, suggesting additional rate-controlling factors. At 700 °C and 800 °C, Cu–2Ag transitions fully to

parabolic kinetics, indicating that Ag no longer has a significant influence on oxidation resistance, and oxidation proceeds similarly to Cu. 145
Figure 6-7 Arrhenius plot of the parabolic oxidation rate constant (k_p) for Cu and Cu–2Ag in the temperature range of 300°C–800°C. The change in slope indicates the presence of two oxidation regimes: Regime (I) (300°C–500°C), where oxidation mechanism is grain boundary diffusion-controlled, and Regime (II) (500°C–800°C), where oxidation mechanism transitions to lattice diffusion-controlled..... 151
Figure 6-8 SEM images and corresponding EDS maps showing the elemental distribution of Cu and O in oxidized Cu at different temperatures of (a) 400 °C, (b) 500 °C, and (c) 600 °C. The oxide layer thickens with increasing temperature, and the EDS maps confirm the formation of an oxygen-rich scale at the surface. 155
Figure 6-9 SEM images and EDS maps showing the elemental distribution of Cu, O, and Ag in oxidized Cu–2Ag at (a) 400 °C, (b) 500 °C, and (c) 600 °C. The oxide layers in Cu–2Ag exhibit a different morphology compared to pure Cu, with Ag distribution observed at the oxide/substrate interface, suggesting a potential influence on oxide scale stability. 156
Figure 6-10 EDS line analysis of the oxide layers in Cu and Cu–2Ag at 400 °C, 500 °C, and 600 °C. The Cu and O profiles confirm the oxide layer composition, with Cu_2O as the primary oxide phase in both materials. In Cu–2Ag, Ag is detected near the oxide-metal interface, indicating possible segregation or phase separation during oxidation..... 157
Figure 6-11 SEM images and corresponding EDS maps and line analysis showing the elemental distribution of Cu and O in Cu oxidized at (a–d) 700 °C and (e–h) 800 °C. At higher temperatures, the oxide layer continues to grow, and Cu2O remains the dominant phase. 159
Figure 6-12 EBSD results of pure Cu oxidized in air at different temperatures, showing the oxide microstructure at (a) 400 °C, (b) 500 °C, (c) 600 °C, (d) 700 °C, and (e) 800 °C..... 160
Figure 6-13 EBSD results of Cu–Ag oxidized in air at different temperatures, showing the oxide microstructure at (a) 400 °C, (b) 500 °C, and (c) 600 °C. 162
Figure 7-1 (a) CAD model of designed TPMS structure alongside with the actual printed samples used for oxidation tests, X-Ray CT images showing pores distribution in (b) Cu and (d) Cu–Ag samples, and 3D view of surface profile measurements of (c) Cu and (e) Cu–Ag, illustrating the surface roughness values..... 169

Figure 7-2 (a) SEM micrograph of as-printed Cu–Ag, with corresponding EDS maps showing the distribution of (b) Cu and (c) Ag. 170
Figure 7-3 EBSD grain maps and corresponding grain size distributions and pole figures of as-printed (a,b,c) Cu and (d,e,f) Cu–Ag, captured from the build direction (BD) cross section. The color bar refers to the intensity of the pole figures. 171
Figure 7-4 Mass change measurement of Cu and Cu–Ag during oxidation in air at temperatures of (a) 300 °C, (b) 600 °C for 30 h, and (c,d) fitted lines of square mass gain. 174
Figure 7-5 SEM micrographs with EDS map analysis for (a) Cu and (c) Cu–Ag oxidation in air at 300 °C after 30 hours, highlighting the oxide layers of Cu_2O. The plots in (b) and (d) correspond to line scans of the pink arrows shown in SEM images (a) and (c), respectively, indicating the element concentration profile away from the surface. 177
Figure 7-6 SEM micrographs with EDS map and point analysis for (a,c) Cu and (e,g) Cu–Ag oxidation in air at 600 °C after 30 hours, highlighting the oxide layers of CuO and Cu_2O. The plots in (b) and (f) correspond to line scans of the pink arrows shown in SEM images (a) and (e), respectively, indicating the element concentration profile away from the surface. The EBSD grain maps in (d) and (h) correspond to Cu_2O oxide layer shown in (c) and (g), respectively. 179

List of Tables

Table 2-1 Reported Cu alloys and their AM processes 8
Table 2-2 Reported process parameters for Cu printed with LPBF 12
Table 2-3 Reported process parameters for Cu–Cr–Zr alloy printed with LPBF 14
Table 3-1 List of process parameters selected for the PBD in the LPBF screening 29
Table 3-2 List of process parameters selected for the CCD in the LPBF optimization 37
Table 3-3 Fixed process parameters and their corresponding values used in the CCD experiments 37
Table 3-4 F-values and P-values from ANOVA for the full quadratic and refined models, highlighting model adequacy and lack-of-fit assessment for relative density and surface roughness in the CCD experiments 44
Table 3-5 R^2 values for the full quadratic and refined models, demonstrating their explanatory and predictive performance for relative density and surface roughness in the CCD experiments 45
Table 3-6 Prediction setting for optimization of *RD* and S_a 49
Table 3-7 Process parameters used for LPBF-made parts to evaluate microstructure and hardness 53
Table 4-1 Process parameters used for LPBF of Cu–Cr–Zr 73
Table 4-2 Dynamic mechanical properties of compressed Cu–Cr–Zr 86
Table 5-1 Process parameters of single tracks for Cu–Ag alloy 114
Table 5-2 Process parameters of single tracks for Cu–Ag alloy 122
Table 5-3 Thermophysical properties of pure Cu [163,164] 123
Table 5-4 Elemental chemical composition (wt.%) obtained from EDS point analysis at selected locations marked with stars in Figure 3-9 for LPBF-made Cu–Ag alloy at 600 mm/s 131
Table 6-1 The rate exponent ($\boldsymbol{n}$ in $\Delta m = kt^n$) of Cu and Cu–Ag at different temperatures 146
Table 6-2 The parabolic oxidation rate constant ($\boldsymbol{k_p}$ in $\Delta m^2 = k_p t$) of Cu and Cu–Ag at different temperatures 149
Table 6-3 The oxidation activation energy ($\boldsymbol{E_a}$) of Cu and Cu–Ag 151
Table 7-1 The rate exponent ($\boldsymbol{n}$ in $\Delta m = kt^n$) and parabolic oxidation rate constant ($\boldsymbol{k_p}$ in $\Delta m^2 = k_p t$) of Cu and Cu–Ag at 300 °C and 600 °C 175

List of Abbreviations

AM	Additive Manufacturing
ANOVA	Analysis of Variance
ASB	Adiabatic Shear Band
BJ	Binder Jetting
BD	Building Direction
CAD	Computer-Aided Design
CCD	Central Composite Design
CI	Confidence Interval
CT	Computed Tomography
DED	Directed Energy Deposition
DOE	Design of Experiments
EB-PBF	Electron Beam Powder Bed Fusion
EBSD	Electron Backscatter Diffraction
EDS	Energy-Dispersive X-ray Spectroscopy
FCC	Face-Centered Cubic
GAM	Grain Average Misorientation
GB	Grain Boundary
GND	Geometrically Necessary Dislocation
HAGB	High-Angle Grain Boundary
HD	Hatch Distance
ID	Impact Direction
IM	Impact Momentum
IQ	Image Quality
IPF	Inverse Pole Figure
KAM	Kernel Average Misorientation
LT	Layer Thickness
LPBF	Laser Powder Bed Fusion
LAGB	Low-Angle Grain Boundary
MPB	Melt Pool Boundary
MRD	Multiples of Random Distribution
MV	Micro-Void
NW	Nanowire
OM	Optical Microscopy
PBD	Plackett–Burman Design
PI	Prediction Interval
PSD	Particle Size Distribution
RF	Radio Frequency
RD	Relative Density
RSM	Response Surface Methodology
SAXS	Small-Angle X-ray Scattering
SE	Specific Energy
SEM	Scanning Electron Microscopy

SFE	Stacking Fault Energy
SHPB	Split Hopkinson Pressure Bar
SRS	Strain Rate Sensitivity
TGA	Thermogravimetric Analysis
TEM	Transmission Electron Microscopy
TPMS	Triply Periodic Minimal Surface
UCS	Ultimate Compressive Strength
UTS	Ultimate Tensile Strength
VED	Volumetric Energy Density
XPS	X-ray Photoelectron Spectroscopy
XRD	X-ray Diffraction
YS	Yield Strength

List of Symbols

P	Laser power [W]
v	Scanning speed [mm/s]
h	Hatch distance [μm]
l	Layer thickness [μm]
G	Temperature gradients [K/m]
R	Solidification rate [m/s]
p	Impulse [kg.m/s]
F	Force [N]
t	Time [s]
σ	Engineering stress [MPa]
ε	Engineering strain
$\dot{\varepsilon}$	Engineering strain rate [s^{-1}]
ε_T	Transmitted strain pulse
ε_R	Reflected strain pulse
σ_t	True stress [MPa]
ε_t	True strain
$\dot{\varepsilon}_t$	True strain rate [s^{-1}]
θ	X-ray incidence angle [°]
Θ	misorientation angle [°]
T	Temperature [K]
W_p	plastic deformation [N.m]
c_p	Specific heat capacity [J/kg.K]
Q_p	Heat [J]
m	Strain rate sensitivity
Ma	Marangoni number
ρ	Mass density [kg/m^3]
μ	Dynamic viscosity [Pa.s]
α	Thermal diffusivity [m^2/s]
k	Thermal conductivity [W/m.K]
η	Viscosity [kg/m.s]
γ	Surface tension [mN/m]
Δm	Mass gain [mg/cm^2]
n	Oxidation rate exponent
k_p	Parabolic oxidation rate constant [$mg^4/cm^2.s$]
E_a	Oxidation activation energy [J/mol]

Chapter 1. Introduction

Advancements in metal additive manufacturing (AM) have opened new possibilities for producing complex, high-performance components. Among these technologies, laser powder bed fusion (LPBF) has emerged as a leading method due to its precision, efficiency, and design flexibility. Despite its potential, processing copper (Cu) alloys via LPBF remains challenging due to their high thermal conductivity and reflectivity. This thesis focuses on addressing these challenges through the development and optimization of LPBF parameters for two Cu-based alloys: Cu–Cr–Zr and Cu–Ag. Each alloy is studied for its unique application potential, Cu–Cr–Zr for mechanical performance and Cu–Ag for oxidation resistance.

1.1. Research motivation

AM is a layer-by-layer fabrication technology driven by a digital model, enabling the production of complex metal components without the need for specialized tooling or intricate assembly processes. This flexibility provides industries with faster turnaround times for new product designs, while also supporting material efficiency and contributing to sustainable manufacturing practices. Among metal AM processes, LPBF is particularly notable for its high precision, design freedom, and growing applicability across a wide range of alloys, including titanium, steels, nickel-based superalloys, and more recently, copper alloys [1,2].

Cu alloys are of particular interest due to their unique combination of properties, including high electrical and thermal conductivity, good corrosion resistance, favorable mechanical strength, and excellent ductility. These attributes make Cu alloys ideal for applications such as heat exchangers, electrical contacts, and radio frequency (RF) components [3]. However, conventional manufacturing routes for Cu alloys typically require complex processing steps and multi-component assemblies, limiting design freedom and increasing production costs. By contrast, LPBF enables the direct fabrication of intricate Cu components, offering both process efficiency and enhanced design flexibility.

Despite these advantages, achieving high-quality Cu alloy components via LPBF remains challenging due to its high thermal conductivity and its high reflectivity at the standard laser wavelength (1060 nm) used in most LPBF systems. High thermal conductivity results in rapid heat

dissipation, causing local thermal gradients, residual stresses, and distortion. Meanwhile, high reflectivity reduces laser absorption, increasing the risk of melt pool instability, balling, and porosity formation [4,5] Although recent advances in high-power laser sources have improved the processability of pure Cu, the systematic study of Cu alloys, including Cu–Cr–Zr and Cu–Ag, remains limited.

Among Cu alloys, Cu–Cr–Zr is particularly known for its ability to undergo precipitation hardening, which enhances its mechanical strength without significantly compromising thermal conductivity [2]. This unique combination of properties makes it well-suited for use in extreme environments, such as propulsion system components in hypersonic vehicles, where both high strength and efficient heat dissipation are critical. However, the final properties of LPBF-made Cu–Cr–Zr depend heavily on process-induced microstructure evolution, including grain morphology, crystallographic texture, and precipitate distribution. These microstructural features are directly governed by the thermal history imposed during LPBF, which is controlled by process parameters such as laser power, scanning speed, hatch spacing, and layer thickness. Therefore, establishing an optimized process window that achieves high relative density and low surface roughness, while simultaneously promoting a controlled microstructure, is essential to fully leverage the potential of this alloy in LPBF applications.

In addition, the dynamic mechanical performance of LPBF-made Cu–Cr–Zr under high strain rate loading has not been systematically explored. Understanding how process parameters shape the microstructure and how that microstructure responds under dynamic deformation conditions is essential for developing Cu–Cr–Zr components for high-performance structural applications. In particular, strain hardening, thermal softening, and the formation of adiabatic shear bands (ASBs) are key phenomena requiring in-depth investigation. This thesis addresses these gaps by applying a statistical process optimization framework followed by microstructural analysis and high strain rate mechanical testing, aiming to directly link process, microstructure, and dynamic performance.

While Cu–Cr–Zr focuses on mechanical performance, Cu–Ag alloys are particularly attractive for applications where high electrical conductivity and oxidation resistance are required. Pure Cu suffers from poor oxidation resistance, forming non-conductive oxide films that degrade both electrical conductivity and RF properties. Alloying with Ag enhances oxidation resistance with minimal impact on conductivity, making Cu–Ag alloys suitable for high-temperature electrical

applications [2]. However, the oxidation behavior of LPBF-made Cu–Ag alloys—and particularly the influence of process parameters on oxidation resistance and oxide scale morphology—remains largely unexplored.

Additionally, LPBF offers the opportunity for in-situ alloying, where blended elemental Cu and Ag powders can be co-melted during the process, eliminating the need for pre-alloyed powders. However, achieving good mixing, homogeneous elemental distribution, and high relative density requires identifying a well-defined process window. This thesis systematically investigates in-situ alloying of Cu–Ag, focusing first on single-track formation, followed by process optimization for multi-layer samples, and ultimately evaluating their oxidation behavior across 300 °C to 800 °C. Special attention is given to the transition from sub-parabolic to parabolic oxidation kinetics, and the role of Ag in refining the oxide scale to enhance long-term oxidation resistance.

1.2. Objectives

The principal objective of this thesis is to advance the processability and performance of Cu-based alloys using LPBF, with the aim of enabling their broader application in high-performance structural and functional components. To support this goal, two representative Cu-based alloys, Cu–1%Cr–0.5%Zr and Cu–2%Ag, are systematically studied. These alloys are selected based on their distinct performance priorities: mechanical strength for Cu–Cr–Zr and oxidation resistance for Cu–Ag. The research involves optimizing process parameters for both alloys, followed by evaluating the mechanical properties of Cu–Cr–Zr and the oxidation behavior of Cu–Ag (Figure 1-1). To accomplish this, the following specific objectives are pursued:

- To identify the most significant LPBF process parameters for Cu–Cr–Zr using a statistical approach, and to establish an optimal processing window to maximize relative density and minimize surface roughness.
- To evaluate the mechanical behavior of LPBF-made Cu–Cr–Zr, particularly under high strain rate loading, with emphasis on understanding the relationship between process-induced microstructure evolution and the resulting deformation mechanisms.
- To establish an optimized LPBF process window for the in-situ alloying of Cu–Ag from blended elemental powders, aiming to achieve sufficient melt pool stability, homogeneous elemental distribution, refined microstructure, and high relative density.

- To investigate the high-temperature oxidation behavior of LPBF-made Cu–Ag components across 300 °C to 800 °C, focusing on oxidation kinetics, oxide scale morphology, and the role of Ag in refining the oxide structure and enhancing oxidation resistance.

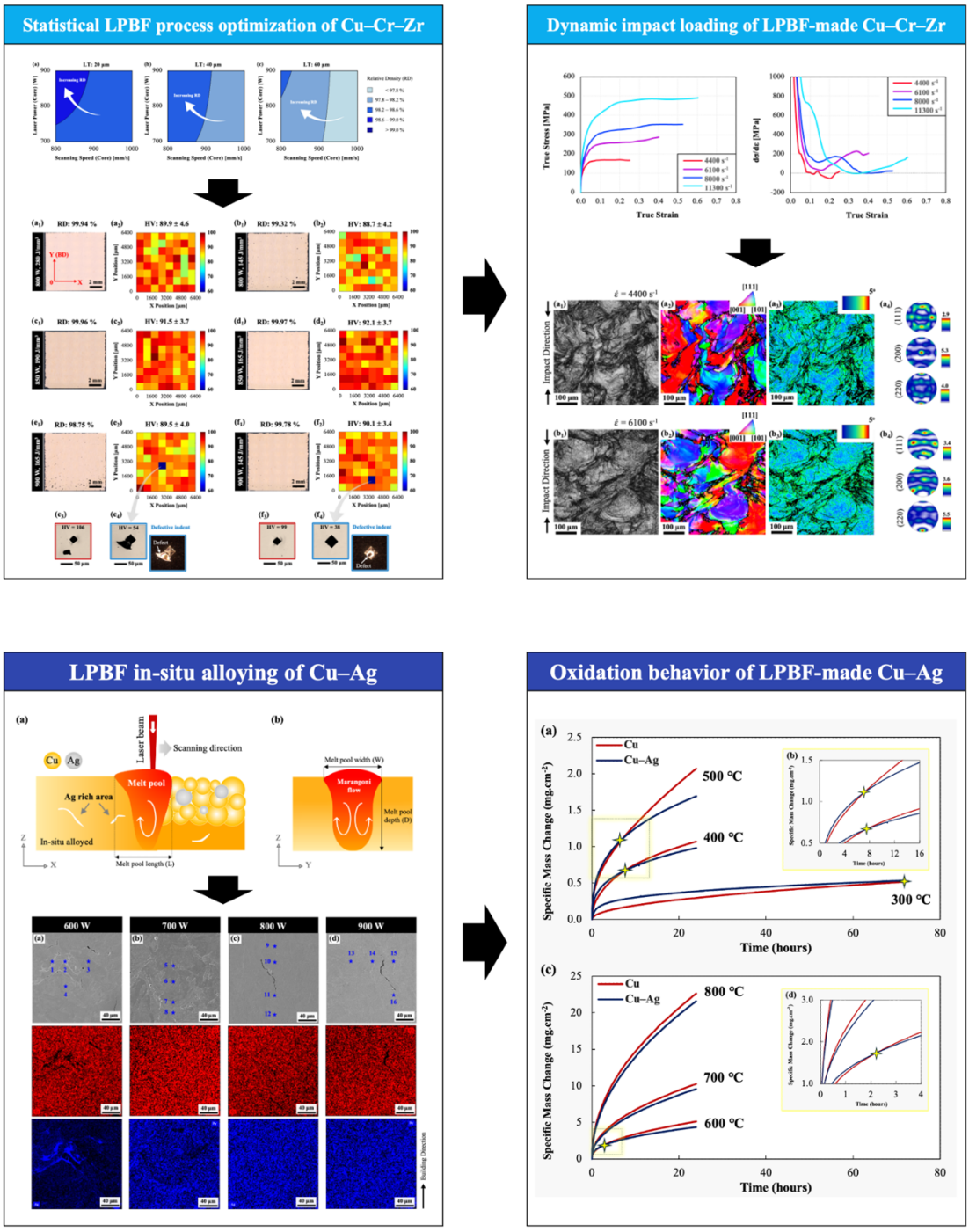


Figure 1-1 Graphical illustration of the objectives for the present thesis.

1.3. Dissertation outline

The organization of the dissertation is as follows:

- Chapter 1 introduces the motivation, objectives, and outline of this research. It is motivated by a lack of knowledge about LPBF of Cu alloys, especially Cu–Ag and Cu–Cr–Zr. The main objectives are to find statistically the best LPBF process window for low surface roughness and high relative density, followed by an analysis of oxidation behavior of Cu–Ag alloy.
- Chapter 2 summarizes the scientific background in LPBF of Cu and Cu alloys. It mainly contains the challenges associated with producing fully dense Cu parts using LPBF. Then, it reviews the process parameters effects on the part quality to determine the solutions for those challenges.
- Chapter 3 focuses on the process optimization of Cu–Cr–Zr alloy using statistical modeling to achieve high relative density, low surface roughness, and controlled microstructure.
- Chapter 4 investigates the high strain rate mechanical behavior of Cu–Cr–Zr, analyzing strain hardening, thermal softening, and adiabatic shear banding, providing insights into its deformation mechanisms.
- Chapter 5 investigates in-situ alloying of Cu–Ag, analyzing melt pool behavior, process parameter effects, and bulk microstructure evolution to optimize the LPBF process.
- Chapter 6 explores the high-temperature oxidation behavior of thin-walled Cu–Ag samples from 300°C to 800°C, analyzing oxidation kinetics, activation energy, and microstructural changes.
- Chapter 7 examines oxidation behavior in Cu–Ag TPMS structures at 300 °C and 600 °C, revealing the impact of Ag on oxidation kinetics and oxide scale morphology.
- Chapter 8 concludes the dissertation by summarizing key findings, discussing their implications, and suggesting future research directions for LPBF-fabricated Cu alloys.

Chapter 2. Background and literature review

2.1. Introduction

This chapter presents a comprehensive review of the existing literature on laser powder bed fusion (LPBF) of pure Cu and Cu alloys, with particular focus on Cu–Cr–Zr and Cu–Ag. It provides an overview of the LPBF process, highlights the key challenges associated with processing Cu alloys due to their high thermal conductivity and high reflectivity, and summarizes the technological advancements aimed at overcoming these limitations. Furthermore, this chapter reviews process optimization, along with studies addressing the microstructure evolution, mechanical properties and oxidation behavior of Cu alloys. Finally, the chapter identifies key knowledge gaps, particularly regarding the dynamic impact loading of Cu–Cr–Zr and in-situ alloying of Cu–Ag.

2.2. Additive manufacturing of Cu and Cu alloys

2.2.1. Overview of LPBF

LPBF is an additive manufacturing (AM) process in which three-dimensional objects are fabricated by selectively melting metal powders layer-by-layer using a high-energy laser beam (Figure 2-1). One of LPBF's key advantages is its high design freedom, enabling the production of complex geometries and intricate internal structures that would be difficult or impossible to achieve through conventional manufacturing methods. This design flexibility, combined with reduced lead times and improved material efficiency, makes LPBF highly attractive for aerospace, automotive, and biomedical applications [1].

LPBF is capable of processing a wide range of high-performance alloys and pure metals, often producing components with properties comparable to those obtained through conventional processes such as casting or forming. Moreover, the rapid solidification inherent to the LPBF process promotes the formation of fine microstructures and epitaxial grain growth, which can enhance mechanical properties. This unique thermal history offers new opportunities for tailoring local microstructures within a part and even for developing new alloy designs optimized for AM-specific processing conditions [6–8].

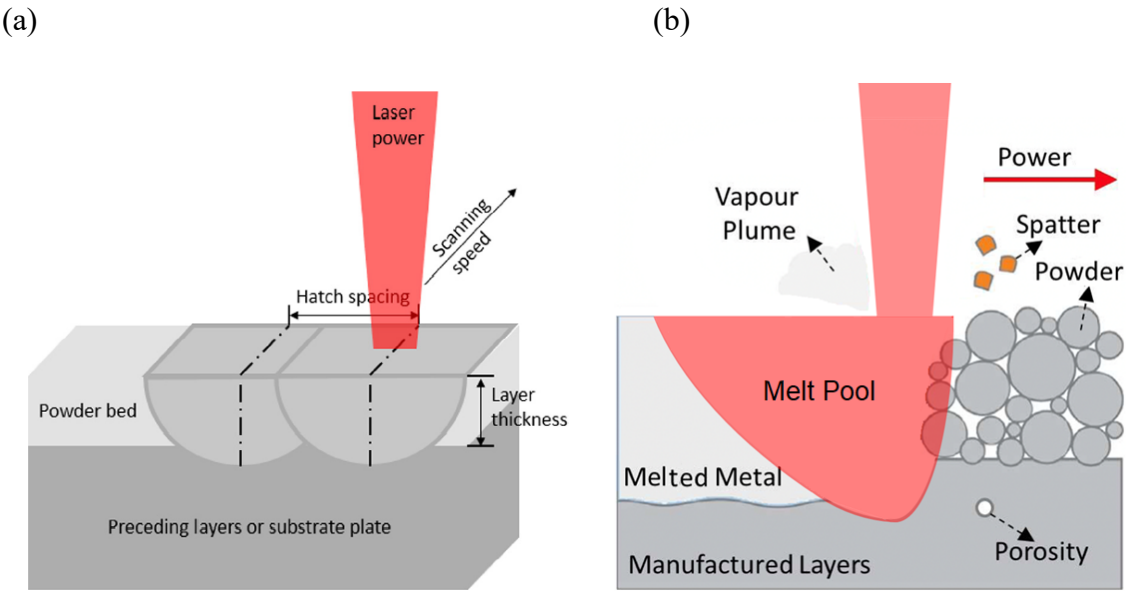


Figure 2-1 Schematic of a typical LPBF process: (a) front view with its main constituting parts [7] and (b) side view with its main parameters [8].

2.2.2. Challenges in LPBF of Cu

In recent years, AM of Cu and its alloys has attracted increasing attention due to its high electrical and thermal conductivity, excellent corrosion resistance, good ductility, high strength, and favorable hardness. These properties make Cu alloys highly suitable for thermal management systems, electrical connectors, and RF components. AM offers a promising route for producing complex Cu components efficiently and economically, particularly using LPBF.

Table 2-1 provides an overview of copper alloys processed using different AM technologies, including LPBF, electron beam powder bed fusion (EB-PBF), directed energy deposition (DED), and binder jetting (BJ). Among these techniques, LPBF is particularly attractive due to its high geometrical accuracy, fine resolution, and design flexibility. However, most studies agree that producing dense, defect-free Cu components using conventional LPBF systems, typically equipped with infrared fiber lasers (power range: 200 W–400 W), remains extremely challenging. As-built parts frequently exhibit unmelted powder particles, lack of fusion defects, and relative densities below 90% [9]. Therefore, efforts are being made to improve the efficiency of LPBF of Cu. To begin with this, an understanding of the challenges is required first.

Table 2-1 Reported Cu alloys and their AM processes

Alloy	AM Process	Ref.
Cu	LPBF	[9–17]
	EB-PBF	[18–21]
	DED	[22,23]
	BJ	[24,25]
Cu–0.5Cr	LPBF	[26,27]
Cu–0.8Cr (UNS.C18400)	LPBF	[28,29]
Cu–(1.3, 2.5)Cr	LPBF	[30]
Cu–20Cr	LPBF	[31]
Cu–25Cr	LPBF	[31]
	EB-PBF	[32]
Cu–(0.5–1.2)Cr–(0.03–0.3)Zr (UNS.C18150)	LPBF	[33–35]
Cu–(0.5–0.7)Cr–(0.06–0.15)Zr	LPBF	[36]
Cu–(0.5–0.7)Cr–(0.02–0.05)Zr–(0.02–0.05)Ti	LPBF	[37]
Cu–3.3Cr–2.9Nb (GRCop-42)	LPBF	[38]
Cu–6.5Cr–5.8Nb (GRCop-84)	LPBF	[39,40]
	DED	[41]
Cu–(10, 20, 30)Ag	LPBF	[42]
Cu–(1.5–2.4)Ni–(0.02–0.5)Si–(0.02–0.07)Cr	LPBF	[43]

The challenges associated with LPBF of Cu primarily originate from the inherent material properties of Cu itself. Its high thermal conductivity leads to rapid heat dissipation from the melt pool, creating steep thermal gradients, which contribute to thermal stresses, distortion, and incomplete melting. In addition, its high reflectivity to infrared laser wavelengths, particularly at the commonly used wavelength of approximately 1 μm, further limits energy absorption, with reported absorptivity values as low as 3% [15].

Due to this insufficient energy absorption, achieving consistent powder melting and high-density Cu components becomes particularly challenging. These process instabilities frequently lead to defects such as balling, elevated edges, and delamination, all of which can ultimately result in build failure. Figure 2-2 illustrates these typical defects observed during LPBF of pure copper, highlighting the critical role of process-material interactions in determining part quality [5].

Consequently, substantial research efforts have been dedicated to improving process efficiency and stability for LPBF of Cu and Cu alloys. Developing effective solutions first requires a comprehensive understanding of these fundamental process-material challenges, which serves as the basis for the advancements discussed in the following section.

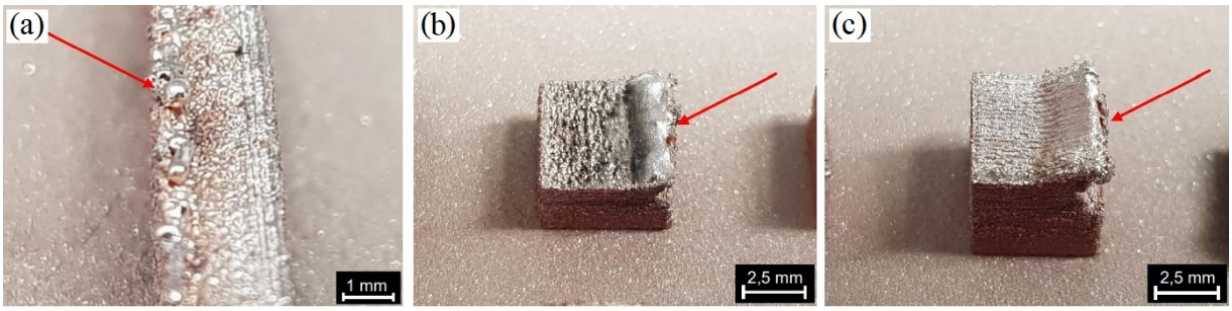


Figure 2-2 The defects caused in LPBF of pure Cu: (a) balling, (b) and (c) delamination [5].

2.2.3. Advancements in LPBF of Cu

To overcome the inherent challenges in LPBF of Cu and Cu alloys, researchers have pursued several technological advancements aimed at improving laser absorption, melt pool stability, and overall process efficiency. One of the most impactful developments has been the introduction of high-power lasers, with powers exceeding 500 W, which significantly improve energy input and promote more reliable melting of Cu powders [16].

In addition to increasing laser power, wavelength-tuned lasers, particularly green (515 nm) and blue (450 nm) lasers, have demonstrated substantial improvements in laser absorptivity compared to conventional infrared fiber lasers operating at 1060 nm [15]. However, green and blue laser systems are currently more expensive than infrared lasers, limiting their widespread adoption, especially in industrial settings where cost-effectiveness remains a priority.

Beyond laser source modifications, researchers have also explored scanning strategies and process parameter optimization to enhance part density and reduce defect formation. Approaches such as contour scanning, energy modulation, and reduced layer thickness have shown promise in addressing balling, incomplete melting, and delamination, all of which are prevalent when processing high-reflectivity metals like Cu.

Despite these advancements, the majority of existing studies have focused on pure Cu, leaving the processing of Cu alloys, including Cu–Cr–Zr and Cu–Ag, significantly less explored. This represents a critical knowledge gap, particularly in understanding how alloying elements, solidification behavior, and microstructure evolution are influenced by LPBF process conditions. Closing these gaps through systematic process optimization and microstructural analysis is essential to enable the development of high-performance LPBF-made Cu alloys for functional and structural applications.

2.3. LPBF process optimization

Optimizing LPBF process parameters is critical for achieving high-quality components with desired density, surface roughness, and microstructure. This is particularly important for Cu and its alloys, where thermal and optical properties introduce additional complexity in achieving stable and defect-free processing. LPBF is a multi-variable process, where factors such as laser power, scanning speed, hatch spacing, layer thickness, and exposure strategies collectively determine the thermal profile, melt pool dynamics, and ultimately the microstructure and properties of the printed part [44].

In LPBF of Cu alloys, achieving high relative density (*RD*) and low surface roughness (S_a) is essential to ensure both mechanical integrity and functional performance, particularly in applications requiring good thermal or electrical conductivity. These attributes are directly governed by process parameters, which control energy input, powder consolidation, and solidification behavior. Key parameters include laser power, scanning speed, hatch spacing, layer thickness, and exposure strategies, each influencing the thermal profile of the melt pool, the stability of layer bonding, and the formation of surface features [45].

For Cu alloys, laser power and scanning speed are particularly critical due to Cu's high reflectivity and high thermal conductivity, which make it challenging to maintain sufficient energy absorption and consistent melting. Insufficient energy density can lead to lack of fusion pores, while excessive energy density can promote keyhole porosity due to unstable vapor depression [46]. Hatch spacing and layer thickness further influence overlapping melt pools and interlayer bonding, both of which are crucial for minimizing porosity [35].

Laser power, scanning speed, hatch distance, and layer thickness are the key process parameters affecting the quality of the LPBF parts. These variables determine the volumetric energy density (*VED*), which indicates the energy input delivered per unit area. It is defined by the ratio of the laser power (P) and the product of the scanning speed (v), the hatch distance (h), and the layer thickness (l) (Equation (2-1)):

$$\text{VED}\ \left(\frac{J}{mm^3}\right) = \frac{P\ (W)}{v\ \left(\frac{mm}{s}\right).h(mm).l(mm)} \tag{2-1}$$

According to the *VED* definition, higher laser powers and slower scanning speeds can effectively provide heat input that facilitates the melting of high reflective Cu powder during LPBF [14–17]. Figure 2-3 indicates how various values of P and v affect relative density of LPBF-made Cu samples. A relative density of more than 99% can be achieved by increasing P and optimizing v.

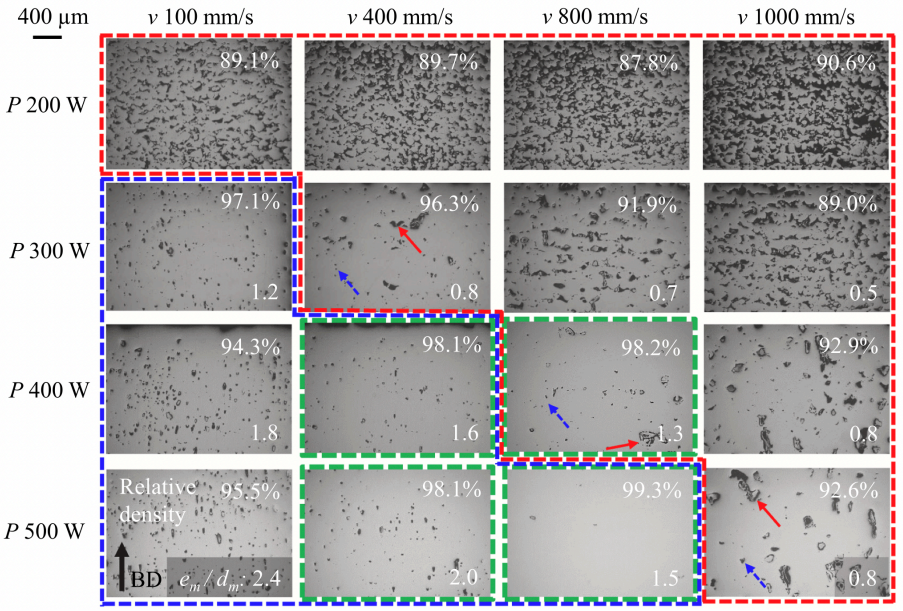


Figure 2-3 The effects of various laser powers and scan speeds on relative density of pure Cu in the LPBF processing at the fixed layer thickness of 0.03 mm and hatch distance of 0.09 mm [11].

The process parameters reported in Table 2-2 summarize the conditions used to achieve high-density Cu parts in previous studies. However, these parameters were primarily determined using conventional trial-and-error approaches. Given the complex interactions among numerous interdependent parameters in LPBF, such empirical methods are both inefficient and impractical. To address this, systematic approaches such as Design of Experiments (DOE) and statistical modeling techniques provide a more effective means of process optimization. These methods allow researchers to identify the most influential parameters and develop predictive models that clearly describe the relationships between process conditions and critical performance metrics, including relative density and surface roughness. By adopting these data-driven approaches, the number of required experiments can be significantly reduced, while simultaneously gaining quantitative insights into how each parameter influences part quality. This facilitates a more efficient and scientifically guided optimization process, which is particularly valuable for challenging materials like Cu and its alloys

Table 2-2 Reported process parameters for Cu printed with LPBF

Material	Power (W)	Scan Speed (mm/s)	Hatch Space (μm)	Layer Thickness (μm)	VED (J/mm^3)	Density (%)	Ref.
Pure Cu	600	1000	70	50	171.4	97.8	[16]
	600	200	90	30	1111.1	>98	[14]
	600	300	90	30	740.7	>98	[14]
	800	400	90	30	740.7	>98	[14]
	800	400	70	30	952.4	>98	[14]
	800	300	100	50	533.3	96.6	[17]
	800	2000	70	50	114.3	98.7	[15]

2.4. Overview of Cu–Cr–Zr alloy

Cu–Cr–Zr is a precipitation-strengthened Cu alloy that provides an optimal balance of high strength, thermal stability, and electrical conductivity, making it suitable for applications requiring both mechanical performance and efficient heat dissipation. These properties are primarily achieved through the combined effects of chromium (Cr) and zirconium (Zr), which contribute to precipitation hardening, grain refinement, and resistance to thermal softening.

The Cu–Cr–Zr alloy system consists of an α-Cu matrix with up to 1.2 wt.% Cr and 0.03–0.3 wt.% Zr. The strengthening mechanisms in this alloy arise from the low solid solubility of Cr in Cu, which is approximately 0.33 wt.% at 960°C. This allows for the formation of fine Cr precipitates upon solution treatment, quenching, and aging. These precipitates act as obstacles to dislocation motion through the Orowan strengthening mechanism, significantly enhancing mechanical strength and thermal stability [47]. In addition to Cr precipitation, the presence of Zr further improves the creep strength and softening resistance of Cu–Cr alloys by promoting a uniform distribution of precipitates and forming Cu–Zr intermetallic phases, which impede grain boundary movement. Unlike many other strengthening mechanisms that negatively impact electrical conductivity, the dispersion of Cr precipitates in Cu–Cr–Zr alloys has minimal effect on electrical and thermal conductivity, allowing the material to maintain an electrical conductivity exceeding 80% IACS in the aged condition [48].

Due to its high-performance characteristics, Cu–Cr–Zr is widely used in industries requiring functional components with complex geometries. It is extensively applied in electrical contacts, bus bars, and switchgear, where high electrical conductivity must be combined with mechanical durability. In the aerospace and energy sectors, this alloy is used for heat sinks and structural components in high-temperature environments, such as fusion and plasma-facing applications. Its high thermal conductivity and wear resistance make it a preferred choice for molds, dies, and tooling applications. Furthermore, Cu–Cr–Zr is commonly employed in welding electrodes and resistance welding equipment, where its thermal and mechanical stability ensures reliable performance under repeated thermal cycles.

Although extensive research has been conducted on Cu–Cr–Zr processed through conventional methods, there is increasing interest in using AM techniques, particularly LPBF, to fabricate high-performance Cu–Cr–Zr components with enhanced microstructural control. The ability of LPBF to produce complex geometries with precise microstructural tailoring presents new opportunities for optimizing the properties of this alloy for advanced engineering applications. The following sections discuss the microstructure evolution and mechanical behavior of LPBF-made Cu–Cr–Zr, with a focus on the influence of processing conditions on final material properties.

2.5. LPBF processing of Cu–Cr–Zr

Cu–Cr–Zr alloys offer advantages for LPBF compared to pure Cu, primarily due to their higher laser absorption coefficient introduced by alloying elements such as Cr and Zr. While the alloy retains relatively high thermal conductivity, the improved laser absorption enhances energy coupling, making it easier to achieve full melting.

However, achieving high-density Cu–Cr–Zr parts still requires careful process optimization due to the persistent high thermal conductivity and resulting rapid heat dissipation. These factors contribute to a narrow process window, where balancing laser power, scanning speed, hatch spacing, and layer thickness is essential to avoid defects like lack of fusion, keyholing, and cracking. The process parameters reported in the literature for producing Cu–Cr–Zr parts via LPBF are summarized in Table 2-3.

Table 2-3 Reported process parameters for Cu–Cr–Zr alloy printed with LPBF

Alloy	Power (W)	Scan Speed (mm/s)	Hatch Space (μm)	Layer Thickness (μm)	VED (J/mm^3)	Density (%)	Ref.
Cu– (0.5–1.2)Cr – (0.03–0.3)Zr	370	500	80	20	463	99.99	[33]
Cu– (0.5–1.2)Cr – (0.03–0.3)Zr	370	400	100	20	463	99.84	[34]
Cu– (0.5–1.2)Cr – (0.03–0.3)Zr	370	300	110	20	560	99.96	[35]
Cu–(0.5–0.7)Cr–(0.06–0.15)Zr	460	700	60	30	365	91.62	[36]
Cu–0.6Cr–0.4Zr	370	650	170	30	112	99.14	[49]
Cu–0.6Cr–0.4Zr	485	450	90	30	399	99.7	[50]

To efficiently identify this process window, Sun et al. [36,51] applied DOE using a Central Composite Design (CCD) approach to systematically explore the influence of key LPBF parameters on relative density and surface roughness of Cu–Cr–Zr. Their statistical modeling provided predictive equations, allowing them to map an optimized process window where near-full densification and minimized surface roughness were simultaneously achieved. This work highlights how DOE is particularly valuable for Cu–Cr–Zr, as it reduces the experimental workload while capturing complex parameter interactions, ultimately offering a more reliable and data-driven route to process optimization.

Along with the effect of individual process parameters, the interaction between process parameters also plays a critical role in determining density, as shown in Figure 2-4 [52]. According to this figure, the interaction between laser power and scan speed is relatively weak, meaning that increasing laser power while reducing scan speed leads to only a gradual increase in relative density. In contrast, the interaction between scan speed and hatch spacing is much more pronounced, indicating that optimizing these two parameters together is essential for achieving high density in Cu–Cr–Zr. This further underscores the importance of statistical approaches, which are designed to capture such interactions comprehensively.

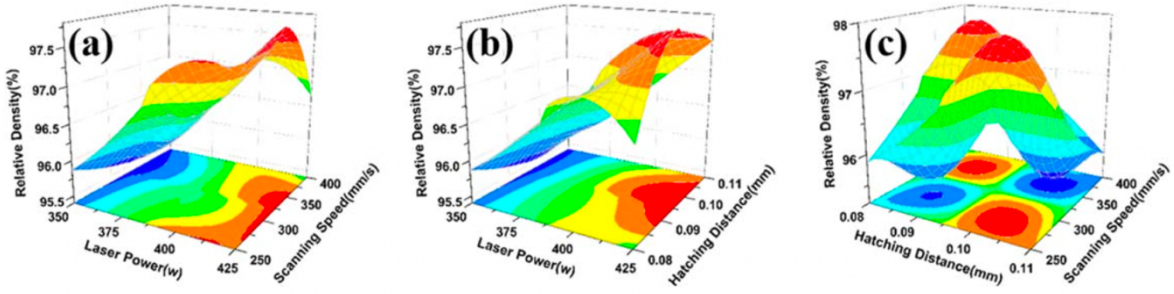


Figure 2-4 Relative density maps of Cu–Cr–Zr alloy showing interaction of different process parameters [52].

2.5.1. Microstructure evolution in LPBF-made Cu–Cr–Zr

The microstructure of LPBF-made Cu–Cr–Zr is strongly influenced by the high cooling rates and steep thermal gradients characteristic of the LPBF process. Due to the rapid solidification, Cu–Cr–Zr exhibits a refined microstructure with columnar grains elongated along the building direction. Figure 2-5 provides a comprehensive view of this microstructural development [53]. In the transverse plane (perpendicular to the building direction: ⊙BD), the microstructure reveals melt pool boundaries and overlapping tracks, while in the longitudinal plane (parallel to the building direction: ↑ BD), grains appear elongated, following the thermal gradient direction.

The as-built Cu–Cr–Zr microstructure is dominated by cellular and columnar grains with an average size of ~115 μm in the transverse plane, increasing to ~217 μm in the longitudinal plane. These grains form through epitaxial growth from the solidified layer below, driven by directional heat dissipation. Within these grains, the development of solidification cells is observed, with an

average cell size around 300 nm. These cells, enriched with dislocations, act as strengthening features due to the high dislocation density introduced during rapid solidification.

Kernel average misorientation (KAM) analysis further highlights the presence of a high initial dislocation density (~8×10^{14} m^{-2}), contributing significantly to the mechanical strength of the as-built alloy. This dislocation density decreases after direct aging heat treatment (DAH), indicating partial recovery and rearrangement of dislocations during aging. However, the grains themselves exhibit only minor coarsening, demonstrating the thermal stability of the LPBF microstructure during post-processing.

Beyond the grain morphology, the distribution of secondary phases also plays a crucial role in defining the microstructural characteristics of Cu–Cr–Zr. The high cooling rates of LPBF result in a supersaturated solid solution of Cr in Cu, delaying the natural precipitation of strengthening phases until post-processing treatments are applied. However, some degree of precipitation can occur within the as-printed state due to localized reheating from subsequent laser passes [49].

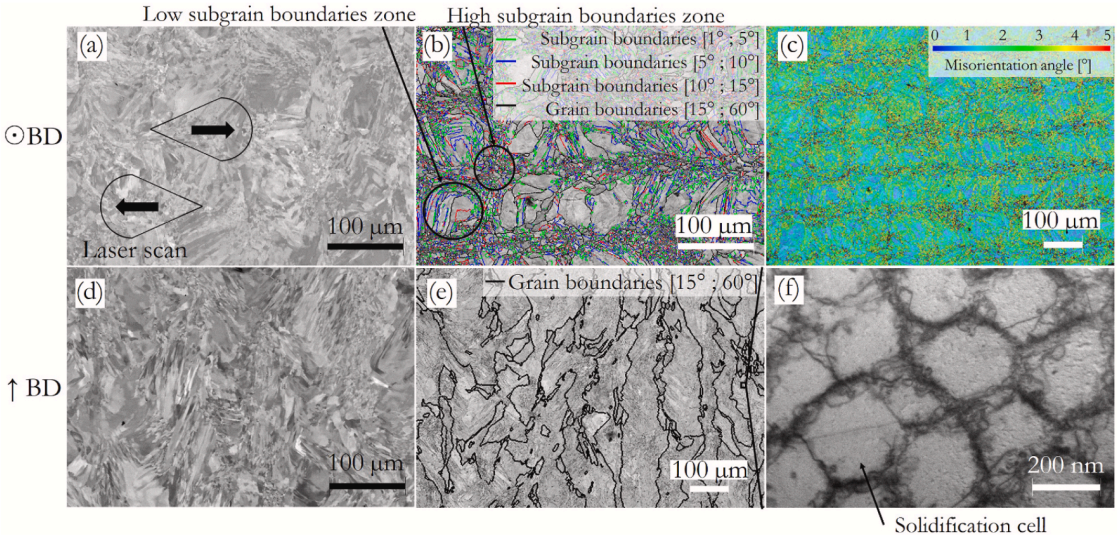


Figure 2-5 Microstructure of LPBF-made Cu–Cr–Zr sample: SEM images in (a) ⊙BD and (d) ↑ BD planes, quality pattern images of (b) ⊙BD and (e) ↑ BD superimposed with grain and sub-grain boundaries, (c) KAM map of ⊙BD, and (f) TEM image of the solidification cells [53].

2.5.2. Mechanical behavior of LPBF-made Cu–Cr–Zr

The mechanical behavior of Cu–Cr–Zr produced by LPBF is a direct consequence of its unique microstructural features, including grain morphology, solidification cells, dislocation density, and the distribution of precipitates. As-built LPBF-made Cu–Cr–Zr benefits from the rapid solidification-induced fine cellular microstructure, while heat-treated samples further gain strength from the precipitation of nanoscale Cr and Cu–Zr particles. These microstructural attributes contribute to a balance between strength and ductility that makes LPBF-made Cu–Cr–Zr suitable for high-performance applications.

Figure 2-6 provides a comparative overview of the mechanical properties of LPBF-made Cu–Cr–Zr, both as-printed and after DAH, benchmarked against conventionally processed Cu–Cr–Zr alloys [54]. As shown, the as-printed LPBF Cu–Cr–Zr exhibits a yield strength (YS) of approximately 204 MPa and an ultimate tensile strength (UTS) of 287 MPa, coupled with an impressive elongation of 33.2%. This relatively high ductility, despite the presence of residual porosity, can be attributed to the fine-grained microstructure and high dislocation density introduced during rapid solidification. The fine cells and columnar grains not only provide structural refinement, but also accommodate plastic deformation effectively, resulting in good strain hardening capacity.

After direct aging at 490 °C for 2 hours, the mechanical properties shift significantly. Yield strength increases to around 361 MPa, and UTS reaches approximately 466 MPa, with elongation reducing to about 12.3%. This increase in strength is due to the precipitation of fine Cr particles and Cu–Zr intermetallic phases, which impede dislocation motion through Orowan strengthening. While the loss in ductility is expected after precipitation hardening, the achieved mechanical properties closely match or exceed those of conventionally processed Cu–Cr–Zr, confirming the potential of LPBF for structural applications where both strength and thermal stability are essential.

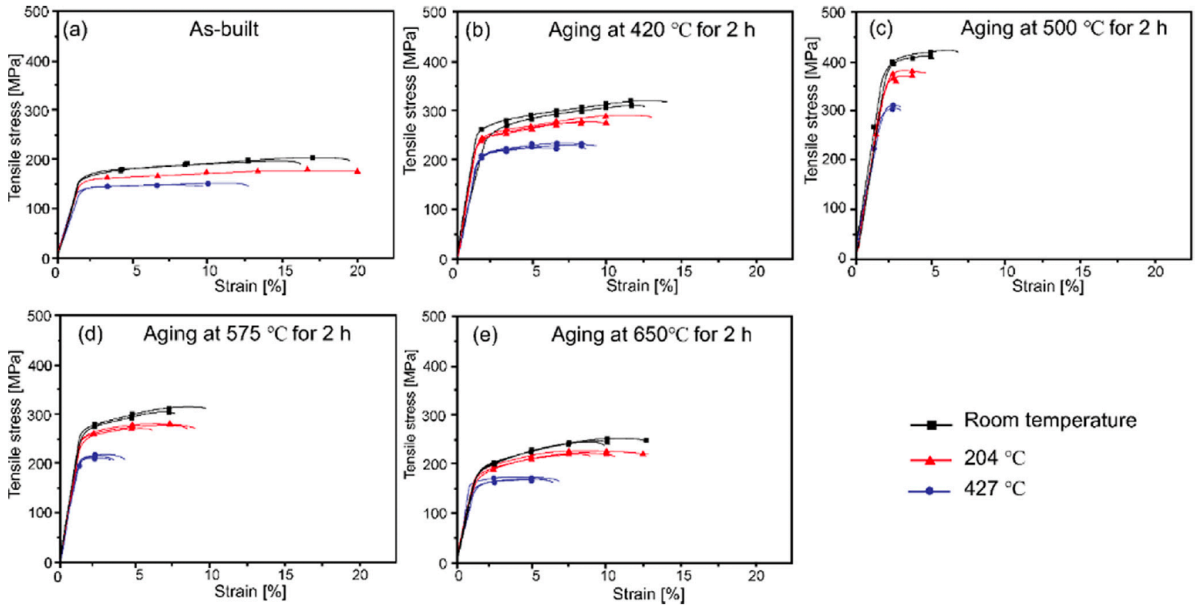


Figure 2-6 Stress–strain curves of LPBF-made Cu–Cr–Zr alloys in different states at room temperature, 204 °C and 427 °C, respectively. (a) the as-built states, (b) aging at 500 °C, (c) aging at 575 °C and (b) aging at 650 °C, respectively [54].

2.6. Overview of Cu–Ag alloy

In the Cu–Ag binary system, Cu and Ag form a simple eutectic system that has a limited substitutional solid solubility. Although Ag has the same crystal structure (FCC) as Cu, the larger atomic radius of Ag restricts its solubility in Cu to approximately 8 wt.% at eutectic temperature (779 ºC), and even less at room temperature. Hypoeutectic alloys with less than 8 wt.% Ag contain two phases: a copper-rich solid solution (α), and a silver-rich solid solution (β) [55]. Figure 2-7 indicates scanning electron microscope (SEM) images of three different as-cast Cu–Ag binary alloys containing 2 wt.%, 4.5 wt.%, and 6 wt.%. It is evident that the microstructures are primarily composed of α-Cu matrix and β-Ag phase distributed along α-Cu dendrites, which reveals that considerable amounts of Ag remain undissolved in Cu matrix [56–58].

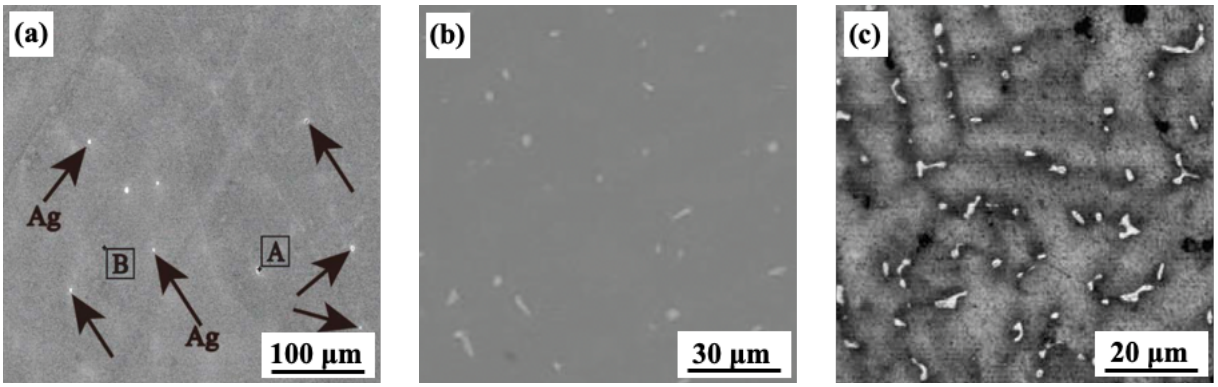


Figure 2-7 SEM images of as-cast (a) Cu–2Ag [56], (b) Cu–4.5Ag [57], and (c) Cu–6Ag [58].

So far, researchers have published several studies on Cu–Ag alloys with Ag contents in the range of 6–24 wt.% [58–62] or only 0.1 wt.% [63], mainly processed by traditional methods. From these reports, Cu–6Ag, Cu–12Ag, and Cu–24Ag have a maximum electrical conductivity of 88, 85, and 75 % IACS, respectively [58]. While Ag content in the range of 0.1–5 wt.% provides higher electrical conductivity [56,57,63,64], which makes the alloy more efficient and cost-effective. Therefore, the use of Cu–Ag alloys containing dilute Ag is applicable in a wide range of electrical applications. Nevertheless, the geometry of these applications is complex enough that requires extensive and expensive fabrication processing paths using conventional methods. By utilizing LPBF, Cu–Ag alloy parts may be produced efficiently and economically.

2.7. LPBF processing of Cu–Ag

Despite the potential advantages of LPBF processing for Cu–Ag alloys, very limited research has been published on this subject. To date, only one study has directly investigated the LPBF processing of Cu–Ag alloys, focusing on how Ag content influences pore defect morphology and mechanical performance [42] In this study, elemental powder blends of Cu and Ag with 10, 20, and 30 wt.% Ag were processed using LPBF.

The pore defect morphology and distribution in the as-built samples were analyzed using X-ray computed tomography (CT), as shown in Figure 2-8. The results demonstrate a clear trend, as the Ag content increases from 10 wt.% to 30 wt.%, the number of pores decreases by 87%, while the average pore size reduces by approximately 40%. This improvement in density at higher Ag content was attributed to enhanced laser absorption and improved wetting behavior caused by Ag addition.

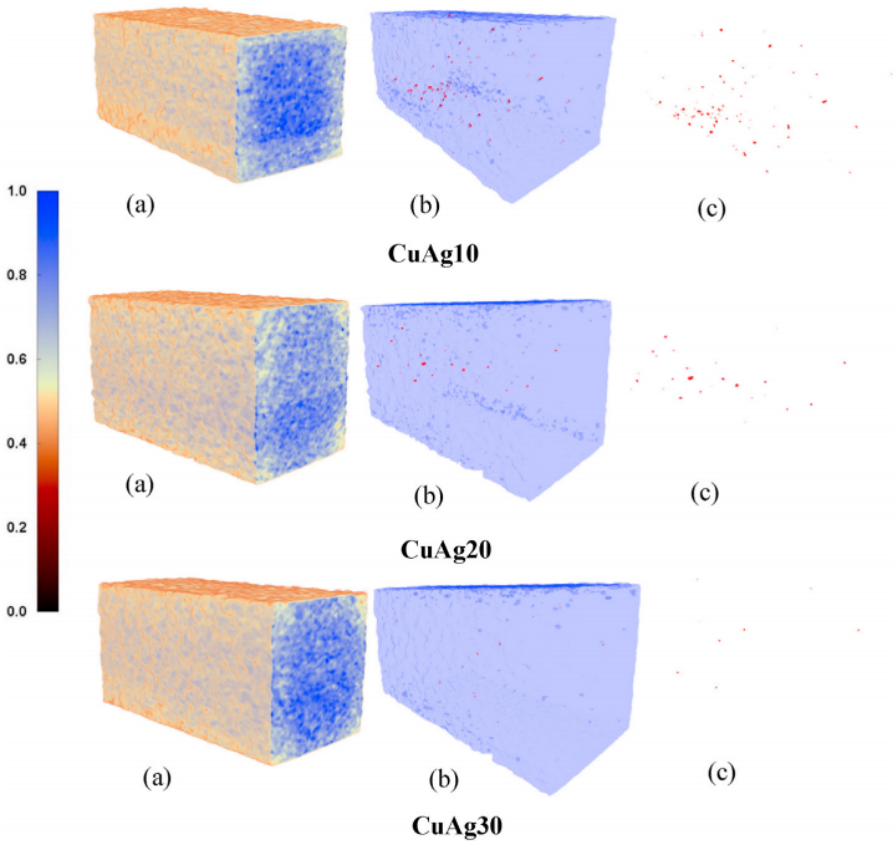


Figure 2-8 X-ray computed tomography 3D visualization of as build Cu–Ag samples under different compositions [42].

2.8. Oxidation behavior of Cu alloys

Since Cu is widely used in applications exposed to oxidizing environments, including electrical components and communication devices, minimizing its oxidation is critical to maintaining performance. The oxidation of Cu alloys is strongly influenced by their chemical composition and microstructure, particularly the grain boundaries and defect sites, which serve as high-energy pathways for oxidation initiation and propagation [65]. As shown in Figure 2-9, oxidation of Cu generally proceeds through the formation of a duplex oxide scale, consisting of an inner Cu_2O layer and an outer CuO layer. The process follows parabolic kinetics at elevated temperatures, with oxygen diffusing inward and copper cations diffusing outward. However, at lower temperatures (below ~800 K), a transition to a more complex mechanism involving CuO whisker formation occurs, contributing to a reduction in activation energy [66].

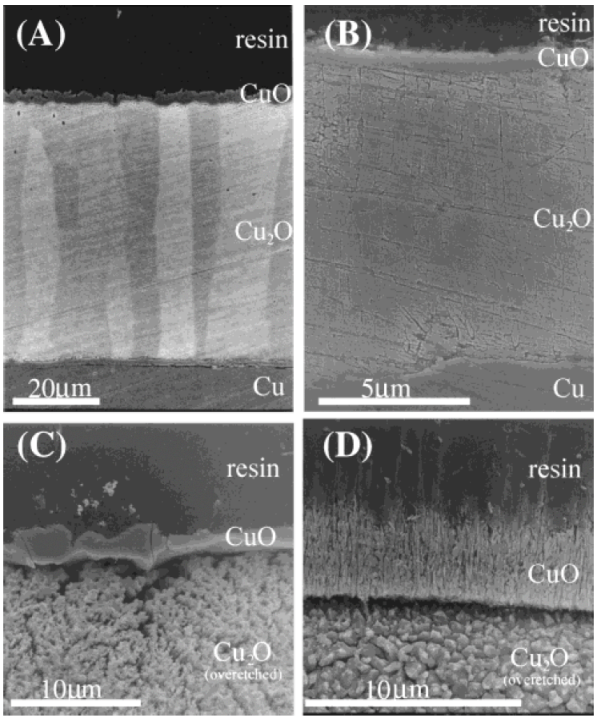


Figure 2-9 (a) Cross-sectional microstructure of the oxide scale formed on high-purity Cu oxidized at 673 K and 1073 K, showing the development of an inner Cu2O layer and an outer CuO layer, with the lower-temperature sample exhibiting a whisker-like CuO structure [66].

Among alloying elements, Ag has the smallest impact on the conductivity and radiation loss of copper [67,68]. In addition, Ag possesses high oxidation resistance which can be a promising candidate to improve oxidation resistance of Cu components [64]. Cu and Ag are completely soluble in Cu–(<5wt.%)Ag alloys at temperatures above 600 °C. Figure 2-10 shows the mass gain change as a function of time for three Cu–5%Ag powders after oxidation at 250 °C as well as their electrical conductivity change with oxidation time. The oxidation rate for both Cu–Ag powder samples (initial and aged samples) begins very slowly, whereas the mass gain of Cu powder increases more rapidly right from the start. In addition, Cu–Ag powder samples exhibit the least reduction in electrical conductivity with increasing oxidation time [64].

Despite these promising results, it is important to highlight that almost all existing studies on the oxidation behavior of Cu and Cu–Ag alloys have been conducted on conventionally processed materials (cast, rolled, or extruded). To date, there is no systematic study available on the oxidation resistance of LPBF-made Cu and Cu–Ag alloys. Given the rapid solidification, fine microstructures, and potential for oxide dispersoid formation during LPBF, it is expected that the oxidation behavior could differ significantly from that of conventionally processed counterparts. This gap in the literature motivates the investigation conducted in this thesis, focusing on the oxidation performance of LPBF-made Cu–Ag alloys at elevated temperatures.

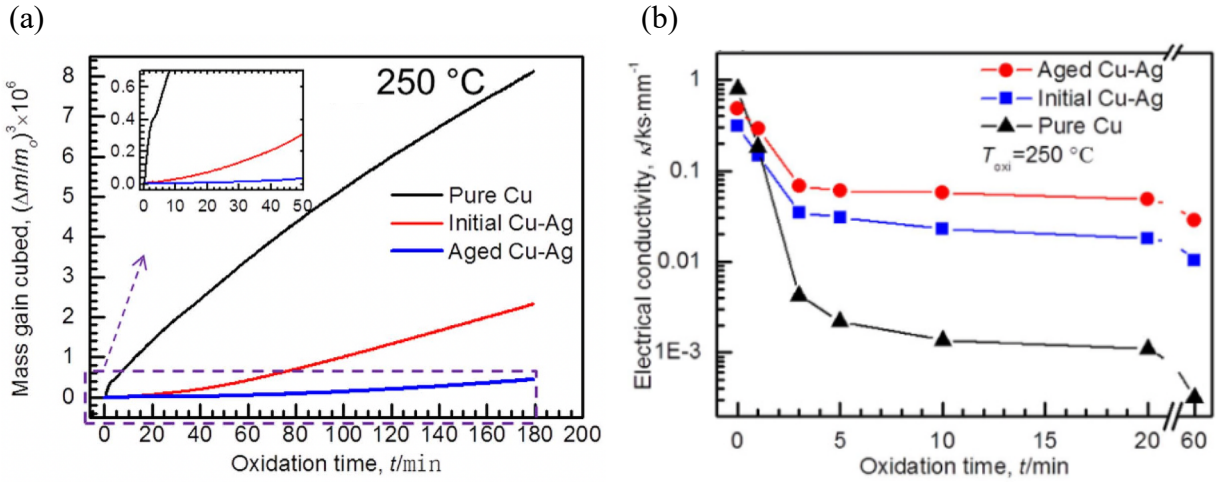


Figure 2-10 (a) oxidation rate of pure Cu and Cu–5Ag powders at 250°C and (b) their electrical conductivity [64].

2.9. Summary and research gap

LPBF of Cu and its alloys faces challenges due to high thermal conductivity and low infrared laser absorptivity, which hinder efficient melting and densification. Recent advances, such as higher laser powers and tailored powders, have improved the processability of Cu alloys, but fully optimizing the process still requires careful control over parameters such as laser power, scan speed, hatch spacing, and layer thickness.

For Cu–Cr–Zr, previous work shows that LPBF can produce high-density parts with refined microstructures, but most process optimization efforts rely on trial-and-error rather than systematic statistical approaches like DOE. Additionally, there is limited understanding of how LPBF processing affects the high strain rate mechanical performance of Cu–Cr–Zr, especially in the as-printed condition.

For Cu–Ag, the oxidation resistance and minimal conductivity loss make it a promising alloy for electrical and thermal applications. However, nearly all oxidation studies focus on conventionally processed Cu–Ag, with no dedicated studies on the high-temperature oxidation behavior of LPBF-made Cu–Ag alloys. The rapid solidification and unique microstructure created by LPBF could significantly influence oxide scale formation and oxidation kinetics, requiring specific investigation.

In summary, the key gaps addressed in this thesis are the lack of systematic process optimization and dynamic mechanical property evaluation for LPBF-made Cu–Cr–Zr, and the absence of studies on the high-temperature oxidation behavior of LPBF-made Cu–Ag alloys. Filling these gaps will advance the understanding of process-structure-property relationships in LPBF of Cu alloys, supporting their broader adoption in demanding structural, electrical, and thermal applications. While the current literature provides a solid foundation for understanding the potential of Cu-based alloys in AM, it lacks critical insight into how LPBF-specific microstructures affect their mechanical and environmental performance. Addressing these gaps is essential for developing application-ready Cu components tailored for applications with enhanced mechanical properties and oxidation resistance.

To this end, the following chapters are structured to directly tackle these unresolved questions. Chapter 3 focuses on statistical process optimization for Cu–Cr–Zr using DOE methods. Chapter 4 investigates the dynamic mechanical behavior of optimized Cu–Cr–Zr samples under high strain rate conditions. Chapter 5 explores the feasibility and process development of in-situ alloying of Cu–Ag using LPBF. Chapters 6 and 7 then investigate oxidation resistance of LPBF-made Cu–Ag, examining how processing influences oxide scale formation and long-term performance at elevated temperatures. This progression is designed to build a comprehensive understanding of process–structure–property relationships in LPBF of Cu alloys.

Chapter 3. High-power laser powder bed fusion of Cu–Cr–Zr alloy: A comprehensive study on statistical process optimization, microstructure, and mechanical properties[1]

3.1. Overview

This study explores high-power laser powder bed fusion (LPBF) of Cu–Cr–Zr alloy, focusing on optimizing process parameters to achieve high relative density (*RD*) and low surface roughness (S_a). A Plackett-Burman design (PBD) identifies layer thickness, laser power, and scanning speed as the most significant parameters. A response surface method (RSM) with central composite design (CCD) further refines the process, yielding an optimized parameter set with an *RD* of 99.96% and S_a of 13.1 μm. After establishing the optimum process window, the process efficiency is examined by increasing layer thickness, demonstrating higher build rates while preserving high *RD* and acceptable S_a. The samples are evaluated for mechanical properties and microstructural evolution. Microhardness mapping reveals a uniform hardness distribution, with values ranging from 90 to 94 HV. Microstructural analysis shows the grain morphology varies with process parameters; thinner layers tend to produce bimodal distributions, whereas thicker layers promote more uniform grain structures. Crystallographic analysis indicates a strong <001> texture in samples processed at high volumetric energy density (*VED*), while subgrain analysis highlights significant fractions of low-angle grain boundaries, reflecting residual stresses and high dislocation density.

3.2. Introduction

Additive manufacturing (AM) of copper (Cu) and its alloys has garnered attention for its ability to overcome the limitations of traditional manufacturing methods such as casting, forging, and rolling [2]. Among various AM techniques, laser powder bed fusion (LPBF) has revolutionized the production of complex metal components by enabling layer-by-layer fabrication. This approach offers exceptional design freedom, facilitating the production of intricate geometries and internal features, such as cooling channels and lattice structures, that are challenging to achieve with

[1] Submitted to *Journal of Manufacturing Processes*, currently under review.

conventional methods [1]. However, the LPBF process of Cu alloys faces several challenges due to their high thermal conductivity and high reflectivity (~97%) to near-infrared wavelength lasers [2,15]. These properties impede effective energy absorption, leading to defects such as porosity, lack of fusion, and delamination [5,13].

Despite these challenges, high-power LPBF has shown promise in fabricating Cu–Cr–Zr components with enhanced functionality and tailored microstructural characteristics [34,35]. Cu–Cr–Zr alloys, known for their outstanding combination of thermal and electrical conductivity, mechanical strength, and corrosion resistance, are widely used in aerospace, electronics, and energy applications [69]. A critical strategy to address the challenges associated with LPBF of such Cu alloys is the use of high-power lasers, which exceed the standard power levels (~400 W) of conventional LPBF systems [16,26]. Higher laser power delivers more energy to the powder bed, improving melting efficiency and enhancing particle fusion.

Chen et al. [70] highlighted the importance of optimizing parameters such as laser power, scanning speed, and hatch distance to minimize defect formation and improve the quality of LPBF-made parts. Salvan et al. [53] optimized LPBF parameters for Cu–Cr–Zr alloys, achieving a relative density (*RD*) of 99.4% using a laser power of 480 W, a scanning speed of 700 mm/s, and a hatch distance of 100 μm. However, to produce higher-quality parts, achieving a *RD* greater than 99.9% remains critical. Also, the complexity of the LPBF process itself, involving over 100 parameters, underscores the need for precise process parameter optimization to achieve high *RD* and defect-free fabrication [71,72]. Through such optimization, LPBF has emerged as a transformative technique for fabricating advanced Cu–Cr–Zr components with exceptional design flexibility and superior performance.

Material properties and performance are fundamentally influenced by their microstructures, making an understanding of microstructure development during the LPBF process crucial for tailoring and optimizing material characteristics [33,54,73]. Ma et al. [49] investigated how scanning speed and hatch distance affect grain size and anisotropy in LPBF-made components. They observed elongated grains aligned with the building direction (BD), a characteristic associated with the rapid cooling and thermal gradients of LPBF. Optimized scanning speeds and hatch spacings were shown to reduce defects, refine microstructures, and enhance yield strength and hardness.

Similarly, Buchmayr et al. [35] analyzed the formation of cellular structures and sub-grains in Cu–Cr–Zr alloys processed via LPBF. Their work emphasized that the anisotropic grain structure, driven by localized melting and thermal gradients, could be improved through precise parameter control. This approach not only promoted uniform microstructure and reduced porosity but also enhanced yield strength and ductility.

Despite significant advancements in LPBF of Cu–Cr–Zr alloys, a lack of systematic optimization across a wide parameter range leads to variability in part quality and process inefficiencies. Furthermore, the effects of increased layer thickness (*LT*) on material properties and energy efficiency remain insufficiently explored. Therefore, the present study focuses on the comprehensive optimization of LPBF process parameters for Cu–Cr–Zr alloys with high-power lasers through a statistically driven approach.

The primary objectives are to achieve high *RD* and minimal surface roughness (S_a), which are critical for ensuring mechanical integrity and functional performance. A novel optimization strategy is implemented, employing Plackett–Burman design (PBD) to screen 23 adjustable parameters, followed by central composite design (CCD) for detailed response surface methodology (RSM) analysis. This two-step approach systematically evaluates and prioritizes process parameters, providing a robust framework for optimizing LPBF conditions. Moreover, sustainability considerations are addressed by analyzing the effects of increased *LT* on energy efficiency. After determining the optimized parameters, microhardness testing and electron backscatter diffraction (EBSD) are used to examine the effects of process parameters on mechanical properties and grain morphology. By optimizing process parameters and introducing innovative approaches to process control, this research contributes to the growing body of knowledge on LPBF-made Cu–Cr–Zr alloys and facilitates their broader industrial adoption.

3.3. Materials and methods

3.3.1. Material

The material utilized in this study was plasma-atomized C18150 (Cu–1Cr–0.5Zr (in wt. %)) powder, supplied by AP&C. This pre-alloyed powder is specifically designed for AM and provides excellent thermal and mechanical properties. Its composition leverages the high thermal and electrical conductivity of Cu, enhanced by the strengthening effects of Cr and Zr.

Figure 3-1 provides an analysis of the virgin powder. Scanning electron microscopy (SEM) image (Figure 3-1a) reveals spherical shape and smooth surface of powder particles, typical of plasma-atomized powders. Such morphology is critical for ensuring uniform layer deposition, reducing defects during the LPBF process, and promoting reliable powder flowability. The particle size distribution (PSD) analysis (Figure 3-1b) confirms the powder's suitability for LPBF. The measured D_{10}, D_{50}, and D_{90} values are 16.8 µm, 37.6 µm, and 64.7 µm, respectively, indicating a narrow distribution range. This balance between flowability and packing density enhances the powder's performance during the LPBF process.

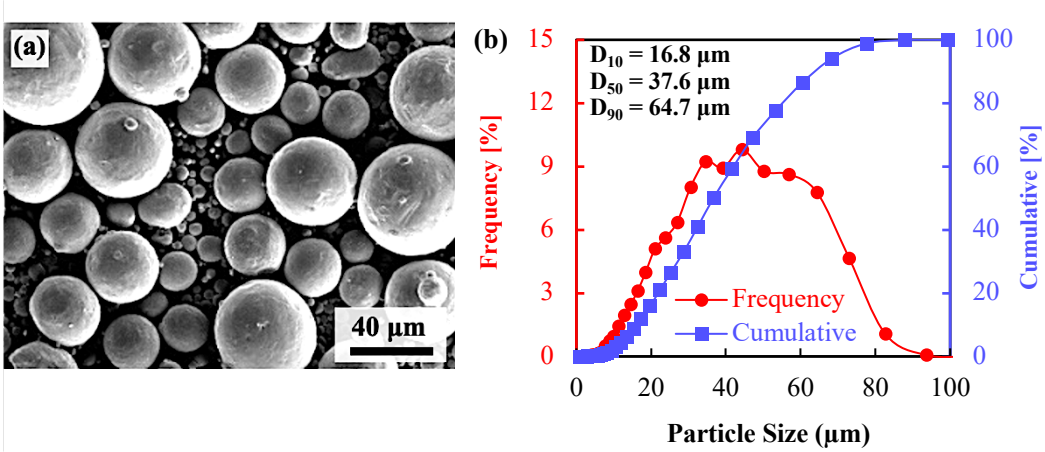


Figure 3-1 (a) SEM image of the virgin pre-alloyed powder of Cu–Cr–Zr, showcasing its morphology, alongside (b) the corresponding particle size distribution (PSD) analysis.

3.3.2. LPBF fabrication and methodology

The LPBF process was performed using an EOS M290 machine equipped with a high-power 1 kW Ytterbium continuous fiber laser, operating at a wavelength of 1060 nm and a spot diameter of ~80 µm. The building process was conducted under a high purity Ar atmosphere, ensuring an oxygen content of less than 0.1% within the process chamber. To optimize the LPBF process parameters, a systematic statistical design of experiments (DOE) was employed, including Plackett-Burman and central composite designs.

The PBD was employed as a screening tool to identify the most significant process parameters influencing key responses such as *RD* and S_a. By evaluating the individual effects of multiple parameters without accounting for their interactions, the PBD efficiently reduces the dimensionality of the experimental space, making it a cost-effective method for preliminary investigations [74].

Following the screening phase, a CCD was used to refine the parameter of the optimization process. Unlike the PBD, the CCD incorporates quadratic and interaction terms, enabling a more detailed exploration of the relationships between process parameters and the responses. This allows for a more precise determination of the optimal parameter combinations, as it captures nonlinear effects and interactions that influence the outcome.

By integrating the PBD and CCD, the DOE framework ensures a systematic and comprehensive optimization process tailored to the LPBF of Cu–Cr–Zr alloy. The following sections will provide a detailed explanation of the application of PBD and CCD in optimizing *RD* and S_a of the LPBF-made Cu–Cr–Zr alloy.

3.3.2.1. Screening key parameters using PBD

PBD with 23 process parameters were generated to identify which process parameters have the most significant impacts on *RD* and S_a of the coupons printed by the LPBF process. The input parameters were selected based on the process knowledge. A list of process parameters is provided in Table 3-1 which is subdivided into pre-exposure, post-exposure, skin, core, and additional process parameters. Each parameter is identified by a code that will be used to refer to the parameter.

It is noteworthy to point out that printing pre-exposure is the first step, followed by fabrication of skin and core of parts, and finally post-exposure. Using the PBD approach, 23 parameter designs are selected to be analyzed in at least 24 treatment combinations. To check the presence of curvature in the model, a set of center points was also added to the conditions. Due to the fact that geometry (W: Cube and Cylinder) and scanning strategy (X: Stripe and Chess) are qualitative parameters without center points, they have only two possible modes. Therefore, all other center points must be treated with these two input parameters. This resulted in 28 conditions (Table A1 PBD matrix for screening of 23 process parameters in LPBF where “+” and “-” symbols represent high and low parameter values, respectively.), and with replication, a total of 56 samples were produced for PBD.

Table 3-1 List of process parameters selected for the PBD in the LPBF screening

Category	#	Code	Parameter	Low	High
Pre-exposure	1	A	Contour Power [W]	0	100
	2	B	Contour Speed [mm/s]	700	1500
Post-exposure	3	C	Contour Power [W]	0	180
	4	D	Contour Speed [mm/s]	700	1500
Skin-exposure	5	E	*Specific Energy [J/mm^2]	5	11
	6	F	Power [W]	350	750
	7	G	Hatch Distance [mm]	0.10	0.15
	8	H	Stripe Width [mm]	4	12
	9	J	Stripe Overlap [mm]	0.01	0.15
	10	K	Skin Thickness X/Y [mm]	0.2	1
	11	L	Skin Thickness Z [mm]	0.2	1
Core-exposure	12	M	*Specific Energy [J/mm^2]	5	11
	13	N	Power [W]	400	800
	14	O	Hatch Distance [mm]	0.12	0.18
	15	P	Stripe Width [mm]	4	12
	16	Q	Stripe Overlap [mm]	0.01	0.15
Support	17	R	Support Area Spacing [mm]	0.6	0.8
	18	S	Support Height [mm]	0	3
Additional	19	T	Layer Thickness [mm]	0.02	0.06
	20	U	Angle [deg]	0	90
	21	V	Print Location [mm]	10	90
	22	X	Hatching Method	Stripes	Chess
	23	W	Geometry	Cylinder	Cube

Among the 23 parameters selected for PBD screening, specific energy (*SE*) is included for both skin-exposure (E) and core-exposure (M) due to its fundamental role in governing energy input per unit area. *SE* is defined as power (P_{laser}) divided by the product of scanning speed (V_{laser}) and hatch distance (*HD*) using Equation (3-1):

$$SE = \frac{P_{laser}}{V_{laser} \cdot HD} \quad [\frac{J}{mm^2}] \tag{3-1}$$

The limits of *SE* values are constrained by material properties to ensure sufficient melting while preventing boiling. If *SE* is too low, incomplete melting leads to lack-of-fusion defects and increased porosity. Conversely, excessive *SE* can cause overheating, keyhole formation, and material vaporization, negatively affecting both density and surface finish [75]. Optimizing *SE* ensures a balanced energy input, allowing for high *RD* and controlled S_a while maintaining process stability.

Figure 3-2 provides a schematic representation of the process parameters listed in Table 3-1, offering a comprehensive visualization of the critical factors considered in PBD for screening significant parameters. Key energy input parameters, such as P_{laser}, V_{laser}, *LT*, and *HD*, are depicted in Figure 3-2a and b.

In PBD, two geometries, cylinder and cube, were selected as test parts, with their dimensions detailed in Figure 3-2c. These geometries were specifically chosen to evaluate the influence of shape and design on the overall surface quality, allowing for a comprehensive assessment of how geometry interacts with various process parameters.

Two scanning strategies with patterns of stripes and chessboard are used with corresponding parameters such as stripe width and overlap, as shown in Figure 3-2d. The parts are exposed using both skin and core strategies, which share similar parameters but target different regions of the build. The skin region, a smaller area with a thickness ranging from 0.2 mm to 1 mm (as listed in Table 3-1), is particularly advantageous for refining surface quality and reducing porosity at the outer layers. This is achieved through precise control of laser exposure in x, y, and z directions. The core exposure primarily focuses on the bulk of the part, allowing for optimization of internal density and overall structural integrity. Together, these strategies enable tailored control of surface quality and bulk properties.

Figure 3-2e depicts the layout of parts on the building plate, with the building area divided into regions based on the distance from the center. This approach facilitates the evaluation of location-based variations in printed part properties. Distances of 10 mm, 50 mm, and 90 mm from the center were targeted. However, due to space constraints, samples intended for the 10 mm position were placed at distances ranging from 10 mm to 30 mm, as indicated in Figure 3-2e. The support structure design, shown in Figure 3-2f, incorporates critical parameters such as support height and area spacing. The samples with a support height of 0 mm (Table 3-1) indicate parts printed without supports, enabling an evaluation of the effect of support structures on part quality.

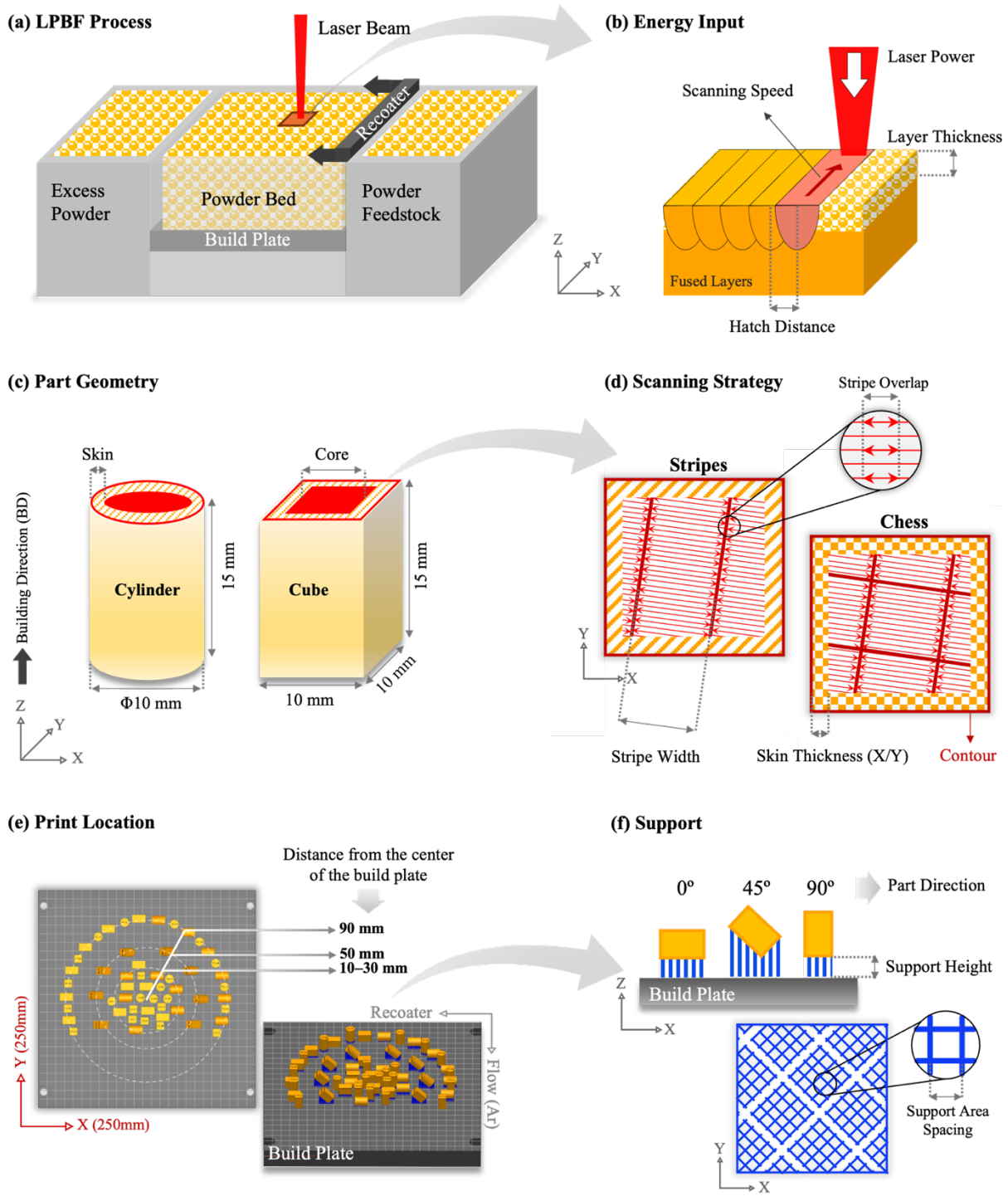


Figure 3-2 Schematic representation of the LPBF process parameters used in the Plackett-Burman design (PBD). These visualizations align with the process parameters listed in Table 3-1.

3.3.2.2. Optimizing parameters using CCD

After screening process parameters, statistical response optimization was conducted using CCD to find parameters that result in the highest achievable relative density and the lowest possible surface roughness. CCD is a fractional factorial design commonly used in response surface models (RSM), which enables analysis of first-order (linear), second-order (quadratic), and interaction effects. The RSM equation for the second-order CCD is given by Equation (3-2):

$$Y = \beta_0 + \sum_{i=1}^{k} \beta_i x_i + \sum_{i=1}^{k} \beta_{ii} x_i^2 + \sum \sum_{i<j} \beta_{ij} x_i x_j + \varepsilon \quad (3\text{-}2)$$

where x_i are the factors or variables, the terms β_i, β_{ii}, and β_{ij} are constant coefficients, and ε is the random error. Constant coefficients are determined using the least squares method. Linear, quadratic, and interaction terms appear in x_i, x^2_i, and $x_i x_j$, respectively. The center points in CCD are augmented by a set of axial points called "star points", which are strategically positioned to allow the estimation of curvature in RSMs. The placement of these star points is determined by the parameter α, which defines their distance from the center of the experimental design space. The value of α influences the type of CCD: circumscribed ($\alpha > 1$) , inscribed ($\alpha < 1$), or face-centered ($\alpha = \pm 1$) [76].

In this study, a face-centered CCD was employed, meaning the axial points were positioned at the centers of each face of the factorial cube, corresponding to the midpoints along each axis. The CCD incorporated nine parameters identified as significant through the initial the PBD analysis. The use of a two-level quarter fractional factorial approach reduced the number of conditions from $2^9 = 512$ (for a full factorial design) to $2^{9-2} = 128$. These were supplemented with axial points (18 conditions) and center points (10 conditions) to account for non-linear effects and estimate experimental variability. Ultimately, the design included a total of 156 conditions, balancing efficiency with the ability to model complex parameter interactions and optimize process outcomes.

3.3.2.3. Evaluating optimized parameters *through experimental fabrication*

Following statistical optimization to maximize *RD* and minimize S_a, four samples were fabricated using the best-achieved parameters to validate the accuracy and reliability of the optimized process conditions. This validation step ensures that the predictive models developed through CCD accurately reflect actual LPBF fabrication outcomes.

In the final stage, the process window identified through optimization was used to assess the feasibility of higher productivity by increasing the *LT*. Six parameter sets within the optimized process window were selected for sample fabrication. After fabrication, porosity, microhardness, and microstructural characteristics were analyzed in detail. This step aims to determine whether higher *LT* can be implemented without compromising part quality, mechanical performance, or process stability.

3.3.3. Characterization

The density of the printed samples from the PBD and CCD experiments was determined using Archimedes method. This involved measuring the weight of the samples in both air and deionized (DI) water with an analytical balance precise to 0.01 mg. The density was averaged from six measurements per sample to ensure reliability. The *RD* of the samples was then calculated by comparing the measured density ($\rho_{measured}$) with theoretical density ($\rho_{theoretical}$), using Equation (3-3):

$$RD = \rho_{measured}/\rho_{theoretical}\ [\%] \tag{3-3}$$

The S_a of the printed samples was quantified using a Keyence VK-X250 confocal microscope with non-contact laser profilometry, which has a vertical accuracy of 0.2 μm. The reported S_a values were averaged from five measurements per sample.

Following the optimization of process parameters using PBD and CCD, the process window was refined to identify optimal settings. Two samples were fabricated using the best parameters within this optimized window to validate the model. The *RD* of these samples was initially measured using the Archimedes method and further analyzed using high-resolution X-ray computed tomography (CT). The CT scans were performed with a ZEISS Xradia 520 Versa system, achieving a voxel size of 15 μm. This provided detailed 3D imaging of the internal structure, enabling a comprehensive evaluation of porosity and internal defects. The CT data was processed and analyzed using Dragonfly software to calculate *RD* and visualize defects, ensuring precise, non-destructive characterization.

For microhardness and microstructural evaluation, the samples were printed within the optimized process window using *LT*s of 20 μm, 40 μm, and 60 μm. Microhardness measurements were conducted using a Clemex CMT hardness tester, applying a load of 100 gf with a dwell time of 10 seconds. The results provided insights into the influence of process parameters on the mechanical properties of the LPBF-made Cu–Cr–Zr alloy. The microstructural analysis was conducted using EBSD on cross-sections perpendicular to the BD.

The sample preparation involved grinding with SiC abrasive papers from 100 to 2400 grit, followed by polishing with a 1-μm MD-Nap abrasive. Final polishing was performed using a Buehler VibroMet2 machine for 5 hours with a non-crystallizing amorphous 0.02 μm colloidal silica suspension to prepare samples for EBSD. Data acquisition was carried out using a TESCAN VEGA3 SEM equipped with BRUKER EBSD detectors, and subsequent analysis was performed with MTEX software. Low-angle grain boundaries (LAGBs) were defined as those with $5° \leq \theta \leq 15°$, while high-angle grain boundaries (HAGBs) were defined as those with $\theta > 15°$. The grain orientation and grain size distribution were then analyzed to understand the influence of process parameters on the microstructure.

3.4. Results and discussion

3.4.1. Statistical LPBF process parameter optimization

3.4.1.1. Identifying key parameters using PBD

To optimize the process parameters of LPBF for Cu–Cr–Zr alloy, PBD involving 23 process parameters (Table 3-1) was employed to screen the key factors influencing *RD* and S_a. The results were analyzed using Minitab® to generate Pareto charts and residual plots, which are pivotal for understanding the statistical significance of each parameter. Figure 3-3 displays the Pareto charts of the standardized effects of the process parameters for *RD* (Figure 3-3a) and S_a (Figure 3-3b), ranking from the largest to the smallest impact.

The reference line at 2.05 represents the statistical significance threshold, which is determined based on the chosen significance level (α = 0.05) and the corresponding t-distribution. Any parameter with a standardized effect exceeding this threshold is considered statistically influential, meaning it has a significant effect on the respective response. Conversely, parameters below this threshold are regarded as less impactful within the studied conditions.

According to the analysis of variance (ANOVA) results shown in Figure 3-3, the most significant parameters were identified as specific energy of skin-exposure (E) for *RD* and layer thickness (T) for S_a.

Figure 3-3c and d present standardized residual plots, which validate the adequacy of the statistical model by visualizing the residuals (the differences between observed and predicted values) across the observation order. The absence of discernible patterns in these plots indicates the residuals are random and independent, confirming that the model assumptions are met. This randomness is essential to ensure the model is free from systematic biases and can reliably predict outcomes. While four residuals fell outside the acceptable range of -2 to +2, further analysis demonstrated that excluding these outliers did not impact the significance of the identified key parameters (specific energy of skin exposure for *RD* and layer thickness for S_a).

The outliers are likely attributed to unaccounted process variability, such as fluctuations in P_{laser}, inconsistencies in powder characteristics, or environmental factors during the LPBF process, which were not explicitly captured in the model. In addition, interaction effects between process parameters may have contributed to the outliers. Complex interactions, where two or more parameters jointly influence the response, could produce deviations that the model does not fully account for, as it may be limited in capturing such intricate relationships.

However, it is important to note that at this stage, the primary goal of the PBD is to screen and identify the most significant parameters influencing *RD* and S_a. Interactions between parameters are not considered in this step, as the focus is on isolating the main effects in a cost-effective and efficient manner. This aligns with the primary purpose of the PBD as a preliminary screening tool. In the next phase, CCD will build upon this foundation by refining the parameter optimization process, explicitly accounting for interactions and nonlinear effects to achieve a comprehensive optimization.

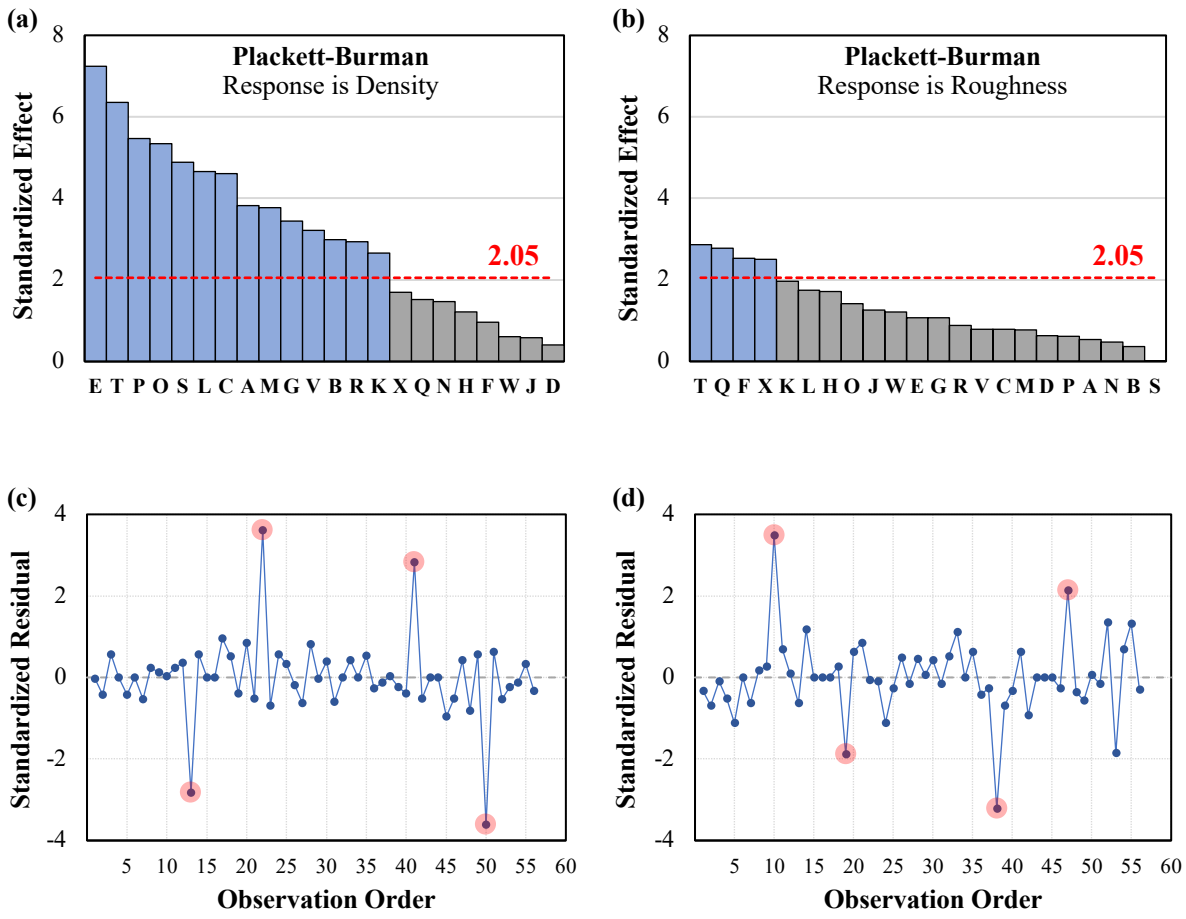


Figure 3-3 Pareto chart of the standardized effects and residual for (a,c) *RD* and (b,d) S_a in the PBD analysis. These charts identify the most significant process parameters influencing *RD* and S_a in the LPBF process of Cu–Cr–Zr alloy.

3.4.1.2. Refining parameters using CCD

Table 3-2 outlines the parameters selected for the CCD used in the subsequent optimization phase to achieve maximum *RD* and minimum S_a in the LPBF process for Cu–Cr–Zr alloy. These parameters were shortlisted based on the initial screening conducted using the PBD. This was made by focusing on the factors that exhibited a strong positive effect on both *RD* and S_a, as determined by the Pareto charts (Figure 3-3a and b). The design involved a total of 156 experimental conditions, of which 10 were center points used to assess the model's reproducibility and validate its predictive accuracy. The center points, representing mid-range values of the selected parameters, provide critical information on the experimental variability and allow for the estimation of curvature in the response surface.

It should be noted that in PBD, *SE* was included as a critical factor to ensure that the process remained within a certain *SE* range, preventing combinations of low V_{laser}, high power, and low *HD* that could lead to excessive energy input and potential failures. However, in CCD, *SE* was excluded and replaced by its individual components (P_{laser}, V_{laser}, and *HD*) allowing for a more precise determination of their optimal values directly. This strategic shift from using *SE* as a combined factor in PBD to analyzing its individual components in the CCD enabled a more detailed exploration of their effects.

Table 3-2 List of process parameters selected for the CCD in the LPBF optimization

Category	#	Code	Parameter	Low	High
Post-exposure	1	A	Contour Power [W]	300	500
Skin-exposure	3	B	Scanning Speed [mm/s]	600	800
	4	C	Power [W]	300	500
	5	D	Hatch Distance [mm]	0.08	0.12
Core-exposure	5	E	Scanning Speed [mm/s]	800	1000
	6	F	Power [W]	700	900
	7	G	Hatch Distance [mm]	0.16	0.20
	8	H	Stripe Overlap [mm]	0.12	0.16
Additional	9	J	Layer Thickness [mm]	0.02	0.06

The remaining 14 parameters were held constant during the CCD experiments. The details of these constant parameters are provided in Table 3-3. All samples in CCD were fabricated using the same geometry, cube with dimensions of 10 mm × 10 mm × 10 mm, and scanning strategy of stripes. No support structures were used, and no pre-exposure steps were applied.

Table 3-3 Fixed process parameters and their corresponding values used in the CCD experiments

Category	#	Parameter	Value
Pre-exposure	1	Contour Power [W]	0
	2	Contour Speed [mm/s]	0
Post-exposure	3	Contour Speed [mm/s]	400
Skin-exposure	4	Stripe Width [mm]	12
	5	Stripe Overlap [mm]	0.06
	6	Skin Thickness X/Y [mm]	0.5
	7	Skin Thickness Z [mm]	0.5
Core-exposure	8	Stripe Width [mm]	12
Support	9	Support Area Spacing [mm]	0
	10	Support Height [mm]	0
Additional	11	Angle [deg]	0
	12	Print Location [mm]	Random
	13	Hatching Method	Stripes
	14	Geometry	Cube ($10\times10\times10$ mm^3)

Figure 3-4 presents the results of CCD for optimizing *RD* and S_a in LPBF-made Cu–Cr–Zr alloy. The colormaps illustrate the impact of varying *LT*, skin, and core parameters on these responses, offering insights into how process parameters influence density and surface quality.

Each point on the colormaps represents a specific combination of process parameters tested in the CCD experiments. These parameter sets are labeled as a_i–p_i (i = 1–16), where *a–p* denote the column identifiers, and i = 1–16 represents the row numbers on the colormaps. These labels uniquely identify the experimental conditions, which include variations in P_{laser}, V_{laser}, *LT*, *HD*, and other selected factors. The full details of these parameter combinations are provided in Table B1 Parameter codes corresponding to Figure 3-4, where each code (a_i–p_i, #i = 1–16) represents the process parameters for samples printed in the CCD experiment..

The color spots on the colormaps represent parameter combinations within the fractional factorial design used in this study. Unlike a full factorial design, where all possible combinations of parameters are tested (resulting in 2^9 = 512 conditions for nine factors), this study employed a quarter fractional factorial design, significantly reducing the number of experimental conditions to 156 while still capturing essential trends and interactions. This approach is not only cost-effective and time-efficient but also minimizes material usage and experimental complexity. Consequently, the colormaps are not fully populated with colors, as only a subset of the parameter space was explored in the design. Despite this, the fractional factorial design provides sufficient information for identifying critical parameters and optimizing process outcomes.

The colormap for *RD* (Figure 3-4a) demonstrates that, overall, samples fabricated with a *LT* of 20 μm exhibit higher density compared to those with thicker *LT* of 60 μm. Samples with a 20 μm *LT* (Figure 3-4d), such as sample k_1 (Figure 3-4e), consistently achieve high *RD* values, with most samples falling within the range of 98%–99%. This highlights the advantages of thinner layers, where the energy input is more evenly distributed, ensuring full melting and minimizing porosity. These findings align with literature emphasizing that thinner layers allow for better control of energy absorption and melting dynamics in LPBF of metals, leading to more uniform density across the sample [77].

In contrast, samples fabricated with a 60 μm *LT* (Figure 3-4b) exhibit a broader *RD* range, typically between 96%–99%, indicating greater variability in density. The wider range observed for thicker layers reflects the increased challenges in achieving uniform fusion, as higher *LT*s require higher energy input to avoid defects such as porosity [78].

Despite these challenges, some parameter combinations for 60 μm layers, such as sample k_1 (Figure 3-4c), achieved a high *RD* of 99.34%. While such high density is less common at this *LT*, it demonstrates the potential for optimizing thicker layers to produce high-quality builds. Achieving high *RD* with thicker layers is particularly promising, as it offers opportunities for reducing processing time and energy consumption while maintaining satisfactory part quality. However, the variability underscores the need for precise parameter control to overcome the inherent difficulties associated with thicker layers.

The colormaps for S_a (Figure 3-4f) further support this observation. The samples fabricated with 20 μm *LT* generally exhibit smoother surfaces and lower S_a values. For example, the samples fabricated with 60 μm layers, such as i_{13} (Figure 3-4h) and m_7 (Figure 3-4i) with respective S_a of 18.9 μm and 45.6 μm, exhibit a wider range of roughness values, extending towards higher S_a. At *LT* of 20 μm, sample e_5 (Figure 3-4k) achieves an S_a of 13.5 μm, whereas the roughest surface within this thickness, sample m_2 (Figure 3-4l), has an S_a of 35.1 μm. This narrower range of roughness values indicates better control over surface finish in thinner layers. This is consistent with studies showing that thinner layers result in better layer-to-layer bonding and smoother surface finishes due to more precise energy distribution [79,80]. While thicker layers increase roughness due to uneven melting and powder particle adhesion on the surface [80]. The broader variability in roughness for thicker layers reflects challenges in maintaining uniform melting and avoiding surface irregularities, such as stair-stepping.

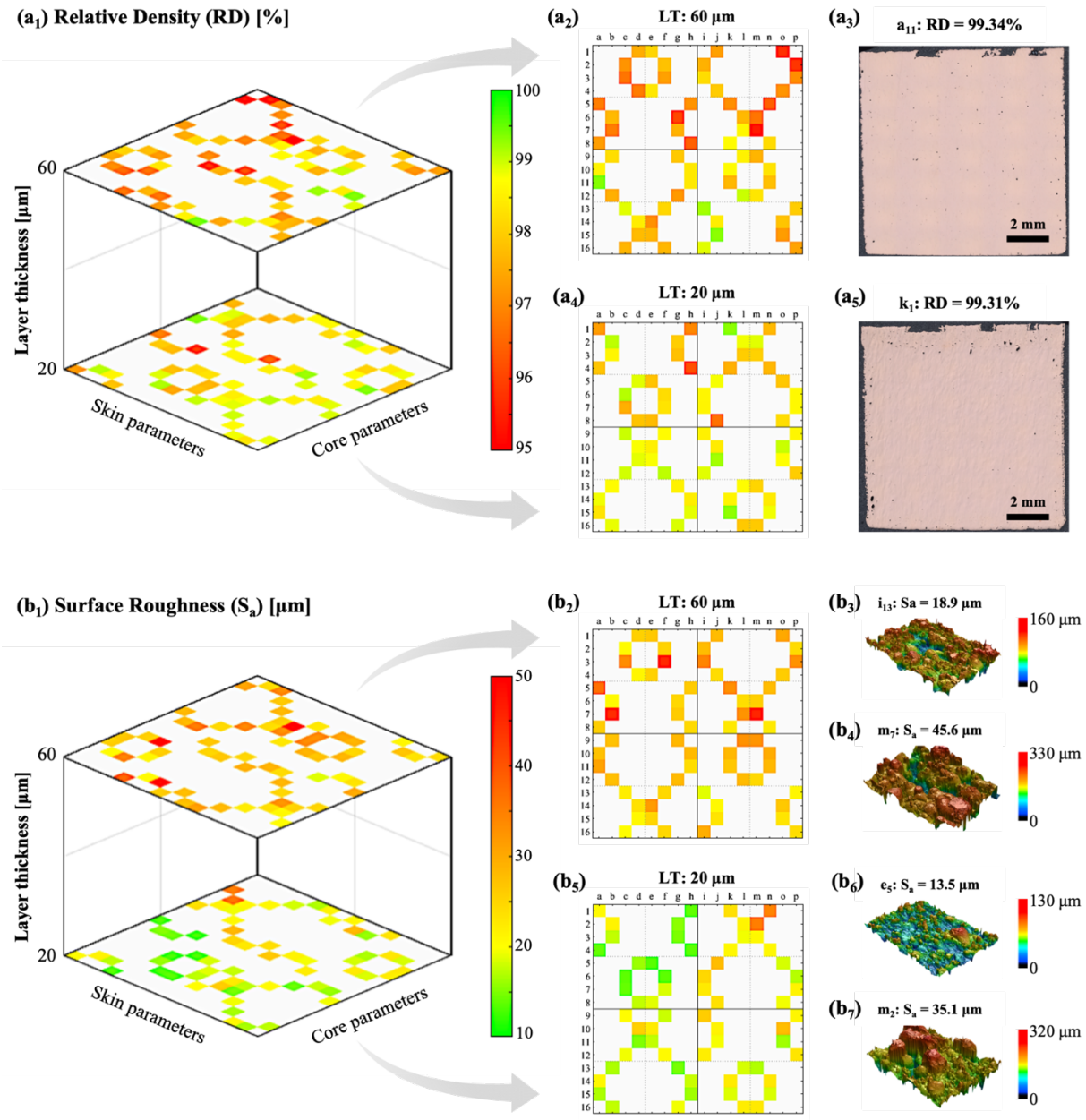


Figure 3-4 Results of CCD for optimizing *RD* and S_a in LPBF-made Cu–Cr–Zr alloy. (a) 3D colormap showing *RD* across combinations of *LT*, skin, and core parameters: (b) 2D colormap for *LT* of 60 µm with an example of (c) high *RD* (99.34%); and (d) 2D colormap for *LT* of 20 µm with an example of (e) high *RD* (99.31%). (f) 3D colormap showing S_a across combinations of *LT*, skin, and core parameters: (g) 2D colormap for *LT* of 60 µm with examples of (h) minimum S_a (18.9 µm) and (i) maximum S_a (45.6 µm); and (j) 2D colormap for *LT* of 20 µm with examples of (k) minimum S_a (13.5 µm) and (l) maximum S_a (35.1 µm). Each point on the colormaps corresponds to a unique parameter set, identified by a_i–p_i (row #i = 1–16), with details provided in Table B1 Parameter codes corresponding to Figure 3-4, where each code (a_i–p_i, #i = 1–16) represents the process parameters for samples printed in the CCD experiment..

The trends observed in *RD* and S_a become even more evident when the results are analyzed as a function of volumetric energy density (*VED*). *VED* is defined as SE divided by *LT* using Equation (3-4):

$$VED = \frac{P_{laser}}{V_{laser}.HD.LT} \ [\frac{J}{mm^3}] \tag{3-4}$$

VED directly influences the melting, fusion, and solidification behavior of the material during the LPBF process, a higher P_{laser} and a slower V_{laser} can effectively provide heat input that facilitates the melting of high reflective Cu powder during LPBF [14,17]. This, in turn, impacts the structural integrity, density, surface quality, and overall uniformity of the fabricated parts.

Figure 3-5 provides a deeper understanding of the relationship between *VED* and material properties, highlighting its critical role in optimizing LPBF-made components. In Figure 3-5a, *RD* is plotted against the *VED* of core exposure, as the core constitutes the largest volume of the part and predominantly determines internal porosity. For samples with a 20 µm *LT*, *RD* values exhibit a consistent trend, with most samples exceeding 97% and showing minimal variation. In contrast, for a 60 µm *LT*, *RD* values vary more widely, ranging from 95% to 99%, reflecting the challenges of achieving uniform fusion in thicker layers.

Similarly, in Figure 3-5b, S_a is plotted against the *VED* of skin exposure, as the skin governs the external surface quality, making its energy input critical for a smooth finish. For the 20 µm *LT*, S_a values are more consistent, with smoother surfaces observed across most samples. In comparison, the 60 µm *LT* demonstrates greater variability in S_a values, with some samples exhibiting rougher finishes. However, it is important to note that in the CCD experiment, multiple parameters are varied simultaneously, making it challenging to isolate and compare the effects of individual factors in the traditional sense. This complexity is inherent in fractional factorial designs, such as the quarter fractional factorial used here, which examines a subset of possible combinations to efficiently explore the parameter space. Therefore, in the following sections, the results will be further analyzed statistically to derive key insights.

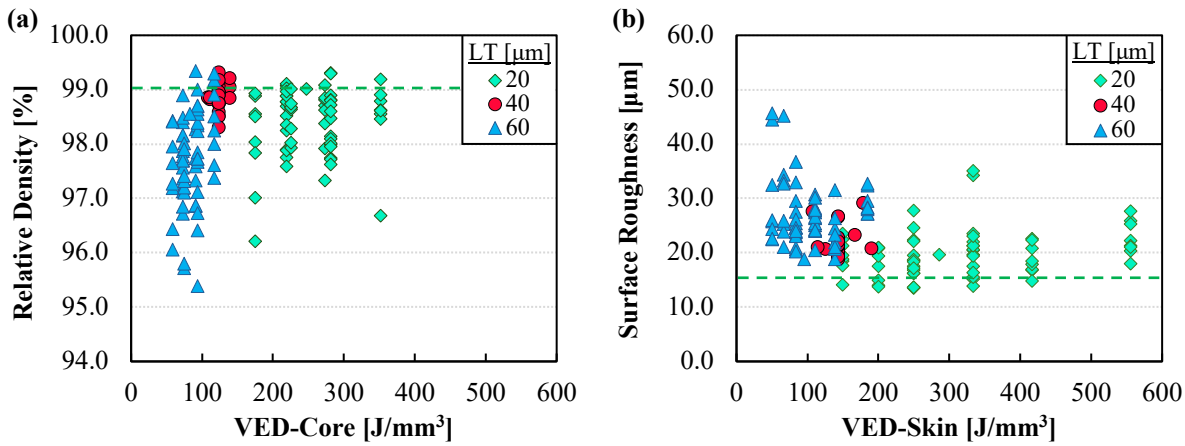


Figure 3-5 Results of CCD showing (a) *RD* changes in terms of *VED* for core exposure and (b) S_a changes in terms of *VED* for skin exposure at different *LT*s of 20 µm, 40 µm, and 60 µm.

To thoroughly analyze the CCD results, Pareto charts were initially generated using Minitab® to rank the significance of process parameters within the full quadratic model (Figure 3-6a for *RD* and Figure 3-6b for S_a). The full quadratic model includes linear terms, squared terms, and interaction terms to account for potential dependencies between variables and the curvature in the response surface. Of the 54 terms included in the model, only the top 25 most significant terms are displayed in the charts, ranked by their level of importance. Terms with P-values greater than 0.05 were considered statistically insignificant and are therefore not shown. This type of model is particularly advantageous when the effects of one parameter depend on another, or when capturing complex curvature in the response surface is essential.

However, the Pareto charts (Figure 3-6a and b) reveal that many second-order terms are statistically insignificant, which can diminish the model's overall effectiveness. To address this issue, the models were refined by removing the non-significant second-order terms and retaining only the significant linear and interaction terms. This refinement improved the models' alignment with the physical processes of LPBF and enhanced their predictive accuracy. The updated models (linear + interaction terms) are represented by new Pareto charts in Figure 3-6c for *RD* and Figure 3-6d for S_a.

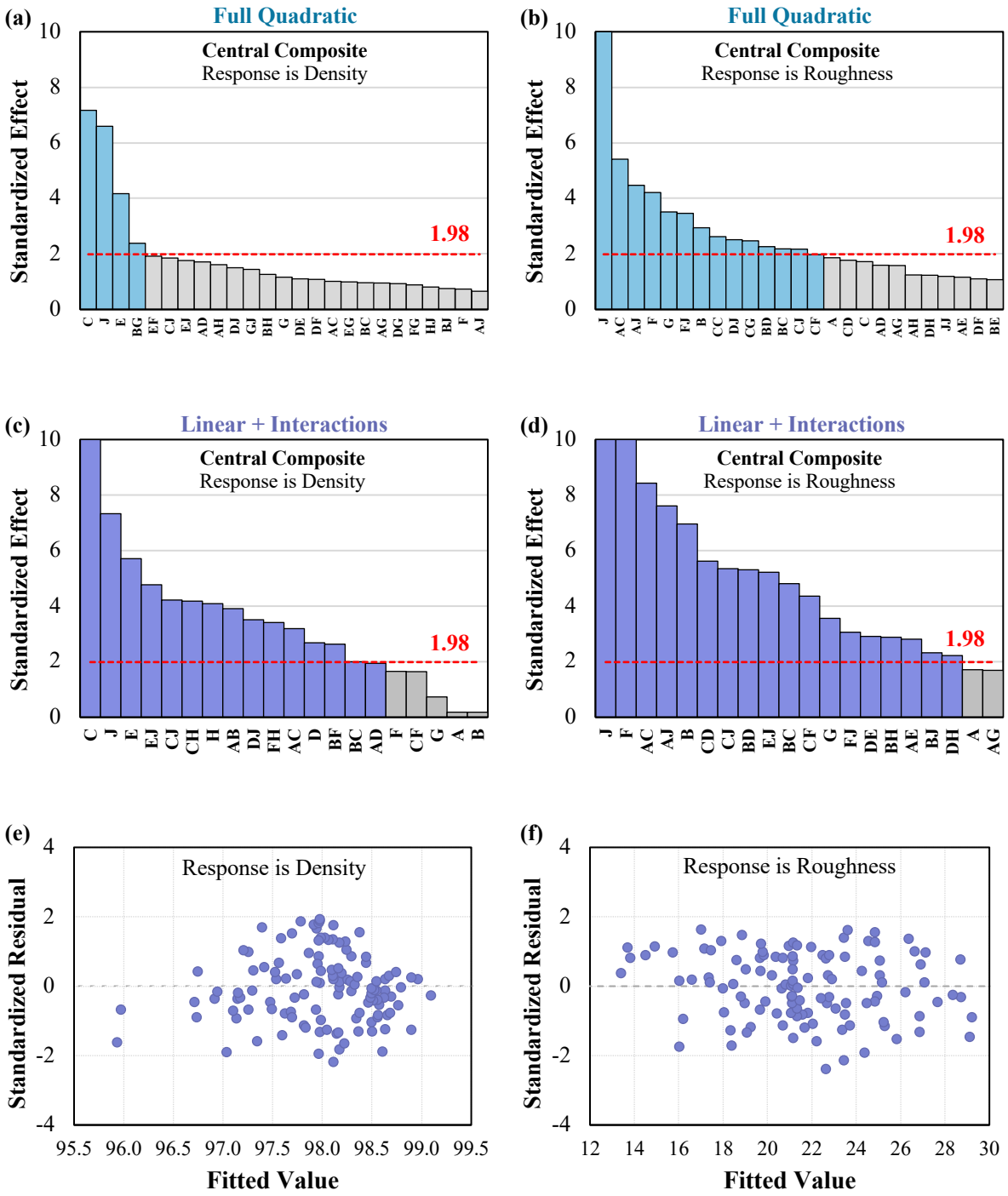


Figure 3-6 Pareto chart of the standardized effects in the full quadratic model: (a) *RD* and (b) S_a, along with standardized effects and residual plots for the modified model: (c,e) *RD* and (d,f) S_a in the CCD analysis. These charts highlight the most significant factors influencing the responses in CCD, both before and after model refinement, offering insights into the optimization of LPBF process parameters for Cu–Cr–Zr alloy.

In Table 3-4, the F-values and corresponding P-values from ANOVA for both the full quadratic model and the refined model (linear + interaction terms) are shown for *RD* and S_a, providing insight into the adequacy of the models. For lack-of-fit testing, low F-values are desirable, as they indicate that the model aligns closely with the data, with residual variance being minimal and resembling random noise. The associated P-value determines the statistical significance of the lack of fit, with $P > 0.05$ suggesting an acceptable model fit and indicating that the residual variability is not significantly different from random error.

For the full quadratic model, the F-value for the lack of fit for *RD* is 3.95, with a P-value of 0.02, suggesting moderate explanatory power but a lack of perfect fit. For S_a, the F-value of 11.56 and a P-value of 0.00 highlight a significant lack of fit, emphasizing the limitations of the full quadratic model in representing the S_a data.

After refining the models by excluding insignificant second-order terms, improvements are evident. For RD, the lack-of-fit F-value decreased slightly to 3.89, with the P-value increasing to 0.095, indicating a better fit and reduced residual variability. Similarly, for S_a, the F-value dropped to 1.69, and the P-value increased to 0.20, showing a substantial improvement in model performance and alignment with the experimental data. The fitted models for *RD* and S_a are provided in the Appendices as Equations (C1) and (C2), respectively.

Table 3-4 F-values and P-values from ANOVA for the full quadratic and refined models, highlighting model adequacy and lack-of-fit assessment for relative density and surface roughness in the CCD experiments

	Relative Density		**Surface Roughness**	
Model	F-Value	P-Value	F-Value	P-Value
Full quadratic				
Lack-of-Fit	3.95	0.02	11.56	0.00
Revised (Linear + Interactions)				
Lack-of-Fit	3.89	0.09	1.69	0.20

The improved performance of the refined models is clearly evidenced by the statistical metrics in Table 3-5, particularly the coefficient of determination (R^2), adjusted R^2 (adj-R^2), and predictive R^2 (pre-R^2). R^2 serves as a key indicator of the model's explanatory power. Adjusted R^2 accounts for the number of predictors, providing a more reliable measure by penalizing the inclusion of non-significant terms. Predictive R^2 evaluates the model's ability to predict new data, offering insight into its robustness and practical utility.

After refining the model, significant improvements were observed. For RD, the R^2 value increased from 65.79% to 75.02%, while the adj-R^2 increased from 47.50% to 70.07%. The pre-R^2 exhibited the most dramatic improvement, increasing from 17.41% to 65.30%. The improvements for S_a are even more pronounced. The R^2 value increased from 76.24% to 90.68%, and the adj-R^2 increased from 63.54% to 85.69%. The pre-R^2 experienced a substantial rise, from 40.02% to 76.76%. These results suggest that the inclusion of numerous non-significant second-order terms in the full quadratic model introduced noise, limiting its generalizability. Removing these terms not only improved the model's alignment with experimental data but also significantly enhanced its predictive power. Therefore, the refined model better captures variability in the data and provides a more reliable predictive framework.

The findings are further supported by standardized residual analysis (Figure 3-6e and f). In the refined models, the residuals exhibit a random distribution around the centerline, with no discernible patterns or systematic trends. This randomness confirms that the errors are normally distributed and independent, satisfying the assumptions of linear regression. As a result, the refined models are considered robust and reliable for optimizing *RD* and S_a in LPBF-made components.

Table 3-5 R^2 values for the full quadratic and refined models, demonstrating their explanatory and predictive performance for relative density and surface roughness in the CCD experiments

	Relative Density			**Surface Roughness**		
Model	**R^2**	**adj-R^2**	**pred-R^2**	**R^2**	**adj-R^2**	**pre-R^2**
Full Quadratic	65.79%	47.50%	17.41%	76.24%	63.54%	40.02%
Linear + Interactions	75.02%	70.07%	65.30%	91.10%	88.92%	85.85%

3.4.1.3. Analyzing process parameter effects on RD and S_a

The refined models, as highlighted by the Pareto charts (Figure 3-6c and d), identify the most significant parameters influencing *RD* and S_a. For RD, the three most significant parameters are laser power of skin exposure (C), layer thickness (J), and scanning speed of core exposure (E). For S_a, the three most significant parameters are layer thickness (J), laser power of core exposure (F), and the interaction of contour power (A) and laser power of skin exposure (C).

The prominence of the skin power parameter (C) for *RD* may be attributed to the critical role of skin/core interface in the samples. Although skin, with a thickness of 0.5 mm, constitutes a smaller volume compared to the overall sample dimensions of 10 mm × 10 mm × 10 mm, its impact on porosity can be substantial. Overlap and fusion at the skin/core boundary are critical to the overall density, and uneven energy distribution in this region may lead to localized porosity, making skin power a significant factor.

Layer thickness (J) is a significant factor influencing both *RD* and S_a. For RD, thicker layers require higher energy inputs to ensure complete melting. If the energy supplied is insufficient, it can lead to incomplete fusion and increased porosity. Conversely, thinner layers are more likely to melt and solidify fully, resulting in fewer defects and higher density. Also, for S_a, thinner layers offer better control over the building process, reducing the stair-stepping effect and improving layer-to-layer bonding, which leads to smoother surfaces. On the other hand, thicker layers can result in rougher surfaces due to the increased height of individual layers in the BD, which amplifies the visibility of layer lines and surface irregularities.

Layer thickness (J) significantly impacts *RD*, where thicker layers require more energy to achieve complete melting. Insufficient energy input can lead to incomplete fusion and increased porosity. Conversely, thinner layers are more likely to fully melt and solidify, yielding fewer defects and higher density. The significance of *LT* in the model highlights its impact on the overall quality and consistency of the build.

The V_{laser} of core exposure (E) is identified as one of the most significant factors influencing *RD* (Figure 3-6c). V_{laser} directly determines the energy input per unit area, with higher speeds delivering less energy to the material. This can result in insufficient melting, leading to incomplete fusion and increased porosity within the core. According to literature, optimal V_{laser} is critical for balancing energy input and maintaining uniform melting to achieve high-density builds [52]. Excessive speeds may compromise bonding between layers, while overly low speeds can cause overheating and other defects, underscoring the delicate balance required [54,81].

Regarding S_a (Figure 3-6d), the power of core exposure (F) plays a critical role. Insufficient core power can lead to incomplete fusion within the core, causing internal defects and inconsistencies that disrupt the integrity of the skin region during melting and solidification. While the core does not directly form the external surfaces, these imperfections at the core/skin interface can propagate into the skin, adversely affecting the smoothness of the side surfaces. Similarly, excessive core power may result in balling or spattering within the core, indirectly degrading the quality of the skin region and the external surface finish. Thus, core power indirectly influences S_a by shaping the interaction between the core and skin regions during the LPBF process.

The interaction between contour power (A) and skin power (C) further impacts S_a by controlling the melting and solidification of the part's outermost layers. Contour power is responsible for defining the perimeter of the part, shaping its geometry and ensuring smooth and well-defined edges. Skin power, on the other hand, governs the fusion and smoothness of the external surfaces within the skin region adjacent to the contour. If either parameter is suboptimal, defects such as uneven or rough surfaces can occur.

Nonetheless, the fitted models underscore the intricate interplay of various process parameters in the LPBF process, highlighting the necessity of precise control to achieve optimal *RD* and S_a. This complexity reflects the importance of understanding both direct and indirect effects of process settings on the final build quality.

3.4.1.4. Validating optimized parameters through experimental assessment

After developing predictive models through CCD, response optimization was performed in Minitab using the response optimizer function to identify a set of process parameters that would simultaneously maximize *RD* and minimize S_a. The function integrates predictive models for both responses and systematically adjusts each input variable within its defined range to assess its impact. The goal is to determine the optimal combination of parameters that yields the highest composite desirability (*d*-value), ensuring a well-balanced trade-off between *RD* and S_a.

Figure 3-7 presents the response optimization results, illustrating how each process parameter (A–J) influences *RD* (Figure 3-7a) and S_a (Figure 3-7b). The optimizer assigns desirability scores to each response based on its proximity to the ideal target (higher *RD* and lower S_a) and then combines them into a single composite desirability function, which reflects the overall effectiveness of the selected process parameters.

Figure 3-7c presents the composite desirability, which quantifies how well the selected parameter set satisfies both objectives simultaneously. The desirability function assigns a value (*d*) between 0 and 1, where values closer to 1 indicate a more effective balance between *RD* and S_a. In this case, a *d*-value of 0.93 confirms that the predicted parameter values may successfully optimize both responses, ensuring an optimal LPBF process configuration.

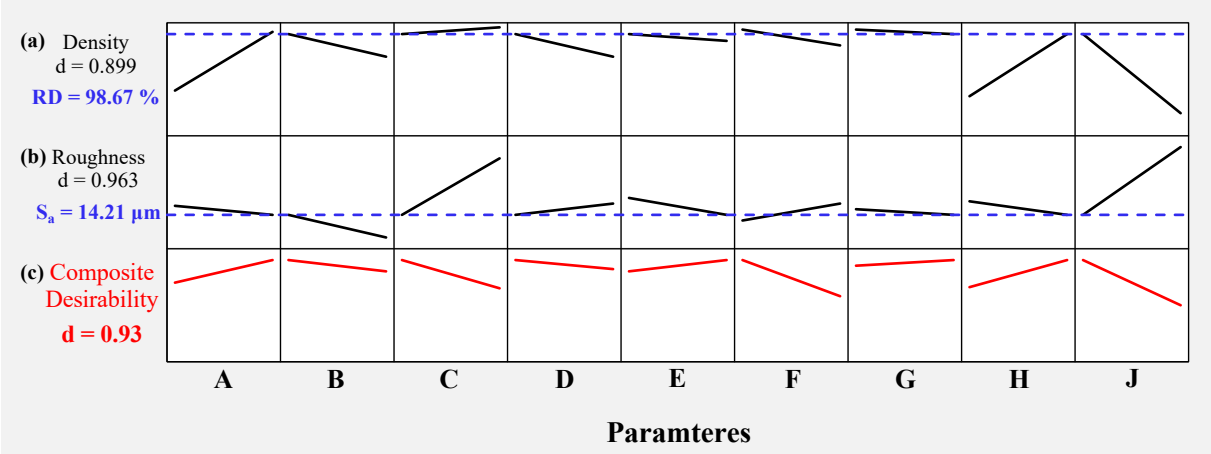


Figure 3-7 Response optimization plot for LPBF process parameters of Cu–Cr–Zr alloy, showing how each parameter (A–J) affects (a) *RD* and (b) S_a, while (c) representing composite desirability. The optimizer identifies an optimal parameter set with a predicted *RD* of 98.67 % and a S_a of 14.21 µm, achieving a high overall desirability (*d* = 0.93).

Table 3-6 summarizes the results of ANOVA of response optimizer, including the 95% confidence interval (CI) and 95% prediction interval (PI) for both responses. The CI represents the range within which the mean value of the population is expected to fall with 95% confidence, providing an estimate of the model's reliability for predicting the average response. In contrast, the PI indicates the range within which an individual future observation is likely to fall with 95% confidence, reflecting the variability and practical predictability of the model. The optimized process parameters predict a *RD* of 98.67 ± 0.18 % and a S_a of 14.21 ± 0.67 µm.

Table 3-6 Prediction setting for optimization of *RD* and S_a

Response	Fit	95% CI	95 % PI
RD [%]	98.67 ± 0.18	(98.31, 99.04)	(97.85, 99.49)
S_a [μm]	14.21 ± 0.67	(12.86, 15.55)	(11.19, 17.22)
Parameter	**Code**	**Range**	**Setting**
Contour Power [W]	A	(300, 500)	483
Scanning Speed – Skin [mm/s]	B	(600, 800)	600
Power – Skin [W]	C	(300, 500)	300
Hatch Distance – Skin [mm]	D	(0.08, 0.12)	0.08
Scanning Speed – Core [mm/s]	E	(800, 1000)	800
Power – Core [W]	F	(700, 900)	811
Hatch Distance – Core [mm]	G	(0.16, 0.20)	0.20
Stripe Overlap – Core [mm]	H	(0.12, 0.16)	0.16
Layer Thickness [mm]	J	(0.20, 0.60)	0.02

To assess the accuracy of the predictions, a series of tests were conducted using the optimized parameter values identified in Table 3-6. The results of the experimental measurements are illustrated in Figure 3-8, which includes computed tomography (CT) scans and laser profilometry images of the samples. The as-built samples achieved an exceptional *RD* of 99.96 ± 0.03 % and a S_a of 13.1 ± 1.9 μm. Notably, the majority of the porosities are concentrated at the skin/core interface, likely due to the challenges associated with achieving uniform overlap and fusion between these regions during the LPBF process. In contrast, the core region exhibited significantly fewer porosities and displayed near-defect-free characteristics, reflecting the effectiveness of the optimized parameters in ensuring thorough melting and consolidation within the core.

The results obtained using the optimized process parameters reveal a strong alignment between the model predictions and experimental outcomes, confirming the model's ability to meet the desired specifications for both *RD* and surface quality. Furthermore, the minimal deviations observed in the validation tests highlight the reliability and robustness of the predictive model in optimizing the LPBF process.

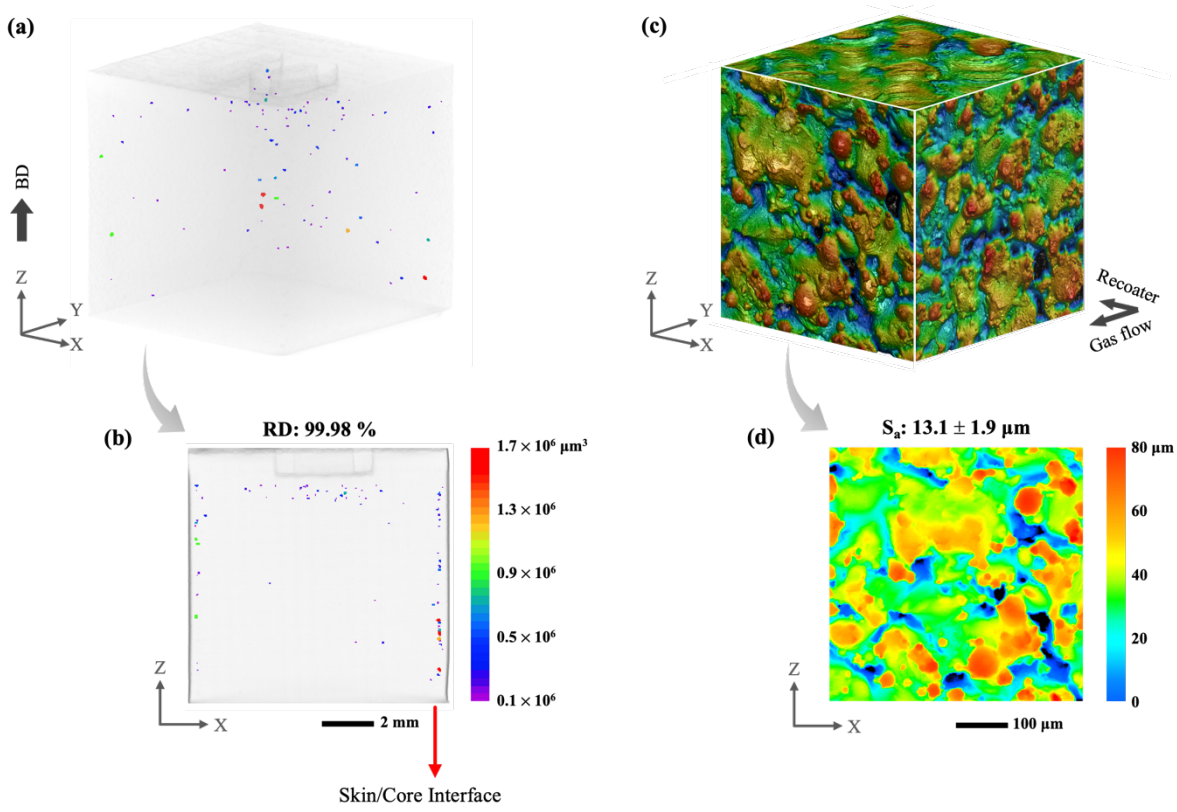


Figure 3-8 Computed tomography (CT) analysis and laser profilometry results of the optimized sample. (a) 3D volume and (b) a 2D cross-sectional view of pore distribution, with pores color-coded by volume as indicated in the legend, highlighting minimal and evenly distributed porosity achieved through optimized process parameters. (c) 3D surface view from multiple angles and (d) 2D front-side view of the S_a, as measured by laser profilometry.

Building on the optimization phase, the following sections leverage the insights gained to assess the feasibility of enhancing productivity by increasing the *LT* from the optimized 20 µm to 40 µm and 60 µm while maintaining process stability and part quality. This will be followed by an evaluation of the mechanical properties and microstructure of the printed samples.

3.4.2. Enhancing process efficiency by increasing layer thickness

The optimized parameter set from the previous phase utilized a *LT* of 20 µm, achieving exceptional results with a high *RD* (~ 99.9%) and excellent surface quality (S_a < 15 µm). However, to enhance process efficiency and sustainability, this section explores the potential for achieving high *RD* while increasing *LT*s. Higher *LT*s offer significant benefits, such as reducing the number of layers required to build a part, thereby decreasing overall processing time and energy consumption.

However, these benefits come with challenges, including increased difficulty in achieving complete melting and a heightened risk of defects like porosity. To address these challenges, this investigation aims to determine the feasibility of adopting thicker layers while preserving the quality and performance benchmarks established during the optimization phase.

Figure 3-9 presents contour plots showing the relationship between P_{laser} and V_{laser} of core exposure for *RD* at three different *LT*s of 20 μm, 40 μm, and 60 μm. These plots, derived from CCD results, define the process windows for achieving high *RD* while holding other parameters constant at their midpoint values (Table 3-3).

Achieving fully-dense parts in LPBF of Cu and Cu alloys is inherently challenging due to their high reflectivity and thermal conductivity [2,45]. As a result, LPBF processing of these materials often necessitates the use of high P_{laser}, particularly for thicker layers, where additional energy input is essential to achieve complete melting. This trend is evident in Figure 3-9, where higher *RD* is achieved with increasing P_{laser} and decreasing V_{laser}, both of which contribute to a higher VED. In addition, as *LT* decreases, the process window for achieving high *RD* expands.

For the *LT* of 20 μm (Figure 3-9a), the results consistently demonstrate high *RD* (98.6% – 99.0%) across a wide range of laser powers and scanning speeds. This is attributed to efficient melting and consolidation, as thinner layers provide more energy input to ensure complete fusion. In comparison, the *LT* of 40 μm (Figure 3-9b) shows a more limited range of RD, predominantly between 98.2 % and 98.6 %. However, certain parameter combinations achieve *RD* comparable to the 20 μm samples (98.6% – 99.0%), indicating that energy-efficient processing at intermediate thicknesses is feasible with precise parameter tuning.

For the *LT* of 60 μm (Figure 3-9c), the high *RD* region is even smaller, highlighting the challenges associated with thicker layers. The thicker layers require higher energy input to achieve complete melting and uniform density, making them more sensitive to variations in P_{laser} and V_{laser}.

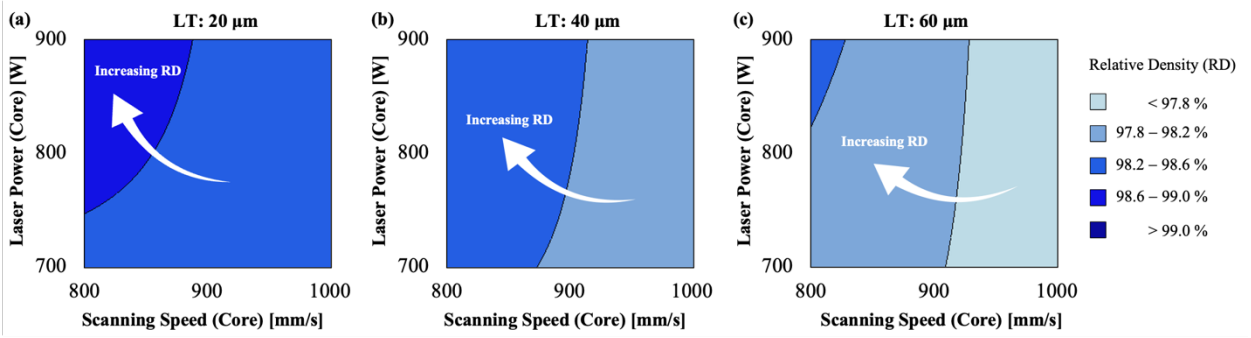


Figure 3-9 Contour plots showing the relationship between laser power and scanning speed of core exposure for *RD* at different *LT*s: (a) 20 µm, (b) 40 µm, and (c) 60 µm. The results are derived from the CCD analysis with other parameters held constant at their midpoint values. Higher relative densities are achieved at lower scanning speeds and higher laser powers, particularly for thinner layers.

Based on the results shown in Figure 3-9, six parameter sets were selected for further investigation: one reference sample printed with 20 µm *LT* (optimized using RSM), two parts with 40 µm *LT*, and three parts with 60 µm *LT*. For each condition, two parts were fabricated to ensure reproducibility. These parameter sets were identified from the high-density regions of the contour plots (Figure 3-9), with laser powers ranging from 800 W to 900 W and scanning speeds lower than 800 mm/s. Table 3-7 provides the process parameters for the six LPBF-made parts selected for hardness and microstructural evaluation. The sample names follow the format (*LT* – *VED*), where the first number represents the *LT* (in µm) and the second indicates the corresponding *VED* (in J/mm^3).

The outcomes highlight the importance of balancing P_{laser} and V_{laser} to avoid defects such as porosity and incomplete fusion. While the thinner layers generally achieved higher densities with relatively broader process windows, the 40 µm parts showed that near-full density could be obtained with careful parameter tuning. Although the results for the 60 µm layers are more variable, they are also promising, indicating the potential for high-quality fabrication at greater *LT*s. To deepen the understanding of how varying *LT*s influence the final properties, the next sections examine the microstructural and mechanical characteristics of the six fabricated samples.

Table 3-7 Process parameters used for LPBF-made parts to evaluate microstructure and hardness

Parameter	Part (a: 20–280)	Part (b: 60–145)	Part (c: 40–190)	Part (d: 40–165)	Part (e: 60–165)	Part (f: 60–145)
Power – Core [W]	800	800	850	850	900	900
Scanning speed – Core [mm/s]	800	600	650	750	600	700
Hatch distance – Core [mm]	0.18	0.15	0.17	0.17	0.15	0.15
Layer thickness [mm]	20	60	40	40	60	60
VED [J/mm^3]	~280	~145	~190	~165	~165	~145

3.4.3. Evaluation of the printed part properties

3.4.3.1. Porosity analysis

Figure 3-10 presents cross-sectional micrographs of the parts fabricated using the process parameters outlined in Table 3-7. This includes the *RD* measurements and microhardness (HV) maps, offering a detailed evaluation of the uniformity and quality of the samples. These parts were specifically designed to evaluate the effects of varying *LT*s, with a focus on *VED*. The *VED* was systematically varied by adjusting P_{laser}, V_{laser}, *HD*, and *LT*. Importantly, these parts were fabricated without a skin region, enabling a focused assessment of the core properties.

Part (a: 20–280) (Figure 3-10a$_1$), with a *LT* of 20 µm, serves as the statistically optimized reference from the initial RSM phase and exhibits an exceptional *RD* of 99.94%. Interestingly, parts (c: 40–190) (Figure 3-10c$_1$) and (d: 40–165) (Figure 3-10d$_1$), fabricated with a *LT* of 40 µm, achieved even higher relative densities of 99.96% and 99.97%, respectively. These findings suggest that increasing the *LT* to 40 µm can still yield high-density builds, although it may scarify the optimized S_a.

Parts (c: 40–190) and (d: 40–165) were printed using the same parameters, except for V_{laser}, which was higher in part (d: 40–165), as shown in Table 3-7. A comparison of their relative densities reveals that part (d: 40–165) may be a better option due to its higher V_{laser}. Moreover, compared to part (a: 20–280), part (d: 40–165) achieves similar exceptional RD, despite having twice the *LT*, further highlighting the feasibility of higher *LT*s under optimal conditions.

For *LT* of 60 µm, parts (b: 60–145) (Figure 3-10b$_1$), (e: 60–165) (Figure 3-10e$_1$), and (f: 60–145) (Figure 3-10f$_1$) showed slightly lower relative densities, ranging from 98.75% to 99.78%. This reduction highlights the increased challenges associated with thicker layers, where achieving full consolidation becomes more difficult due to incomplete melting and the higher likelihood of

residual porosity. However, the *RD* of 99.78% observed in part (f: 60–145) is particularly noteworthy, as it underscores the potential for achieving high-density builds even with thicker layers when process parameters and *VED* are precisely tuned.

A comparison of parts (e: 60–165) and (f: 60–145), both produced with identical *VED* of ~145 J/mm^3, *HD* of 0.15 mm, and *LT* of 60 μm, reveals that the simultaneous increase in P_{laser} and V_{laser} improved the *RD* from 99.32% in part (b: 60–145) to 99.78% in part (f: 60–145). In contrast, part (e: 60–165), also with *LT* of 60 μm, demonstrated a lower *RD* of 98.75% despite having a higher *VED* (~165 J/mm^3) than parts (b: 60–145) and (f: 60–145). These indicate that optimizing the balance between P_{laser} and V_{laser} can significantly enhance the melting and consolidation process, even within the same *VED* range.

Adjusting P_{laser} and V_{laser} directly impacts the energy delivered (*VED*) to the powder bed. Insufficient *VED* often results in incomplete melting, leading to lack-of-fusion porosities [82], as observed in parts (b: 60–145) and (e: 60–165). For instance, Figure 3-10e$_4$ shows typical irregular-shaped porosities near the microhardness indent in part (e: 60–165), likely caused by inadequate energy input that failed to fully melt and consolidate the material. In comparison, part (f: 60–145), processed with a P_{laser} of 900 W, exhibits fewer porosities than part (b: 60–145), which used a lower power of 800 W. The increased power in part (f: 60–145) likely improved melting and consolidation, enhancing its *RD*. However, in part (e: 60–165), the combination of reduced V_{laser} and higher P_{laser} negatively impacted *RD*. The excessive energy density likely caused a deep and unstable vapor cavity during solidification [82,83], resulting in spherical keyhole porosities and adding complexity to process parameter optimization.

It should be noted that reducing the *HD* can further enhance melting and consolidation by increasing the overlap between adjacent scanning tracks [77,82], which is essential for achieving uniform melting in thicker layers. In this study, the *HD* was reduced to 0.15 mm for a 60 μm *LT*, compared to 0.18 mm for the 20 μm *LT*, to address lack-of-fusion issues. Higher P_{laser} was also employed to create deeper and wider melt pools [84,85], effectively accommodating the increased *LT*. However, the machine's power limitations restricted further increases in P_{laser}. As a result, further reducing the *HD* emerges as a potential strategy for eliminating lack-of-fusion defects in thicker layers, ensuring better melting and consolidation within the process constraints.

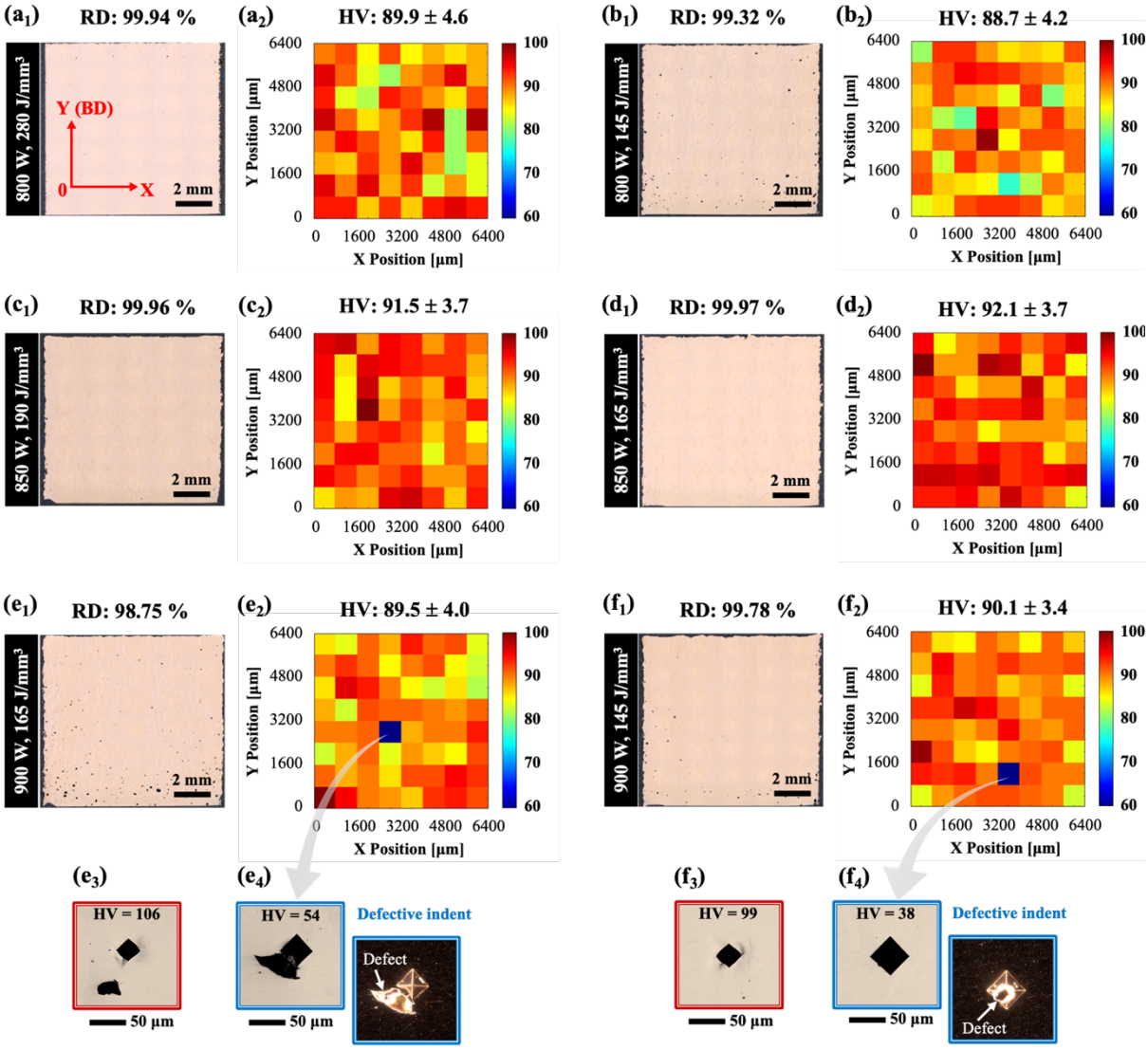


Figure 3-10 *RD* and microhardness (HV) maps of LPBF-made Cu–Cr–Zr alloy processed at different *VED*s. (a_1–f_1) Cross-sectional optical micrographs showing *RD* values ranging from 98.75% to 99.97%. (a_2–f_2) microardness maps showing the HV change across each sample. Representative hardness indents correspond to the (e_3,f_3) highest and (e_4,f_4) lowest measured values.

3.4.3.2. Mechanical behavior assessment

While optimizing density is fundamental to the success of LPBF-made components, ensuring favorable mechanical properties is equally critical. This balance is particularly important for Cu–Cr–Zr alloy, which is widely used in applications such as aerospace, where reliable performance under mechanical loads is essential. Figure 3-10a_2–f_2 provides microhardness (HV) maps across the cross-sections of the samples, corresponding to the *RD* results shown in Figure 3-10a_1–f_1. These maps allow an evaluation of how variations in process parameters influence mechanical behavior.

Typically, there is a direct correlation between *RD* and hardness, as reduced porosity enhances load distribution and structural integrity, thereby improving hardness [83,86]. This trend is evident in parts (a: 20–280), (c: 40–190), and (d: 40–165), which achieved the highest *RD* (> 99.9%) and exhibited the most uniform hardness distributions, with average values ranging from 89.9 HV to 92.1 HV.

In contrast, parts (b: 60–145), (e: 60–165), and (f: 60–145) showed slightly lower average hardness values and, more importantly, reduced uniformity. These variations can be attributed to residual porosity within these samples. For instance, the hardness map of part (e: 60–165) reveals localized reductions caused by porosity, as illustrated in Figure 3-10e_4, showing defective indents with a low hardness value of 54 HV. Similarly, part (f: 60–145), despite achieving a high *RD* of 99.78%, showed variations in hardness due to defects, including an indent measuring 38 HV (Figure 3-10f_4). While these localized defects are notable, the overall results demonstrate that hardness values remain within a relatively narrow range across all samples, suggesting that process parameters exert minimal influence on hardness. This observation aligns with previous studies on LPBF-made Cu–Cr–Zr alloys, which report that hardness values remain stable across optimized process parameters [87]. Uniform density, as achieved in most samples, emerges as a critical factor in ensuring consistent mechanical properties, reinforcing the importance of precise parameter control during fabrication.

Variations in process parameters, such as P_{laser} and V_{laser}, likely introduce differences in thermal histories, which in turn affect grain size, morphology, and orientation [88,89]. A more detailed investigation of the microstructure is therefore essential to fully understand how process parameters influence material behavior, enabling more precise control over the mechanical properties of LPBF-made Cu–Cr–Zr components. The next section will delve into the microstructure in detail.

3.4.3.3. Surface roughness measurement

Figure 3-11 presents 3D surface roughness maps of LPBF-made Cu–Cr–Zr samples, illustrating the effect of *LT* on surface morphology. The topographical variations, represented by the color gradient (red: peaks, blue: valleys), highlight differences S_a under different *LT* conditions.

Notably, parts with *LT*s of 20 µm (Figure 3-11a) and 40 µm (Figure 3-11c and d) exhibit smoother surfaces, indicating better fusion and reduced surface defects. These parts show lower peak-to-valley differences, suggesting a more uniform melt pool and improved layer bonding. In contrast, parts with *LT* of 60 µm (Figure 3-11b, e, and f) display higher roughness, characterized by larger irregularities, deeper valleys, and pronounced peaks. This aligns with previous findings that increasing *LT* leads to higher S_a, as the increased *LT* amplifies the stair-stepping effect and melt pool instabilities. In addition, thicker layers require higher energy input to ensure complete melting, and any insufficient energy density can result in partial fusion, increased balling, and surface irregularities.

Despite the increase in S_a with higher *LT*, the overall roughness values remain within an acceptable range, particularly given the high *RD* achieved in these samples. While thicker layers contribute to increased S_a, the process still maintains a balance between surface quality and densification, making it a viable approach where productivity gains outweigh minor surface imperfections.

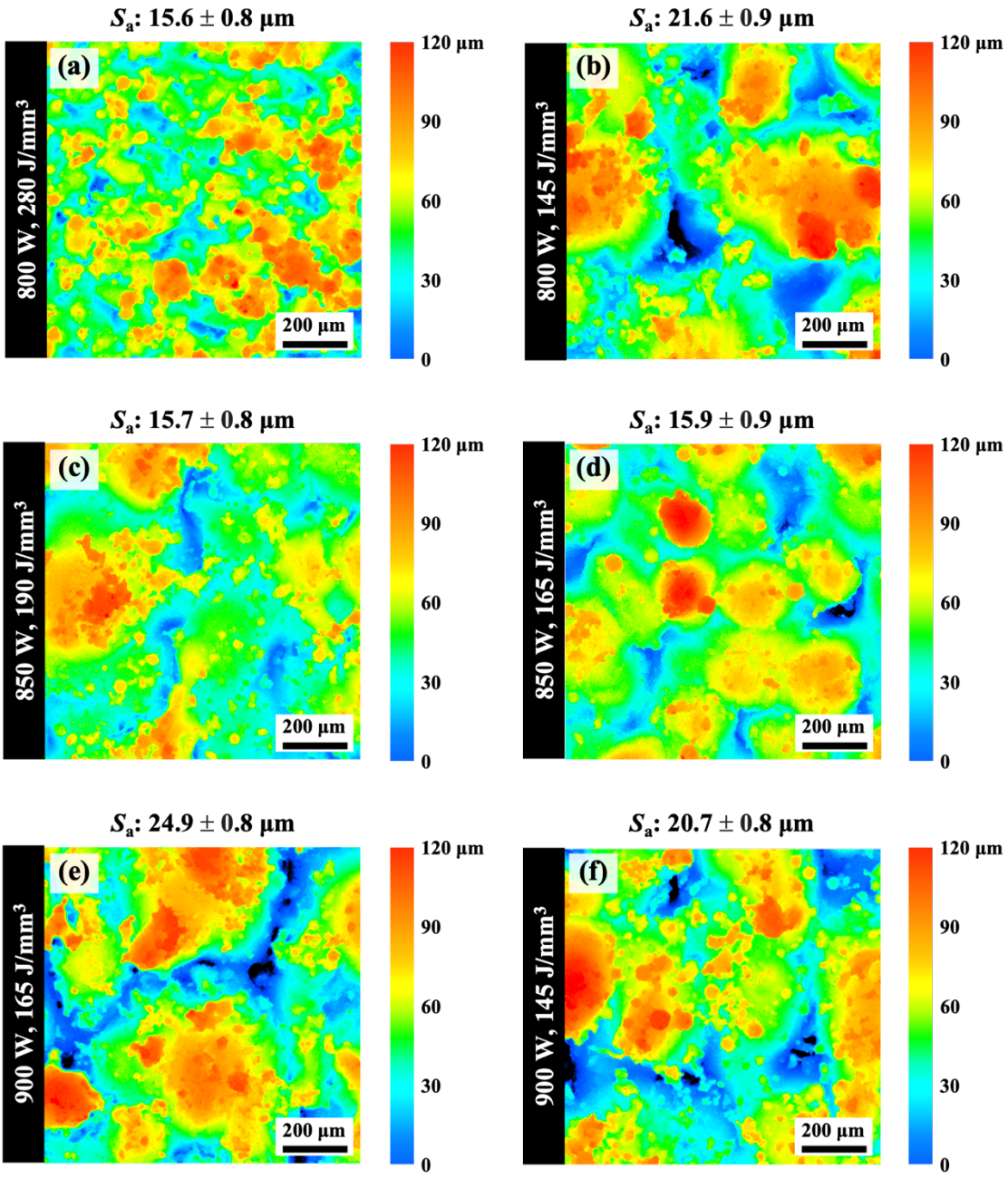


Figure 3-11 3D surface topography maps showing the S_a of LPBF-made Cu–Cr–Zr parts fabricated with different process parameters. The color scale represents height variations, with red indicating elevated regions and blue representing lower valleys. (a, c, d) correspond to parts printed with 20 µm and 40 µm *LT*, exhibiting relatively smoother surfaces. In contrast, (b, e, f) represent parts with 60 µm *LT*, showing increased surface irregularities.

3.4.3.4. Microstructural analysis

To explore the influence of process parameters on microstructural evolution, EBSD was performed on cross-sections parallel to the BD. Figure 3-12 presents grain maps and corresponding grain size distribution histograms for parts fabricated with the parameters outlined in Table 3-7. These results provide detailed insights into the grain morphology and size, highlighting how variations in processing parameters influence the microstructure of LPBF-made Cu–Cr–Zr alloy.

The grain maps (Figure 3-12a_1–f_1) reveal predominantly columnar and elongated grains aligned along the BD. The grain morphology is a direct consequence of the thermal gradients (G) and solidification rate (R), both of which are strongly influenced by P_{laser} and V_{laser} [90]. High P_{laser} increases G near the melt pool boundary by providing greater energy input, steepening the temperature gradient between the liquid and solid regions. This steeper gradient promotes directional solidification along the heat flow direction, stabilizing columnar grain structures while suppressing the nucleation of equiaxed grains. Conversely, higher scanning speeds increase R, which can refine the grains and potentially drive a transition toward equiaxed grains. The rapid cooling associated with higher scanning speeds limits grain growth, resulting in narrower and less elongated grains. This relationship between grain morphology and process parameters can be better understood through the stability parameter, G/R, which links G and R during the LPBF process [91].

The ratio G/R is a critical determinant of grain morphology. Higher values of G/R favor columnar grain growth, whereas lower values can promote equiaxed grain formation [92]. In the LPBF-made parts examined here, grains are consistently columnar and elongated across the tested range of P_{laser} and V_{laser}, indicating that G/R remains sufficiently high to stabilize the columnar growth mode. For Cu alloys, the high thermal conductivity of the material further amplifies G, contributing to a generally large G value. This characteristic strongly favors the formation of columnar grains, consistent with prior studies on LPBF of Cu alloys where efficient heat dissipation reinforces unidirectional grain growth along the BD [53,93].

While the grain morphology remains predominantly columnar, subtle differences in grain size are evident among the samples, highlighting the influence of specific process parameters. To quantitatively assess grain size and distribution, histograms are presented in Figure 3-12a_2–f_2. Grains intersecting the edges of the analyzed area are excluded to avoid inaccuracies, as some grains extend beyond the field of view. For example, in part (a: 20–280), grains longer than 1500 μm exceed the field of view, potentially underestimating the fraction of very large grains.

A comparison of grain size distribution shows that part (a: 20–280), with the highest *VED* (280 J/mm^3), exhibits a non-uniform distribution, as indicated by a bimodal histogram (Figure 3-12a_2). The thinner *LT* (20 μm) in this sample enhances interaction between successive layers, as the next layer scanning provides additional thermal energy to the previously solidified layer. This extended thermal exposure promotes grain growth, leading to the formation of larger grains alongside smaller grains.

In contrast, part (b: 60–145), fabricated with a 60 μm *LT* and a significantly lower *VED* (145 J/mm^3), shows a more uniform grain size distribution. The histogram (Figure 3-12b_2) indicates a monomodal distribution characterized by a balanced mix of grain sizes. In this sample, the P_{laser} was kept the same as in part (a: 20–280), but the V_{laser} and *HD* were reduced while the *LT* was increased. These changes significantly altered the thermal environment during solidification.

The increased *LT* in part (b: 60–145) increases the volume of material per layer, reducing thermal exposure due to the greater thermal mass. This leads to a lower effective energy density per unit volume, which diminishes *G* and slows *R* compared to part (a: 20–280), thereby promoting more uniform grain growth. Furthermore, the reduced V_{laser} increases the dwell time of the laser on the material, allowing more energy to accumulate and further facilitating the growth of larger grains. The reduced *HD* enhances thermal uniformity by increasing overlap between adjacent melt pools, consolidating grain growth and contributing to the overall uniformity of the microstructure. Therefore, part (b: 60–145) exhibits a reduced fraction of narrower grains compared to part (a: 20–280), likely due to the lower energy density and slower V_{laser}.

Parts (c: 40–190) (Figure 3-12c_2) and (d: 40–165) (Figure 3-12d_2), both exhibit a bimodal grain size distribution similar to part (a: 20–280), but with lower fractions of small grains and less pronounced elongated grains compared to part (a: 20–280).

The slightly higher P_{laser} in parts (c: 40–190) and (d: 40–165) compared to part (a: 20–280) increases the energy delivered to the material during processing. Moreover, the slower scanning speeds in these parts prolong the laser-material interaction time. This extended interaction promotes deeper heat penetration and greater energy diffusion, influencing *G* and R, which in turn affect the grain structure. Although the *LT* is increased in parts (c: 40–190) and (d: 40–165), the overall combination of process parameters results in a grain structure where the bimodal distribution persists but shifts toward greater uniformity, with fewer extreme large or small grains compared to part (a: 20–280) (Figure 3-12a). However, this uniformity is not as pronounced as in part (b: 60–145), which exhibited a monomodal distribution (Figure 3-12b).

When comparing parts (d: 40–165) and (e: 60–165), which have the same *VED* but different *LT*s, part (e: 60–165) (Figure 3-12e) shows larger grains. This can be attributed to the higher P_{laser}, slower V_{laser}, and smaller *HD* in part (e: 60–165), which extend thermal exposure and promote grain coarsening. In contrast, part (f: 60–145) (Figure 3-12f), with similar process parameters to part (e: 60–165) but a higher V_{laser}, exhibits narrower grains. The increased V_{laser} in part (f: 60–145) reduces energy input, limiting grain growth. This emphasizes the critical role of V_{laser} in shaping grain morphology.

To understand the minimal differences in hardness observed across the parts in Figure 3-10, the Hall–Petch relationship offers valuable insight. This principle establishes that smaller grain sizes enhance material strength by impeding dislocation motion, which directly influences yield strength and, consequently, hardness [94]. Parts (a: 20–280), (c: 40–190), and (d: 40–165), with a higher fraction of smaller grains, would typically be expected to exhibit slightly higher hardness compared to parts (b: 60–145), (e: 60–165), and (f: 60–145), where larger grains are more prevalent. However, the measured hardness values show negligible variation across the samples. This is likely due to the overall similarity in their microstructures, where elongated columnar grains dominate. The elongated grain structure, observed in all samples, may diminish the strengthening effect of smaller grains, resulting in comparable hardness values.

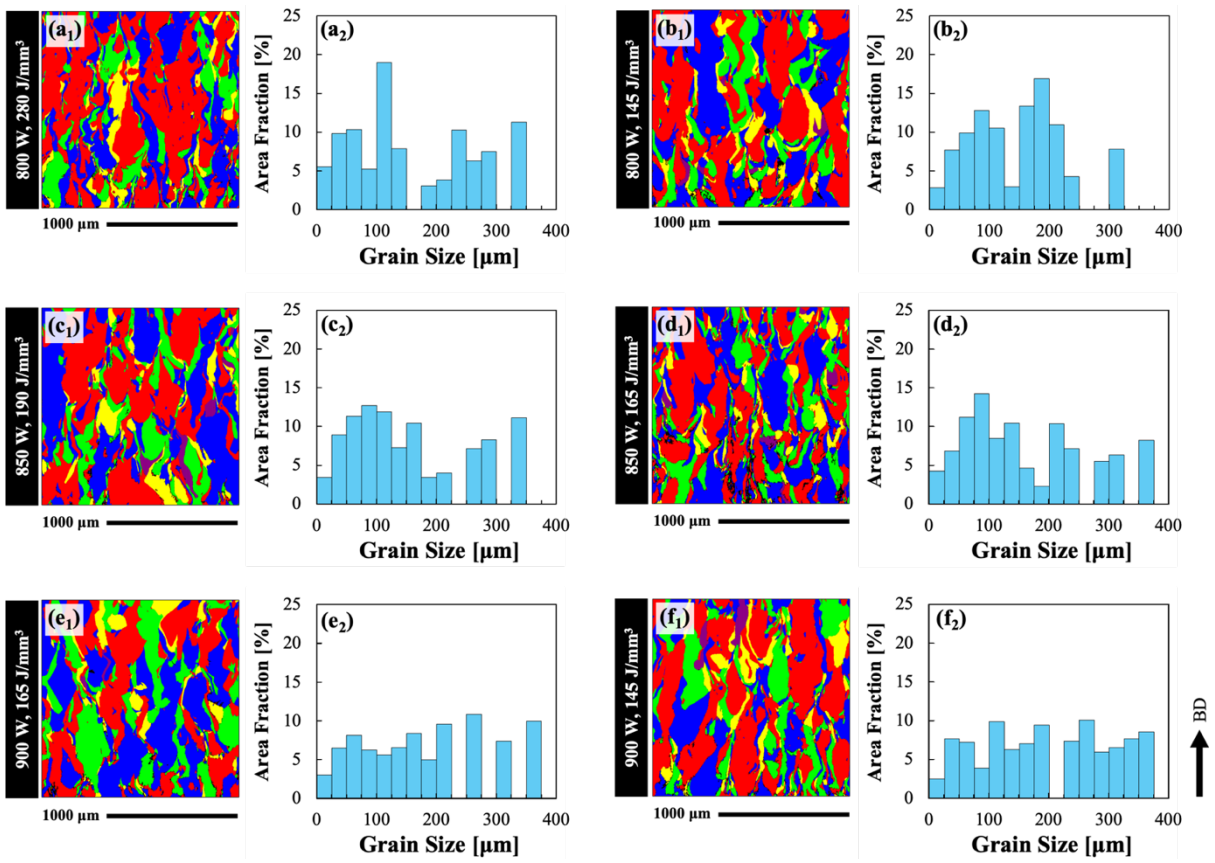


Figure 3-12 (a_1–f_1) Grain maps of LPBF-made Cu–Cr–Zr alloy processed at different *VED*s, showing the morphology of grains along the BD. (a_2–f_2) Corresponding histograms of grain size distribution, highlighting variations in grain size influenced by process parameters. Grains intersecting the field of view boundaries are excluded from the distribution.

Following the discussion of grain morphology and size distribution in Figure 3-12, additional insights into the crystallographic characteristics of LPBF-made Cu–Cr–Zr alloy are provided in Figure 3-13. The inverse pole figure (IPF) maps (Figure 3-13a_1–f_1) give valuable information about the crystallographic orientation of grains along the BD (Z-axis). The texture observed in these maps is a direct consequence of the solidification process, which is heavily influenced by the thermal conditions inherent to LPBF.

In LPBF, the steep thermal gradients and rapid solidification rates promote unidirectional heat dissipation along the BD [89,95]. These conditions favor the growth of grains oriented with their crystallographic axes aligned to the thermal gradient, typically resulting in a strong <001> texture along the Z-axis for cubic crystal systems such as Cu alloys [96]. This <001> texture is often preferred in LPBF due to its lower energy barrier for growth in the direction of heat flow,

stabilizing grain structures during solidification. During LPBF, newly solidified grains act as a template for the subsequent layer's solidification, propagating the crystallographic orientation from one layer to the next. This layer-by-layer epitaxial growth reinforces directional grain alignment, particularly along the thermal gradient. However, process parameters such as P_{laser}, V_{laser}, *HD*, and *LT* significantly influence the development of texture [97–99].

Part (a: 20–280), fabricated with the highest *VED* (280 J/mm^3) and the thinnest *LT* (20 μm), exhibits a strong <001> texture (red regions in the IPF-Z map). The high *VED* provides a pronounced thermal gradient, enhancing directional grain growth along the BD. The thin *LT* allows for increased thermal interaction between successive layers, as the heat from subsequent scans provides additional energy to the previously solidified layers. This extended thermal exposure promotes epitaxial growth, reinforcing the <001> orientation.

In parts (b)–(f), with lower *VED* and thicker layers, the texture becomes less pronounced and more random compared to part (a: 20–280). Despite the reduced V_{laser} and *HD* in these samples, the thicker *LT*s (40 μm and 60 μm) increases the thermal mass, which moderates the G. The higher P_{laser} in these parts provides more energy input, but the combination of increased *LT* and larger melt pools reduces the sharpness of the thermal gradient. This limits the driving force for directional grain growth, weakening the <001> texture and allowing grains with other orientations to form.

The grain average misorientation (GAM) maps shown in Figure 3-13a_2–f_2 offer valuable insights into the internal misorientation within grains, providing information about residual thermal stress and dislocation density induced by the LPBF process. GAM represents the average misorientation between a given point within a grain and all other points in the same grain, serving as an indicator of subgrain structure resulting from rapid cooling and steep thermal gradients. Higher GAM values are associated with regions of significant internal misorientation within a grain, typically caused by dislocation accumulation during the rapid solidification inherent in LPBF.

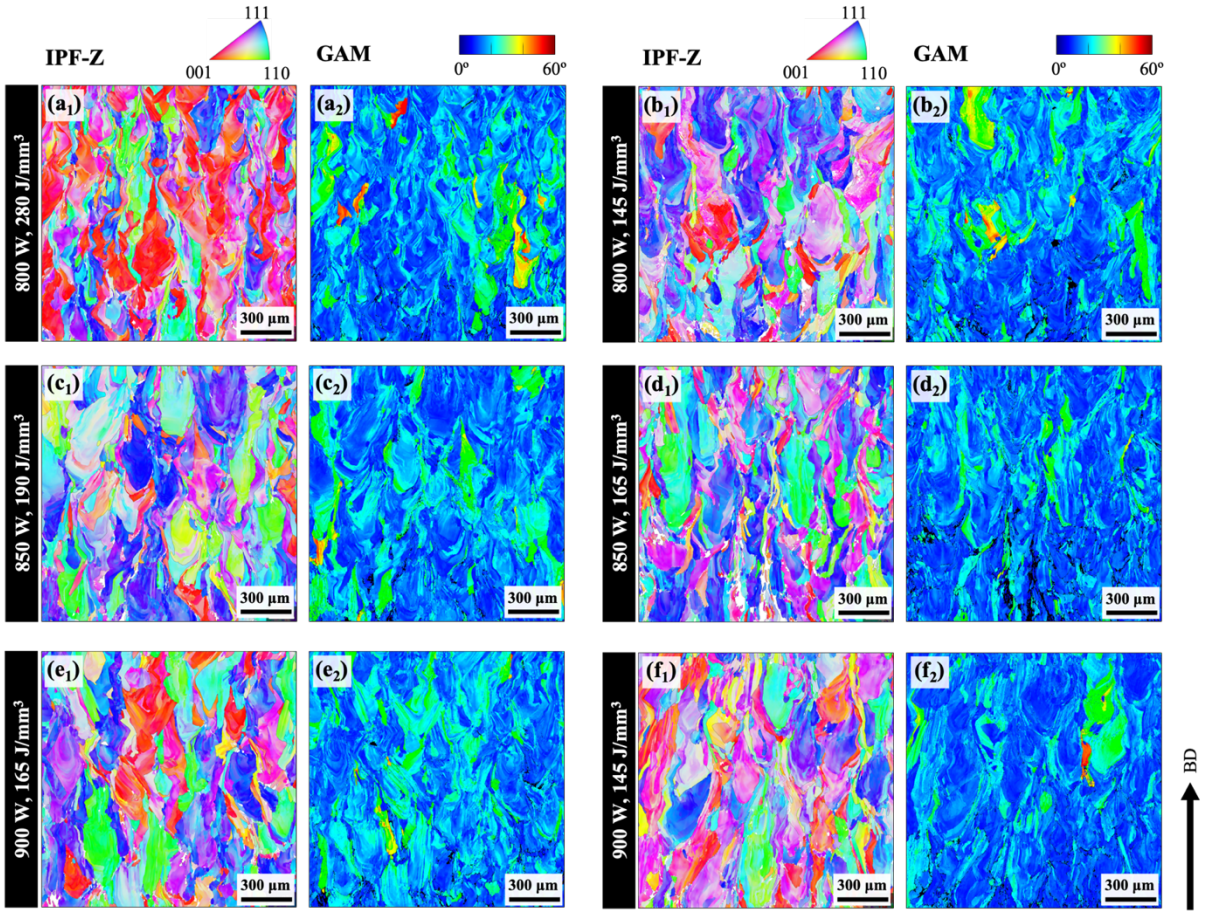


Figure 3-13 (a_1–f_1) Inverse pole figure (IPF-Z) maps of LPBF-made Cu–Cr–Zr alloy processed at different *VED*s, illustrating the grain orientation along the BD and highlighting the elongated columnar grain structures typical of LPBF. (a_2–f_2) Corresponding grain average misorientation (GAM) maps, visualizing local misorientation within grains, with higher values indicating potential residual stress or subgrain formation.

In LPBF, rapid solidification generates substantial dislocation density within the grains [53]. These dislocations accommodate the thermal stress and contribute to the formation of subgrain structures. Across all parts in Figure 3-13, GAM values are generally moderate, reflecting a relatively uniform distribution of residual stresses and dislocation density within the microstructure. However, in part (a: 20–280), distinct regions with higher GAM values (red regions in Figure 3-13a_2) are evident. As discussed, this sample exhibits a bimodal grain size distribution, with a notable fraction of smaller grains (Figure 3-12a_2). Smaller grains are more susceptible to the accumulation of dislocations, leading to localized strain concentration and higher GAM values. These elevated GAM regions often signify areas with more subgrain structures and higher dislocation density, reflecting the influence of the thermal history during the process.

Figure 3-14 examines the subgrain structures and grain boundary characteristics of LPBF-made Cu–Cr–Zr alloy, focusing on the distribution of low-angle grain boundaries (LAGBs) and high-angle grain boundaries (HAGBs). The criterion for distinguishing LAGBs from HAGBs is set at the standard threshold of 15°. The grain boundary maps (Figure 3-14a_2–f_2) show that all parts exhibit a high fraction of LAGBs within grains. LAGBs form due to dislocation accumulation during rapid solidification, a characteristic feature of the LPBF processes. These boundaries indicate the presence of subgrain structures, reflecting the high dislocation densities and residual thermal stresses induced by steep thermal gradients and rapid cooling rates. The persistence of LAGBs suggests that while significant subgrain formation occur during solidification, the rapid thermal cycles in LPBF lack the time and energy required for these boundaries to evolve into HAGBs.

The distribution of LAGBs and HAGBs varies across the samples, reflecting differences in thermal and solidification conditions. HAGBs are predominantly aligned along the BD, driven by unidirectional grain growth resulting from steep thermal gradients. However, slight deviations from the BD are observed, likely influenced by localized thermal effects, such as melt pool dynamics and non-uniform heat dissipation. In some regions, small equiaxed grains surrounded by HAGBs are evident, particularly in parts (a: 20–280), (c: 40–190), and (d: 40–165) (Figure 3-14a_2, c_2, and d_2), aligning with the higher fraction of small grains identified in Figure 3-12.

Interestingly, in some cases, such as part (b: 60–145) (Figure 3-14b_2), equiaxed subgrains with LAGBs are observed within larger columnar grains. Equiaxed grains can form at the center of melt pools due to localized thermal and solidification conditions unique to this region. The thermal gradient at the center is typically weaker than at the edges, as heat dissipation is more isotropic, reducing the driving force for directional columnar growth. This weaker gradient, combined with increased undercooling, enhances nucleation rates relative to growth rates, thereby favoring equiaxed grain formation. Melt pool dynamics, such as convective flow, can further disrupt the directionality of solidification and contribute to the random orientation of grains in the center. In addition, in alloys, solute redistribution toward the melt pool center increases constitutional undercooling, further promoting equiaxed nucleation.

However, the subgrains with LAGBs likely did not transition to HAGBs due to the rapid cooling rates in LPBF, which restrict grain boundary mobility and limit the misorientation necessary for forming HAGBs. The high thermal conductivity of Cu alloys further exacerbates this effect by facilitating efficient heat dissipation, leaving many grain boundaries as LAGBs.

Furthermore, the overlapping of successive layers in LPBF introduces reheating and partial remelting, creating conditions that may promote recrystallization and equiaxed grain formation during subsequent solidification. However, recrystallization is often incomplete due to the rapid solidification inherent in LPBF, which provides insufficient time for grain boundary migration and the complete elimination of subgrain boundaries. The melting time of previously solidified layers is extremely short due to the rapid motion of the laser beam in LPBF. This limited melting time prevents complete recrystallization, leaving a significant number of residual LAGBs in the microstructure [87,100]. The high thermal conductivity of Cu alloys further exacerbates this limitation by accelerating heat dissipation, thereby reducing the time at elevated temperatures necessary for complete recrystallization.

While these microstructural features may not cause significant differences in hardness (as shown in Figure 3-10), they could significantly impact other mechanical properties such as tensile strength and wear resistance [101–103]. A broader evaluation of the mechanical properties of LPBF-made Cu–Cr–Zr components, including impact loading tests, will be conducted in a future study.

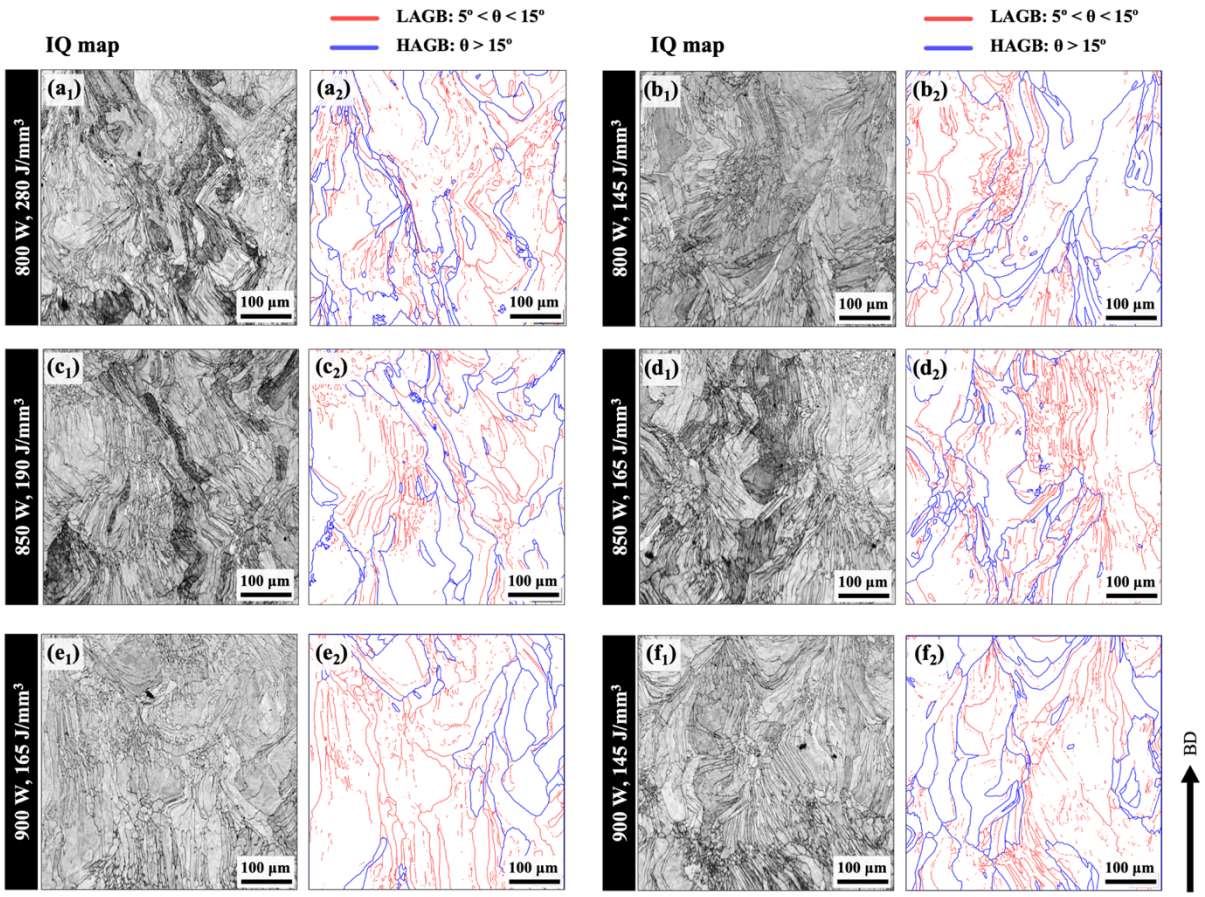


Figure 3-14 (a_1–f_1) Image quality (IQ) maps and (a_2–f_2) corresponding grain boundary maps of LPBF-made Cu–Cr–Zr alloy processed at different *VED*s. The maps illustrate subgrain evolution, highlighting low-angle grain boundaries (LAGBs, 5° < θ < 15°, red) and high-angle grain boundaries (HAGBs, θ > 15°, blue).

3.5. Summary

This study investigates the high-power LPBF of Cu–Cr–Zr alloy, focusing on process parameter optimization and its effects on microstructure and mechanical properties. Key conclusions are as follows:

- The Plackett-Burman design effectively screened 23 process parameters, identifying layer thickness and specific energy as the most significant factors influencing relative density and surface roughness.
- Using central composite design, robust predictive models were developed, emphasizing the critical role of layer thickness, laser power, and scanning speed.

- Response optimization validated these models, achieving a maximum relative density of 99.96% and surface roughness as low as 13.1 μm, demonstrating the effectiveness of the optimization strategy.
- The optimized process parameters identified using CCD allowed successful fabrication of high-quality parts across varying layer thicknesses, with even the thickest layers (60 μm) achieving high relative density of 99.78% and minimal defects.
- IPF-Z maps revealed a strong <001> texture along the BD for parts with higher *VED*, attributed to directional solidification along the sharp thermal gradients. Conversely, lower *VED* parts showed more random crystallographic orientations.
- Subgrain analysis indicated a high fraction of LAGBs, reflecting high dislocation density and the rapid cooling rates characteristic of LPBF.
- These crystallographic observations highlight the strong link between process conditions and grain orientation, which plays a key role in determining mechanical performance.

These findings set the foundation for the next chapter, which investigates how these microstructural features influence dynamic deformation behavior under high strain rate loading.

Chapter 4. On the microstructure and dynamic mechanical behavior of Cu–Cr–Zr alloy manufactured by high-power laser powder bed fusion[2]

4.1. Overview

This study explores high-power laser powder bed fusion (LPBF) processing of Cu–Cr–Zr alloy, focusing on its high strain rate dynamic mechanical response and microstructural evolution. The alloy undergoes significant strain hardening during dynamic impact loading, primarily attributed to intensified dislocation interactions and multiplication. This is accompanied by thermal softening induced by adiabatic heating, therefore improving strain accommodation. As the strain rate increases from 4400 s^{-1} to 11300 s^{-1}, the ultimate compressive strength (UCS) enhances from 173 ± 8 MPa to 489 ± 14 MPa, demonstrating a high strain rate sensitivity (SRS) of ~1. Microstructural examinations reveal that higher strain rates intensify the occurrence of adiabatic shear bands (ASBs), leading to severe localized plastic deformation. These ASBs generate localized stress concentrations, which in turn accelerate crack initiation and propagation through pore formation and coalescence within the ASBs. Despite this severe plastic deformation, texture analysis indicates that the crystallographic texture remains largely stable which suggests that the deformation mechanism is primarily governed by dislocation motion and interaction, rather than by crystal structure reorientation. Overall, the alloy balances strain hardening and strain accommodation at high strain rates, making it well-suited for applications requiring strength and resilience under dynamic impacts.

4.2. Introduction

Copper and its alloys have garnered attention due to their exceptional properties, such as high thermal and electrical conductivity, excellent corrosion resistance, and ease of fabrication [3,104]. These characteristics make copper alloys indispensable in various industrial applications, including heat exchangers, electrical wiring, and components for aerospace and nuclear reactors. Among these alloys, Cu–Cr–Zr stands out for its unique balance of high strength and high conductivity [105,106].

[2] Published in *Materials & Design*, 2025.

The development of high-strength, high-conductivity Cu–Cr–Zr alloys has traditionally relied on methods such as casting [106,107], rolling [108,109], and hot forming [110,111] to achieve the desired balance between strength and conductivity. These methods, however, face limitations when producing complex geometries required for advanced engineering applications. The advent of additive manufacturing (AM), particularly laser powder bed fusion (LPBF), has opened new avenues for fabricating intricate Cu alloy components with precision [1].

LPBF offers significant advantages, including the ability to produce parts with complex internal structures, such as cooling channels and lattice frameworks, which are challenging to achieve through conventional manufacturing techniques. Besides, the rapid cooling rates (~10^6–10^7 K.s^{-1}) in LPBF lead to the formation of unique microstructures that are difficult to achieve with conventional processing methods [90,112,113].

The traditional methods of processing Cu–Cr–Zr alloys typically involve solution treatment to dissolve Cr in the Cu matrix, followed by aging to precipitate fine Cr-rich particles, which enhance the alloy's strength through the Orowan mechanism [48,114]. Moreover, the presence of Zr further improves the mechanical properties by promoting uniform precipitation and forming intermetallic Cu–Zr phases that inhibit grain boundary movement, thereby enhancing creep strength and resistance to thermal softening [115,116]. However, in the LPBF process of Cu–Cr–Zr alloys, the rapid solidification and inherent remelting of successive layers can lead to the formation of extremely fine nanoparticles, significantly enhancing the alloy's strength [50,54].

Zhang et al. [27] investigated the microstructure of LPBF-made Cu–0.5Cr alloy and observed fine cellular substructures, formed due to the high cooling rates typical of the LPBF process. This rapid solidification results in Cr being primarily dissolved into the Cu matrix, with only a small fraction precipitating as nanoparticles. Similarly, Zhou et al. [117] found that in the LPBF-manufacture of Cu–0.8Cr–0.1Zr alloy, most Cr atoms were dissolved in the Cu matrix, with a small amount precipitating as nanoparticles due to the complex thermal history during LPBF. Furthermore, Salvan et al. [53] reported that the LPBF process produced an anisotropic microstructure with elongated grains along the building direction (BD) and pavement-like grains in the plane normal to the BD. This anisotropy is attributed to the specific thermal conditions and scanning strategy employed during the LPBF process.

The rapid solidification inherent in LPBF also results in high dislocation densities and the formation of dislocation cells within the microstructure which eventually enhanced the tensile properties of the alloy. Bai et al. [99] demonstrated that the as-built Cu–Cr–Zr alloy produced by LPBF exhibits a refined microstructure and enhanced ductility, making it a strong candidate for applications requiring both strength and ductility. The as-built sample achieved a yield strength of 218 MPa, comparable to the solution heat-treated and aged samples (231 MPa), but offers significantly higher ductility of 46.5% elongation at fracture compared to 19.1% for the solution heat-treated and aged samples.

While significant progress has been achieved in the development and processing of LPBF-made Cu–Cr–Zr alloys [34,36,118], there is still a considerable gap in understanding their performance under dynamic impact loading conditions, such as those encountered in shock or high-velocity impact scenarios. Previous studies on Cu–Cr–Zr alloys have primarily focused on moderate strain rate ranges, such as 500–2200 s^{-1}, highlighting strain rate hardening behavior and the critical role of strain rate in mechanical responses under dynamic loading [119].

Similarly, investigations on LPBF-made Cu–Cr–Zr alloys have demonstrated strain rate sensitivity thresholds above 800 s^{-1}, underscoring their potential for positive strain rate sensitivities under dynamic conditions [120]. However, the performance of LPBF-made Cu–Cr–Zr alloys at higher strain rates remains unexplored, where factors like strain rate sensitivity and thermal softening could significantly affect mechanical properties. The present study aims to address this gap by evaluating the behavior of Cu–Cr–Zr alloys at higher strain rates.

The primary objective of this study is to conduct shock loading tests on the LPBF-made samples to assess the performance of Cu–Cr–Zr alloy under dynamic impact loading. The investigation will include a detailed analysis of the microstructure, texture, and mechanical behavior of the alloy to advance the understanding of LPBF-made Cu–Cr–Zr alloys and provide guidelines for their effective use in industries requiring high-performance materials. The findings from this study are highly promising. They suggest that the alloy can maintain its structural integrity under dynamic loading conditions, offering an optimal balance between resilience and durability. Such characteristics make the Cu–Cr–Zr alloy highly suitable for applications requiring both high impact resistance and long-term structural reliability.

4.3. Materials and methods

4.3.1. Material

In this study, plasma atomized powder (AP&C, Montreal, QC, Canada) with chemical composition of C18150 (Cu–1Cr–0.5Zr (in wt. %)) was utilized. Figure 4-1 provides a comprehensive analysis of virgin pre-alloyed powder. Scanning electron microscopy (SEM) image (Figure 4-1a) reveals spherical shape and smooth surface of powder particles, typical of plasma-atomized powders. Particle size distribution (PSD) (Figure 4-1b) values for D_{10}, D_{50}, and D_{90} are 16.8 µm, 37.6 µm, and 64.7 µm, respectively. These powder characteristics ensure reliable flowability and packing density during the LPBF process. In addition, energy-dispersive X-ray spectroscopy (EDS) elemental maps (Figure 4-1d–f) of the cross-sectional view of the powder particles show the homogeneous distribution of Cu, Cr, and Zr within the particles.

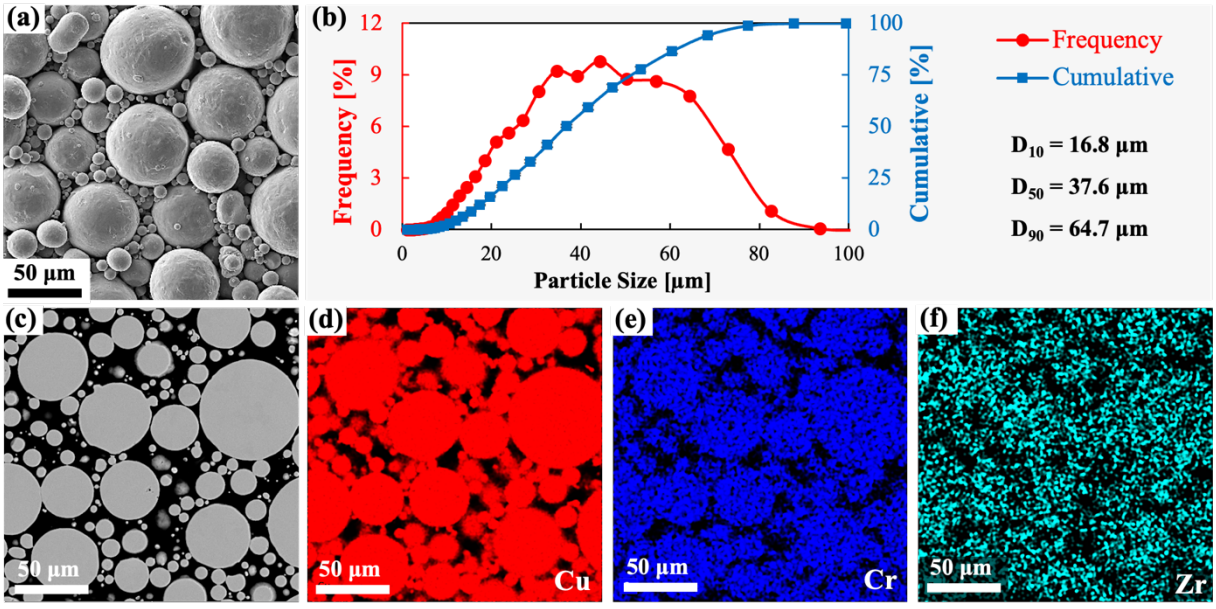


Figure 4-1 Comprehensive characterization of virgin pre-alloyed Cu–Cr–Zr powder: (a) SEM micrograph reveals the spherical morphology of the powder particles with smooth surfaces. (b) PSD graph shows D_{10}, D_{50}, and D_{90} values of 16.8 µm, 37.6 µm, and 64.7 µm, respectively. (c) Cross-sectional SEM image, with EDS elemental maps displaying the uniform distribution of (d) Cu, (e) Cr, and (f) Zr within the powder particles, confirming homogeneity.

4.3.2. LPBF process

The LPBF process was performed using a customized LPBF machine (AMCM, EOS M290 machine, Germany), which is equipped with a high-power 1 kW Ytterbium continuous fiber laser, featuring a wavelength of 1060 nm and a spot diameter of ~80 μm. The process was carried out under a high-purity Ar atmosphere, maintaining an oxygen content of less than 0.1% within the process chamber. To investigate the dynamic impact response of the Cu–Cr–Zr alloy, cylindrical samples with dimensions of 9.2 mm in height and 8 mm in diameter were printed using specific process parameters, detailed in Table 4-1. These parameters were selected through a two-step statistical optimization method conducted in a separate study. First, the Plackett-Burman design was used to identify the most significant process parameters. The selected parameters were then further refined using the central composite design (CCD) to thoroughly analyze interactions between parameters. This systematic approach enabled the identification of an optimal combination of parameters ensuring high density and minimal defects in the final parts.

Table 4-1 Process parameters used for LPBF of Cu–Cr–Zr

Parameter	Value
Contour Power [W]	450
Contour Speed [mm/s]	350
Laser Power [W]	800
Scanning Speed [mm/s]	800
Hatch Distance [μm]	180
Layer Thickness [μm]	20
Scanning Strategy	Stripe

4.3.3. Dynamic mechanical testing

The as-built samples were subjected to dynamic (high velocity) impact tests using a split Hopkinson pressure bar (SHPB) system (Figure 4-2). In this study, the impact direction (ID) was aligned parallel to the BD of the samples. During testing, the samples were positioned between the input (incident) and output (transmitted) bars and compressed by a striker bar, which impacted the input bar at controlled firing pressures. To minimize interfacial friction due to radial inertia during high-rate deformation, pure petroleum jelly was applied as a lubricant to the ends of the cylindrical samples. This lubrication reduced the coefficient of friction at the sample ends, preventing significant multiaxial stress distribution and ensuring the uniform uniaxial loading assumed in the analysis.

A pulse-shaping technique was also employed to mitigate the effects of ringing and wave dispersion. A thin aluminum disk, matching the diameter of the incident bar, was placed on the impact end of the incident bar to minimize wave dispersion. This method was specifically designed to achieve stress equilibrium in the early stages of loading, thereby capturing the elastic and early yielding responses of the ductile specimens.

The experiments were conducted at firing pressures of 100 kPa, 150 kPa, 200 kPa, and 250 kPa, with at least four samples tested per pressure level to ensure consistency. The average stress and strain values for each firing pressure were reported based on these tests. The actual speed of the projectile was recorded using a timer system positioned near the end of the gun barrel, allowing impact momentum (IM) to be used as a measure of impact magnitude, which generally correlates with the firing pressure [121]. IM is defined as follows:

$$p = \int F.dt = mv \tag{4-1}$$

where p, F, t, m, and v represent impulse (kg.m/s), force applied during the impact loading (N), impact duration time (s), mass (kg), and firing velocity (m/s) of the projectile, respectively. The impact momenta used in this study varied within a negligible tolerance of less than 2.5%. To measure the elastic waves in the input and output bars, two strain gauges were employed, capturing incident, reflected, and transmitted waves. The recorded signals were subsequently amplified and converted into voltage data as a function of time. Engineering stress (σ), engineering strain (ε), and engineering strain rate ($\dot{\varepsilon}$), were then calculated as follows [122]:

$$\sigma = \frac{A_B}{A_S} E_B \varepsilon_T \tag{4-2}$$

$$\varepsilon = -2\frac{C_B}{L_S}\int_0^t \varepsilon_R dt \tag{4-3}$$

$$\dot{\varepsilon} = -2\frac{C_B}{L_S}\varepsilon_R \tag{4-4}$$

where A_B and E_B are the cross-sectional area (mm^2) and Young's modulus (GPa) of the bar, respectively. A_S and L_S refer to the original cross-sectional area (mm^2) and length of the sample (mm), respectively. ε_T and ε_R denote transmitted and reflected strain pulses, respectively. C_B is the velocity of elastic waves in the bars (m/s) and t is the deformation time (s). The desired outputs, including true stress (σ_t), true strain (ε_t), and strain rate ($\dot{\varepsilon}_t$), were obtained from Equations (4-5)–(4-7) [123]:

$$\sigma_t = \sigma[1 - \varepsilon] \tag{4-5}$$

$$\varepsilon_t = -\ln[1 - \varepsilon] \tag{4-6}$$

$$\dot{\varepsilon}_t = \frac{\dot{\varepsilon}}{1 - \varepsilon} \tag{4-7}$$

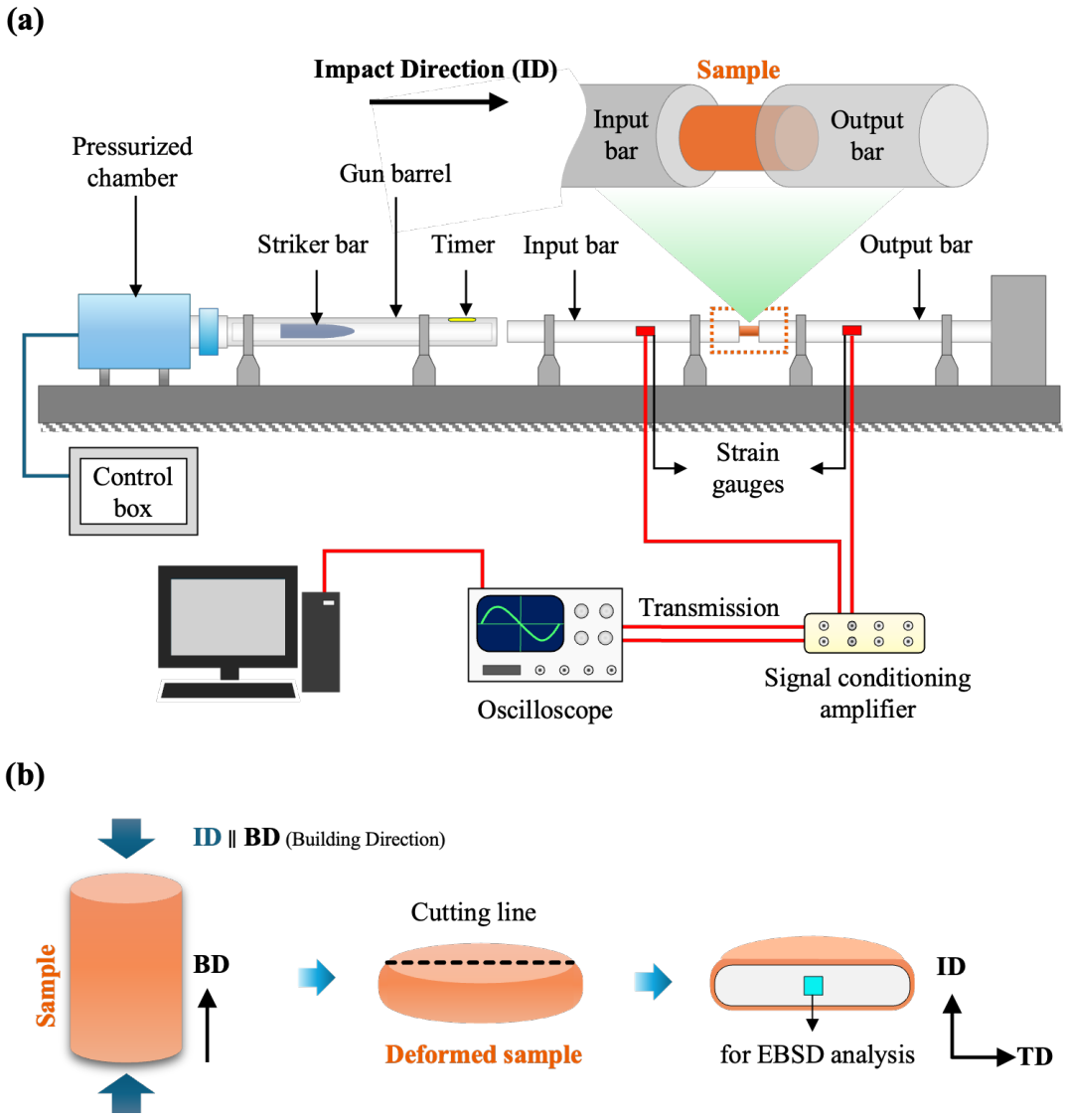


Figure 4-2 (a) Schematic of the split Hopkinson pressure bar (SHPB) setup used for dynamic impact loading of the Cu–Cr–Zr samples, with the impact direction (ID) aligned parallel to the building direction (BD). (b) Magnified view showing the area subjected to EBSD analysis after testing at various firing pressures, ranging from 100 kPa to 250 kPa.

4.3.4. Microstructural characterization

Sample preparation for microstructural evaluation involved grinding with SiC papers from 100 to 2400 grit, followed by polishing with 1-μm MD-Nap abrasive. A final polishing step was performed using a Buehler VibroMet2 machine for 5 hours with a non-crystallizing amorphous 0.02 μm colloidal silica suspension to prepare samples for electron backscatter diffraction (EBSD). Microstructural analysis was conducted on cross sections perpendicular to the BD in as-built samples and the ID in deformed samples using a TESCAN VEGA3 SEM equipped with BRUKER EDS and EBSD detectors.

Grain boundaries were identified in the EBSD data as continuous regions with a misorientation angle (Θ) greater than 5°. Low-angle grain boundaries (LAGB) were defined as those with $5° \leq \Theta \leq 15°$, while high-angle grain boundaries (HAGB) were defined as those with $\Theta > 15°$. Microtexture intensity was quantified in multiples of random distribution (MRD) units, where $MRD \leq 1$ indicates a random texture, and higher values signify a more pronounced texture [124].

For macrotexture analysis in both as-built and deformed samples, X-ray diffraction (XRD) was performed using monochromatic Co-Kα radiation ($\lambda = 1.79$ Å), targeting the (111), (200), and (220) planes. The resulting data of microtexture and macrotexture was processed in MTEX software to generate pole figures, providing insights into the crystallographic orientation distribution. Furthermore, XRD was utilized on the as-built samples for phase identification, with scans set over a 2θ range of 15° to 115° (θ: X-ray incidence angle). To observe broader microstructural features such as porosities, melt pool boundaries (MPBs), and deformed zones, optical microscopy (OM) images were captured using a Keyence VHX-7000 microscope. The samples were etched with iron (III) chloride solution (2% $FeCl_3$, 13% HCl, 85% de-ionized water) to enhance the visibility of these features.

For density measurement, high-resolution X-ray computed tomography (CT) scans were performed using a ZEISS Xradia 520 Versa, with a voxel size of 15 μm. This allowed detailed 3D imaging of the internal structure of LPBF-made Cu–Cr–Zr samples, enabling comprehensive evaluation of porosity and internal defects. The acquired data was processed and analyzed using Dragonfly software to calculate relative density (RD) and visualize defects, ensuring accurate, non-destructive characterization.

In addition, the surface roughness (S_a) was quantified using Keyence VK-X250 confocal microscopy with non-contact laser profilometry. These techniques enabled a thorough examination of the samples, offering crucial insights into both their internal structure and surface characteristics.

4.4. Results and discussion

4.4.1. Microstructural observation before deformation

The high reflectivity and thermal conductivity of Cu–Cr–Zr alloy significantly influence laser processing parameters [35], particularly in shaping the melt pool, which directly affects the solidification behavior. Moreover, Cu and Cu alloys exhibit a low absorption at ~1 μm laser wavelength commonly used in LPBF processes, leading to insufficient energy transfer and incomplete fusion during melting [2,5,15,45]. Many studies have focused on optimizing process parameters for Cu and Cu alloys in LPBF to address challenges like high reflectivity and thermal conductivity [98,125,126]. In the present study, we concentrate on investigating the mechanical behavior and microstructural evolution of the LBPF-made Cu–Cr–Zr alloy under dynamic loading conditions. A detailed investigation of parameter optimization methods, such as design of experiments (DOE), will be presented in a separate study. Nevertheless, ensuring the quality of LPBF-made parts, which reflects both the process effectiveness and the structural integrity of the final product, remains crucial for confirming that the components meet the necessary standards for subsequent mechanical testing.

The results of experimental measurements of RD and S_a for the shock loading test samples are presented in Figure 4-3. The CT scan (Figure 4-3a) provides a comprehensive view of the internal structure, revealing a high RD of 99.97%, indicative of minimal internal porosity and voids. The laser profilometry analysis (Figure 4-3b) of the as-built samples demonstrated S_a of 11.9 ± 2.3 μm, reflecting a finely controlled fabrication process that achieved a smooth and consistent surface finish. These combined results underscore the effectiveness of the optimized LPBF parameters in creating high-quality Cu–Cr–Zr alloy components with both excellent internal density and surface characteristics, which are critical for their performance under dynamic loading conditions.

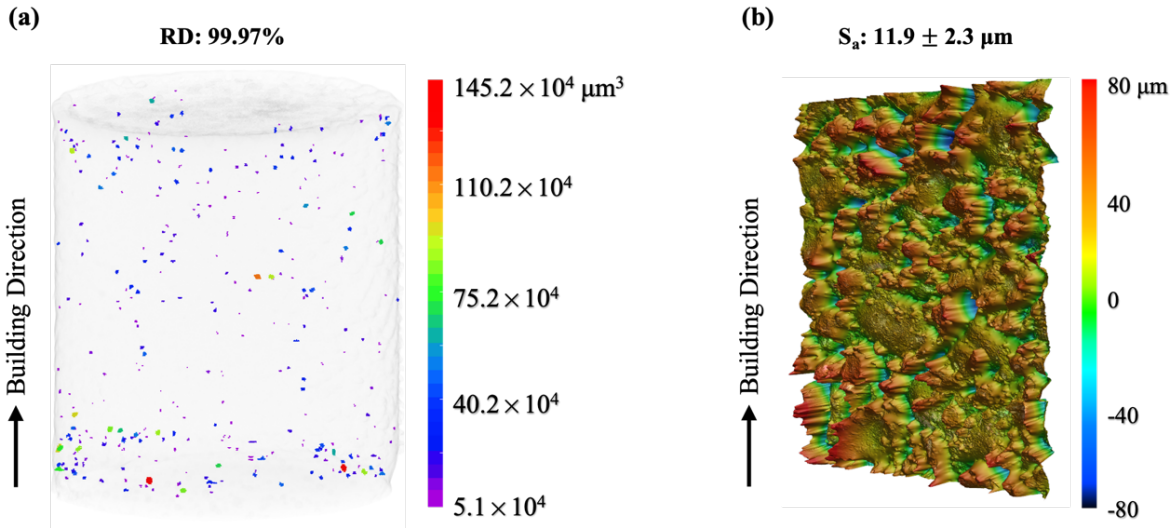


Figure 4-3 The overall quality of the as-built Cu–Cr–Zr cylindrical coupon produced via LPBF: (a) The CT scan result reveals a high relative density (RD) of 99.97%, indicating minimal internal porosity. (b) The laser profilometer analysis shows the surface roughness (S_a) of 11.9 ± 2.3 µm, underscoring the smooth and consistent surface finish achieved.

Characterizing the initial microstructure of the alloy before mechanical testing is crucial, as it provides valuable insights into how its inherent features, such as grain structure and crystallographic texture, might influence mechanical behavior. The microstructure of as-built parts, in particular, can reveal critical information about the thermal history and processing conditions, playing a direct role in shaping key mechanical characteristics such as strength, ductility, and toughness.

Figure 4-4 presents the microstructure and elemental distribution within the undeformed as-built Cu–Cr–Zr sample. The OM micrographs in Figure 4-4a and Figure 4-4b reveal the typical layered microstructure of the LPBF process, showing visible melt pools and columnar grains formed along the BD. These images were captured using different lighting modes: Figure 4-4a was taken with full coaxial lighting, providing a bright field observation that highlights the overall grain structure. Figure 4-4b was obtained using partial coaxial lighting, where the bright field was adjusted to enhance and reveal finer details, such as the MPBs, within the microstructure. The arrangement of print courses and the alignment of grains within the fused layers reflect the material's solidification pattern.

During LPBF, the rapid solidification rates and high thermal gradients, influenced by the high thermal conductivity of Cu–Cr–Zr alloy, encourage the formation of a columnar grain structure

[98,126]. The high thermal conductivity of the alloy facilitates quick heat dissipation, contributing to sharp thermal gradients that drive the directional solidification process. The observed columnar grains are aligned along the BD, indicating directional solidification. This is a direct result of the high thermal gradients and rapid solidification rates inherent to the LPBF process [89]. The columnar grains grow epitaxially from the previously solidified layers, oriented in the direction of heat extraction. Generally, in the LPBF process, the low energy barrier for epitaxial growth facilitates the preferential alignment of grains at the MPBs along specific crystallographic directions [95].

The SEM images in Figure 4-4c and Figure 4-4d provide a closer view of the melt pools and grain structure. In Figure 4-4c, the blue dotted lines highlight the MPBs, delineating the regions where each successive layer solidifies during the LPBF process. The grains are not confined to these boundaries but extend across multiple layers, aligning preferentially along the BD. This alignment is driven by the interplay between the thermal gradient and the crystallographic orientation, particularly favoring the <100> orientation for cubic metals [95,96]. The temperature gradient and heat flow are primarily aligned with the BD, causing columnar grains to elongate along this thermal gradient. However, the competitive growth mechanism, influenced by both the thermal gradient and the easy growth direction <100>, determines the grain's final orientation, which can sometimes deviate to orientations such as <110>, depending on the melt pool's geometry and process parameters [127]. Figure 4-4d shows that both columnar crystals and cellular subgrains are directed toward the center of the melt pool, following the path of heat flow during solidification. This phenomenon is driven by directional heat flow and the competitive growth of grains during fabrication [97,128].

Another microstructural feature visible in the SEM images (Figure 4-4e and f) is the presence of near-spherical pores. These pores likely formed due to the entrapment of gas within the chamber during solidification typically resulted from the keyhole phenomenon. This entrapment or vapor-filled depressions can form at high laser power when the recoil pressure becomes intense. In such cases, gas bubbles, either from the processing atmosphere or within the powder bed, are unable to escape due to keyhole collapse or before the surrounding material solidifies [129]. The EDS maps (Figure 4-4e_x–g_x) provide insight into the elemental distribution around the pores. Notably, there is a higher concentration of Cr and Zr at the edge of the pore, while a relative depletion of Cu is observed.

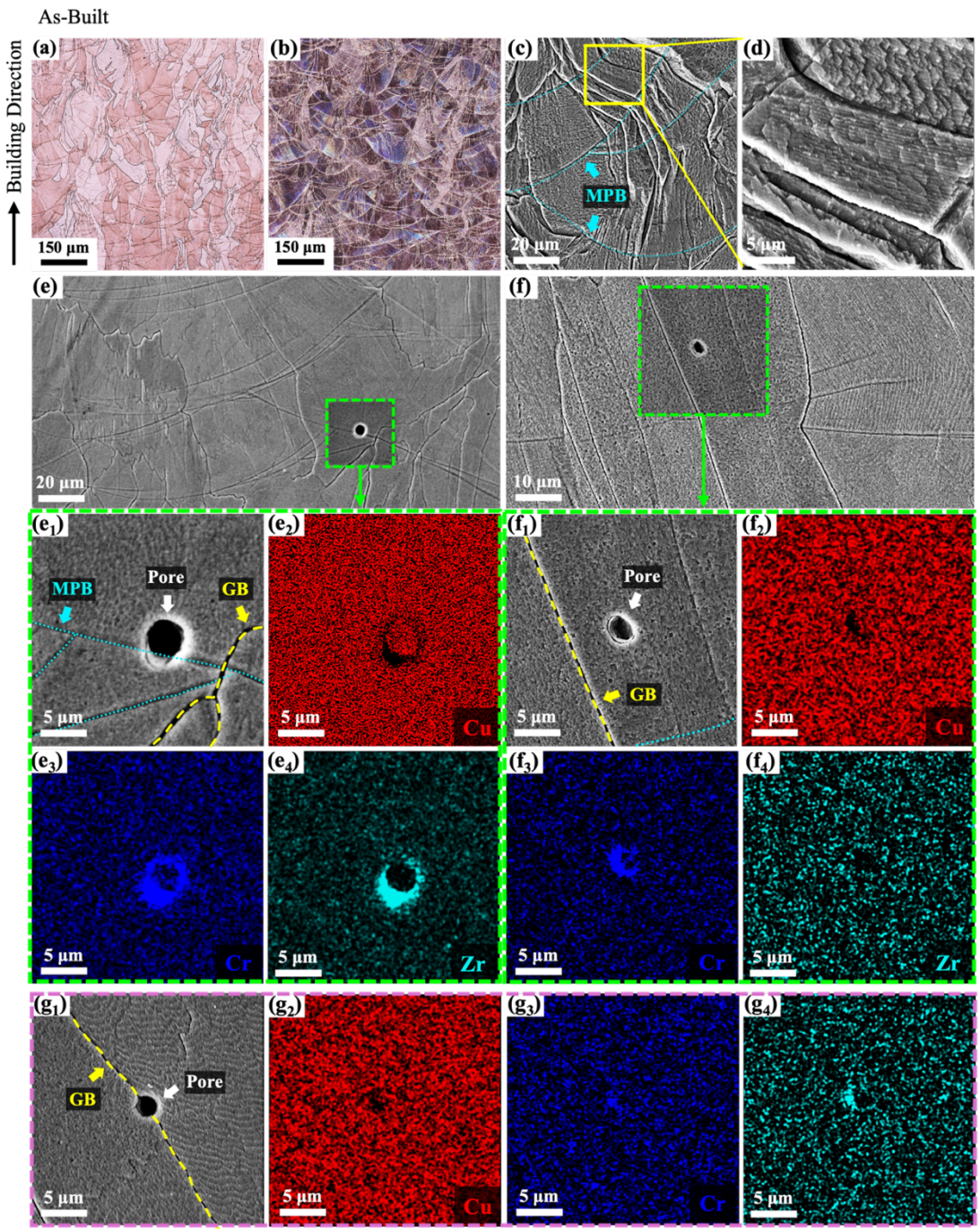


Figure 4-4 OM images of the as-built sample under (a) full and (b) partial coaxial lighting, showing the overall grain structure and layered microstructure typical of the LPBF process, including visible melt pool boundaries (MPBs) and columnar grains aligned along the BD. SEM micrographs provide a closer view of detailed features, revealing (c,d) the cellular structure within the grains and (e,f) pores formed during solidification due to gas entrapment. EDS maps of the region around the pores in (e_1,f_1,g_1) show the elemental distribution of (e_2,f_2,g_2) Cu, (e_3,f_3,g_3) Cr, and (e_4,f_4,g_4) Zr. (**GB:** grain boundary).

The elemental segregation of Cr and Zr during LPBF can be attributed to the solidification dynamics specific to the process, where high temperature gradients (G) and rapid solidification rates (R) play crucial roles [85]. Due to their higher melting points (Cr: 1907 °C, Zr: 1855 °C) compared to Cu (1083 °C), Cr and Zr solidify earlier during the rapid, non-equilibrium cooling characteristic of LPBF. In addition, the Marangoni effect, induced by temperature-dependent surface tension gradients, drives convective flow within the melt pool from hotter to cooler regions [130]. However, due to the lower diffusivity of Cr and Zr in the liquid state, this flow largely affects Cu, allowing Cr and Zr to remain concentrated near cooler zones, such as at pore edges. The sharp thermal gradients and rapid cooling near these pore edges may promote segregation, as Cr and Zr cannot diffuse back into the liquid phase before solidification completes. This may explain the localized elemental enrichment at the pore edges, where Cr and Zr become locked, potentially contributing to the distinct Cr and Zr peaks observed in the XRD pattern (Figure 4-5).

In the XRD pattern of the as-built Cu–Cr–Zr sample shown in Figure 4-5, the low-intensity peaks at $2\theta \sim 41°$ and 53° correspond to Zr and Cr phases, respectively. This can be interpreted through two possible mechanisms. First, these peaks may result from the segregation of Cr and Zr at pore edges, as evidenced by EDS maps (Figure 4-4e_x–g_x). Alternatively, in-situ precipitation during LPBF can be the second plausible explanation. According to the literature, some studies propose that Cr and Zr remain in a supersaturated solid solution due to the rapid solidification of LPBF, which inhibits their ability to precipitate as distinct phases [34,53].

Other studies report that Cr and Zr can precipitate during LPBF, often forming nanoscale phases [30,117]. The sequential heating inherent to LPBF can partially remelt or affect previously solidified layers, particularly in high thermal conductive materials like Cu alloys. This phenomenon, often described as in-situ heat treatment [131,132], may promote the precipitation of nanoscale Cr and Zr phases. Given the high laser power (800 W) used in this study, such heat treatment effects are highly probable. In addition to Cr and Zr peaks, there is a small peak at $2\theta \sim 46°$ (Figure 4-5) that could be attributed to Cu_xZr_y compounds [99,133], although their ultra-fine size likely renders them undetectable by SEM. Confirming the presence and exact nature of these nanoscale phases would require advanced characterization techniques, such as transmission electron microscopy (TEM) or small-angle X-ray scattering (SAXS), which is the future work of this research.

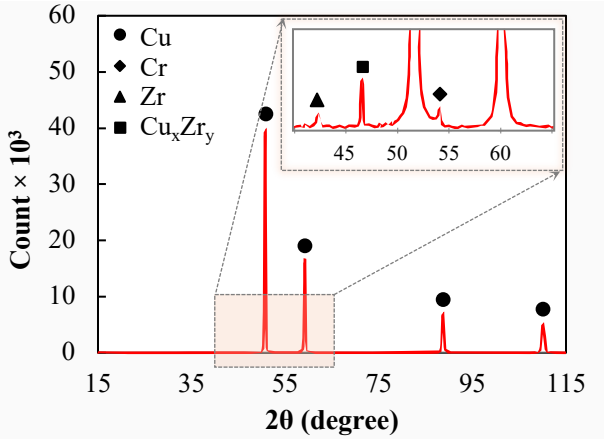


Figure 4-5 XRD pattern of the as-built LPBF-made Cu–Cr–Zr alloy, showing prominent diffraction peaks corresponding to the α-Cu phase, along with low-intensity peaks at 2θ ~ 41° and 53°, attributed to Zr and Cr phases. Moreover, a small peak at 2θ ~ 46° suggests the possible presence of Cu_xZr_y compounds, which may have formed during LPBF.

While previous characterization methods have provided valuable insights into the microstructure of the as-built Cu–Cr–Zr sample, understanding its crystallography is equally essential for a comprehensive analysis. Crystallographic characteristics, such as grain orientation, offer critical information about the material's texture and anisotropy. Meanwhile, dislocation density, though not directly a crystallographic feature, plays a significant role in revealing the internal stresses and defect structures induced by the LPBF process, further influencing the material's mechanical behavior.

Figure 4-6 presents the microstructural and crystallographic characteristics of the as-built Cu–Cr–Zr sample through EBSD. The image quality (IQ) map (Figure 4-6a) displays the overall microstructure of the sample, with HAGBs superimposed as black lines. This map highlights variations in the quality of diffraction patterns across the sample. Higher quality areas generally correlate with well-formed, defect-free grains, while lower quality regions may indicate areas with more defects or complex microstructures. This distinction is particularly important when analyzing the deformed microstructure (4.4.6).

The inverse pole figure Z (IPF-Z) map (Figure 4-6b) reveals the crystallographic orientation of grains relative to the BD, showing a clear alignment of columnar grains along the BD in the investigated area. As previously discussed, this alignment results from the directional solidification inherent to the LPBF process, where the sharp thermal gradients during cooling promote grain growth along the heat extraction direction. Notably, within individual grains, a gradient in colors can be observed (Figure 4-6b), indicating the presence of LAGBs with misorientation angles of $\Theta \leq 15°$. This suggests the presence of defects such as geometrically necessary dislocations (GNDs) within the grains. Accordingly, based on analysis of the XRD data (Figure 4-5), the Williamson–Hall method was used to estimate the dislocation density (ρ) of the alloy [134]. The calculated ρ is ~29.5×10^{13} m^{-2}, which is significantly higher compared to the solution-treated Cu–Cr–Zr alloy reported in the literature (~5.3×10^{13} m^{-2}) [107]. The high dislocation density observed in LPBF-made materials is a direct consequence of the rapid cooling rates characteristic of this process. The rapid solidification process limits the time available for dislocation annihilation and grain relaxation, resulting in the retention of substantial internal stresses, grain misorientation, and a high density of crystalline defects, such as dislocations.

Further, the kernel average misorientation (KAM) map (Figure 4-6c) confirms the presence of low angle misorientations within grains, providing the local strain distribution. Regions with higher KAM values, represented by warmer colors, indicate areas of increased dislocation density and localized strain. The buildup of strain within these regions is likely related to the rapid solidification and cooling rate during the LPBF process, inducing high internal stresses and promoting the formation of dislocations. These dislocations contribute to the material's overall strain hardening and can affect its mechanical properties, such as strength and ductility.

Figure 4-6d shows the pole figures for the (111), (200), and (220) planes, offering some details on the microtexture characteristics of the as-built Cu–Cr–Zr sample. The texture intensity is more noticeable in the (200) and (220) planes, with an MRD of 3.8 and 3.7, respectively. The observed texture components, although not strong, can be attributed to the high thermal conductivity of the Cu–Cr–Zr alloy and the significant thermal gradients during the LPBF process, which promote the preferential growth of grains along specific crystallographic orientations [96]. This microtexture is influenced by the scanning strategy and melt pool dynamics, leading to competitive grain growth along the BD. A thorough examination of the crystallographic texture and its evolution will be further discussed in 4.4.7, focusing on macrotexture analysis.

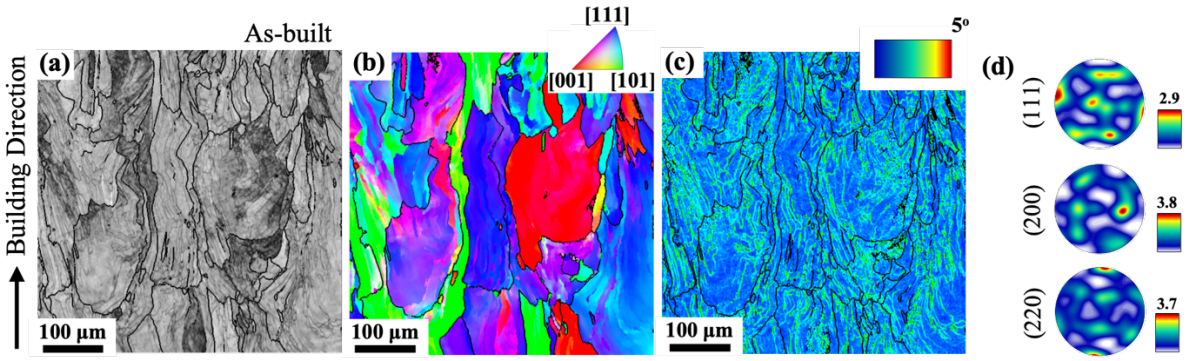


Figure 4-6 EBSD analysis of the as-built Cu–Cr–Zr sample showing microstructural and crystallographic characteristics: (a) The IQ map displays grain quality across the sample, with HAGBs superimposed as black lines. (b) The IPF-Z map reveals the alignment of columnar grains along the BD, with a color gradient within individual grains indicating LAGBs and suggesting the presence of defects. (c) The KAM map highlights regions of local strain, reflecting higher dislocation densities. (d) Pole figures for (111), (200), and (220) planes illustrate the microtexture, with the highest texture intensity observed in the (200) and (220) planes.

4.4.2. Dynamic mechanical response

After performing the SHPB test, the results were plotted to illustrate the dynamic mechanical behavior of LPBF-made Cu–Cr–Zr samples under various strain rates. Figure 4-7 presents the true stress–true strain curves, demonstrating how stress evolves under the dynamic conditions. The results are averaged over four tests for each condition, with the maximum strain rate value used to characterize the experimental results. The strain rates achieved include 4400 s^{-1}, 6100 s^{-1}, 8000 s^{-1}, and 11300 s^{-1}, which correspond to firing pressures of 100 kPa, 150 kPa, 200 kPa, and 250 kPa, respectively. The higher firing pressure imparts more momentum and energy to the material, causing it to strain at a faster rate and undergo more intense deformation.

According to the dynamic stress–strain curves (Figure 4-7) the material progressively experiences higher stress levels as deformation proceeds. The increase in strength with strain is primarily driven by dislocation–dislocation interactions and dislocation multiplication during straining [121,135]. At all tested strain rates, the flow curves exhibit initial strain hardening, progressing toward the yield stress (YS). As strain continues to increase, the material reaches its ultimate compressive strength (UCS); however, the rate of flow stress increment decreases. This reflects the competition between strain hardening from dynamic deformation and thermal softening caused by the temperature rise within the specimens during high strain rate deformation.

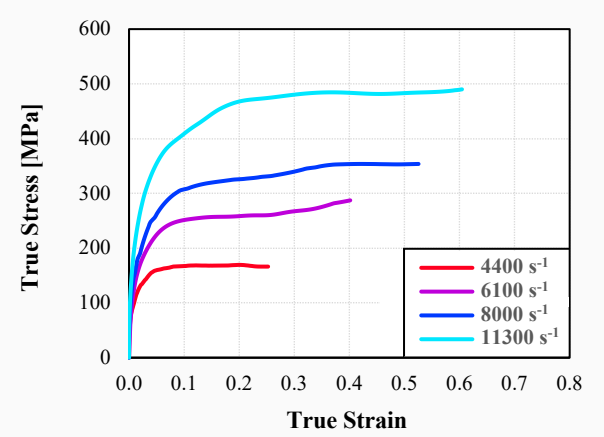


Figure 4-7 True stress–true strain curves showing dynamic mechanical response of LPBF-made Cu–Cr–Zr samples at varying firing pressures (100 kPa, 150 kPa, 200 kPa, and 250 kPa) during SHPB test. The corresponding maximum strain rates for each pressure are 4400 s^{-1}, 6100 s^{-1}, 8000 s^{-1}, and 11300 s^{-1}.

In high strain rate tests, deformation is typically governed by three main factors: strain hardening from increasing deformation, strain rate hardening, and thermal softening due to adiabatic heating [136]. A substantial portion of the plastic work can be converted into heat during dynamic deformation of metals and alloys, resulting in adiabatic conditions characterized by localized temperature increases [137]. This temperature increase can lead to a localized reduction in load-carrying capacity, causing plastic deformation to become inhomogeneous and strain to concentrate in narrow regions leading to the formation of adiabatic shear bands (ASBs) [138].

The ASBs are narrow paths of intense strain localization in the material during the dynamic impact loading. As deformation progresses, the heat generated from intense plastic deformation may not dissipate quickly, resulting in heat accumulation and a further rise in local temperature within the shear band regions. The temperature rise during such deformation can be quantitatively assessed using Equation (4-8) [138]:

$$\Delta T = T - T_0 = \frac{\beta W_p}{\rho c_p} \tag{4-8}$$

where T_0 represents the room temperature (°C), T denotes the temperature of the sample after dynamic compression tests (°C), W_p refers to the plastic work resulting from the high strain rate deformation (N.m). The parameters ρ and c_p stand for the mass density and specific heat capacity at constant volume, with values of 8.9 $g.cm^{-3}$ and 380 ± 20 $J.kg^{-1}.°C^{-1}$ for Cu–Cr–Zr, respectively.

The Taylor-Quinney parameter β, which defines the fraction of the plastic deformation (W_p) converted into heat (Q_p), can be calculated using Equations (4-9) and (4-10):

$$\beta = \frac{Q_p}{W_p} \tag{4-9}$$

$$W_p = \int \sigma . d\varepsilon \tag{4-10}$$

In the present study, the Taylor–Quinney coefficient is assumed to be 0.9, indicating that 90% of the projectile's kinetic energy is converted into heat [121,139]. This assumption aligns with experimental observations and molecular dynamics simulations of face-centered cubic (FCC) metals like Cu, which reveal that most of the plastic work in shear deformation is dissipated as heat [140,141]. The temperature rise observed in the deformed samples is detailed in Table 4-2. It is important to note that this calculation represents the bulk temperature rise of the material and does not account for localized temperature variations, such as those occurring within ASBs or near microstructural features.

Table 4-2 Dynamic mechanical properties of compressed Cu–Cr–Zr

Pressure (kPa)	Strain Rate (s^{-1})	YS (MPa)	UCS (MPa)	Total strain (%)	Toughness (MJ/m^3)	Temperature Rise (°C)
100	4400	73 ± 4	173 ± 8	25.3 ± 0.5	40.3 ± 4.2	10.7 ± 1.1
150	6100	88 ± 5	297 ± 13	41.6 ± 0.3	100.3 ± 8.3	26.7 ± 2.2
200	8000	114 ± 7	354 ± 20	52.6 ± 0.5	168.7 ± 14.6	44.9 ± 3.9
250	11300	179 ± 7	489 ± 14	60.5 ± 0.1	271.6 ± 18.0	72.3 ± 4.8

At higher strain rates, the rapid deformation generates more heat in a shorter time, with limited opportunity for heat dissipation, leading to greater localized temperature increases (Table 4-2). The temperature rise during dynamic deformation can significantly influence the material's behavior, particularly by promoting the formation of ASBs, which locally soften the alloy. Although this softening effect counteracts work hardening, it can enhance local deformation capacity and strain accommodation within the material, allowing it to deform more efficiently in localized regions. As a result, the material becomes more ductile at higher strain rates. For instance, the specimen deformed at the strain rate of 11300 s^{-1}, exhibited ~35% higher total strain compared to the specimen deformed at the strain rate of 4400 s^{-1}, primarily due to the increased thermal softening at higher strain rates.

In addition to the observed increase in total strain with rising strain rates, a significant improvement in strength is also evident (Figure 4-7), which contributes to higher toughness in the alloy (Table 4-2). As the strain rate increases, both YS and UCS exhibit noticeable increases, reflecting the strain rate sensitivity (SRS) of the material. The increasing trend of YS and UCS with higher strain rates is clearly presented in Figure 4-8a. To ensure statistical reliability, all reported mechanical properties, including UCS and YS, are averaged from four independent tests conducted at each strain rate, with standard deviations shown as error bars in Figure 4-8a and detailed in Table 4-2. The recorded average UCS values are 173 ± 8 MPa, 297 ± 13 MPa, 354 ± 20 MPa, and 489 ± 14 MPa at strain rates of 4400 s^{-1}, 6100 s^{-1}, 8000 s^{-1}, and 11300 s^{-1}, respectively (Table 4-2).

The significant increases in UCS with strain rate can be attributed to the strain rate hardening, where the increased deformation rate intensifies the interaction and multiplication of dislocations. At higher strain rates, the material deforms more rapidly, limiting the time available for dislocation motion and recovery processes. This results in the accumulation of dislocations, which increases the material's resistance to further deformation, as reflected in the higher YS and UCS values.

The relationship between true stress and true strain rate is denoted in Equations (4-11) and (4-12):

$$\sigma_t = C\dot{\varepsilon}_t^m \quad \text{or} \quad \log\sigma_t = \log C + m\log\dot{\varepsilon}_t \tag{4-11}$$

$$m = \frac{\log(\sigma_2/\sigma_1)}{\log(\dot{\varepsilon}_2/\dot{\varepsilon}_1)} \tag{4-12}$$

where m and C are SRS and materials constant, respectively. Figure 4-8b demonstrates the relationship between $\log\sigma_t$ vs. $\log\dot{\varepsilon}_t$, where the stress values (σ_t) correspond to the yield stresses obtained at different strain rates. The slope of the linear fit (m), representing the SRS value, was determined to be ~1, with an R^2 value of 97%. A high SRS value suggests that the flow stress of the alloy is highly sensitive to changes in the strain rate. This means that as the strain rate increases, the material exhibits a considerable increase in flow stress, implying a strong strain-rate hardening effect.

In FCC materials, like Cu–Cr–Zr alloy, the mechanisms governing plastic deformation at high strain rates typically involve complex interactions between dislocations and barriers to their motion [142,143]. The observed SRS value of ~1 suggests that the hardening mechanisms are particularly active in the LPBF-made Cu–Cr–Zr alloy, leading to a marked increase in strength as the strain rate rises (Figure 4-7).

Unlike some other FCC alloys, which exhibit an abrupt increase in SRS [144], Figure 4-8b demonstrates that Cu–Cr–Zr alloy maintains a steady SRS curve across the tested strain rates. In many FCC materials, an abrupt rise in SRS is linked to a shift from thermally activated dislocation motion to a regime dominated by viscous drag at higher strain rates [145]. However, Cu–Cr–Zr alloy does not show this transition, suggesting that its deformation behavior is likely governed by dislocation slip mechanisms.

Overall, the high SRS value highlights the excellent performance and reliability of the Cu–Cr–Zr alloy under dynamic loading conditions. The pronounced strain rate hardening effect enhances the alloy's capacity to absorb energy at high strain rates, making it potentially advantageous for use in environments where high-impact resistance is crucial. While high SRS is often associated with concerns over reduced ductility and toughness (due to the potential for increased brittleness under intense hardening) the results of this study are promising. They indicate that, as the strain rate increases, the alloy not only becomes stronger but also exhibits improvements in ductility and toughness.

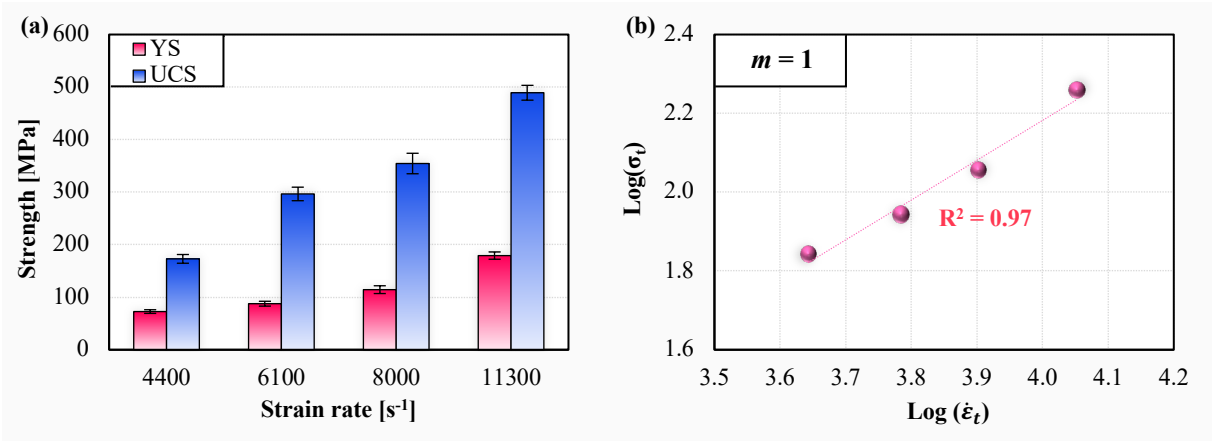


Figure 4-8 (a) The increasing trend of YS and UCS with strain rates for dynamically deformed LPBF-made Cu–Cr–Zr alloy. As strain rates increase, both YS and UCS show significant improvement due to strain rate hardening. (b) The relation between $\log\sigma_t$ and $\log\dot{\varepsilon}_t$. The slope (m) of linear fit highlights the material's sensitivity to strain rate, where flow stress rises substantially with increasing strain rates.

4.4.3. Work hardening behavior

To comprehend the hardening and softening behavior during high strain rate deformation under compressive loading, the work hardening rate ($d\sigma/d\varepsilon$) of the samples was plotted against strain, as shown in Figure 4-9a. The work hardening rate curves generally exhibit four distinct regimes (Figure 4-9b): (I) an initial drop in work hardening, (II) a continued decrease at a lower slope compared to stage (I), (III) an increase in work hardening rate, and (IV) a final decrease in work hardening rate.

In stage (I), the work hardening rate decreases as strain increases, reflecting the transition from elastic to elastoplastic behavior. In stage (II), the slope of this reduction lessens, indicating the activation of softening mechanisms including the initial stages of ASB formation. Stage (III) is characterized by an increase in work hardening rate, possibly due to enhanced dislocation-dislocation interactions. Finally, in stage (IV), the work hardening rate declines again, likely attributed to stress concentration within the microstructure and the pronounced formation of ASBs, driven by intense strain localization and temperature rise during dynamic deformation.

According to Figure 4-9a, strain rate significantly influences the work hardening behavior of materials. At the strain rate of 4400 s^{-1}, the work hardening rate intercepted the x-axis at the strain of ~11% (Figure 4-9a). It then briefly increases before decreasing again and eventually becomes negative, indicating that softening processes dominate over work hardening.

However, at the higher strain rates, the curves intersect the x-axis at higher strain levels and do not exhibit negative work hardening rates, demonstrating the dominance of work hardening over softening at these strain rates. Moreover, stages (II) and (III) are increasingly delayed at higher strain rates. The rapid accumulation of dislocations and their frequent interactions may lead to a more complex microstructural evolution, which prolongs the hardening stages and delays the transition to subsequent stages.

As the strain rate increases, the generation and interaction of dislocations intensify, thereby enhancing the material's resistance to deformation. This results in more pronounced work hardening and more moderated reduction in the work hardening at higher strain rates across each stage (Figure 4-9a). This could be ascribed to the accelerated deformation and the reduced time available for dislocation movement, which may lead to a slower progression of the work hardening rate.

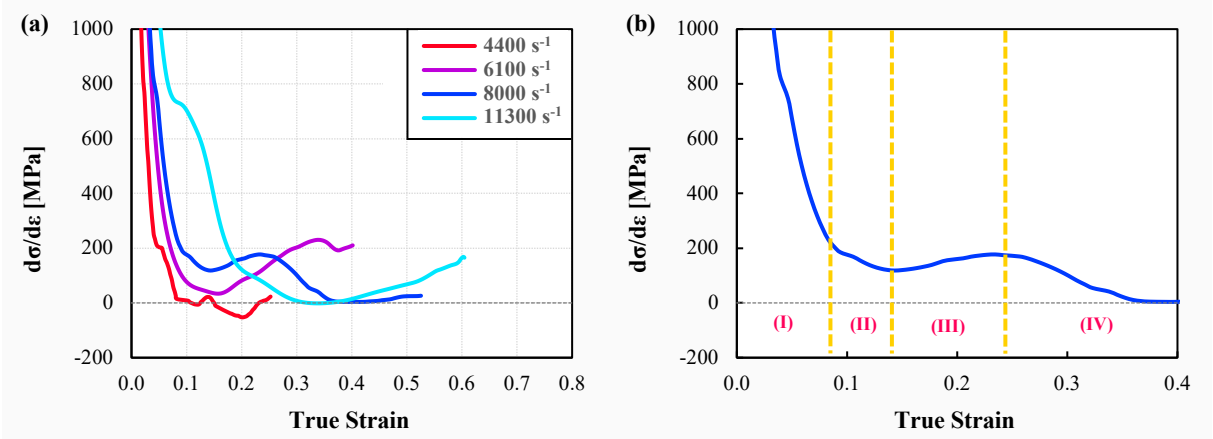


Figure 4-9 (a) Work hardening rate curves of the dynamically deformed LPBF-made Cu–Cr–Zr samples at various strain rates of 4400 s^{-1}, 6100 s^{-1}, 8000 s^{-1}, and 11300 s^{-1}, demonstrating how increasing strain rate moderates the work hardening progression. (b) Schematic representation of four distinct stages of work hardening rate: (I) initial drop, (II) reduced slope, (III) increase in hardening rate, and (IV) final decrease due to strain localization and adiabatic shear band (ASB) formation.

4.4.4. Microstructural evolution after dynamic deformation

As previously mentioned, ASBs are localized zones of intense plastic deformation that form during dynamic loading when plastic work generates heat, causing a rise in temperature and leading to thermal softening and strain localization [138]. The localized temperature rise requires adiabatic conditions, achieved when the heat generation rate during deformation exceeds the heat dissipation rate, which often happens under high strain rates. As a result, ASB formation depends largely on the material's thermal and mechanical properties, requiring the material to reach a critical point where thermal softening overcomes strain and strain rate hardening [138,146]. The microstructural analysis in Figure 4-10–Figure 4-12 provides insights into ASB distribution and density across varying strain rates for LPBF-made Cu–Cr–Zr alloy during impact testing.

In Cu alloys, plastic deformation is typically governed by dislocation slipping and recrystallization [147,148]. However, in extreme conditions like shock loading or high-impact events, where localized heating drives shear localization, ASBs can also form [149]. In Figure 4-10, the OM (Figure 4-10a and b) and SEM (Figure 4-10c and d) images at the strain rate of 4400 s^{-1} show sparse and underdeveloped ASBs, indicating moderate localized plastic deformation. This might be attributed to the high thermal conductivity of the Cu–Cr–Zr alloy, which facilitates rapid heat dissipation and delays the localized temperature rise required for complete ASB formation.

Materials with high thermal conductivity, like Cu, require significantly higher strain rates to achieve the adiabatic conditions necessary for shear localization [146]. While materials with higher strength are generally more susceptible to shear localization [150], the development of ASBs is ultimately determined by the interplay between strain hardening and thermal softening. At a strain rate of 4400 s^{-1}, this balance seems to favor strain hardening over thermal softening, limiting the progression of ASBs. This is supported by the flow stress behavior shown in Figure 4-7, where no evidence of plastic instability, typically indicated by a drop in flow stress after reaching the peak, is observed.

The dynamic impact loading using SHPB affects other microstructural features, such as gas pores formed during the LPBF process. The presence of elongated and irregular-shaped pores (Figure 4-10e and f) could be ascribed to the fact that the original spherical gas pores (Figure 4-4e and f) may have undergone significant deformation. These gas pores, initially spherical, become irregular in shape and align normally to the ID. The EDS maps (Figure 4-10e_x and f_x) further confirm the elemental presence of Cu, Cr, and Zr around these pores, corroborating their origin from the LPBF process (Figure 4-4e_x–g_x). These deformed pores can act as weak points in the material, facilitating crack initiation as shown in Figure 4-10e and f.

According to the literature, porosity plays a critical role in the formation and growth of ASBs as well as in the nucleation of voids [151,152]. They can contribute to the initiation and expansion of ASBs, which, in turn, can accelerate material failure through mechanisms such as crack propagation. Research conducted by Vishnu et al. [151], which focused on additively manufactured alloys like AlSi10Mg, 316L stainless steel, Ti–6Al–4V, and Inconel 718, demonstrated that larger and more irregularly distributed pores significantly increase sensitivity to ASB formation. Larger pores, up to 110 μm in size, were found to initiate ASBs more readily, and the presence of a higher porosity fraction further facilitated their expansion. The larger pores serve as nucleation sites for ASBs, and the increased porosity volume fraction lowers the material's critical shear strain. This will drive the propagation of ASBs and contribute to the material's overall susceptibility to failure.

In the current study, however, the pores observed are spherical and notably smaller, typically less than 5 μm. Although these smaller pores can still act as stress concentration sites, as demonstrated by their role in crack initiation in Figure 4-10e and f, they are likely to have a reduced effect on promoting ASB formation compared to larger pores. Nevertheless, the influence of these pores on crack initiation cannot be ignored, as even small stress concentrations can lead to material failure under dynamic loading conditions.

As the strain rate increases from 4400 s^{-1} to 6100 s^{-1}, the ASBs become more densely packed and interconnected, reflecting a higher degree of localized plastic deformation (Figure 4-10g and h). However, at this stage, the ASBs are still not fully developed, likely due to insufficient thermal softening to overcome strain hardening entirely. The intensified plastic deformation at this strain rate leads to the formation of micro-voids (MVs), likely due to localized stress concentrations and strain incompatibilities within the ASBs. This increased ASB density and void formation at higher strain rates aligns with the literature, where elevated strain rates are known to exacerbate material degradation and failure [153].

As shown in Figure 4-10l, these MVs are embedded within the ASBs and represent the early stages of damage initiation and growth. These voids play a critical role in the progression of damage by serving as nucleation sites for further material deterioration. This mechanism will be further elaborated in 4.4.5. Overall, the microstructures at 4400 s^{-1} and 6100 s^{-1} represent an intermediate stage of shear localization, predominantly influenced by strain hardening. The cracks observed in the localized shear zones are likely a result of accumulated localized stress and strain, which may limit further deformation and ultimately contribute to failure.

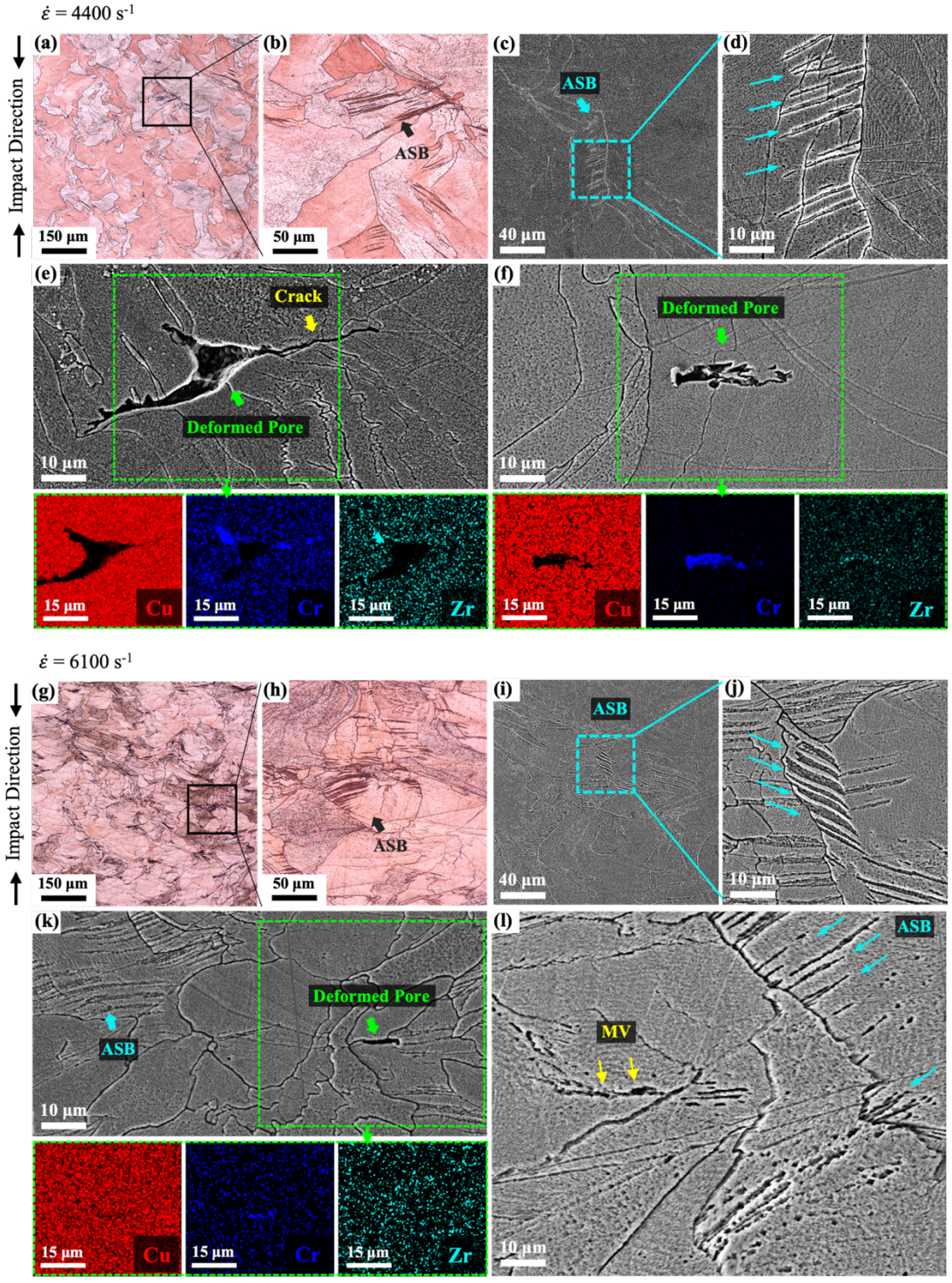


Figure 4-10 Microstructural analysis of the LPBF-made Cu–Cr–Zr samples deformed at strain rates of (a–f) 4400 s^{-1} and (g–l) 6100 s^{-1}: (a,b) OM and (c,d) SEM images at 4400 s^{-1} showing underdeveloped ASBs. (e,f) SEM images of deformed gas pores with corresponding EDS maps. (g,h) OM and (i,j) SEM images at 6100 s^{-1} revealing denser, interconnected ASBs. (k) SEM image with corresponding EDS maps showing deformed pores. (l) SEM image showing micro-voids (MVs) within the ASBs.

At the higher strain rates of 8000 s^{-1} (Figure 4-11) and 11300 s^{-1} (Figure 4-12), the localized deformation intensifies significantly. The microstructural analysis in Figure 4-11a–e and Figure 4-12a–e reveals a dense network of ASBs, demonstrating severe localized plastic deformation. These ASBs become increasingly interconnected and more pronounced as strain rate increases, which clearly indicates a direct correlation between strain rate and the extent of localized deformation. The greater complexity and density of ASBs reflect an increased accumulation of strain energy within the alloy, which initially contributes to work hardening but is counteracted by thermal softening as deformation progresses, as seen in the flow stress curves (Figure 4-7). Moreover, the heat generated within these narrow ASB regions leads to localized weakening of the material due to thermal softening, thereby promoting further deformation in these zones. This interplay between thermal softening and strain localization effectively explains the higher strain levels observed at elevated strain rates (Figure 4-7).

A notable observation in the microstructure of the deformed samples is the evident inhomogeneity. Figure 4-11a and Figure 4-12a present reconstruction of OM images from the cross-sections of the samples deformed at strain rates of 8000 s^{-1} and 11300 s^{-1}, respectively. The images reveal the inhomogeneous deformation within the samples, highlighting three distinct zones: (I) a heavily deformed microstructure at the center of the samples, characterized by intense shearing and a high density of ASBs, where strain is predominantly concentrated, (II) a “dead metal” zone near the surfaces, resulting from frictional forces due to contact with input and output bars, and (III) a moderately deformed area at the periphery. The schematic representation of these three zones is shown in Figure 4-13a.

The intense shearing observed in the central zone sharply contrasts with the relatively undeformed surface regions. While the columnar grains produced during the LPBF process in the surface areas exhibit minimal compression, the central zone experiences severe deformation. This disparity in deformation leads to an uneven distribution of stress within the material, which might result in localized points of failure during testing due to the concentration of stress in specific areas. Such inhomogeneous deformation suggests the need for careful consideration of microstructural integrity when evaluating the material’s performance under high strain rate conditions.

Localized deformation zones, such as ASBs, significantly contribute to stress concentration, acting as initiation points for cracks and ultimately compromising the material's structural integrity. At higher strain rates of 8000 s^{-1} (Figure 4-11h) and 11300 s^{-1} (Figure 4-12f), more pronounced and extensive cracking is observed in the deformed samples. As strain rates increase, ASBs intensify void growth, which eventually coalesces into larger defects, promoting crack propagation and ultimately resulting in material failure [138].

In addition, the cracks observed around deformed pores in Figure 4-12i and k emphasize the critical role these pores play in initiating and propagating failure under extreme conditions at the strain rate of 11300 s^{-1}. The fact that the continued propagation of cracks from these deformed pores highlights their contribution to weakening the material and accelerating failure. These defects can act as focal points for failure, reducing the material's ability to withstand further deformation and ultimately leading to fracture [151]. However, despite the presence of internal cracks, no surface fractures were observed in the deformed samples (Figure 4-13a), suggesting that the alloy retains a high capacity to accommodate strain without immediate surface failure. The following section will explore the damage evolution under dynamic loading in more depth.

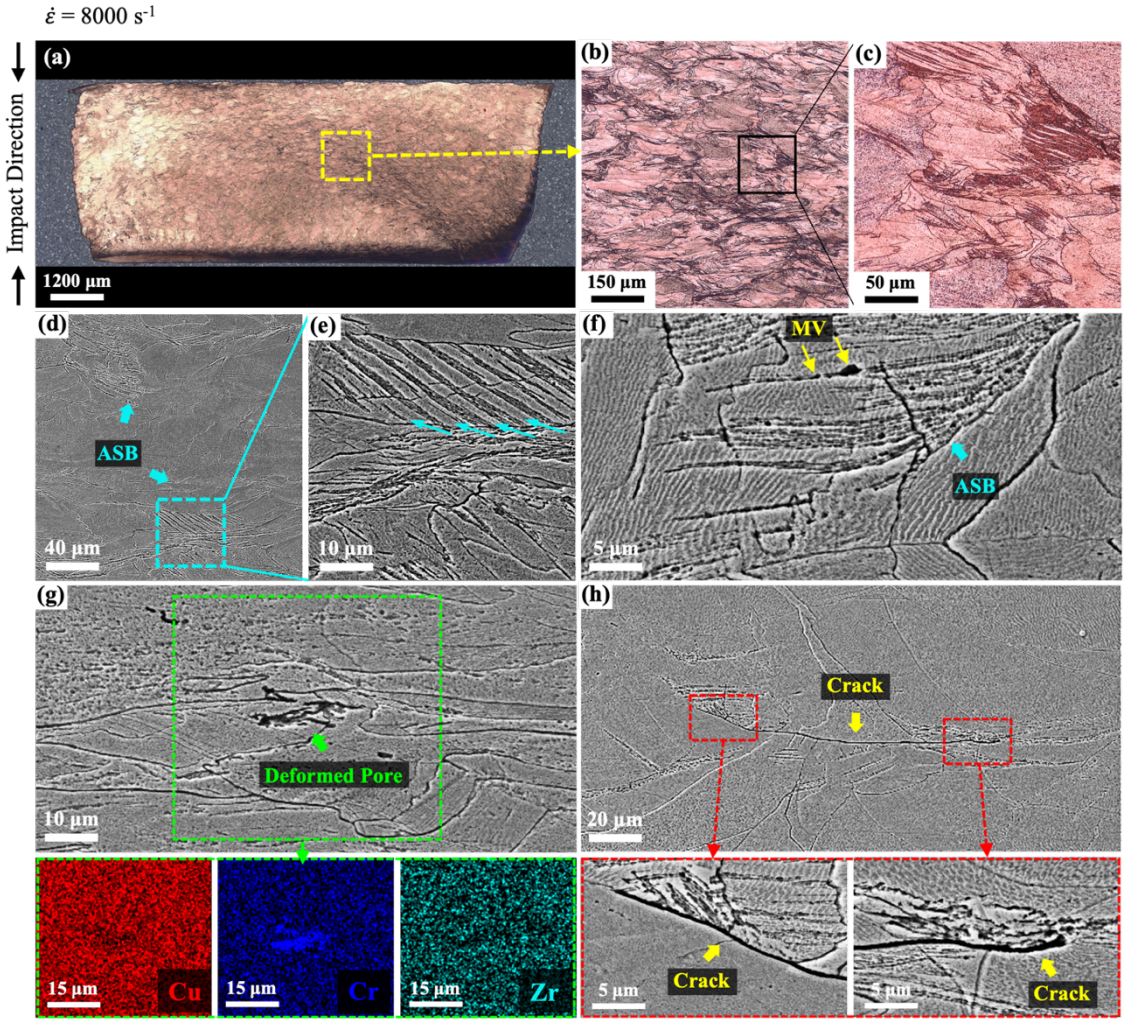


Figure 4-11 Microstructural analysis of the LPBF-made Cu–Cr–Zr samples deformed at the strain rate of 8000 s^{-1}: (a) Reconstructed OM images revealing inhomogeneous deformation within the sample, showing regions of intense strain localization. (b,c) OM images highlighting the formation of ASBs, which demonstrate severe localized plastic deformation, indicating significant strain accumulation. (d,e) SEM micrographs providing a closer examination of ASBs, revealing a more pronounced and interconnected ASB network, consistent with high strain rate conditions. (f) The presence of MVs within the ASBs, which serve as indicators of damage and potential sites for material failure. (g) SEM image showing elongated and irregularly shaped gas pores, acting as weak points for crack initiation. EDS maps confirm the elemental composition surrounding these pores, identifying (g_1) Cu, (g_2) Cr, and (g_3) Zr, confirming their origin from the LPBF process.

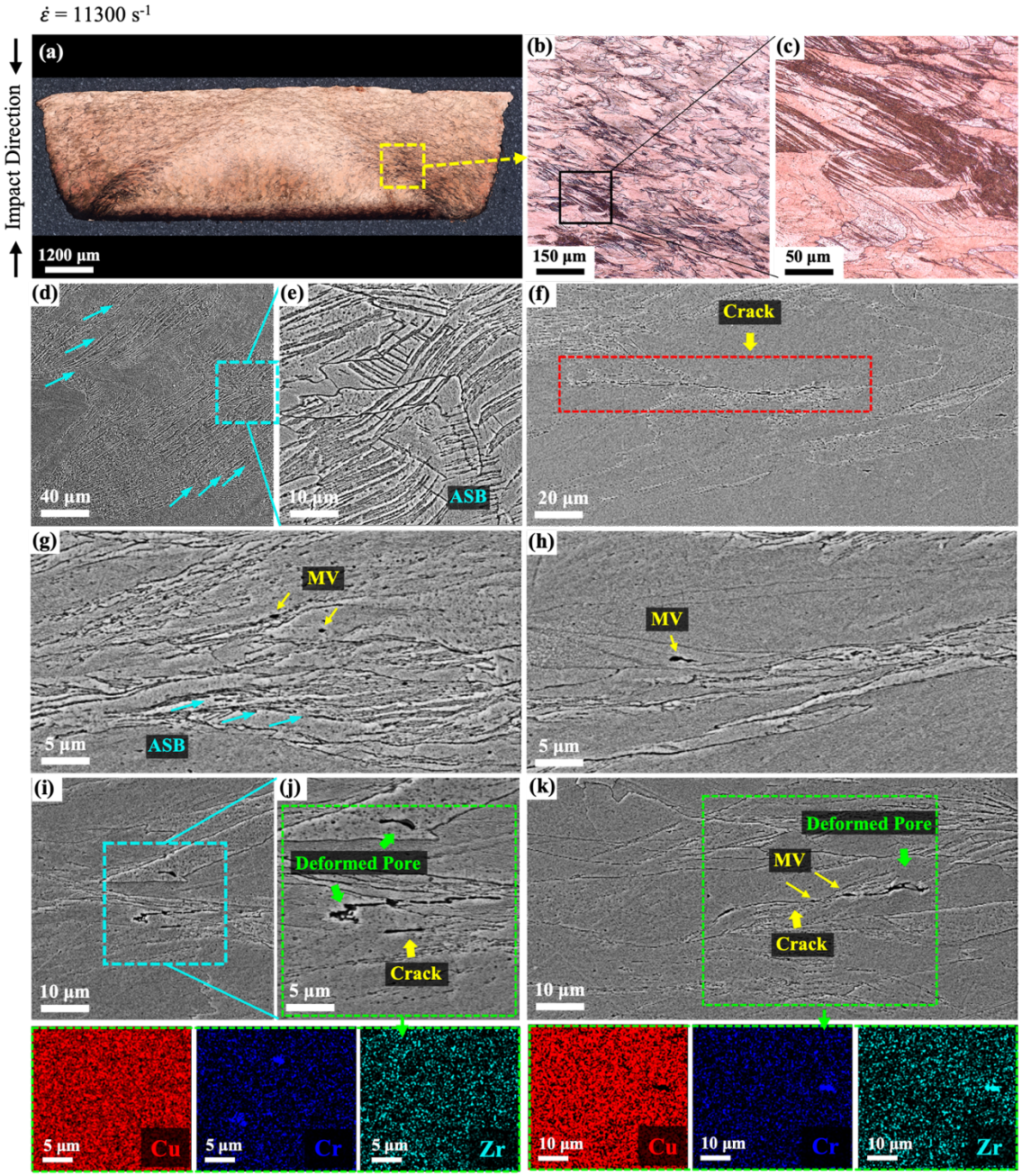


Figure 4-12 Microstructural analysis of the LPBF-made Cu–Cr–Zr samples deformed at the strain rate of 11300 s^{-1}: (a) Reconstructed OM images showing inhomogeneous deformation within the sample, with (b,c) regions of intense strain localization. (d,e) SEM micrographs indicating the intersection of ASBs, reflecting severe localized plastic deformation and complex strain accommodation. The presence of (f) crack and (g,h) MVs within the ASBs, serving as indicators of damage and potential sites for material failure. (i–k) SEM images showing deformed pores, acting as weak points for crack initiation. EDS maps confirm the elemental composition surrounding these pores, identifying (j_1,k_1) Cu, (j_2,k_2) Cr, and (j_3,k_3) Zr.

4.4.5. Damage evolution during dynamic deformation

Figure 4-13 provides key insights into the progression of damage evolution during dynamic deformation of LPBF-made Cu–Cr–Zr alloy under varying strain rates. The figure illustrates the complex interaction between ASBs, MVs, and crack formation, offering insights into the failure mechanisms that occur under high strain rates. The schematics in Figure 4-13a present the overall deformation characteristics observed during dynamic tests, revealing that deformation is highly localized. Three distinct zones of deformation are identified: (I) central zone, characterized by severe deformation, (II) surface zone, which remains nearly undeformed, and (III) peripheral zone, experiencing moderate deformation. As strain rates increase, these localized regions, particularly the central zone, become more intensified under dynamic loading. This behavior mirrors the observations made at strain rates of 8000 s^{-1} (Figure 4-11a) and 11300 s^{-1} (Figure 4-12a).

Figure 4-13b focuses on the progression of ASBs as strain rate increases. The schematic representation and SEM images highlight how the formation and evolution of ASBs become more pronounced with increasing strain rate, accompanied by a growing number of MVs. At the lower strain rate of 4400 s^{-1}, ASBs are limited in number, and the material exhibits more distributed deformation. As the strain rate rises to 6100 s^{-1}, MVs begin to nucleate within the ASB areas. The nucleation of MVs signifies the initiation of material degradation, as voids act as precursors to crack formation. At this strain rate, micro-voiding may occur without immediate failure, but as the strain rate rises, these voids coalesce rapidly, forming macro-cracks.

At strain rate of 8000 s^{-1}, cracks begin to appear, linking with the formed MVs. This marks a significant turning point in the material's failure progression, as the MVs coalesce into micro-cracks, reducing the material's ability to absorb further strain. The coalescence of MVs leads to irreversible damage, evidenced by crack formation and propagation (Figure 4-11h). At higher strain rate of 11300 s^{-1}, ASBs are highly interconnected, and cracks are more widespread. These interconnected ASBs and cracks point to severe material degradation, highlighting the inability of the material to withstand additional deformation. The SEM images confirm this progression, illustrating the increasing density of ASBs and the corresponding damage evolution in the form of void coalescence and crack propagation. ASBs may act as zones of weak discontinuity, which eventually transform into zones of strong discontinuity (micro-voids). These micro-voids impose additional strain on the material, eventually leading to material failure [138,153].

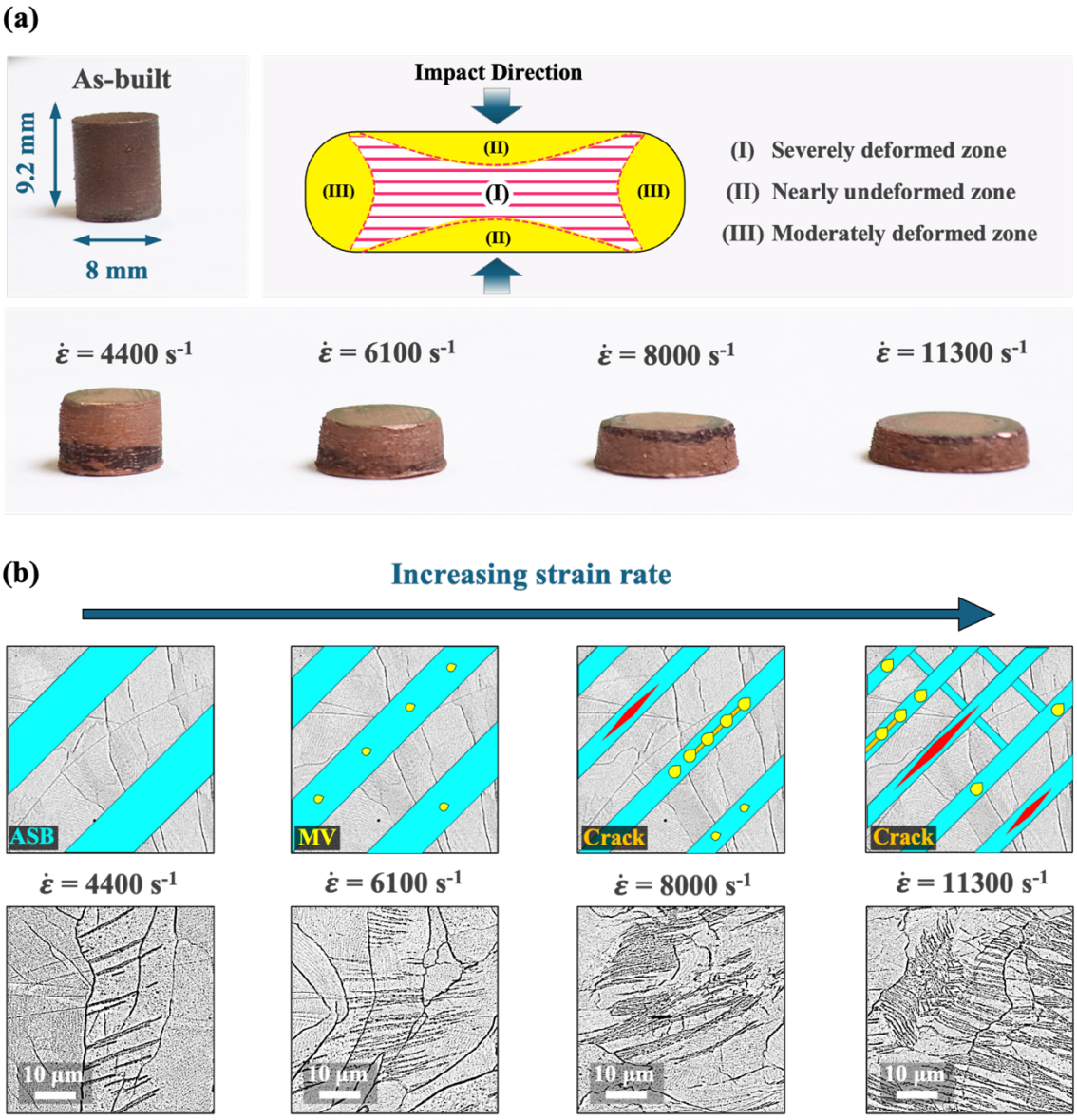


Figure 4-13 (a) Schematic representation of deformed zones in dynamic tests, illustrating strain localization in distinct regions under high strain rates, alongside actual images of the deformed samples. (b) Schematic of ASB formation at varying strain rates, with corresponding SEM images for each strain rate. As strain rates increase, ASBs become more pronounced and localized, leading to intensified plastic deformation. MVs nucleate within the ASBs, serving as precursors to crack initiation. At higher strain rates, these MVs coalesce, contributing to material softening and ultimately resulting in crack formation and propagation, marking the progression toward material failure under extreme conditions.

4.4.6. EBSD analysis after dynamic deformation

To provide a more comprehensive analysis of the microstructural evolution under varying strain rates, EBSD results from the deformed regions of LPBF-made Cu–Cr–Zr samples are presented in Figure 4-14. The analysis focuses on cross-sections that are perpendicular to both BD and ID,

with BD and ID being parallel. The IQ maps (Figure 4-14a_1,b_1,c_1,d_1) and IPFZ maps (Figure 4-14a_2,b_2,c_2,d_2) offer a visual representation of the quality of the EBSD data and the overall grain structure. Higher IQ regions generally represent well-formed, defect-free grains with minimal lattice distortion and high crystallinity, producing sharp and well-defined diffraction patterns. In contrast, lower IQ regions are typically associated with areas of higher defect density, significant lattice distortion, or more complex microstructures.

As shown in Figure 4-14, the grains undergo significant compression with increasing strain rate, becoming progressively more flattened in the cross-sectional view. At strain rate of 4400 s^{-1} (Figure 4-14a), slight compression is observed in the grains compared to their elongated structure in the as-built condition (Figure 4-6). At 6100 s^{-1} (Figure 4-14b), further deformation is evident, with more pronounced changes in grain shape. This indicates a shift toward higher levels of plastic deformation, as deviations from the original grain structure become more significant.

At higher strain rates of 8000 s^{-1} (Figure 4-14c), the compression becomes increasingly severe, with the grains appearing highly flattened in the cross-sectional view. This flattening is particularly severe at 11300 s^{-1} (Figure 4-14d), representing the most extreme deformation observed. In addition to grain deformation, extensive areas of low IQ (darker regions in the images) are observed at these higher strain rates (Figure 4-14c_1 and d_1). These low-IQ areas likely correspond to regions of ASBs, where intense localized deformation has led to severe lattice distortion and potential changes in lattice parameters, thereby reducing the diffraction pattern quality.

The pole figures for the (111), (200), and (220) planes (Figure 4-14a_4,b_4,c_4,d_4) highlight the evolution of microtexture in the severely deformed regions of the samples, particularly within zone (I) as described in Figure 4-13a. These pole figures reveal that despite the grains becoming flattened along the normal direction to the ID, there is minimal change in their crystallographic orientations. The MRD values for the (111), (200), and (220) planes remain relatively stable across different strain rates, which suggests that while the grains are undergoing substantial morphological changes, their crystallographic orientations remain largely unchanged. For instance, at the highest strain rate of 11300 s^{-1}, the MRD for the (111) plane is 3.2, compared to 2.9 at 4400 s^{-1}. Similarly, the MRD values for the (200) and (220) planes display only minor variations with strain rate, indicating that the overall microtexture remains fairly consistent despite severe plastic deformation.

The stability in the MRD values, along with the nearly identical “hot zones” in the pole figures, suggests that the deformation in the Cu–Cr–Zr alloy is predominantly accommodated through dislocation movement and grain shape changes, rather than significant lattice reorientation. This phenomenon is corroborated by the IPF maps (Figure 4-14a_2,b_2,c_2,d_2), which show that the color representing crystallographic orientation remains almost consistent, indicating minimal rotation of the crystal lattice. This behavior could be explained by the extremely high strain rates, which likely limit the time available for full crystallographic reorientation. Under such intense dynamic loading, the material’s response might be dominated by rapid dislocation movement and grain shape changes, with less opportunity for lattice reorientation or recrystallization, phenomena typically observed at lower strain rates.

The KAM maps (Figure 4-14a_3,b_3,c_3,d_3) highlight a subtle rotation (<5°), particularly in grains located near ASBs. This slight rotation at the subgrain level reflects localized strain accommodation within these regions, which often experience higher degrees of plastic deformation due to the formation of GNDs. These GNDs are crucial in maintaining compatibility between differently oriented regions of a grain [154], particularly under conditions of non-uniform deformation. As the strain rate increases, the KAM values also rise, especially in regions adjacent to the ASBs. Higher KAM values, represented by warmer colors, suggest a greater accumulation of GNDs, which are characteristic of highly strained regions where the crystal lattice has been severely distorted [155].

The tendency for lattice rotation within the grains is further supported by the quantitative analysis presented in Figure 4-15, which compares KAM distributions before and after deformation at different strain rates. As can be seen, there is a noticeable shift in the peak KAM values from the as-built sample to the deformed samples under higher strain rates. In the as-built condition, the peak KAM values are concentrated at lower angles with a higher fraction, indicating relatively low internal strain formed during the LPBF process. However, as the strain rate increases, the peak KAM values shift towards higher angles, indicating that the grains are experiencing greater internal strain and distortion as the deformation becomes more severe. This can result in the progressive hardening of the material as it responds to the increasing strain rate, which is a direct consequence of the intense localized deformation within ASBs.

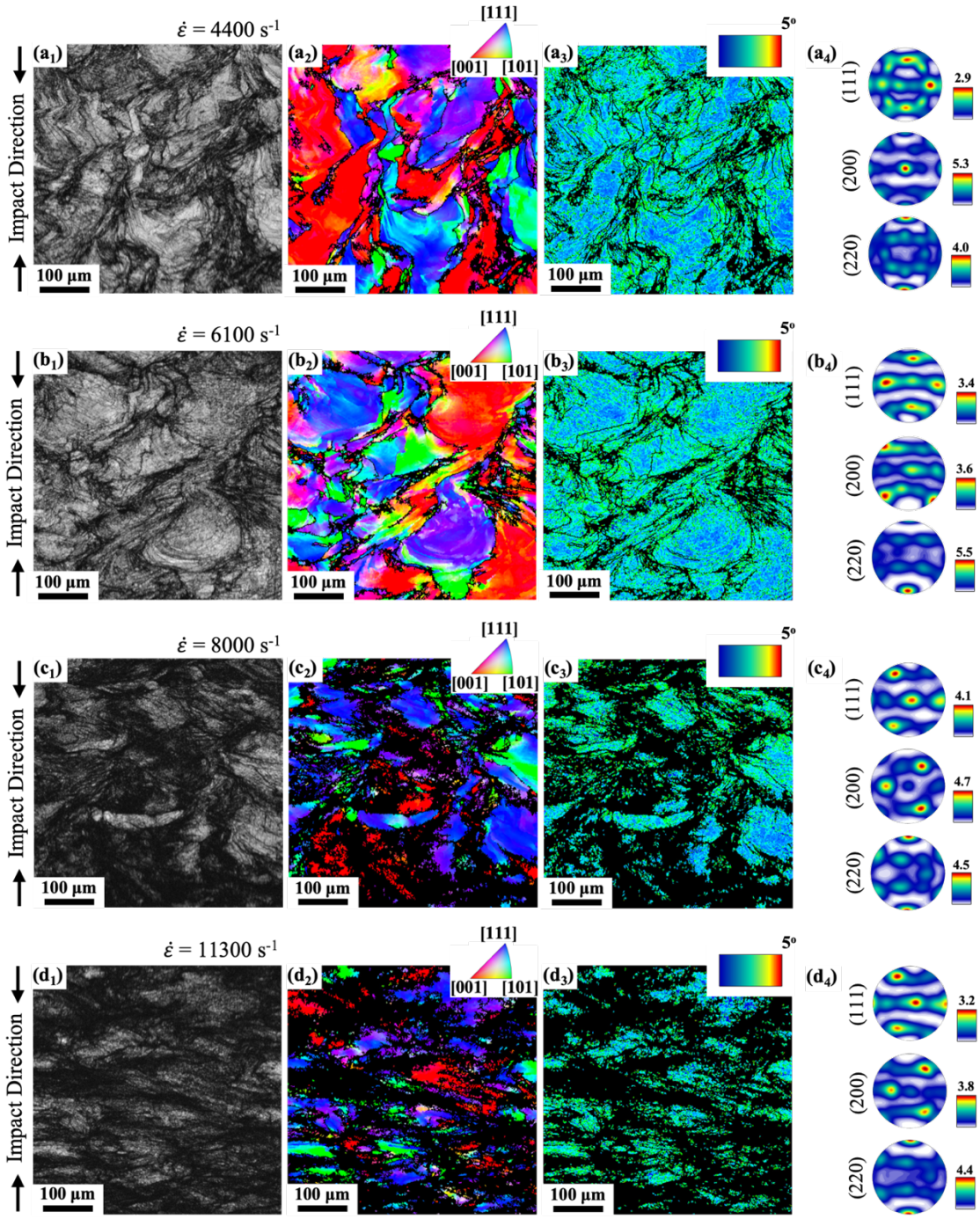


Figure 4-14 EBSD results of LPBF-made Cu–Cr–Zr alloy deformed at various strain rates of: (a_1–a_4) 4400 s^{-1}, (b_1–b_4) 6100 s^{-1}, (c_1–c_4) 8000 s^{-1}, and (d_1–d_4) 11300 s^{-1}. The data includes (a_1,b_1,c_1,d_1) IQ map, (a_2,b_2,c_2,d_2) IPFZ map, (a_3,b_3,c_3,d_3) KAM map, and (a_4,b_4,c_4,d_4) pole figures of (111), (200), and (220) planes, corresponding with the analyzed region.

In addition, the increase in KAM values (Figure 4-14a_3,b_3,c_3,d_3) reflects a greater degree of plastic deformation, consistent with the earlier discussion that strain localization is more pronounced at higher strain rates. Increased KAM values can contribute to work hardening through increased dislocation density. This correlation between KAM values and dislocation density is well-established in the literature, where higher KAM values indicate increased GND density, leading to greater strain accommodation and stored energy [156]. As strain rates increase, the material undergoes greater strain hardening, driven by the rising dislocation density. This is in line with the Taylor hardening law [157], which links dislocation density to YS and UCS.

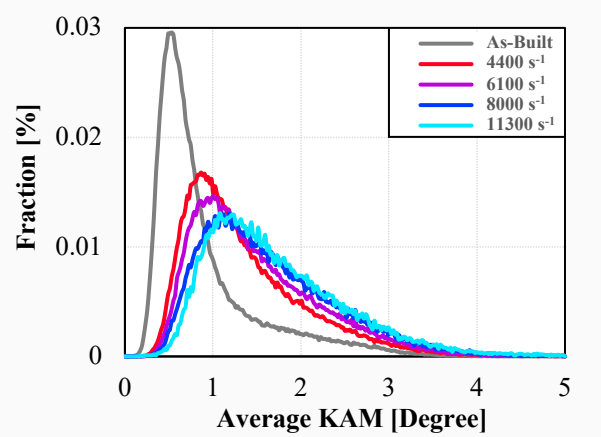


Figure 4-15 Comparison of KAM distributions between deformed LPBF-made Cu–Cr–Zr samples at various strain rates and the as-built sample.

To further explore on the analysis of GNDs, the distribution of dislocation density is examined in Figure 4-16, which was generated using MTEX. The dislocation density, correlating with the accumulation of dislocations within the material, provides crucial information regarding strain hardening, plastic deformation, and overall mechanical performance under dynamic loading conditions. In the undeformed as-built sample (Figure 4-16a), the microstructure predominantly features regions with lower dislocation density, represented by cooler blue shades (~10^{12} m^{-2}). In addition, some red streaks, indicating higher dislocation densities (~10^{15} m^{-2}) are visible within the grains. This reflects the inherent dislocations generated by the rapid cooling and solidification during the LPBF process.

On the other hand, in the deformed samples (Figure 4-16b and c), significant differences in the distribution of dislocation density emerge, especially at elevated strain rates. The color gradient from warmer reds near the grain boundaries (highlighted by black lines representing HAGBs) transitioning to cooler blues in the grain interiors suggests a higher concentration of dislocations at the boundaries. This indicates intense dislocation interactions near the boundaries, a common feature during severe plastic deformation. The gradient of dislocation density from boundary to grain center reflects a transition in strain accommodation. Such high dislocation density contributes to strain hardening, increasing the material's resistance to further deformation.

However, the dislocation accumulation can also potentially weaken the material's integrity under extreme conditions, as the high density of dislocations near the boundaries may act as sites for crack initiation (Figure 4-12f). This balance between dislocation-driven hardening and the onset of failure mechanisms is key to understanding the alloy's mechanical performance.

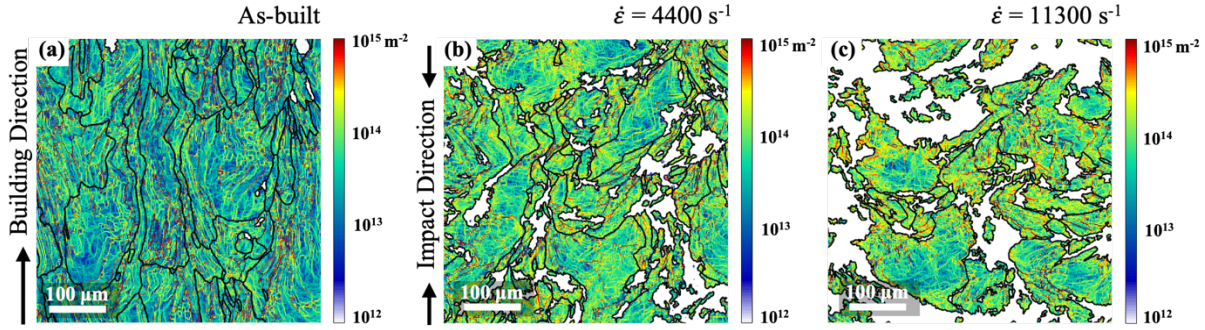


Figure 4-16 Distribution of dislocation density across the microstructure of (a) undeformed as-built LPBF-made Cu–Cr–Zr sample and deformed samples at strain rates of (b) 4400 s^{-1} and (c) 11300 s^{-1}, with values ranging from 10^{12} m^{-2} to 10^{15} m^{-2} (red regions). The red zones indicate areas of extreme dislocation accumulation, while the blue zones represent areas with lower dislocation density, corresponding to areas with less strain accumulation. White areas denote regions that were not indexed during the EBSD scan.

4.4.7. Macrotextural analysis after dynamic deformation

In the context of dynamic deformation, understanding how the crystallographic texture evolves on a macro-scale enhance the comprehension of the behavior of the materials under high strain rates. Figure 4-17 presents the macrotexture analysis of LPBF-made Cu–Cr–Zr samples conducted using XRD to examine the evolution of crystallographic texture under varying strain rates. The data was obtained from cross-sections perpendicular to BD and ID, where BD and ID are parallel. The results comprise pole figures and maximum intensity values of texture for the (111), (200), and

(220) planes, allowing for a comparative assessment between the as-built sample and those deformed at strain rates of 4400 s^{-1}, 6100 s^{-1}, 8000 s^{-1}, and 11300 s^{-1}. The crystallographic texture remains largely consistent under deformation, despite slight variations in the maximum intensity (MRD) of the planes.

In the as-built sample, the (220) plane shows a distinct “hot zone” with an MRD value of 6.1, reflecting a strong preferred orientation formed during LPBF. This preferred orientation is a result of the thermal gradients inherent in the process, which promote the development of columnar grains aligned with the BD. Specifically, the location of “hot zone” near the poles of the pole figures of (220) suggests that the (220) planes are predominantly oriented parallel to or at low angles relative to the BD. Under compression during high strain rate deformation, the grains experience flattening (Figure 4-14), particularly at higher strain rates. Although this compression might be expected to cause significant changes in texture, the data indicates that the overall texture remains largely unchanged (Figure 4-17).

The MRD values for the (111) and (200) planes show only minor fluctuations, with values remaining relatively low compared to the (220) plane. This indicates that while some grain rotation and minor reorientation occur, these changes are not sufficient to drastically alter the macrotexture of the material. Furthermore, the consistent orientation observed in the (220) plane, even after deformation, suggests that the grain flattening due to compression minimally impacts the preferred crystallographic orientations established during the LPBF process. The slight decrease in MRD values may indicate some degree of grain reorientation; however, this change is insufficient to cause a significant alteration in texture.

The observed macrotexture is consistent with the microtexture analysis, further reinforcing that the overall texture remains largely unaffected by severe plastic deformation at higher strain rates. This agreement between macro and microtexture implies that the dominant mechanisms affecting mechanical properties are more likely related to dislocation density and localized strain accommodation, rather than crystallographic texture reorientation. As a result, it is plausible that texture plays a minimal role in altering mechanical properties as strain rates increase. The retention of texture stability could be attributed to the inherent characteristics of the LPBF process, which induces a unique microstructure with fine grain sizes and high dislocation densities. These factors

may result in a material that is more resistant to texture transformation during deformation, even under extreme strain rates.

The dominant deformation mechanism in this study is likely dislocation-mediated plasticity including dislocation motion and interaction. This is supported by the flow stress curves (Figure 4-7), where strain hardening consistently surpasses softening effects, indicating that hardening plays a more significant role under the tested conditions. While softening mechanisms are present, as shown by the reduction in the work hardening rate (Figure 4-9) and the formation of ASBs in the microstructure (Figure 4-10–Figure 4-12), strain hardening remains the primary factor. It should be noted that other softening mechanism like localized dynamic recrystallization may also occur due to intense plastic deformation and heat generation, especially near ASB regions [149,158]. However, no clear evidence of recrystallization was observed in the EBSD results, possibly since the grains are too small to detect with this technique.

In addition, phase transformation and dynamic precipitation are other aspects that merit further exploration. XRD analysis (Figure 4-5) identified the presence of Cr and Zr particles within the microstructure, but their small size likely exceeds the resolution limits of SEM. Advanced techniques, such as TEM or SAXS, are crucial for accurately assessing changes in the size, distribution, and fraction of these particles, as well as any potential precipitation. Future work will focus on incorporating TEM analysis to validate and characterize recrystallization phenomena, particularly around ASBs, and to investigate potential phase transformations.

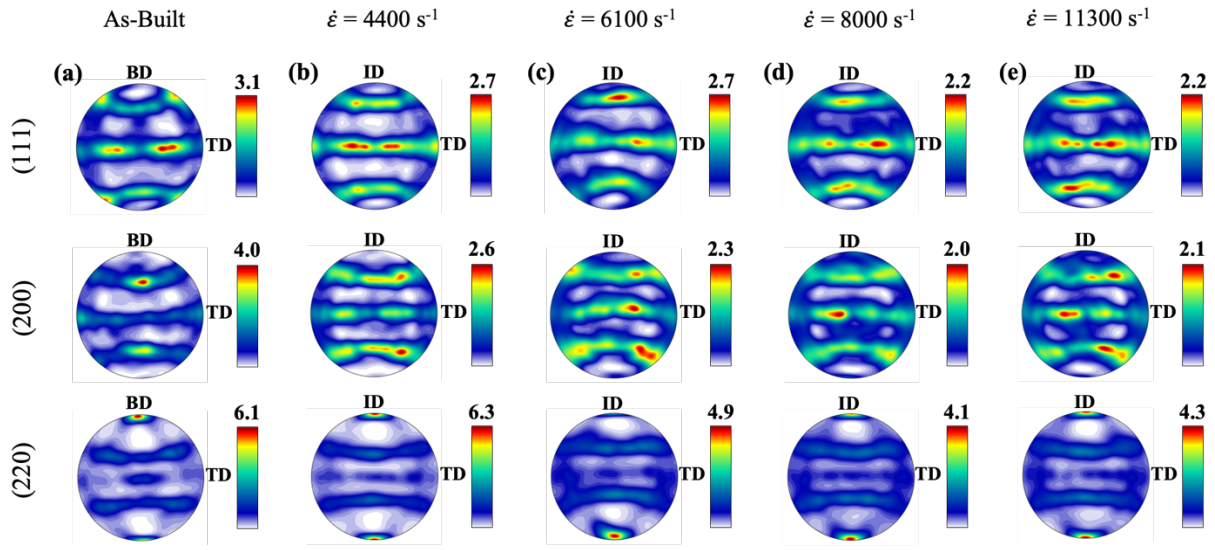


Figure 4-17 Macrotexture analysis of LPBF-made Cu–Cr–Zr samples, including (a) undeformed (as-built) and deformed at strain rates of (b) 4400 s^{-1}, (c) 6100 s^{-1}, (d) 8000 s^{-1}, and (e) 11300 s^{-1}, highlighting how increasing strain rates impact the material's overall texture.

4.5. Summary

This study focused on high-power laser powder bed fusion of Cu–Cr–Zr alloy, encompassing microstructural analysis and experimental investigations of high strain rate mechanical behavior at room temperature. Based on the results obtained, the following conclusions can be drawn:

- The microstructural examination of the as-built Cu–Cr–Zr alloy processed via LPBF demonstrates the formation of a columnar grain structure, predominantly aligned along the BD with dislocation density of ~29.5 × 10^{13} m^{-2}.
- In the dynamic high strain rate testing of LPBF-made Cu–Cr–Zr alloy, the alloy exhibits strain hardening, likely due to the intensified interaction and multiplication of dislocations. This is accompanied by thermal softening caused by adiabatic heating, which enhances strain accommodation.
- The high SRS of ~1 indicates that the alloy's flow stress is highly responsive to changes in strain rate, leading to significant increases in strength as the strain rate increases. At strain rate of 11300 s^{-1}, the UCS reached 489 ± 14 MPa, compared to 173 ± 8 MPa at strain rate of 4400 s^{-1}. In addition, the total strain increased by ~35% at strain rate of 11300 s^{-1} relative to the total strain observed at the lower strain rate of 4400 s^{-1}.

- The work hardening behavior of the alloy under high strain rate deformation involves a balance of hardening and softening mechanisms. Overall, the work hardening rate decreases, with this reduction becoming more gradual at higher strain rates, reflecting the accelerated deformation and reduced time for dislocation movement.
- Microstructural analysis of deformed Cu–Cr–Zr alloy reveals the formation of ASBs as zones of intense plastic deformation, with their density and complexity intensifying at higher strain rates, especially at 8000 s^{-1} and 11300 s^{-1}.
- The macrotexture and microtexture analyses both indicate that the crystallographic texture remains relatively stable under dynamic deformation, despite significant plastic deformation. The stability of the texture suggests that changes in mechanical properties are primarily driven by factors such as dislocation movement and strain accommodation.

Future work will extend this research by performing elevated-temperature dynamic impact tests to develop and validate the Johnson-Cook (JC) constitutive model, which will allow for a more detailed understanding of the material's deformation mechanisms across different conditions. Numerical simulations will also be conducted and validated against experimental results to further explore the material's response under high strain rates.

Chapter 5. In-Situ alloying of Cu–Ag using high-power laser powder bed fusion: From melt pool analysis to bulk microstructure

5.1. Overview

This study systematically investigated the in-situ alloying of Cu–Ag via laser powder bed fusion (LPBF), with a focus on understanding melt pool dynamics, microstructural evolution, and elemental distribution to establish optimal processing conditions. Single-track analysis identified that moderate scanning speeds (500 mm/s–700 mm/s) combined with high laser powers (700 W–900 W) produced stable and continuous tracks, whereas higher scanning speeds introduced discontinuities and balling defects due to insufficient energy input and unstable melt pools. Melt pool geometry analysis showed that both melt pool depth and width decreased with increasing speed, highlighting the importance of sufficient energy input for achieving proper fusion. Analytical modeling using Rosenthal's equation, together with the calculation of the Marangoni number (Ma), provided deeper insight into thermal gradients and surface tension-driven convection, emphasizing their critical role in ensuring homogeneous alloying. Bulk samples produced with refined processing parameters exhibited high relative densities, reaching ~99.19% at 600 mm/s and 800 W, and further improving to ~99.49% at 600 mm/s and 900 W. Microstructural analysis using scanning electron microscopy (SEM) and energy dispersive spectroscopy (EDS) demonstrated that Ag distribution was more uniform at 600 mm/s and 800 W, confirming that this combination provided the best balance between density, mixing efficiency, and compositional homogeneity. Finally, X-ray diffraction (XRD) analysis confirmed successful in-situ alloying, with a peak shift toward lower angles indicating that Ag atoms were incorporated into the Cu lattice, expanding the lattice parameter in accordance with Vegard's law. These results show that, under carefully optimized conditions, LPBF can effectively achieve in-situ alloying of Cu–Ag, providing a promising pathway for fabricating customized Cu-based alloys with tailored properties.

5.2. Introduction

Copper-silver (Cu–Ag) alloys have gained significant attention for applications requiring high electrical and thermal conductivity, such as electronic components, heat exchangers, and high-performance connectors [58,60,159]. Cu provides excellent conductivity, while Ag enhances

mechanical strength, oxidation resistance, and wear resistance. However, conventional manufacturing methods for Cu–Ag alloys, such as casting and powder metallurgy, often result in limited solubility of Ag in Cu, segregation, and non-uniform microstructures due to slow solidification rates [62]. These challenges limit the alloy's performance and manufacturability, necessitating alternative fabrication approaches to achieve a homogeneous microstructure and tailored properties.

Laser powder bed fusion (LPBF), an additive manufacturing (AM) technique, offers a promising route for fabricating Cu–Ag alloys through in-situ alloying. Unlike traditional methods, LPBF enables localized melting and rapid solidification, which can significantly enhance solute distribution and microstructural refinement. The high cooling rates in LPBF promote a more homogeneous solid solution by suppressing solute segregation and secondary phase formation. Additionally, LPBF provides flexibility in tuning processing parameters, such as laser power and scanning speed, to control melt pool dynamics, element mixing, and final material properties [1]. Despite these advantages, achieving effective in-situ alloying in Cu–Ag systems remains challenging due to the large difference in melting points (Cu: 1085°C, Ag: 961°C), thermal conductivities, and surface tensions, which influence melt pool stability, convection-driven mixing, and solidification behavior.

A key factor influencing in-situ alloying during LPBF is the Marangoni effect, where surface tension gradients drive convection within the melt pool, promoting elemental mixing and homogeneity. The strength of Marangoni-driven flow depends on the Marangoni number (Ma), scanning speed, and energy input, which dictate the melt pool's shape, depth, and flow intensity [81,85]. Understanding and optimizing these parameters is crucial for minimizing segregation, porosity, and cracking, thereby ensuring a high-quality alloyed structure. In addition, melt pool geometry (depth and width) and stability directly impact alloying efficiency, making it essential to analyze single tracks before bulk sample fabrication.

In this study, the influence of laser power and scanning speed on melt pool characteristics, microstructural evolution, and elemental distribution is systematically investigated to establish optimized process conditions for in-situ alloying of Cu–2Ag. Single-track experiments are conducted to analyze track stability, melt pool morphology, and the role of Marangoni-driven convection in promoting element mixing. Based on these findings, bulk samples are fabricated

using the most promising parameter combinations, and their densification behavior is evaluated by measuring relative density and porosity content. The microstructural characteristics of the bulk samples are examined through scanning electron microscopy (SEM) and energy-dispersive spectroscopy (EDS) to assess Ag distribution and verify the uniformity of the alloying process. Further validation of in-situ alloying is performed using X-ray diffraction (XRD), where peak shifts in the diffraction pattern provide evidence of Ag incorporation into the Cu matrix through lattice expansion.

By establishing the relationships between processing parameters, melt pool behavior, and alloy homogeneity, this study provides a comprehensive understanding of in-situ alloying of Cu–Ag via LPBF. The findings will serve as the basis for the next phase of research, where the high-temperature oxidation behavior of the fabricated samples will be evaluated to determine their thermal stability and oxidation resistance in practical applications.

5.3. Materials and methods

5.3.1. Material

Gas-atomized pure Cu (CP Cu) and pure Ag (99.9% Ag) powders were used as the initial materials to produce a Cu–2wt.% Ag alloy. The Cu powder was supplied by AP&C, and the Ag powder was obtained from Thermo Fisher. To achieve the target composition, the elemental powders were precisely weighed and thoroughly mixed in a tumbler mixer for 20 hours before LPBF processing.

Figure 5-1 presents scanning electron microscope (SEM) images of the individual elemental powders along with an energy-dispersive X-ray spectroscopy (EDS) image of the blended mixture. Both powders exhibit a nearly spherical morphology, which enhances powder flowability and ensures consistent layer deposition during LPBF. Furthermore, EDS analysis of the mixed powders confirms a homogeneous distribution of Cu and Ag particles, which is critical for achieving uniform in-situ alloying during the melting process. The particle size distribution (PSD) of both powders follows a monomodal distribution. The Ag powder has finer particle size with a narrower PSD compared to the Cu powder. The measured D_{10}, D_{50}, and D_{90} values for Cu–2Ag blend are 15.9 μm, 31.7 μm, and 56.7 μm, respectively.

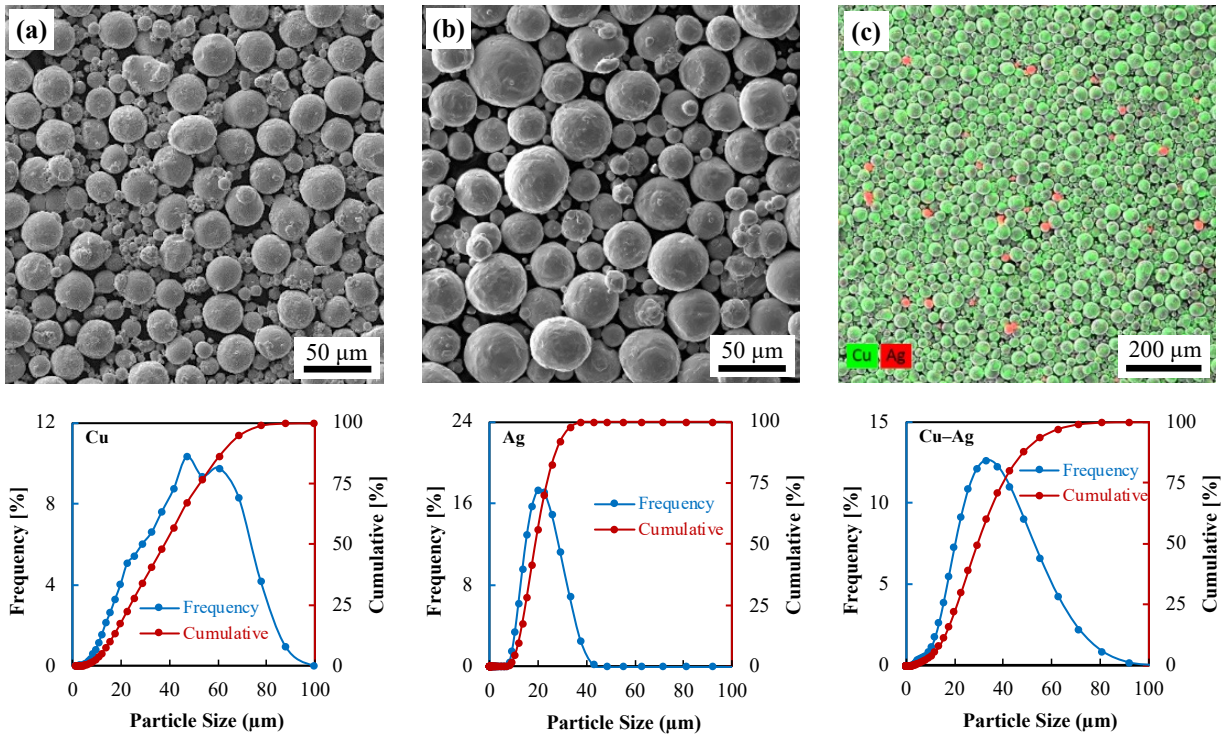


Figure 5-1 SEM images of the virgin elemental powders of (a) Cu, (b) Ag, and (c) Cu–2Ag and corresponding particle size distributions.

5.3.2. LPBF process

The LPBF process was carried out using a customized EOS M290 machine (AMCM, Germany), equipped with a high-power 1 kW Ytterbium continuous fiber laser operating at a wavelength of 1060 nm and a spot diameter of ~80 µm. To prevent oxidation and ensure process stability, the build chamber was filled with high-purity Ar, maintaining an oxygen content below 0.1% throughout the fabrication. Since LPBF of Cu–2Ag has not been previously investigated, determining suitable processing parameters was a critical first step. Achieving a fully fused and homogeneously alloyed microstructure requires a well-controlled melt pool and efficient mixing of Cu and Ag during laser processing. A schematic representation of the LPBF process and melt pool geometry is provided in Figure 5-2.

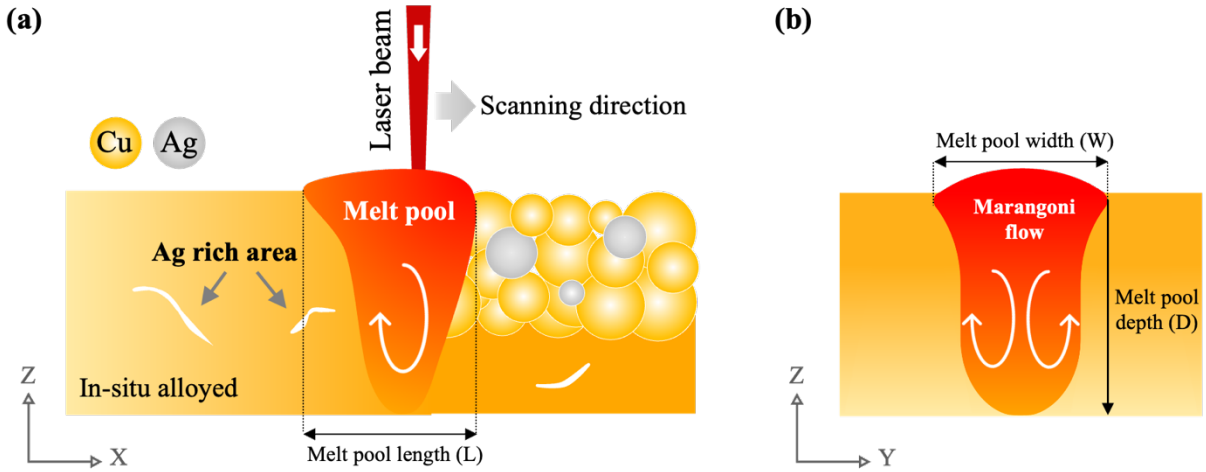


Figure 5-2 Schematic representation of the in-situ alloying process in LPBF of Cu–Ag. (a) illustration of laser interaction with the powder bed and (b) cross-sectional view of the melt pool, highlighting the Marangoni-driven convection within the melt pool, which influences melt pool depth and promotes element mixing.

To systematically develop a robust process for this new material system, a two-step approach was adopted. First, single-track experiments were performed to establish a processing window with stable melt pools and effective in-situ alloying. Once the optimal conditions were identified, bulk samples were fabricated to evaluate relative density, microstructure evolution, and the scalability of in-situ alloying at a larger scale.

5.3.2.1. Single tracks

Single-track studies are fundamental in LPBF process development, as they provide key insights into melt pool behavior, Marangoni convection, element dissolution, and process stability, all of which directly influence relative density, alloy homogeneity, and final microstructure. These preliminary experiments help determine the optimal energy input required for a well-fused and compositionally uniform material, guiding subsequent multi-layer and bulk sample fabrication.

To investigate these effects, single tracks were printed on LPBF-made Cu–2Ag substrates using laser powers ranging from 600 W to 900 W, scanning speeds between 500 mm/s and 1000 mm/s, and a fixed layer thickness of 40 µm. Table 5-1 provides detailed information on the selected process parameters and their corresponding energy densities. To ensure reproducibility and statistical reliability, each processing condition was replicated three times.

Table 5-1 Process parameters of single tracks for Cu–Ag alloy

Power [W]	Speed [mm/s]	Energy Density [J/mm^2]	Power [W]	Speed [mm/s]	Energy Density [J/mm^2]
600	500	30.0	800	500	40.0
	600	25.0		600	33.3
	700	21.4		700	28.6
	800	18.8		800	25.0
	900	16.7		900	22.2
	1000	15.0		1000	20.0
700	500	35.0	900	500	45.0
	600	29.2		600	37.5
	700	25.0		700	32.1
	800	21.9		800	28.1
	900	19.4		900	25.0
	1000	17.5		1000	22.5

Energy density = Power/ (scanning speed × layer thickness)

5.3.2.2. Bulk samples

After defining a process window using single-track experiments, bulk cube samples with dimensions of 10mm × 10mm × 10mm were fabricated to validate in-situ alloying and evaluate relative density and microstructure evolution. The bulk samples allowed for a comprehensive assessment of phase formation and elemental homogeneity, ensuring that the optimized single-track parameters successfully translate to larger-scale fabrication.

5.3.3. Microstructural characterization

For microstructural characterization, samples underwent polishing and etching to reveal their melt pool boundaries (MPBs). The polishing procedure involved sequential grinding with SiC abrasive papers (100 to 2400 grit), followed by 1-μm MD-Nap abrasive polishing. A final vibratory polishing step was performed using a Buehler VibroMet2 machine for 5 hours with a 0.02 μm colloidal silica suspension, ensuring a high-quality surface finish suitable for microstructural analysis.

To enhance the visibility of MPBs, the polished samples were chemically etched using an iron (III) chloride solution composed of 2% $FeCl_3$, 13% HCl, and 85% deionized water. Melt pool dimensions, including width and depth, were subsequently measured using an optical microscope (Keyence VHX-7000). Since single-track stability and continuity are critical for process optimization, the track morphology was analyzed using a Keyence VK-X250 confocal microscope equipped with non-contact laser profilometry.

For a more detailed assessment, SEM and EDS were performed on cross-sections parallel to the building direction (BD) of cubes using a TESCAN VEGA electron microscope. These analyses facilitated the evaluation of porosity distribution, phase segregation, and the uniformity of in-situ alloying in the LPBF-made Cu–Ag samples.

Once the relative density and microstructural homogeneity were deemed satisfactory, X-ray diffraction (XRD) analysis was conducted to confirm the occurrence of in-situ alloying. The analysis was performed using the Co-K_α radiation method, enabling the identification of phase composition. This step ensured the successful incorporation of Ag into the Cu matrix, validating the alloying mechanism.

To further examine the internal structure and defect distribution, high-resolution X-ray computed tomography (CT) was performed using a ZEISS Xradia 520 Versa system, achieving a voxel size of 15 μm. The CT scans provided detailed three-dimensional imaging of the internal features, facilitating a comprehensive assessment of porosity, internal defects, and potential cracking. The acquired CT data was processed and analyzed using Dragonfly software, allowing for quantitative relative density calculations and defect visualization through non-destructive characterization.

5.4. Results and discussion

5.4.1. Cu–Ag single track analysis

A critical aspect of single-track analysis is the evaluation of melt pool geometry, as it provides direct insight into process stability and fusion quality. The melt pool dimensions (Figure 5-2), including length (L), width (W), and depth (D) are fundamental parameters that dictate heat distribution, solidification behavior, and element mixing during LPBF.

Figure 5-3 presents the top view of single tracks produced with varying laser power (600 W – 900 W) and scanning speed (500 mm/s – 1000 mm/s), illustrating the effect of process parameters on track stability, continuity, and defect formation. At lower scanning speeds, particularly in the range of 500 mm/s to 700 mm/s, the tracks appear continuous and well-defined, especially at power levels of 700 W and 800 W. The smooth and uniform track morphology observed in these conditions suggests sufficient laser-material interaction time, allowing for stable melt pool formation and good wettability. These conditions promote proper molten material flow, minimizing discontinuities and irregularities.

As scanning speed increases beyond 800 mm/s, track stability deteriorates, leading to the formation of discontinuous segments and irregular track morphologies. The balling effect becomes more pronounced at 1000 mm/s, particularly at lower power levels, where insufficient energy input results in unstable melt pools. This instability prevents proper wetting of the substrate, causing the molten material to contract due to surface tension and form discrete droplets instead of a continuous track [1,81].

At higher power levels, such as 900 W, excessive spreading is evident at low speeds, which can be attributed to overheating and increased melt pool fluidity. Conversely, at high speeds and high power (900 W, 1000 mm/s), the severe track discontinuity suggests that the rapid solidification rate limits melt pool flow before proper fusion can occur.

These observations highlight the delicate balance between laser power and scanning speed in achieving stable track formation. While low-speed, high-power conditions facilitate well-defined tracks, they may also lead to excessive spreading. In contrast, high-speed conditions promote balling due to unstable melt pools and limited fusion. Among the different process conditions, tracks produced at 700 W – 800 W with speeds between 500 mm/s and 700 mm/s exhibit the most stable morphology, making these conditions promising candidates for bulk sample fabrication.

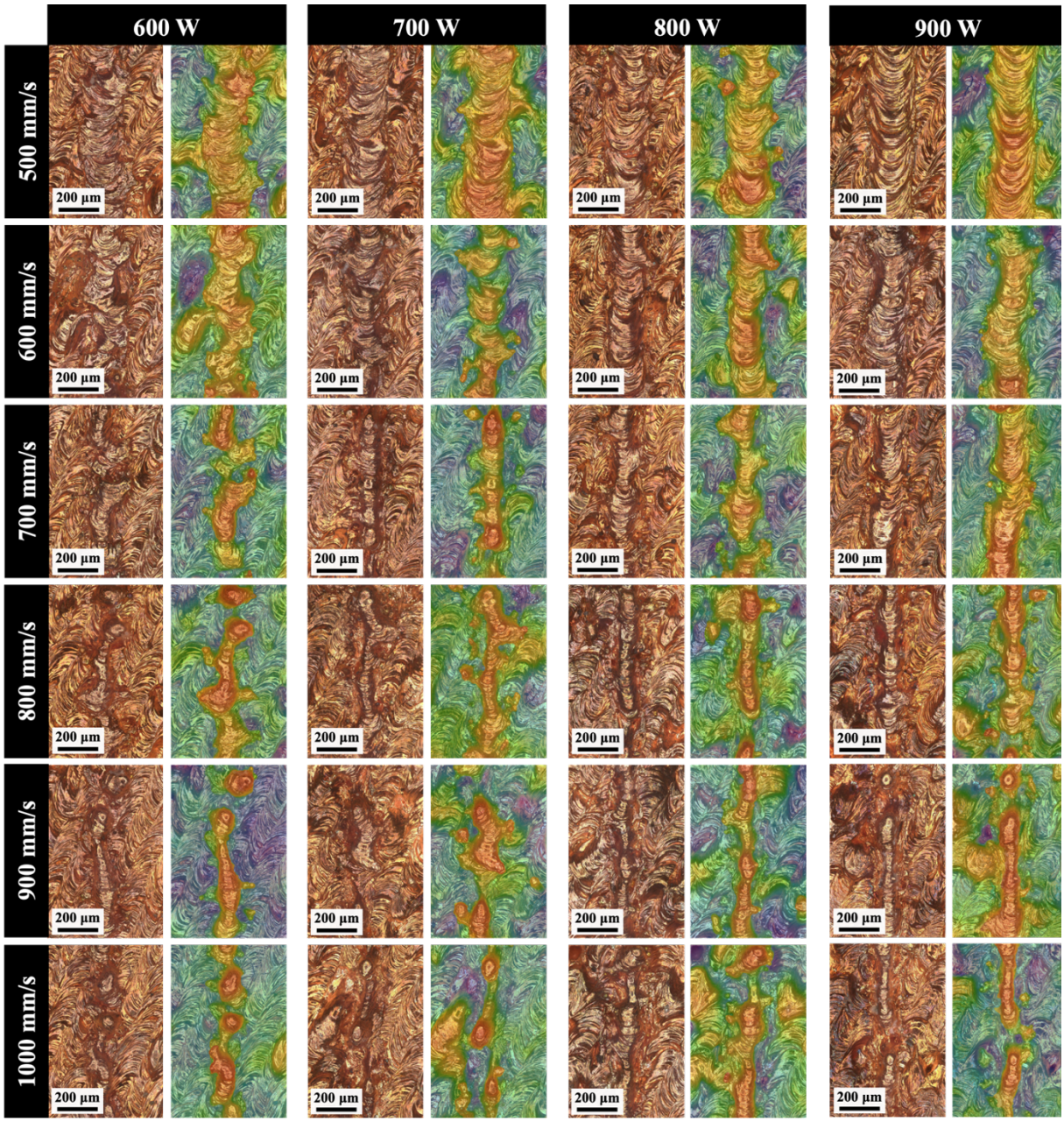


Figure 5-3 Top view of LPBF-processed single tracks of in-situ alloyed Cu–Ag under varying laser power and scanning speed. Lower speeds produce continuous and stable tracks, while higher speeds lead to instability, discontinuities, and balling defects. Excessive spreading occurs at high power and low speed, whereas high-speed conditions exacerbate track irregularities.

To gain deeper insight into the effects of laser power and scanning speed on melt pool formation, cross-sectional analyses of single tracks were conducted. By examining the melt pool depth and width at different energy inputs, it is possible to assess track stability, penetration depth, and the effectiveness of laser-material interaction.

Figure 5-4 shows optical micrographs of melt pools formed at 600 W and 900 W laser power levels, processed at varying scanning speeds, captured under both full (Figure 5-4a and c) and partial (Figure 5-4b and d) coaxial lighting. These images provide a visual representation of how energy input influences melt pool geometry, solidification characteristics, and overall process stability, laying the foundation for further quantitative analysis.

At 600 W, the melt pools exhibit shallower penetration and narrower widths, particularly at higher scanning speeds. This reduction in melt pool dimensions is expected due to the decreased laser-material interaction time, resulting in lower energy absorption and reduced melting. At higher speeds (1000 mm/s), track instability and irregular fusion zones become apparent, indicating the onset of insufficient fusion and the potential for lack-of-fusion defects.

At 900 W, the increased laser power leads to deeper and wider melt pools, promoting greater material melting and penetration into the substrate. The larger melt pools facilitate enhanced element mixing, improving alloy homogeneity in the Cu–Ag system. However, at high speeds, excessive heat input can induce instabilities, excessive vaporization, or keyhole formation, affecting track consistency.

The next step involves quantitative analysis of melt pool depth and width, as shown in Figure 5-5, which provides a more comprehensive understanding of how processing parameters affect melt pool formation.

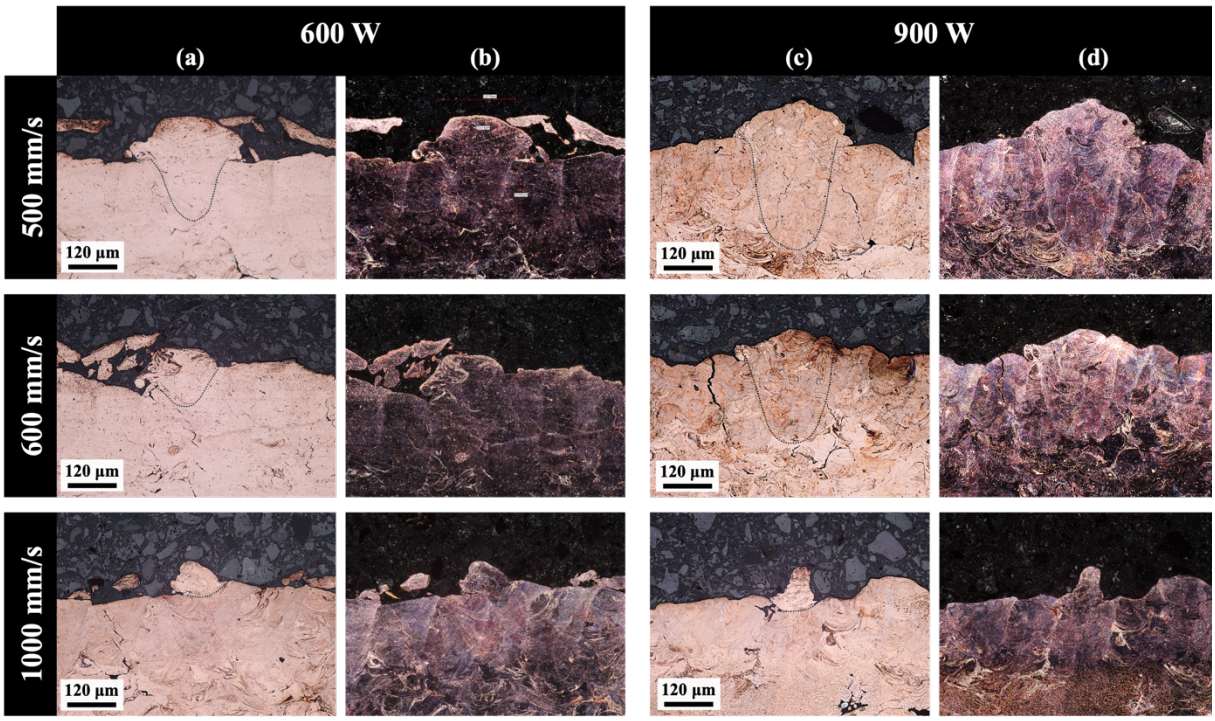


Figure 5-4 Optical micrographs of single-track cross-sections for laser powers of 600 W and 900 W, processed at different scanning speeds (500 mm/s, 600 mm/s, and 1000 mm/s). (a) and (c) captured under full coaxial lighting, outlining melt pool boundaries to highlight variations in melt pool depth and width. (b) and (d) captured under partial coaxial lighting, enhancing the visibility of melt pool boundaries

Figure 5-5 shows the measured melt pool depth (Figure 5-5a) and melt pool width (Figure 5-5b) as a function of scanning speed for different laser powers. At lower scanning speeds (500 mm/s – 700 mm/s), both melt pool width and depth decrease as speed increases. At a given scanning speed, higher laser power leads to deeper and wider melt pools due to increased heat input, promoting greater material melting and penetration into the substrate.

However, at scanning speeds above 700 mm/s, melt pool measurements were not consistently possible due to track instability and balling effects, as observed in Figure 5-3. At these high speeds, insufficient energy input led to irregular track formation, preventing reliable measurement of melt pool dimensions. The rapid solidification and weak wetting of the melt pool in these unstable conditions further contributed to measurement challenges.

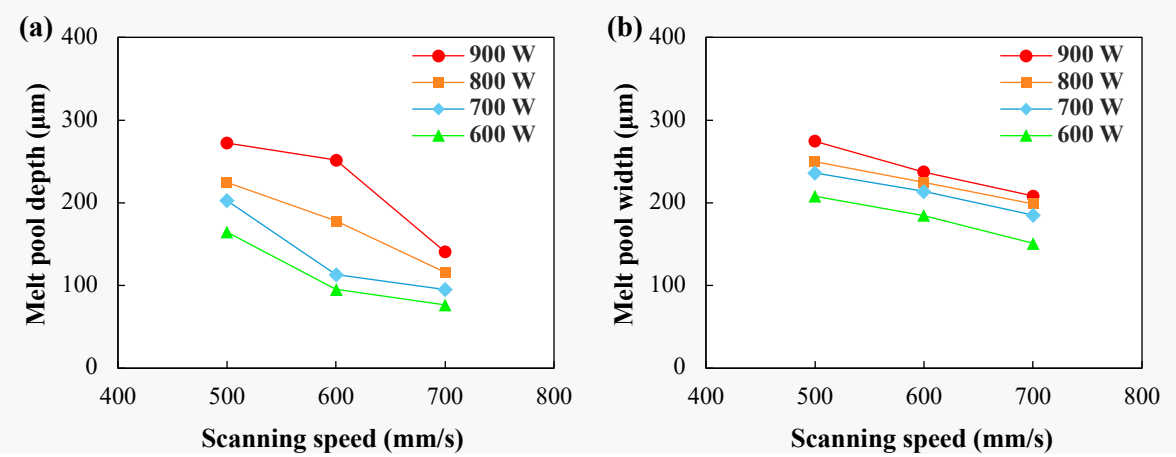


Figure 5-5 Measured melt pool geometry of LPBF-made Cu–Ag single tracks at different laser powers and scanning speeds. (a) Melt pool depth decreases with increasing scanning speed due to reduced laser-material interaction time. (b) Melt pool width follows a similar trend, with higher power levels producing wider melt pools.

These results emphasize the importance of balancing laser power and scanning speed to ensure stable melt pool formation. Lower scanning speeds provide greater energy input per unit length, allowing for deeper penetration and improved fusion. However, excessively high speeds reduce laser-material interaction time, leading to poor track continuity and inconsistent melt pool formation, which can negatively impact in-situ alloying efficiency.

The measured melt pool dimensions will be used in the following section to calculate the Marangoni number, which quantifies surface tension-driven convection within the melt pool. This calculation is crucial for understanding how fluid flow influences element transport, mixing efficiency, and overall alloy homogeneity during the LPBF process.

5.4.2. Marangoni number analysis and its implications for LPBF of Cu–Ag

The use of non-dimensional numbers, such as the Marangoni number (Ma), is valuable for characterizing the structure, defects, and properties of components produced by the LPBF process [160,161]. Ma quantifies the Marangoni stress, which governs fluid flow within the melt pool by describing the competition between surface tension-driven flow and viscosity-driven flow.

In LPBF, surface tension gradients are induced by temperature differences within the melt pool, causing thermo-capillary flow. A high Ma signifies that surface tension-driven convection dominates, leading to enhanced element mixing and heat distribution. However, if Ma becomes excessively high, it can introduce melt pool instability, increasing the risk of keyhole formation,

spatter, and irregular solidification. Conversely, a low Ma indicates that viscous forces play a more significant role, potentially leading to weaker fluid motion and less uniform element distribution [160,161].

By analyzing Ma, the balance between heat input, convection, and alloying efficiency can be better understood, allowing for optimized LPBF processing conditions. Ma is defined by Equation (5-1):

$$Ma = -\frac{d\gamma}{dT}\frac{L\Delta T}{\mu\alpha} \tag{5-1}$$

where μ is the dynamic viscosity, α is the thermal diffusivity of the alloy, L is the characteristic length of the melt pool (such as melt pool width), ΔT is the difference between the maximum temperature inside the pool and the solidus temperature of an alloy, and $d\gamma/dT$ is the sensitivity of surface tension gradient with respect to temperature .

To estimate ΔT, which directly influences melt pool dynamics and Marangoni-driven convection, it is necessary to determine the peak temperature (T_{max}) within the melt pool. This was achieved using Rosenthal's equation (Equation (5-2)), which describes the temperature distribution in a material subjected to a moving heat source. Originally developed for high-conductivity metals, Rosenthal's model provides a simplified analytical approach for approximating peak temperatures [1].

However, it is important to acknowledge the limitations of this equation. While it effectively models heat distribution, it does not account for factors such as latent heat effects, convective losses, or phase transformations. As a result, absolute temperature values derived from this equation may not be entirely accurate. Nonetheless, because systematic deviations occur consistently, Rosenthal's solution remains a valuable tool for comparative studies, allowing for the evaluation of relative trends in melt pool temperature variation. The equation is expressed as:

$$T - T_0 = \frac{\beta P}{2\pi k R}\exp\left(-\frac{v\,(x+R)}{2\alpha}\right) \tag{5-2}$$

Here, β, P, v, k, and α are the laser absorptivity coefficient, laser power, scanning speed, thermal conductivity ($k = \alpha\rho C_p$), and thermal diffusivity of the material, respectively. Since T_{max} occurs at the center of the laser beam, x was set to 0 to calculate T_{max} at the point of highest heat input. Additionally, to approximate the heat source size, R was replaced with the laser spot radius (R_{beam} ~ 40 μm), resulting in the following simplified equation:

$$T_{max} = T_0 + \frac{\beta P}{2\pi k R_{beam}} \exp\left(-\frac{v\, R_{beam}}{2\alpha}\right) \quad (5\text{-}3)$$

The peak temperature estimation enables the calculation of ΔT as:

$$\Delta T = T_{max} - T_s \quad (5\text{-}4)$$

T_s is the solidus temperature of Cu–Ag. The calculated ΔT values for all parameter sets are summarized in Table 5-2. It should be noted that determining β is crucial, as it directly affects energy absorption, melt pool formation, and process stability. Due to its high reflectivity and thermal conductivity, Cu presents challenges in achieving effective laser absorption, particularly at conventional infrared wavelengths (~1070 nm).

For solid Cu, absorptivity is extremely low, typically ranging between 2% and 5%, which necessitates higher laser power to achieve sufficient melting. However, copper powder exhibits slightly higher absorptivity due to multiple reflections and increased surface area interaction. Studies have reported that pure Cu powder has an absorptivity of ~ 15% at a wavelength of 1070 nm [162].

Given these findings, this study assumes an absorptivity value of 20% (β = 0.20) for the calculations, ensuring a realistic estimation of energy absorption and thermal response in LPBF-made Cu–Ag alloys. For parameter sets where the calculated T_{max} exceeds the boiling temperature (T_b) of Cu, the maximum temperature was capped at T_b to account for energy losses due to evaporation, vaporization effects, and process limitations in LPBF.

Table 5-2 Process parameters of single tracks for Cu–Ag alloy

Power [W]	**Speed [mm/s]**	**ΔT [K]**	**Power [W]**	**Speed [mm/s]**	**ΔT [K]**
600	500	667	800	500	1242
	600	586		600	1134
	700	508		700	1030
	800	434		800	932
	900	364		900	838
	1000	297		1000	748
700	500	955	900	500	1479
	600	860		600	1408
	700	769		700	1291
	800	683		800	1180
	900	601		900	1075
	1000	523		1000	974

The melting temperature (T_m) and solidus temperature (T_s) were considered the same because the Cu–2Ag alloy is highly dilute. In dilute alloys, the presence of small amounts of alloying elements does not significantly lower the solidus temperature compared to the pure metal. Given that the solidus and liquidus temperatures of Cu–2Ag remain very close to the melting point of pure copper (~1356 K), treating ($T_m = T_s$) provides a reasonable approximation for thermal calculations in this study.

The calculated ΔT values were subsequently used in the determination of the Marangoni number, which characterizes surface tension-driven convection and its influence on element mixing and alloying efficiency. The thermophysical properties of pure Cu, which were used in both Rosenthal's equation and the Marangoni number calculations, are summarized in Table 5-3.

Table 5-3 Thermophysical properties of pure Cu [163,164]

Parameter (unit)	**Value**
Melting point, T_m (K)	1356
Density of solid @ 298 K, ρ_s (kg/m^3)	8930
Density of liquid, ρ_l (kg/m^3)	$7960 - 0.76\ (T - T_m)$
Thermal expansion coefficient @ 298 K, α (1/K)	1.67×10^{-5}
Thermal expansion coefficient @ 1300 K, α (1/K)	2.58×10^{-5}
Specific heat of solid, C_p^s [298 – T_m] (J/mol K)	$5.41 + 1.4 \times 10^{-3}\ T$
Specific heat of liquid, C_p^l (J/mol K)	7.50
Thermal conductivity of solid, k_s (W/m K)	330
Thermal conductivity of liquid, k_l (W/m K)	$163 + 2.67 \times 10^{-5}\ (T - T_m)$
Viscosity of liquid @ T_m, η (kg/m s)	4.10×10^{-3}
Surface tension @ T_m, γ (mN/m)	1285
Temperature coefficient of surface tension, –dγ/dT (mN/m K)	0.13

Using Equation (5-1) and the data presented in For parameter sets where the calculated T_{max} exceeds the boiling temperature (T_b) of Cu, the maximum temperature was capped at T_b to account for energy losses due to evaporation, vaporization effects, and process limitations in LPBF.

Table 5-2, Ma was calculated and plotted as a function of scanning speed for various laser power levels in Figure 5-6. In these calculations, the melt pool width was used as the characteristic length (L), while the thermophysical properties listed in Table 5-3 were incorporated to effectively characterize the material's thermal response.

As shown in Figure 5-6, Ma decreases with increasing scanning speed across all power levels. This trend is expected, as higher scanning speeds reduce laser-material interaction time, leading to lower temperature gradients and weaker surface tension-driven convection in the melt pool. At a given scanning speed, higher laser power results in a greater Ma, indicating stronger Marangoni-driven flow due to enhanced surface tension gradients. The highest Ma values are observed at 900 W, followed by 800 W, 700 W, and 600 W, reflecting the greater heat input and increased melt pool convection at higher power levels.

A higher Marangoni number signifies greater liquid metal flow within the melt pool, which in turn leads to a wider melt pool and more complete fusion between successive layers and hatches. Additionally, the higher temperature gradients in the melt pool during LPBF promote more intense convection, which accelerates homogenization and in-situ alloying within the molten region.

It is important to note that melt pool measurements could not be obtained at scanning speeds of 800 mm/s, 900 mm/s, and 1000 mm/s due to instabilities in track formation and balling effects, which prevented reliable characterization. These conditions likely resulted in disruptions in melt pool continuity, further limiting surface tension-driven flow and reducing Ma. If measurements at these speeds had been possible, the decreasing trend in Ma would likely have continued, indicating a further reduction in melt pool stability.

Therefore, with increasing scanning speed, the Marangoni number decreases, suggesting that at higher speeds, in-situ alloying becomes more challenging due to weaker convective mixing and shorter interaction times. The effectiveness of in-situ alloying in this alloy system is strongly influenced by the Marangoni-driven flow, and maintaining an adequate Ma value is essential to ensure sufficient element mixing and homogenization. Therefore, an appropriate Marangoni number range must be achieved to facilitate successful in-situ alloying in Cu–2Ag, ensuring proper composition distribution and avoiding microstructural inconsistencies.

While Ma provides insight into convection-driven mixing, its impact on Ag distribution must be experimentally validated. To assess elemental homogeneity, EDS analysis was conducted, as presented in the following section.

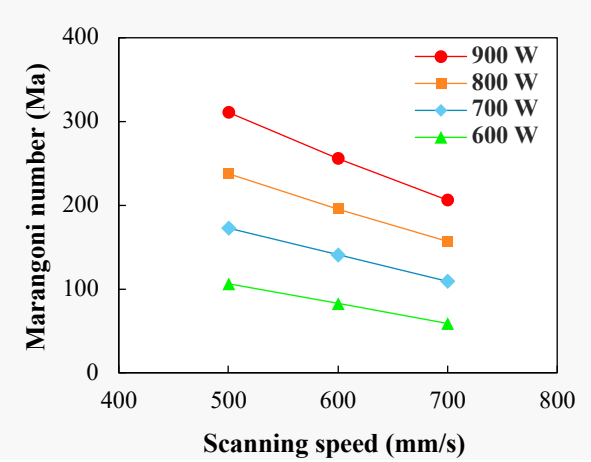


Figure 5-6 Variation of Ma with scanning speed for Cu–2Ag single tracks at different laser power levels. A decreasing trend in Ma is observed with increasing scanning speed, while higher power enhances Ma, indicating stronger thermo-capillary flow.

5.4.3. Experimental analysis of in-situ alloyed Cu–Ag bulks

Figure 5-7 presents the relative density (RD) of bulk Cu–Ag samples processed with refined parameters derived from the single-track analysis. The samples were printed at laser powers ranging from 600 W to 900 W and scanning speeds of 600 mm/s and 800 mm/s, with *RD* values indicated in each image.

At a scanning speed of 600 mm/s, the samples generally show high relative densities, ranging from 97.73% at 600 W to over 99.49% at 900 W. This high densification indicates that sufficient energy input at moderate speeds promotes stable melt pool formation and effective fusion between tracks and layers. However, cracks are observed in all samples at 600 mm/s, regardless of laser power. These cracks are likely associated with thermal stresses generated during rapid solidification, compounded by shrinkage of Cu–Ag alloys under LPBF conditions. Interestingly, the severity and frequency of cracks appear to decrease with increasing laser power.

Increasing laser power can lead to larger and more stable melt pools. These enhanced melt pools promote better fusion between layers and tracks, which can reduce the formation of defects such as cracks. The improved stability and size of the melt pool at higher laser powers facilitate more uniform solidification, thereby minimizing residual stresses that contribute to cracking. Studies

have shown that adjusting laser power and scanning speed can influence melt pool characteristics, affecting defect formation in LPBF-made alloys.

In contrast, at 800 mm/s, a significant reduction in relative density is observed, with values dropping to 92.96% at 600 W and gradually improving to 96.97% at 900 W. The presence of large irregular pores in these samples suggests that at higher scanning speeds, insufficient energy input leads to lack-of-fusion porosity, as the rapid movement of the laser beam prevents adequate bonding between adjacent melt pools. Even at the highest power level (900 W), while the density improves compared to lower power conditions, porosity is still more pronounced than in the 600 mm/s samples.

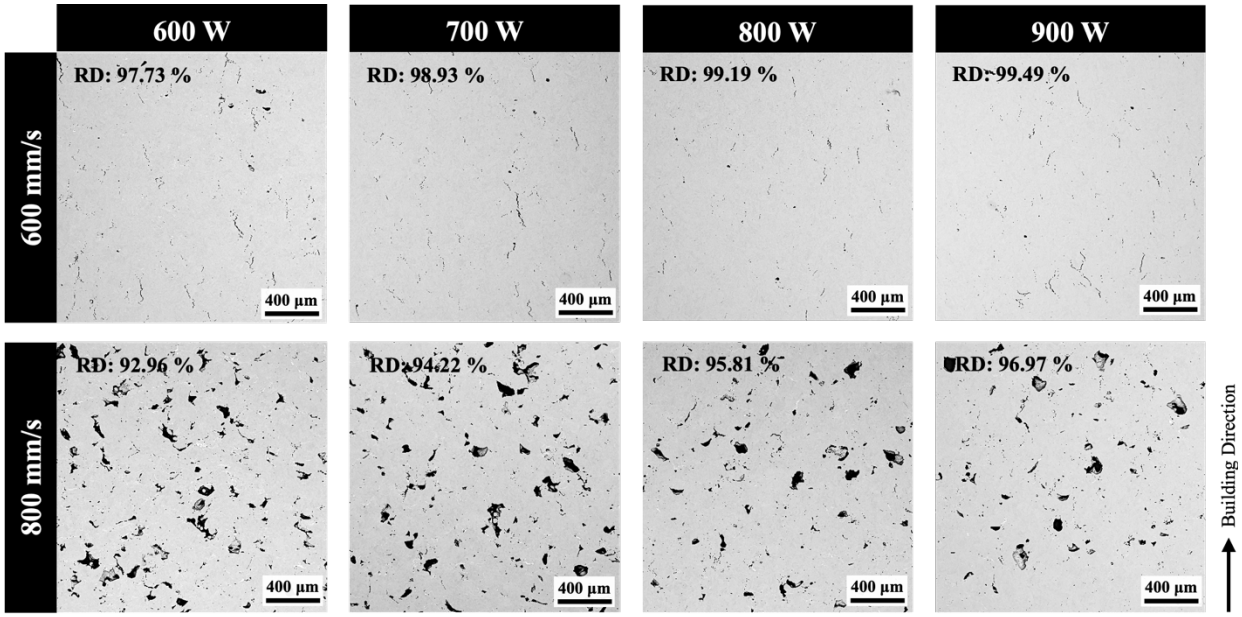


Figure 5-7 Relative density of LPBF-made Cu–Ag bulk samples at different laser powers and scanning speeds. At 600 mm/s, samples exhibit high relative densities, with the highest densification (RD ~99.49%) observed at 900 W. In contrast, at 800 mm/s, increased porosity leads to lower densities, indicating lack-of-fusion defects due to insufficient energy input. These results confirm that lower scanning speeds combined with higher power levels promote better fusion and densification.

Following the analysis of relative density and defect formation, the next step is to assess the elemental homogeneity of the LPBF-made Cu–Ag samples, which directly reflects the effectiveness of in-situ alloying. As discussed earlier, Marangoni convection, driven by surface tension gradients within the melt pool, plays a key role in enhancing mixing between Cu and Ag during laser processing. However, the strength of this flow, and thus the quality of in-situ alloying, is strongly influenced by process parameters, especially scanning speed and laser power.

To evaluate how effectively Ag is distributed within the Cu matrix under different conditions, EDS mapping was performed. This provides a direct visualization of Ag distribution, allowing the link between Marangoni flow, melt pool stability, and final chemical homogeneity to be clearly established. The results are presented in Figure 5-8 and Figure 5-9, comparing the elemental maps at scanning speeds of 800 mm/s and 600 mm/s, respectively, where differences in mixing behavior are evident.

Figure 5-8 corresponds to samples processed at 800 mm/s, where Ag distribution is highly non-uniform. Large Ag-rich regions are visible, indicating insufficient mixing during the LPBF process. The high scanning speed limits melt pool residence time, reducing convection-driven mixing and promoting Ag segregation. This results in localized regions of Ag accumulation, suggesting that the Marangoni-driven flow is not strong enough to ensure homogeneous elemental distribution. Additionally, the presence of large porosity in the 600 W sample further disrupts uniformity.

Figure 5-9, on the other hand, corresponds to 600 mm/s, where a more uniform Ag distribution is observed. The stars mark the analysis points where Ag is more evenly dispersed throughout the Cu matrix, confirming improved in-situ alloying. The lower scanning speed allows for better melt pool stability and longer interaction time, enhancing the convective mixing of Ag within the Cu matrix.

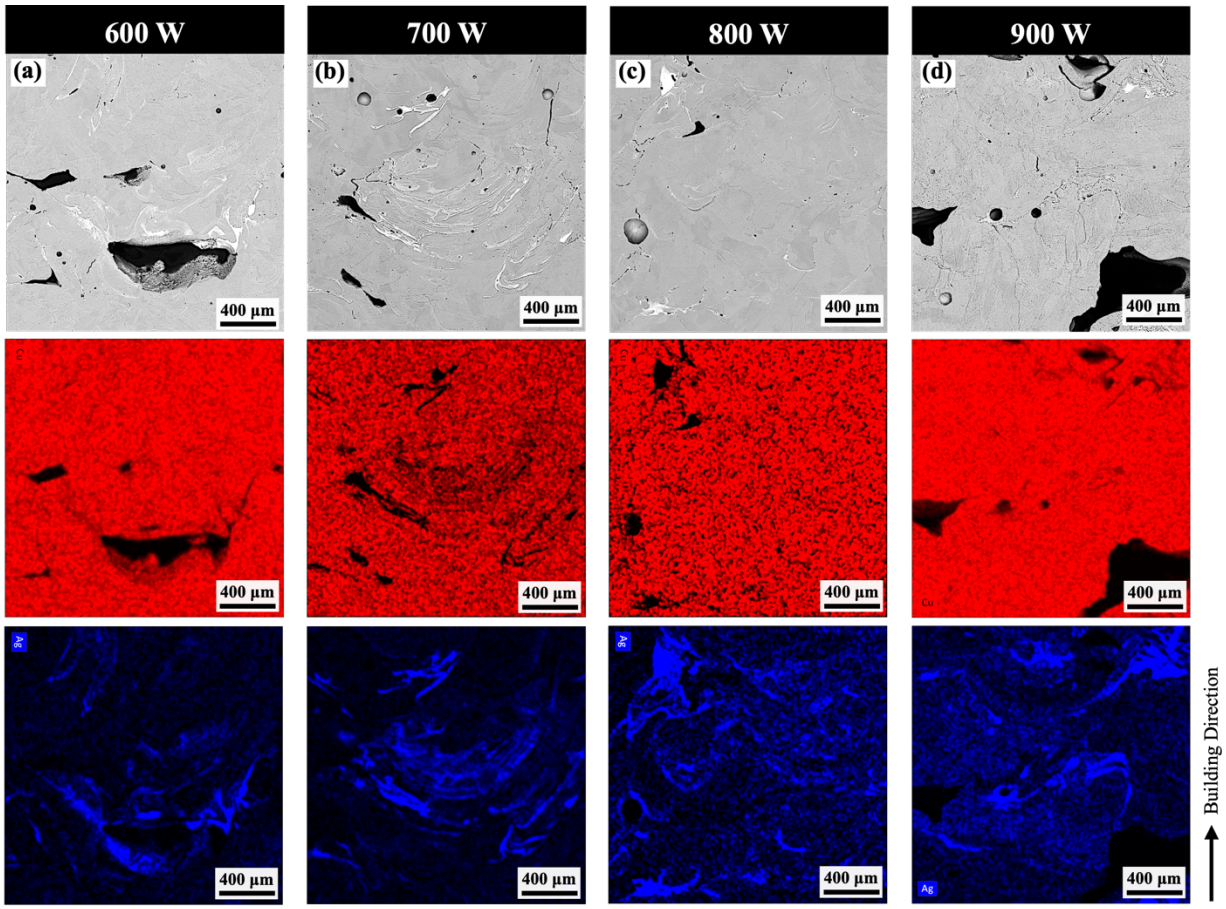


Figure 5-8 SEM and EDS elemental maps of Cu–Ag bulk samples processed at 800 mm/s, showing non-uniform Ag distribution. The SEM images reveal Ag segregation, with Cu (red) and Ag (blue) maps confirming poor mixing. High scanning speed results in limited melt pool residence time, restricting Marangoni flow-driven mixing and leading to localized Ag-rich regions.

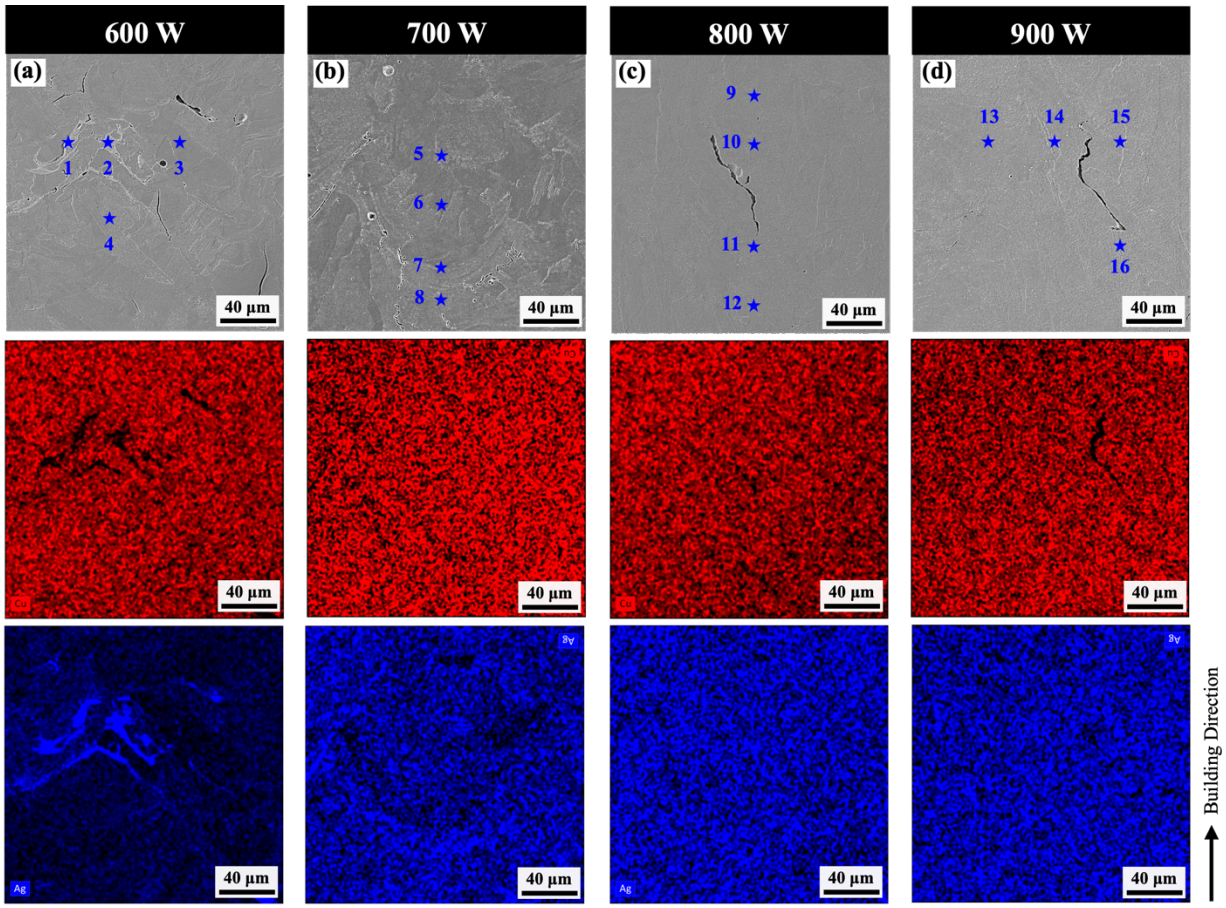


Figure 5-9 SEM and EDS elemental maps of Cu–Ag bulk samples processed at 600 mm/s, showing improved Ag uniformity. The SEM images indicate better in-situ alloying, with Cu (red) and Ag (blue) maps confirming a more homogeneous elemental distribution. The analysis points marked by stars highlight regions where Ag is well-dispersed, demonstrating the positive effect of lower scanning speed on mixing efficiency.

To further evaluate elemental homogeneity, EDS point analysis was performed at selected locations, indicated by the stars in Figure 5-9. The corresponding elemental composition (wt.%) at these points is summarized in Table 5-4.

The results show that at 600 W, the Ag content at different points varies widely, ranging from 0.1 wt.% to 27.5 wt.%, indicating severe compositional heterogeneity. This non-uniformity suggests incomplete mixing of Ag within the Cu matrix, likely caused by weaker Marangoni convection and less stable melt pools at lower power.

At 700 W, the Agr content becomes more consistent, with most points showing values below 4 wt.%, demonstrating some improvement in mixing quality compared to 600 W. However, minor Ag-rich pockets still exist, reflecting that convection and mixing remain limited at this power level.

At 800 W, the elemental distribution becomes more uniform, with Ag content ranging from 2.1 wt.% to 2.4 wt.%, which is very close to the target composition of 2 wt.% Ag. This improvement corresponds directly to the higher Marangoni number observed at this power level (Figure 5-6), confirming that enhanced Marangoni-driven convection supports more efficient element mixing and homogenization within the melt pool. This indicates that 800 W provides sufficient thermal input and convective flow to ensure effective in-situ alloying.

Finally, at 900 W, the silver content is similarly consistent, with values ranging from 2.3 wt.% to 3.0 wt.%, confirming that higher power levels effectively promote convective mixing and ensure more uniform alloying. While this demonstrates effective in-situ alloying at both 800 W and 900 W, the slight increase in Ag content at certain points (up to 3 wt.%) may indicate localized enrichment due to melt pool dynamics, which should be carefully considered in process optimization.

These results demonstrate that scanning speed and laser power both play critical roles in the in-situ alloying process of Cu–Ag during LPBF. Higher scanning speeds, while beneficial for increasing productivity, significantly hinder convective mixing, resulting in Ag segregation and compositional non-uniformity. In contrast, moderate scanning speeds, such as 600 mm/s, provide more stable melt pools and longer interaction times, enabling more effective Marangoni-driven mixing and more uniform elemental distribution.

Additionally, higher laser power enhances melt pool size and convection intensity, further improving Ag dissolution and homogeneity. The combination of moderate scanning speed and higher power, such as 600 mm/s at 800 W or 900 W, emerges as the most favorable processing window, offering uniform composition, high relative density, and reduced defect formation, ultimately leading to a well-alloyed and structurally sound Cu–Ag component.

Table 5-4 Elemental chemical composition (wt.%) obtained from EDS point analysis at selected locations marked with stars in Figure 5-9 for LPBF-made Cu–Ag alloy at 600 mm/s

Element	600 W				700 W				800 W				900 W			
(wt.%)	1	2	3	4	5	6	7	8	9	10	11	12	13	14	15	16
Cu	82.4	72.5	99.9	95.5	98.5	96.2	98.2	98.2	97.9	97.9	97.8	97.6	97.7	97.7	97.0	97.5
Ag	17.6	27.5	0.1	4.5	1.5	3.8	1.8	1.5	2.1	2.1	2.2	2.4	2.3	2.3	3.0	2.5

After optimizing the LPBF process parameters to achieve high relative density and uniform elemental distribution, it is crucial to confirm whether successful in-situ alloying occurred at the atomic scale. To achieve this, XRD analysis was performed on the Cu–2Ag sample processed at 800 W and 600 mm/s, the condition identified as providing the best combination of density, microstructural homogeneity, and process stability. Comparing the XRD pattern of this sample to that of pure Cu allows direct evaluation of how silver incorporation influenced the crystal structure, providing further evidence of effective in-situ alloying.

Figure 5-10 presents the X-ray diffraction (XRD) patterns of pure Cu and the in-situ alloyed Cu–2Ag sample produced at 800 W and 600 mm/s, the condition identified as optimal for ensuring high density, stable melt pool formation, and uniform Ag distribution. Both materials exhibit the characteristic diffraction peaks of face-centered cubic (FCC) copper, indicating that the primary crystal structure is preserved in the Cu–Ag alloy.

However, a noticeable peak shift toward lower diffraction angles is observed for the Cu–2Ag sample, as shown in the magnified regions (Figure 5-10b–d). This shift directly results from the dissolution of Ag atoms into the Cu lattice, causing a lattice expansion in line with Vegard's law [165]. Since Ag atoms have a larger atomic radius than Cu, their incorporation into the Cu lattice generates lattice strain, which reduces the 2θ values compared to pure Cu. This peak shift provides clear evidence of successful in-situ alloying, confirming that Ag was incorporated into the Cu matrix rather than forming separate Ag phases.

Additionally, the absence of any secondary phases in the XRD pattern suggests that the rapid solidification rates inherent to LPBF suppressed phase separation and facilitated the formation of a single-phase Cu–Ag solid solution. This result further confirms that the LPBF process was capable of not only melting and fusing Cu and Ag powders, but also dissolving Ag into Cu during solidification, achieving a chemically homogeneous alloy at the microstructural scale.

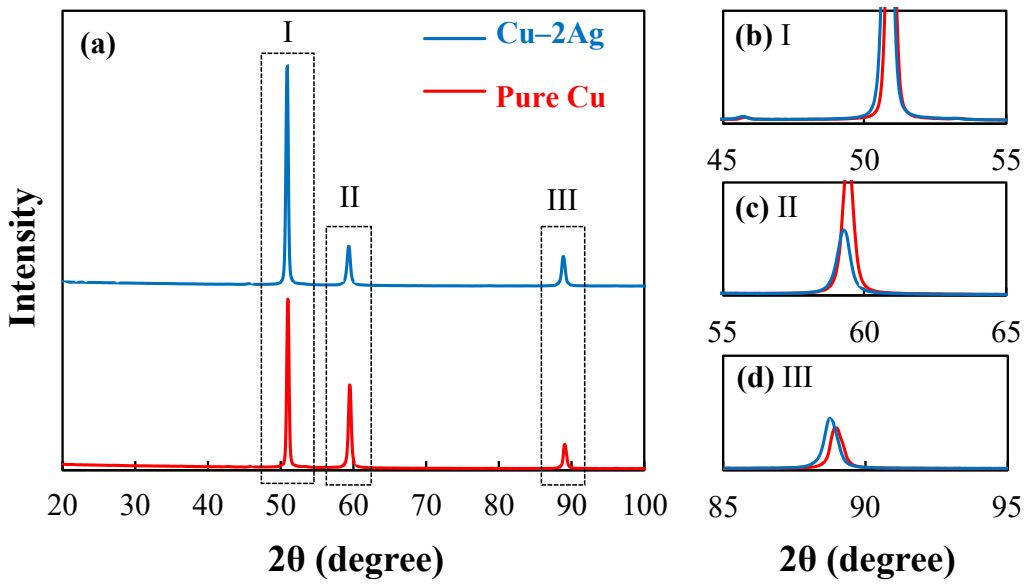


Figure 5-10 XRD patterns of pure Cu and in-situ alloyed Cu–2Ag. (a) Both materials exhibit three main Cu diffraction peaks, but Cu–2Ag shows a shift towards lower angles. (b–d) Magnified views highlight this peak shift, which results from Ag incorporation into the Cu matrix, causing lattice expansion. This confirms the successful formation of an in-situ alloyed solid solution during LPBF processing. With alloying validated, these samples are now prepared for the next stage: oxidation evaluation to assess high-temperature performance.

All of these processing and alloying optimizations were performed with a specific application in mind: developing a Cu-based alloy with enhanced oxidation resistance compared to pure Cu, while still maintaining high electrical conductivity. For this purpose, achieving high relative density was prioritized, since porosity can significantly degrade electrical conductivity. The optimized LPBF parameters resulted in a relative density of ~99.2%, meeting this requirement.

Surface roughness was also evaluated, as surface topography influences oxidation behavior in service environments. The final surface roughness of the optimized samples was measured at ~13.4 μm, well within the acceptable range for the intended application (target <15 μm), confirming that the LPBF process produced parts with suitable surface quality.

Although the direct electrical conductivity testing was conducted on a specific functional geometry, the results were very promising, showing notable improvement over pure Cu. Due to confidentiality requirements, these electrical results are not presented in this chapter. However, the findings provided strong motivation for the next phase of research, investigating the high-temperature oxidation behavior of the optimized Cu–2Ag alloy. This oxidation performance evaluation will be covered in Chapter 6, where the role of Ag in enhancing the thermal stability and oxidation resistance of Cu–Ag will be systematically examined.

5.5. Summary

This study explored the in-situ alloying of Cu–Ag via LPBF, focusing on melt pool characteristics, microstructural evolution, and elemental distribution. Single-track analysis showed that moderate speeds (500–700 mm/s) and power levels (700–800 W) produced stable tracks, while higher speeds caused discontinuities and balling. Melt pool geometry analysis confirmed that both depth and width decreased with increasing speed, emphasizing the need for sufficient energy input. Analytical modeling using Rosenthal's equation and Marangoni number calculations highlighted the role of convection-driven mixing in alloy homogeneity. Bulk samples printed with refined parameters exhibited the highest relative density (~99.49%) at 600 mm/s and 900 W, while higher speeds (800 mm/s) led to increased porosity. SEM and EDS analysis confirmed that Ag distribution was more uniform at 600 mm/s, validating the effectiveness of in-situ alloying. XRD analysis further verified Ag incorporation into the Cu lattice through peak shifts to lower angles, confirming a well-alloyed structure. Building upon this process development, the next chapter investigates the high-temperature oxidation behavior of the optimized Cu–Ag samples. This study aims to understand how the LPBF-induced microstructure and Ag content influence oxide scale growth and long-term oxidation resistance, which are critical for high-temperature functional applications.

Chapter 6. High-temperature oxidation behavior of thin-walled Cu–Ag in-situ manufactured via laser powder bed fusion: Analysis from 300°C to 800°C

6.1. Overview

The high-temperature oxidation behavior of thin-walled Cu and Cu–2wt.%Ag samples manufactured via laser powder bed fusion (LPBF) was investigated over a temperature range of 300 °C to 800 °C. The oxidation kinetics were analyzed through thermogravimetric analysis (TGA), revealing a transition from sub-parabolic to parabolic behavior as temperature increased. At lower temperatures (300 °C –600 °C), Cu–2Ag initially oxidized more rapidly than pure Cu, but its oxidation rate decreased significantly over time, leading to lower total mass gain. At higher temperatures (700 °C –800 °C), Cu–2Ag demonstrated superior oxidation resistance from the outset. Activation energy (E_a) calculations confirmed two distinct oxidation regimes: grain boundary diffusion-controlled oxidation at 300–500°C and lattice diffusion-controlled oxidation at 500–800°C, with Cu–2Ag showing slightly higher activation energy in both regimes. Microstructural analysis via scanning electron microscopy (SEM), energy-dispersive spectroscopy (EDS), and electron backscatter diffraction (EBSD) revealed that the oxide layer in Cu–2Ag was thinner and more compact than in pure Cu, suggesting that Ag influenced oxide scale morphology and stability. EBSD maps showed that Cu_2O grains were smaller and more refined in Cu–2Ag, potentially contributing to enhanced oxidation resistance. These findings demonstrate that Ag addition alters oxidation kinetics and oxide scale formation in LPBF-made Cu, offering a pathway for improving the high-temperature durability of Cu-based components while maintaining electrical and thermal performance.

6.2. Introduction

Copper (Cu) and its alloys are widely utilized in various industries due to their exceptional electrical and thermal conductivity, ease of fabrication, and inherent resistance to corrosion. These properties make Cu indispensable in applications such as automotive, aerospace, electronics, and electrical power systems, particularly in high-temperature environments where oxidation and corrosion present significant challenges. The oxidation of Cu at elevated temperatures can lead to the formation of oxide layers that degrade its electrical conductivity and mechanical integrity, thereby limiting its long-term performance [166,167].

Pure Cu undergoes oxidation primarily through the formation of two copper oxides: cuprous oxide (Cu_2O) and cupric oxide (CuO), each exhibiting distinct growth mechanisms and stability. The oxidation behavior of Cu is influenced by temperature, with Cu_2O predominantly forming at lower temperatures, while CuO becomes more prevalent at higher temperatures [66,168,169] . The oxidation kinetics transition from grain boundary diffusion-controlled mechanisms at lower temperatures to lattice diffusion-controlled mechanisms at higher temperatures. Understanding these mechanisms is critical for improving oxidation resistance and extending the service life of Cu-based components in extreme environments.

One approach to enhancing the oxidation resistance of Cu is through alloying. However, many alloying elements significantly reduce electrical conductivity, making it difficult to balance oxidation resistance with performance requirements. Among potential alloying elements, silver (Ag) is particularly attractive due to its limited impact on electrical conductivity while improving oxidation resistance. Ag has been shown to alter the oxide microstructure and diffusion pathways, potentially leading to a more protective and stable oxide scale [64].

Most studies on Cu–Ag oxidation behavior have focused on conventionally manufactured alloys, with limited research on oxidation resistance in additively manufactured (AM) components. Laser powder bed fusion (LPBF) enables the fabrication of complex geometries with refined microstructures, which can significantly impact oxidation kinetics. Prior research has demonstrated that LPBF-fabricated materials often exhibit distinct oxidation behaviors compared to their conventionally processed counterparts. For example, LPBF-processed Ni-based superalloys have shown up to 30% faster oxidation kinetics due to differences in microstructure and grain boundary density [170].

Despite these insights, the oxidation behavior of LPBF-made Cu–Ag alloys remains largely unexplored. This study aims to investigate the high-temperature oxidation behavior of thin-walled Cu and Cu–2Ag samples manufactured via LPBF, addressing a critical gap in understanding how LPBF processing influences oxidation kinetics and oxide scale formation. By analyzing oxidation rates, activation energies, and microstructural evolution from 300 °C to 800 °C, this work provides a comprehensive assessment of how Ag affects oxidation resistance in LPBF-processed Cu alloys. The findings will contribute to the development of oxidation-resistant Cu-based alloys for high-temperature applications while maintaining electrical and thermal performance.

6.3. Materials and methods

The specimens were manufactured on an EOS M290 LPBF machine equipped with a 1kW Ytterbium continuous fiber laser with a wavelength of 1060 nm and a spot diameter of ~80 μm. The process was carried out under a high purity Ar atmosphere containing less than 0.1% oxygen in the process chamber. Cu and Cu–2Ag thin wall samples with dimensions of 10mm×10mm×1mm were printed by LPBF to investigate the impact of Ag addition on the oxidation behavior of Cu.

The quality of these samples, including surface roughness of lower than 15 μm and relative density of more than 99%, was optimized according to requirements of an industrial application of this alloy. The surface roughness was quantified using Keyence VK-X250 confocal microscopy with non-contact laser profilometry. Computed tomography (CT) was performed using a ZEISS Xradia 520 Versa to find the defects distribution in printed parts. The 3D images were constructed using a beam hardening constant of 0.05 and analyzed in Dragonfly 3.1.

The oxidation tests were conducted at temperature range of 300°C to 800°C via thermogravimetric analysis (TGA) using STA 449 F1 Jupiter machine equipped with a 1000°C furnace. To begin the tests, temperature was raised by heat rate of 10°C/min starting from 25°C to the test temperature under argon 99.9%. At the test temperature, air (with the composition of 19.5–23.5% O_2, 2.0 ppm H2O, 0.5 ppm CO_2, 0.5 ppm CO, 0.1 ppm THC) was introduced for 5 hours meanwhile the mass gain was recorded in terms of time to determine the oxidation rate of the samples.
For microstructural examination of the alloys processed by LPBF, optical microscopy (OM) and scanning electron microscopy (SEM) were performed on cross-sections parallel to the build direction (BD) (side view) using Keyence VHX-7000 optical microscope and TESCAN VEGA electron microscope, respectively.

The metallographic samples were grinded till 4000 SiC papers, polished with MD-Nap 1 micron, and then repolished using Buehler VibroMet2 machine in non-crystallizing amorphous 0.02 μm colloidal silica suspension for 5 hours. X-ray diffraction (XRD) was carried out to using the Co-Kα radiation method, allowing for the identification of the intensity distribution of (111) pole figures to assess macro-texture evolution.

6.4. Results and discussion

6.4.1. Characteristics of as-printed Cu and Cu–Ag

Figure 6-1 presents a comparative analysis of the as-printed surface roughness and internal porosity in pure Cu and Cu–2Ag thin-walled samples fabricated via LPBF. The 3D surface roughness maps (Figure 6-1a and b) indicate that both materials exhibit almost similar surface morphologies, with average surface roughness values (S_a) of 11.2 ± 1.0 µm for pure Cu and 13.4 ± 1.1 µm for Cu–2Ag. This outcome aligns with previous optimization efforts focused on minimizing surface roughness in Cu–Ag alloys to meet specific application requirements. The optimization strategy effectively reduced surface roughness to values below 15 µm, meeting the target for the intended application and maintaining surface quality comparable to that of pure Cu.

The X-Ray CT images (Figure 6-1c and d) demonstrate that both samples achieved high relative densities of 99.81% for Cu and 99.62% for Cu–2Ag, reflecting the success of the parameter optimization in minimizing internal defects. It is noteworthy that, as discussed in Chapter 5, cracking was a significant challenge in Cu–Ag alloys during LPBF fabrication, requiring additional process adjustments to reduce crack formation. Despite these improvements, residual micro-cracks persist in the Cu–2Ag samples that might influence oxidation behavior at elevated temperatures.

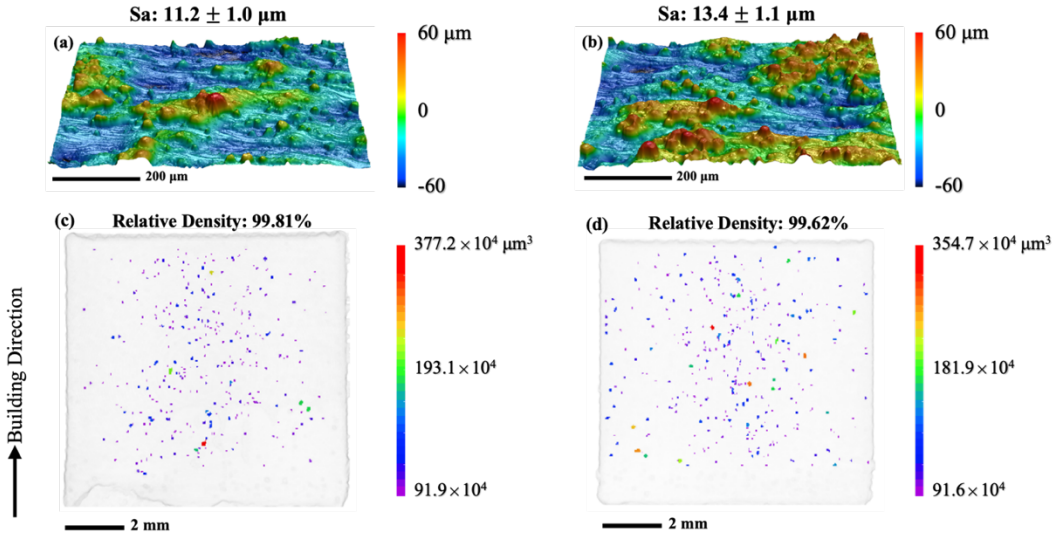


Figure 6-1 3D view of surface profile measurements and X-Ray CT images of LPBF-made thin-walled samples: (a,c) pure Cu and (b,d) Cu–2Ag.

Figure 6-2 shows the SEM micrograph and corresponding EDS elemental maps of the as-printed Cu–2Ag thin-walled sample, providing insights into the elemental distribution within the alloy. In Figure 6-2a, nine points (marked with blue stars) were selected for point analysis to evaluate the local Ag concentration across different regions. The average Ag content, measured at 1.66 ± 0.17 wt.%, is close to the target composition of ~2 wt.%, confirming the effectiveness of the in-situ alloying process during LPBF. The slight variations in Ag content among the points are within an acceptable range, reflecting the typical microstructural heterogeneity associated with in-situ alloying in LPBF.

Furthermore, a micro-crack is observed in Figure 6-2a, which is likely a solidification crack. Such cracks often initiate along grain boundaries during the final stages of solidification, when the material is partially molten and cannot fully accommodate thermal shrinkage or stress. In the context of in-situ alloying, the difference in melting points between Cu (1083 °C) and Ag (961 °C) may lead to uneven melting and solute segregation, potentially introducing localized thermal gradients and stress concentrations. Additionally, residual thermal stresses, rapid cooling, and thermal expansion mismatch between Cu and Ag may further contribute to crack formation during the LPBF process.

Importantly, the EDS elemental maps (Figure 6-2b,c) show a uniform distribution of both Cu and Ag, with no significant segregation of elements around the crack area. The homogeneous distribution of Ag throughout the Cu matrix is particularly critical for oxidation behavior, as uniform alloying can enhance the formation of stable protective oxides, improving high-temperature performance.

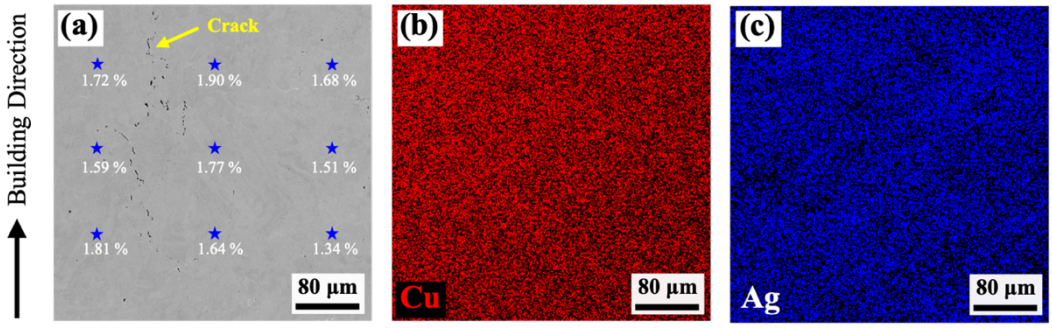


Figure 6-2 (a) SEM micrograph and EDS elemental maps of LPBF-made Cu–2Ag thin-walled sample, showing the distribution of (b) Cu and (c) Ag. The blue stars in (a) indicate the locations of point analyses used to determine the local chemical composition, with measured Ag contents provided.

To explore the effect of Ag on the microstructure of Cu, Figure 6-3 presents the EBSD results of as-printed pure Cu and Cu–2Ag thin-walled samples. The grain maps show that pure Cu (Figure 6-3a) has an average grain size of 77.3 ± 8.9 μm, while Cu–2Ag (Figure 6-3d) exhibits a slightly refined grain structure with an average grain size of 64.1 ± 8.1 μm. Although this difference is not highly significant, it suggests that Ag influences grain formation by modifying the solidification dynamics. The refinement effect is attributed to Ag acting as a solute element, which affects nucleation and grain growth during solidification.

Silver, with its lower melting point than Cu, alters the thermal conditions of the melt pool, affecting the local undercooling and promoting heterogeneous nucleation. The presence of Ag increases the availability of nucleation sites by reducing the critical energy barrier for new grain formation, leading to a more refined microstructure. Furthermore, Ag in the melt contributes to solute drag, where Ag atoms may segregate at grain boundaries, impeding grain boundary motion and preventing excessive grain coarsening. This mechanism, widely reported in Cu-based alloys, plays a crucial role in grain refinement by stabilizing grain boundaries and reducing grain growth kinetics [171].

In addition, the inverse pole figure (IPF-Z) maps indicate that both pure Cu (Figure 6-3b) and Cu–2Ag (Figure 6-3e) exhibit a random crystallographic texture, with no strong preferential orientations. This differs from the typical columnar grain growth often observed in LPBF-made metals [172,173]. The absence of strong texture can be attributed to the thin-walled geometry of the samples, with thickness of 1 mm.

In thin-walled structures, the high surface-area-to-volume ratio leads to rapid heat dissipation through the surrounding powder bed and the build plate. This causes the thermal gradient to be lower than in bulk samples, suppressing the strong directional solidification that typically promotes columnar grains. Instead, the melt pool experiences multidirectional heat extraction, leading to more isotropic grain growth and a lack of a dominant crystallographic texture. Similar trends have been observed in LPBF-made Hastelloy X thin-walled samples, where thinner walls exhibited finer, randomly oriented grains due to enhanced cooling rates and lower heat accumulation [174,175]. Furthermore, modeling and experimental studies confirm that decreasing the thickness of thin-

walled structures increases the temperature gradient and alters the melt pool dynamics, ultimately influencing the grain morphology [175].

The (200) pole figures obtained from XRD further highlight the influence of Ag on texture evolution. The addition of Ag results in a slight shift in the maximum texture density toward lower angles, accompanied by a reduction in overall texture intensity from 3.7 in pure Cu (Figure 6-3c) to 3.2 in Cu–2Ag (Figure 6-3f). This change can be attributed to the effect of Ag on the stacking fault energy (SFE) of Cu. The presence of Ag in solid solution can alter dislocation movement and modify slip system activity, thereby influencing preferred grain orientations [176]. A lower SFE can promote increased slip on {111} planes, which may explain the shift in texture density toward lower angles. Besides, Ag may slightly disrupt the preferred growth direction by affecting thermal gradients and local undercooling, leading to a more randomized grain orientation and a decrease in overall texture intensity.

These microstructural modifications have direct implications for oxidation behavior. The slight grain refinement observed in Cu–2Ag increases the density of grain boundaries, which serve as diffusion pathways for oxygen, potentially accelerating the initial oxidation process. However, the formation of a dense and protective oxide layer could subsequently act as a barrier, limiting further oxidation and ultimately enhancing oxidation resistance [177].

Furthermore, the random texture observed in both pure Cu and Cu–2Ag ensures that oxidation behavior remains largely isotropic, leading to the formation of a more uniform oxide scale. The subtle texture modifications in Cu–2Ag may also influence oxidation kinetics by altering the diffusion pathways of both oxygen and metal ions. These effects will be further examined in the following sections, providing deeper insights into the role of Ag in enhancing high-temperature oxidation resistance.

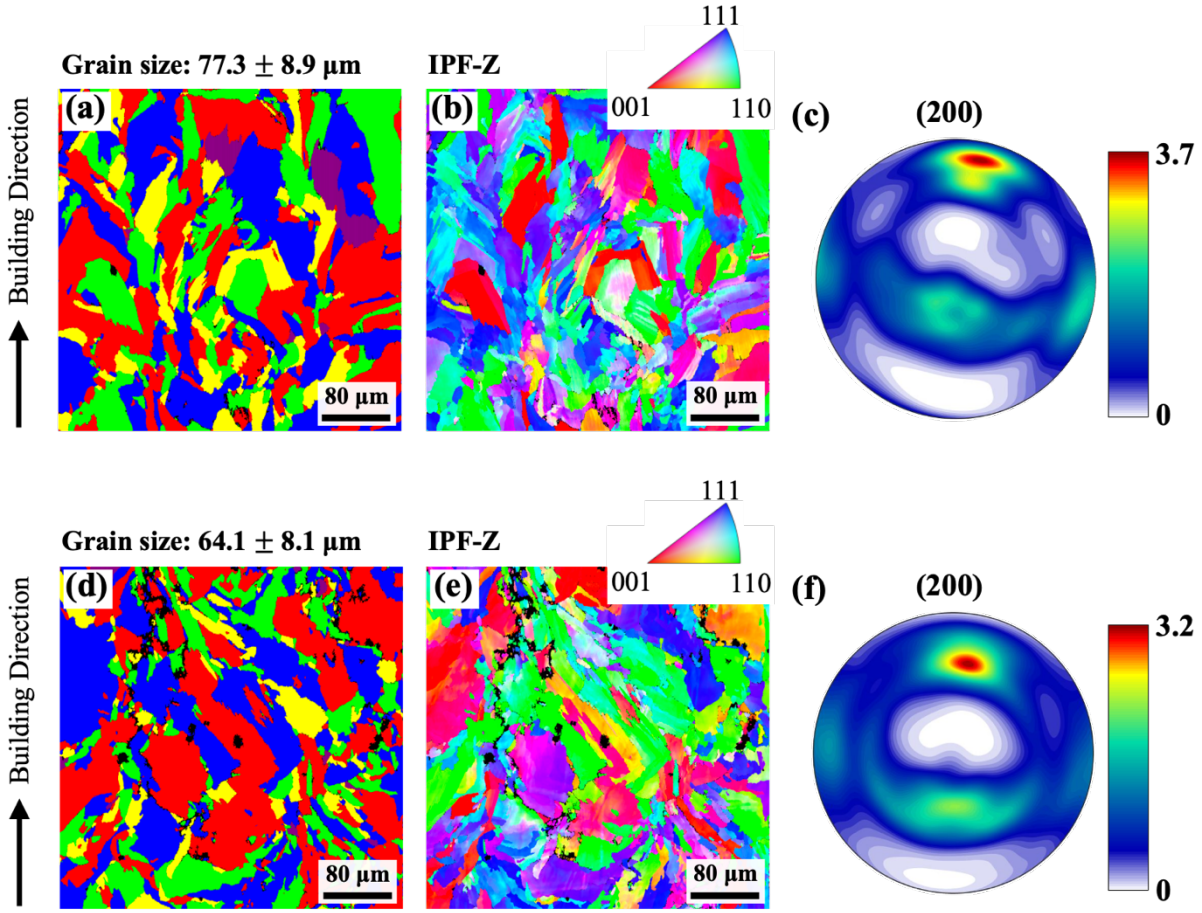


Figure 6-3 EBSD results of as-printed pure Cu and Cu–2Ag thin-walled samples. (a) Grain map of pure Cu, showing an average grain size of 77.3 ± 8.9 µm, and (b) corresponding IPF-Z map. (d) Grain map of Cu–2Ag, with an average grain size of 64.1 ± 8.1 µm, and (e) corresponding IPF-Z map. The (200) pole figures, obtained from XRD, are shown for (c) pure Cu and (f) Cu–2Ag. Both materials exhibit random texture, while the addition of Ag results in slight grain refinement and a shift in the maximum texture intensity to lower angles with reduced overall intensity.

6.4.2. Oxidation resistance of LPBF-made Cu and Cu–Ag

To evaluate the oxidation behavior of LPBF-made pure Cu and Cu–2Ag thin-walled samples, mass gain measurements were recorded after 24 hours of exposure to flowing air (~20% O_2) at temperatures ranging from 300 °C to 800 °C. Figure 6-4 presents the final specific mass gain, providing an initial comparison of the oxidation resistance of both materials. At first glance, Cu–2Ag appears to exhibit higher oxidation resistance at most temperatures, as indicated by its lower total mass gain compared to pure Cu. However, at 300 °C, the trend is reversed, with pure Cu showing less mass gain than Cu–2Ag, suggesting better resistance under these conditions.

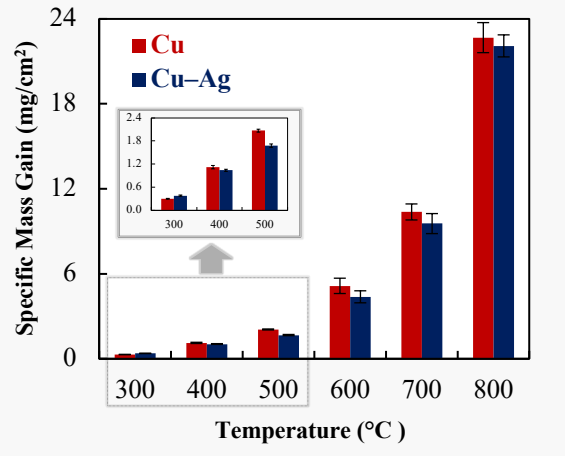


Figure 6-4 Mass gain of LPBF-made Cu and Cu–2Ag thin-walled samples after 24 hours of oxidation in air at different temperatures.

While Figure 6-4 offers a preliminary assessment of oxidation resistance, it does not capture how oxidation evolves over time. The oxidation rate over time is crucial in determining oxidation behavior, as it reveals whether oxidation progresses continuously or stabilizes at a protective limit. To analyze oxidation rate in detail, Figure 6-5 shows the specific mass change (Δm) as a function of time, allowing for a more accurate evaluation of how each material reacts at different temperatures.

As shown in Figure 6-5, the oxidation rate increases with temperature due to the enhanced diffusion of oxygen and metal ions, which accelerates oxide layer growth. At higher temperatures, the increased mobility of Cu and O atoms leads to faster oxidation kinetics and the formation of a thicker oxide layer [169]. However, the effect of temperature on oxidation behavior is not identical in both materials. While Cu and Cu–2Ag both experience higher oxidation rates at elevated temperatures, their oxidation kinetics differ.

At temperatures below 700 °C, Cu–2Ag initially oxidizes faster than pure Cu, meaning it gains mass more quickly in the early stages. However, over time, the oxidation rate of Cu–2Ag slows down significantly, and at a certain point, the curves intersect, meaning Cu–2Ag starts gaining less mass than pure Cu. This indicates that while Cu–2Ag undergoes faster oxidation at first, it eventually stabilizes and forms a more protective oxide layer, limiting further oxidation.

The initial rapid oxidation of Cu–2Ag may be attributed to its microstructure (Figure 6-3). The finer microstructure of Cu–2Ag provides a higher density of grain boundaries, which may initially facilitate faster oxygen diffusion, leading to the more rapid early-stage oxidation. However, as oxidation progresses, the presence of Ag appears to promote the development of a denser and more stable oxide layer in Cu–2Ag, which can act as a diffusion barrier, effectively reducing the oxidation rate in later stages. At higher temperatures, the stabilization occurs earlier, preventing the prolonged initial oxidation phase observed at lower temperatures [178].

As temperature increases, the intersection point in the oxidation curves shifts to earlier times, indicating that the transition from rapid initial oxidation to a more stable oxidation regime occurs more quickly at elevated temperatures. At 300 °C (Figure 6-5a), Cu–2Ag exhibits a higher mass gain than Cu for ~72 h. At 400 °C and 500 °C (Figure 6-5b), the transition happens earlier, after ~8 h and ~7 h, respectively. At 600 °C (Figure 6-5d), the mass gain of Cu–2Ag drops below that of Cu after ~2 h. At 700 °C and 800 °C (Figure 6-5c and d), no intersection occurs since Cu–2Ag exhibits better oxidation resistance from the outset, maintaining a lower oxidation rate than pure Cu throughout the test duration.

This phenomenon can be attributed to temperature-dependent diffusion mechanisms governing oxidation kinetics. At lower temperatures, oxidation in Cu–2Ag progresses more gradually, with the protective oxide layer forming over an extended period. In contrast, at higher temperatures, oxidation kinetics are dominated by the enhanced diffusion of oxygen and metal ions, leading to faster oxide formation and earlier stabilization of the oxidation rate [169,178].

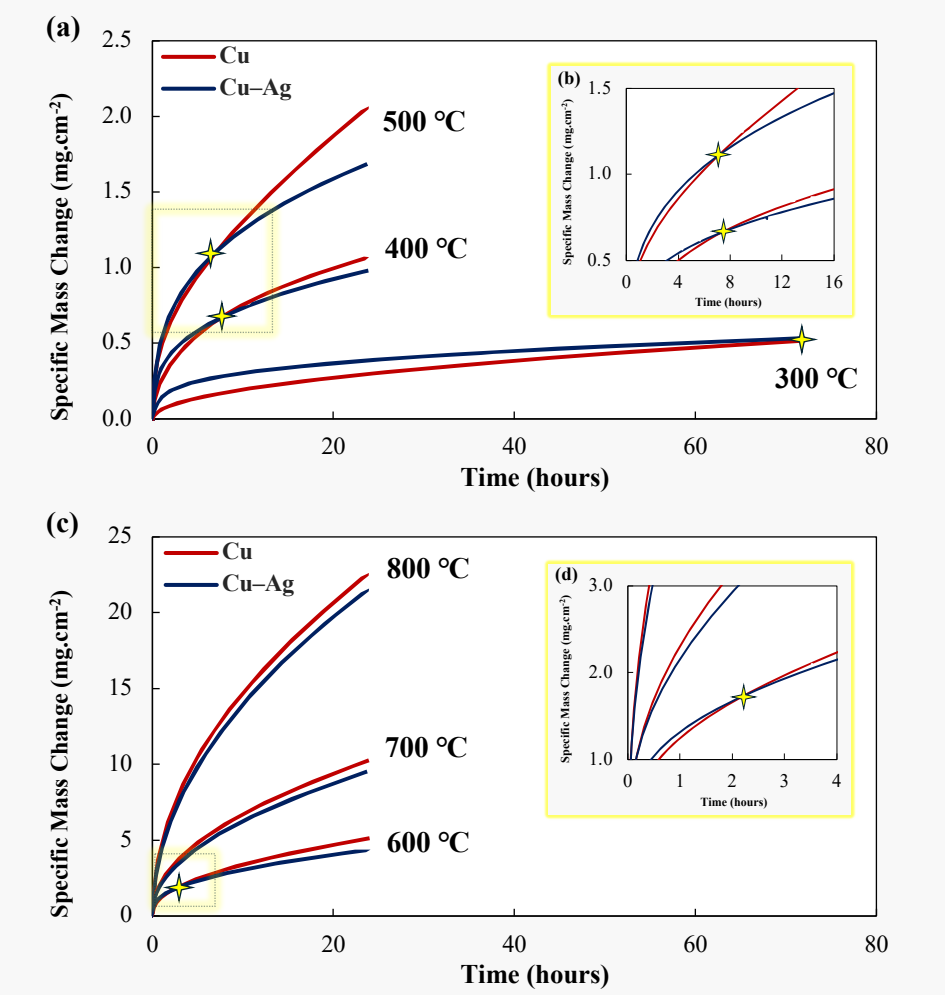


Figure 6-5 Oxidation rate of Cu and Cu–2Ag at different temperatures, showing mass gain as a function of time. At temperatures below 700 °C, Cu–2Ag initially oxidizes at a faster rate than pure Cu but later exhibits a lower oxidation rate.

6.4.3. Oxidation kinetics of LPBF-made Cu and Cu–Ag

To gain a deeper understanding of the oxidation behavior of the materials, the TGA data is analyzed to assess the nature of oxidation kinetics. The nonlinear trend observed in the mass gain curves in Figure 6-5, particularly their concave shape, indicates that oxidation progresses at a rate slower than linear, which is characteristic of parabolic oxidation behavior [66]. To verify this, the squared mass gain (Δm^2) is plotted as a function of time for all temperatures, as shown in Figure 6-6, providing a clearer evaluation of oxidation kinetics.

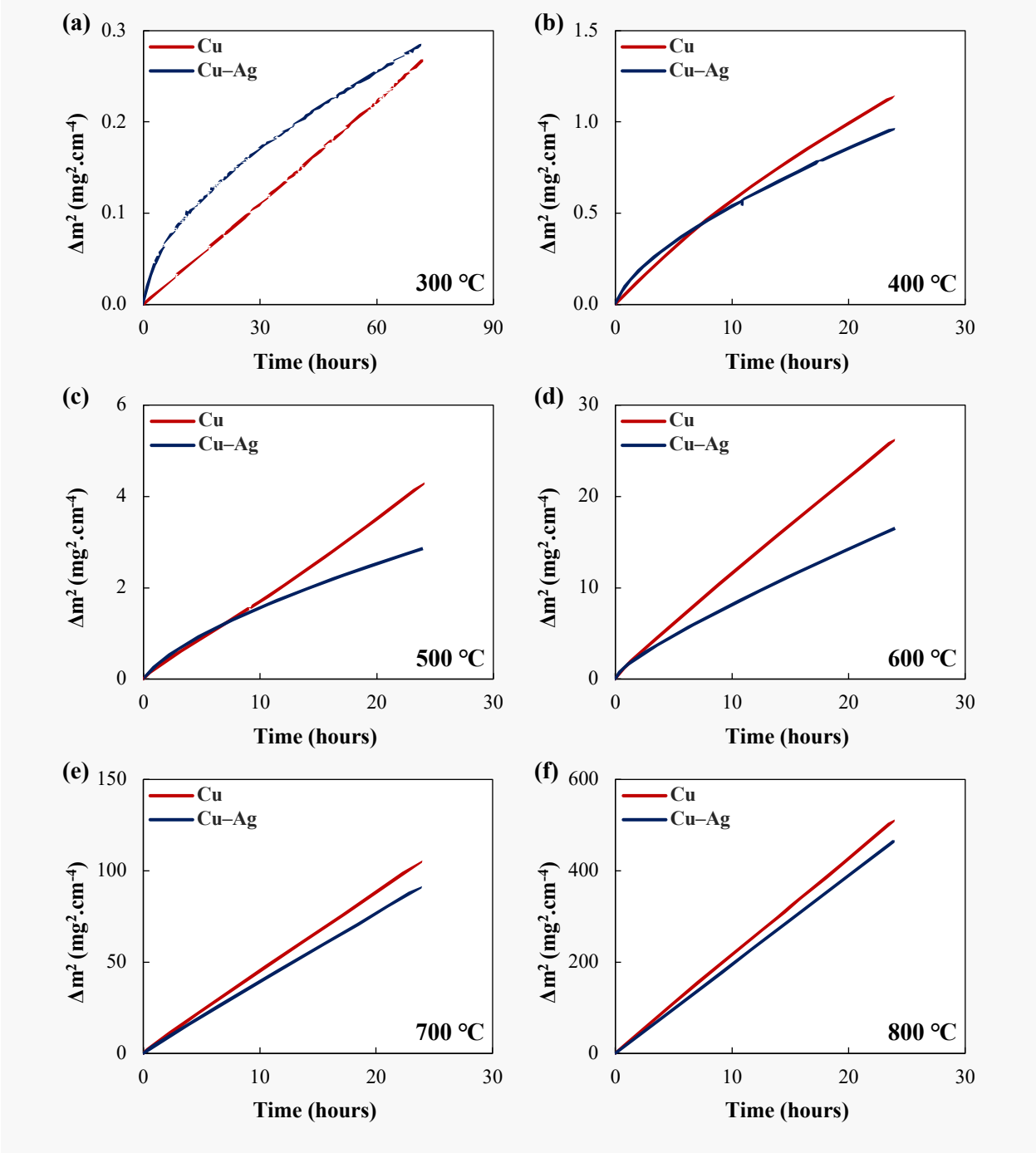


Figure 6-6 Parabolic analysis of oxidation kinetics in LPBF-made Cu and Cu–2Ag thin-walled samples, showing squared mass gain (Δm^2) as a function of time. Cu follows a parabolic oxidation law at all temperatures, indicating diffusion-controlled oxidation. In contrast, Cu–2Ag exhibits sub-parabolic behavior at 300–600 °C, where the oxidation rate slows more significantly, suggesting additional rate-controlling factors. At 700 °C and 800 °C, Cu–2Ag transitions fully to parabolic kinetics, indicating that Ag no longer has a significant influence on oxidation resistance, and oxidation proceeds similarly to Cu.

Parabolic oxidation behavior is typically associated with the rapid initial formation of a continuous oxide layer, after which oxidation slows as the rate of further oxide growth becomes diffusion-controlled. In such cases, the oxidation kinetics can be analyzed using the power law equation:

$$\Delta m = kt^n \tag{6-1}$$

where Δm represents the mass gain per unit area ($mg.cm^{-2}$), k is the oxidation rate constant, t is the exposure time (s), and n is the rate exponent.

If $n = 1$, the oxidation follows a linear rate where oxidation rate remains constant, suggesting that diffusion is not the primary rate-limiting step. This is often observed when a non-protective oxide layer forms, allowing continuous oxidation. If $n = 0.5$, the oxidation follows a parabolic law, meaning the growth of the oxide layer slows over time due to the increasing thickness acting as a diffusion barrier. This is characteristic of protective oxides, where the rate of oxidation decreases as the layer thickens. For values of $n < 0.5$, oxidation follows a sub-parabolic behavior, where the rate slows even more significantly. This is typically associated with the formation of a highly protective oxide layer or the presence of additional diffusion barriers, indicating that oxidation is controlled by mechanisms beyond standard parabolic growth, such as microstructural changes or altered transport pathways [66,169]. Table 6-1 presents the n values obtained from the power law fitting.

Table 6-1 The rate exponent (***n*** in $\Delta m = kt^n$) of Cu and Cu–Ag at different temperatures

	rate exponent (*n*-value) at different temperatures					
Material	300 °C	400 °C	500 °C	600 °C	700 °C	800 °C
Cu	0.51	0.46	0.48	0.46	0.49	0.52
Cu–Ag	0.32	0.37	0.38	0.39	0.49	0.53

For pure Cu, oxidation kinetics strictly adhere to the parabolic rate law at all temperatures, with $n \approx 0.5$. This behavior suggests that oxidation is governed by diffusion through a growing oxide scale, which progressively limits further oxidation. The initial rapid increase in mass gain at early stages indicates the rapid formation of Cu_2O, which then transitions into a more protective oxide layer over time [66]. This protective effect is evidenced by the decreasing slope of the mass gain curve (Figure 6-5), which confirms that oxidation slows as the oxide scale thickens and acts as a barrier to further oxygen diffusion.

However, for Cu–2Ag, oxidation behavior deviates from that of pure Cu at temperatures between 300 °C and 600 °C, where the n value ranges from 0.32 to 0.39 ($n < 0.5$). This indicates that oxidation progresses at a rate slower than parabolic, suggesting that additional mechanisms influence oxidation kinetics. At 700 °C and 800 °C, the oxidation kinetics of Cu–2Ag fully transition to a parabolic regime, with $n \approx 0.5$. This suggests that at higher temperatures, the oxidation mechanism becomes similar to that of pure Cu. The shift from non-parabolic to parabolic behavior indicates that at elevated temperatures, Ag no longer significantly alters the oxidation rate, possibly because its influence on the oxide microstructure diminishes as temperature increases.

The reduction in the effect of Ag on the oxidation at higher temperatures can be explained by a decrease in solute drag effects and a shift from grain boundary diffusion to lattice-controlled oxidation mechanisms. At lower temperatures (300–600 °C), solute drag occurs when Ag atoms segregate at grain boundaries, impeding the outward diffusion of Cu and modifying oxidation kinetics. This interaction alters the oxide scale formation, leading to a slower-than-parabolic oxidation rate, as observed in Cu–2Ag, where the oxidation rate exponent (n) is lower than 0.5. However, as temperature increases to 700–800 °C, the diffusion of Cu and O becomes more thermally activated, reducing the ability of Ag to influence oxidation pathways. The increased mobility of atoms weakens solute drag effects, allowing oxidation in Cu–2Ag to transition to a parabolic regime ($n \approx 0.5$), similar to pure Cu.

This change may also be attributed to a shift in the dominant oxidation mechanism. At lower temperatures, oxidation is primarily grain boundary-controlled, meaning oxygen and metal ion transport occurs preferentially along grain boundaries, where diffusion is easier. The presence of Ag, which increases grain boundary density due to grain refinement, influences these pathways and alters oxidation behavior. However, as temperature rises, the oxidation process transitions from grain boundary diffusion to lattice diffusion, where Cu ions move through the bulk of the oxide rather than along grain boundaries. This shift makes grain boundary effects, including those influenced by Ag, less significant, leading to oxidation kinetics that closely resemble those of pure Cu.

To quantitatively compare the oxidation resistance of Cu and Cu–2Ag, the parabolic oxidation rate constant (k_p) was determined using Equation (6-2):

$$\Delta m^2 = k_p t \quad (6\text{-}2)$$

where k_p is a key parameter that describes the rate at which the oxide layer thickens over time. A lower k_p value indicates slower oxidation kinetics and suggests that the material develops a more protective oxide layer, thereby enhancing its long-term oxidation resistance. The values of k_p for both materials at different temperatures are summarized in Table 6-2.

A comparison of k_p values in Table 6-2 reveals that Cu–Ag consistently exhibits lower oxidation rate constants than pure Cu across all temperatures, confirming its superior oxidation resistance. Despite Figure 6-4 showing that the total mass gain after 72 h at 300 °C remained higher for Cu–2Ag compared to pure Cu, the comparison of k_p values provides a more comprehensive understanding of oxidation behavior. While Cu initially appears to resist oxidation more effectively at this temperature, the lower k_p of Cu–Ag suggests that its overall oxidation progresses at a slower rate, meaning that over longer exposure times, its protective oxide layer may provide greater stability.

While this reduction may seem minor (k_p = 1.0 × 10^{-6} $mg^4.cm^{-2}.s^{-1}$ for Cu and k_p = 0.9 × 10^{-6} $mg^4.cm^{-2}.s^{-1}$ for Cu–Ag), even small differences in oxidation rate can become highly significant over prolonged exposure, particularly in high-temperature applications where oxidation-related degradation accumulates over time. The lower oxidation rate constant for Cu–Ag suggests that the presence of Ag plays a role in stabilizing the oxide layer, reducing further oxidation, and improving the overall durability of the material in oxidizing environments.

As temperature increases, the oxidation rate of both materials rises due to enhanced oxygen and metal ion diffusion, yet Cu–Ag consistently maintains a lower k_p than pure Cu, further supporting the fact that Ag addition improves oxidation resistance. However, despite the observed improvement, it is important to note that the k_p values measured in this study remain higher than those reported in the literature for conventionally processed Cu [178]. This discrepancy highlights the impact of the initial microstructure and the LPBF manufacturing process on oxidation behavior.

The unique microstructure such as high dislocation density and residual stress state associated with LPBF may contribute to differences in oxidation kinetics compared to conventionally processed Cu. Overall, the consistent reduction in for Cu–Ag confirms that Ag addition effectively retards oxidation, enhancing the material's stability and longevity in oxidizing environments. These findings also emphasize the importance of considering the role of microstructure and processing conditions when evaluating oxidation behavior, as AM techniques such as LPBF may introduce unique oxidation characteristics that differ from those observed in conventionally processed materials.

Table 6-2 The parabolic oxidation rate constant ($\boldsymbol{k_p}$ in $\Delta m^2 = k_p t$) of Cu and Cu–Ag at different temperatures

	k_p [mg^2.cm^{-4}.s^{-1}] at different temperatures					
Material	300 °C	400 °C	500 °C	600 °C	700 °C	800 °C
Cu	1.0×10^{-6}	13.3×10^{-6}	49.6×10^{-6}	304.9×10^{-6}	1224.6×10^{-6}	5942.2×10^{-6}
Cu–Ag	0.9×10^{-6}	11.2×10^{-6}	33.1×10^{-6}	221.3×10^{-6}	1062.6×10^{-6}	5414.7×10^{-6}

6.4.4. Oxidation mechanism of LPBF-made Cu and Cu–Ag

As previously discussed, the oxidation behavior of Cu–2Ag transitions from sub-parabolic to parabolic kinetics at temperatures about 600 °C. To further investigate the underlying mechanisms governing oxidation at different temperatures, an Arrhenius analysis of the parabolic rate constant (k_p) was performed. This analysis aims to identify whether a transition temperature exists, marking a shift in the dominant oxidation mechanism.

k_p typically follows an Arrhenius-type temperature dependence, which is mathematically expressed as:

$$k_p = A \exp\left(\frac{-E_a}{RT}\right) \tag{6-3}$$

where k_p is the oxidation rate constant from Table 6-2, A is the pre-exponential factor, E_a is the oxidation activation energy (J.mol^{-1}), R is the universal gas constant (8.314 J.mol^{-1}.K^{-1}), and T is the absolute temperature (K).

To identify oxidation regime transitions, E_a was determined by rearranging Equation (6-3) into Equation (6-4):

$$\ln k_p = \ln A - \frac{E_a}{RT} \tag{6-4}$$

where E_a is determined from the slope of the ln k_p – 1/T plot. Figure 6-7 shows the relationship between ln k_p and 1/T for both materials across the tested temperature range. The plot reveals a clear change in slope, indicating the presence of two distinct oxidation regimes: Regime (I) (300 °C–500 °C) and Regime (II) (600 °C–800 °C). This transition aligns with the previously observed shift in oxidation kinetics (Table 6-1), where Cu–2Ag changed from sub-parabolic to parabolic behavior above 600 °C. Such a shift suggests that the underlying oxidation mechanism evolves with temperature, requiring a more detailed examination of activation energies to identify the dominant diffusion processes in each regime. To further investigate this, the E_a values were calculated for each regime and recorded in Table 6-3.

The E_a values provide insight into the oxidation mechanisms operating at different temperature ranges. In Regime (I) (300 °C – 500 °C), E_a is 65.2 kJ.mol^{-1} for Cu and 70.7 kJ.mol^{-1} for Cu–2Ag, while in Regime (II) (600 °C – 800 °C), the activation energy increases to 108.2 kJ.mol^{-1} for Cu and 115.9 kJ.mol^{-1} for Cu–2Ag. The lower E_a in Regime (I) suggests that oxidation is primarily grain boundary diffusion-controlled, whereas the higher E_a in Regime (II) indicates a shift to lattice diffusion-controlled oxidation.

This observation aligns with previously reported studies, where activation energy values for Cu were found to be 40–52 kJ.mol^{-1} in the 350 °C – 500 °C range, and 93–111 kJ.mol^{-1} at 600 °C – 800 °C, confirming a transition in oxidation mechanisms with increasing temperature. Oxidation in Cu generally follows three distinct mechanisms across different temperature ranges (350 °C – 1050 °C). At lower temperatures (350 °C – 500 °C), oxidation is dominated by grain boundary diffusion, where oxygen transport and Cu ion migration occur primarily along grain boundaries, which act as easy diffusion pathways. This mechanism results in a relatively low activation energy of approximately 40–70 kJ.mol^{-1}.

As the temperature increases (600 °C – 800 °C), oxidation transitions to a lattice diffusion-controlled mechanism, where Cu ions diffuse through the bulk of the oxide layer instead of along grain boundaries. This shift increases the activation energy to around 90–120 kJ.mol^{-1}, as lattice diffusion requires greater energy for Cu ion migration. The transition from grain boundary to lattice diffusion is consistent with the observed higher E_a values in Regime (II) for both Cu and Cu–2Ag.

At even higher temperatures (900 °C – 1050 °C), oxidation may become influenced by a combination of lattice diffusion and gas-phase transport, where oxygen transport through the outer oxide layer or vapor-phase transport plays a role in oxidation kinetics. The activation energy in this range varies widely, depending on the formation of oxide layer and its thickness.

Accordingly, based on the observed activation energy values in Table 6-3, Regime (I) can be identified as grain boundary diffusion-controlled oxidation, where oxidation progresses along grain boundaries within the oxide scale, while Regime (II) corresponds to lattice diffusion-controlled oxidation, where Cu ions must migrate through the bulk of the oxide layer, requiring higher energy.

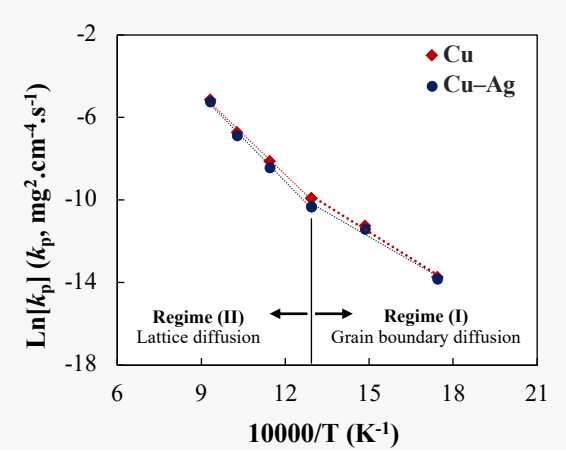


Figure 6-7 Arrhenius plot of the parabolic oxidation rate constant (k_p) for Cu and Cu–2Ag in the temperature range of 300°C–800°C. The change in slope indicates the presence of two oxidation regimes: Regime (I) (300°C–500°C), where oxidation mechanism is grain boundary diffusion-controlled, and Regime (II) (500°C–800°C), where oxidation mechanism transitions to lattice diffusion-controlled.

Table 6-3 The oxidation activation energy (E_a) of Cu and Cu–Ag

	E_a [kJ.mol^{-1}] at different temperature regimes	
Material	Regime (I): 300 °C – 500 °C	Regime (II): 600 °C – 800 °C
Cu	65.2	108.2
Cu–Ag	70.7	115.9

The presence of Ag clearly increases E_a in both oxidation regimes, indicating its influence on diffusion kinetics within the oxide layer. The higher activation energy observed for Cu–2Ag compared to pure Cu can be attributed to differences in atomic diffusion behavior and the specific role of Ag in oxidation. Ag atoms are larger than Cu atoms (Ag: 144 pm and Cu: 128 pm), which affects atomic mobility and diffusion pathways within the oxide scale. Since diffusion is strongly dependent on atomic size, bonding strength, and defect interactions, the presence of Ag can reduce the mobility of Cu ions, making oxidation more difficult and requiring more energy [64].

A possible explanation for this effect is that Ag may segregate at grain boundaries, subtly impeding grain boundary diffusion in Regime (I) (300 °C – 500 °C), where oxidation is predominantly grain boundary-controlled. In Regime (II) (600 °C – 800 °C), where oxidation transitions to lattice diffusion, Ag could influence the oxide microstructure by modifying defect structures and vacancy concentrations, thereby increasing the energy required for Cu ion transport through the oxide scale. Additionally, Ag may act as a solute drag element, interacting with Cu ions and restricting their diffusion within the oxide layer, further contributing to the increased activation energy observed in Cu–2Ag.

The slightly higher activation energy of Cu–2Ag suggests that Ag alters the diffusion mechanism by introducing additional resistance to Cu ion migration. This effect may contribute to changes in oxide layer growth and stability, potentially influencing oxidation resistance at elevated temperatures. However, further analysis is required to determine whether Ag plays a role in modifying the oxide structure and adhesion. To investigate this, the microstructure will be analyzed in the next section to examine the morphology and composition of the oxide layer, providing deeper insight into the role of Ag in oxidation behavior.

6.4.5. Microstructure analysis of oxidized Cu and Cu–Ag

Cu oxidation generally results in the formation of two primary oxides: cuprous oxide (Cu_2O) and cupric oxide (CuO). These oxides differ in their stoichiometry, structure, and formation conditions, which directly influence the oxidation kinetics and scale morphology. Cu_2O, is a red-colored, cubic-structured oxide that typically forms first at lower oxygen partial pressures, while CuO is a black, monoclinic oxide that requires higher oxygen availability to form. The relative proportion of these oxides plays a crucial role in determining the oxidation rate and the stability of the oxide scale.

At lower temperatures (350°C–600°C), Cu_2O is the dominant oxide phase, but a noticeable fraction of CuO forms on the outermost layer, particularly at the surface, where it appears as whisker-like structures [168,169,178]. The formation of CuO at these temperatures is attributed to surface-controlled reactions, where localized oxygen availability allows for CuO nucleation. This can influence the oxidation rate by altering the scale's adherence, porosity, and growth rate. Additionally, at these temperatures, oxidation is primarily grain boundary diffusion-controlled, meaning oxygen and Cu ions migrate along grain boundaries within the Cu_2O layer, contributing to a relatively lower activation energy.

At higher temperatures (600 °C–1050 °C), oxidation is predominantly controlled by Cu_2O growth, as it remains the primary oxide phase. The oxidation mechanism transitions from grain boundary diffusion to lattice diffusion, where Cu ions migrate through the bulk of the Cu_2O layer rather than along grain boundaries. In this regime, the oxide layer becomes denser and more stable, exhibiting parabolic oxidation kinetics, as Cu_2O growth is governed by outward Cu diffusion. Although CuO formation is still possible at high temperatures, it is typically present in only small amounts, dispersed throughout the Cu_2O layer rather than forming whisker-like structures [169].

Given these differences in oxide formation across temperature ranges, examining the microstructure of oxidized Cu and Cu–Ag is essential to understanding how Ag influences oxide scale composition, morphology, and stability. Figures Figure 6-8–Figure 6-11 present SEM images and EDS analysis, including elemental distribution maps and line analysis, of the oxide layers formed on Cu and Cu–2Ag at different oxidation temperatures.

The SEM images and EDS analyses in Figures Figure 6-8 and Figure 6-9 provide insight into the evolution of the oxide layers formed on Cu and Cu–2Ag at 400°C, 500°C, and 600°C. The corresponding line analysis in Figure 6-10 further clarifies the oxide layer composition and thickness variations between both materials.

At 400°C, both Cu and Cu–2Ag exhibit a thin and continuous oxide layer, with Cu_2O as the dominant phase, as confirmed by the Cu and O distributions in the EDS maps and line analysis in Figure 6-10a–d. The oxide layer appears thinner in Cu–2Ag, while in pure Cu, the layer shows thicker oxide scale with localized variations in thickness. This suggests that the presence of Ag influences oxidation kinetics even at lower temperatures, possibly affecting nucleation and growth mechanisms of the oxide scale. The line scans (Figure 6-10) confirm that the oxide is primarily Cu_2O, with no significant CuO detected at this stage.

At 500°C, the oxide layer thickens in both materials, and differences in morphology become more apparent. The oxide scale still grows unevenly, displaying localized roughness. In Cu–2Ag, the oxide layer remains more compact and continuous. The EDS analysis reveals that Ag is not homogeneously distributed but rather localized near the oxide-metal interface, suggesting possible Ag segregation or limited solubility in the oxide layer.

At 600°C, the oxide layer continues to thicken, with significant microstructural differences observed between Cu and Cu–2Ag. The oxidation front advances deeper in pure Cu, leading to a more porous and irregular oxide structure. In Cu–2Ag, the oxide scale is still more compact, and the Ag distribution in the EDS maps suggests that Ag remains near the interface rather than diffusing into the oxide layer. The EDS line scans confirm that Cu_2O remains the primary oxide phase, though an increase in CuO formation is possible at the outermost layer, as reported in previous studies at this temperature range [66,169].

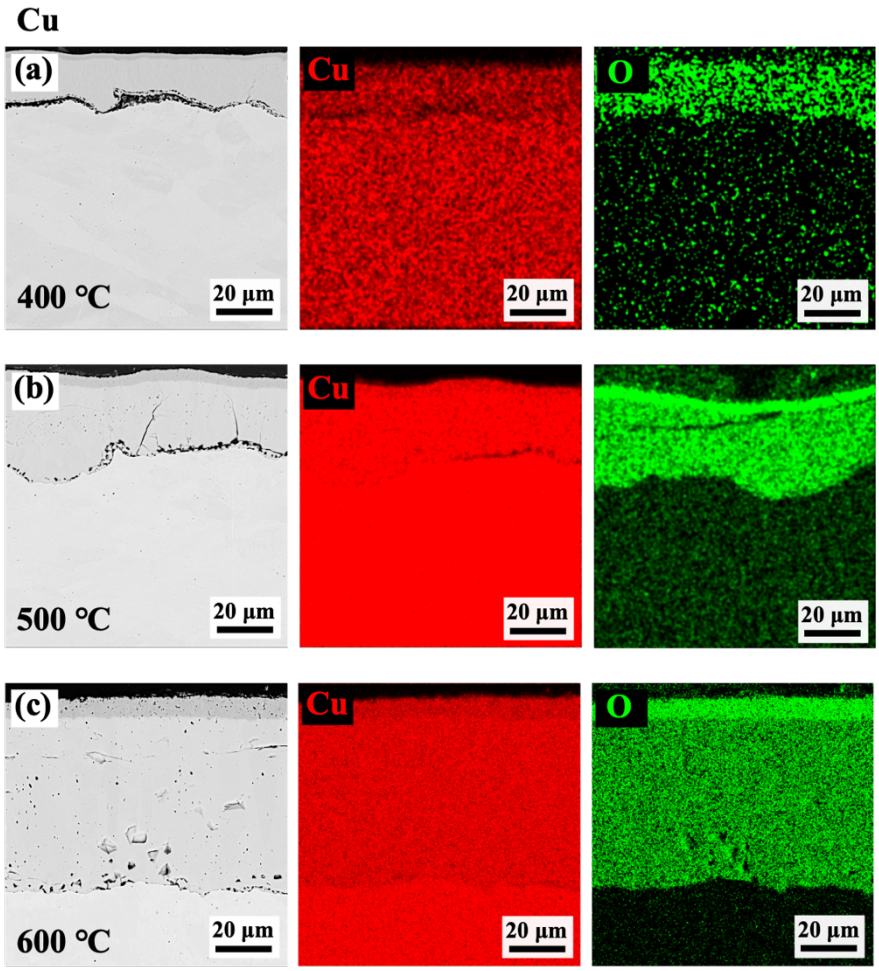


Figure 6-8 SEM images and corresponding EDS maps showing the elemental distribution of Cu and O in oxidized Cu at different temperatures of (a) 400 °C, (b) 500 °C, and (c) 600 °C. The oxide layer thickens with increasing temperature, and the EDS maps confirm the formation of an oxygen-rich scale at the surface.

The differences in oxidation behavior between Cu and Cu–2Ag at these temperatures are consistent with the previously discussed oxidation kinetics. The lower oxidation rate constant (k_p) in Cu–2Ag suggests that Ag plays a role in modifying diffusion pathways or enhancing the stability of the oxide layer, ultimately leading to a more protective scale that slows further oxidation. This effect is clearly evident in the oxide layer thickness observed in Figure 6-9 for Cu–2Ag. At all temperatures, the oxide layer in Cu–2Ag is consistently thinner compared to that of Cu (Figure 6-8), indicating a slower oxidation rate. This directly supports the beneficial role of Ag in improving the oxidation resistance of Cu by reducing the rate of oxide growth and enhancing the protective nature of the formed scale.

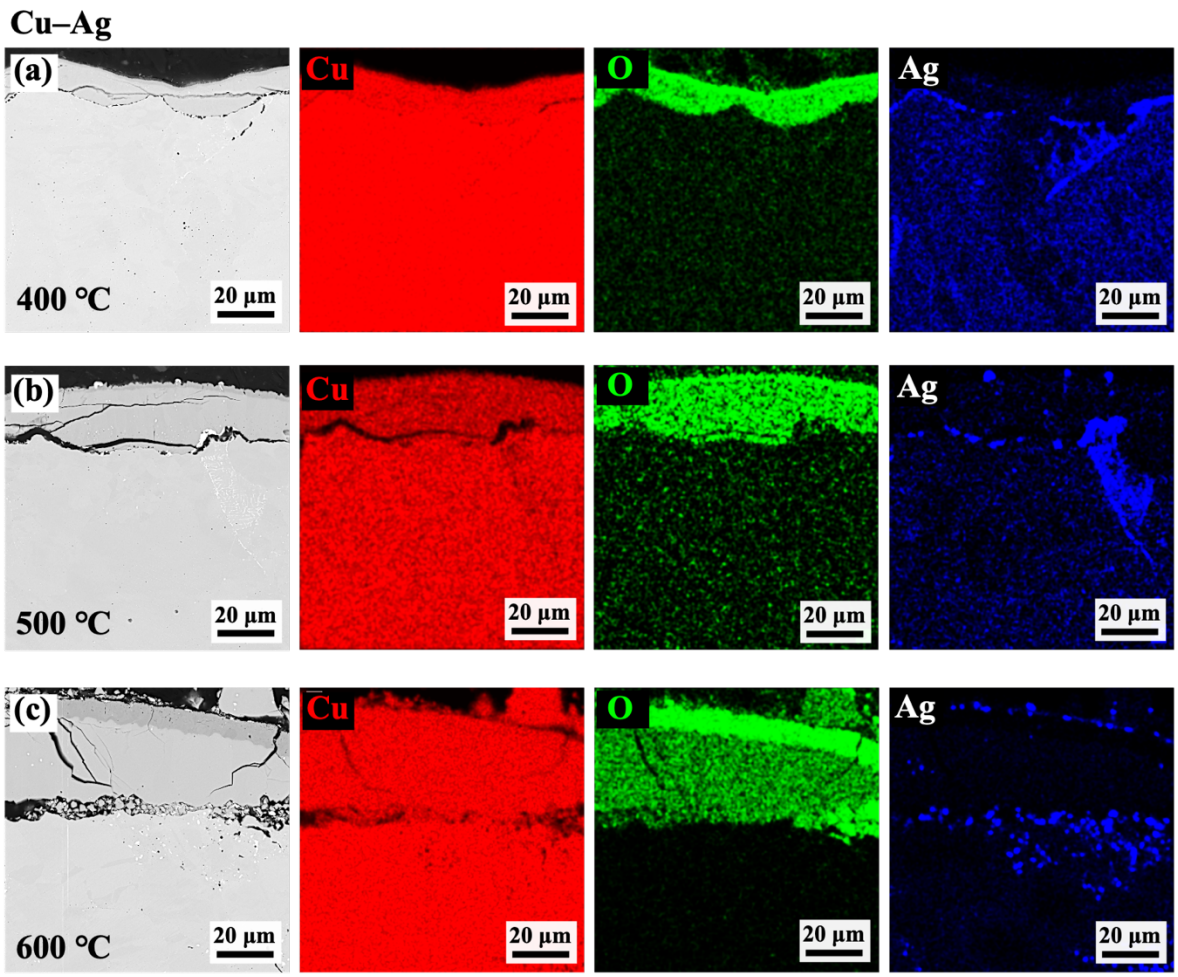


Figure 6-9 SEM images and EDS maps showing the elemental distribution of Cu, O, and Ag in oxidized Cu–2Ag at (a) 400 °C, (b) 500 °C, and (c) 600 °C. The oxide layers in Cu–2Ag exhibit a different morphology compared to pure Cu, with Ag distribution observed at the oxide/substrate interface, suggesting a potential influence on oxide scale stability.

In Figure 6-10, the differences in oxide layer thickness between Cu and Cu–2Ag at various temperatures are more clearly defined. At 400 °C, the Cu_2O layer in pure Cu measures ~20 µm (Figure 6-10a), while in Cu–2Ag (Figure 6-10c), it is slightly thinner at ~16 µm, indicating a slower oxidation rate. A notable observation is the segregation of Ag at the interface between the base alloy and the oxide layer, suggesting that Ag does not significantly dissolve into the oxide but rather accumulates at this boundary. In both materials, the outermost oxide layer appears to be CuO, as indicated by the EDS line analysis, though its thickness remains minimal at this stage.

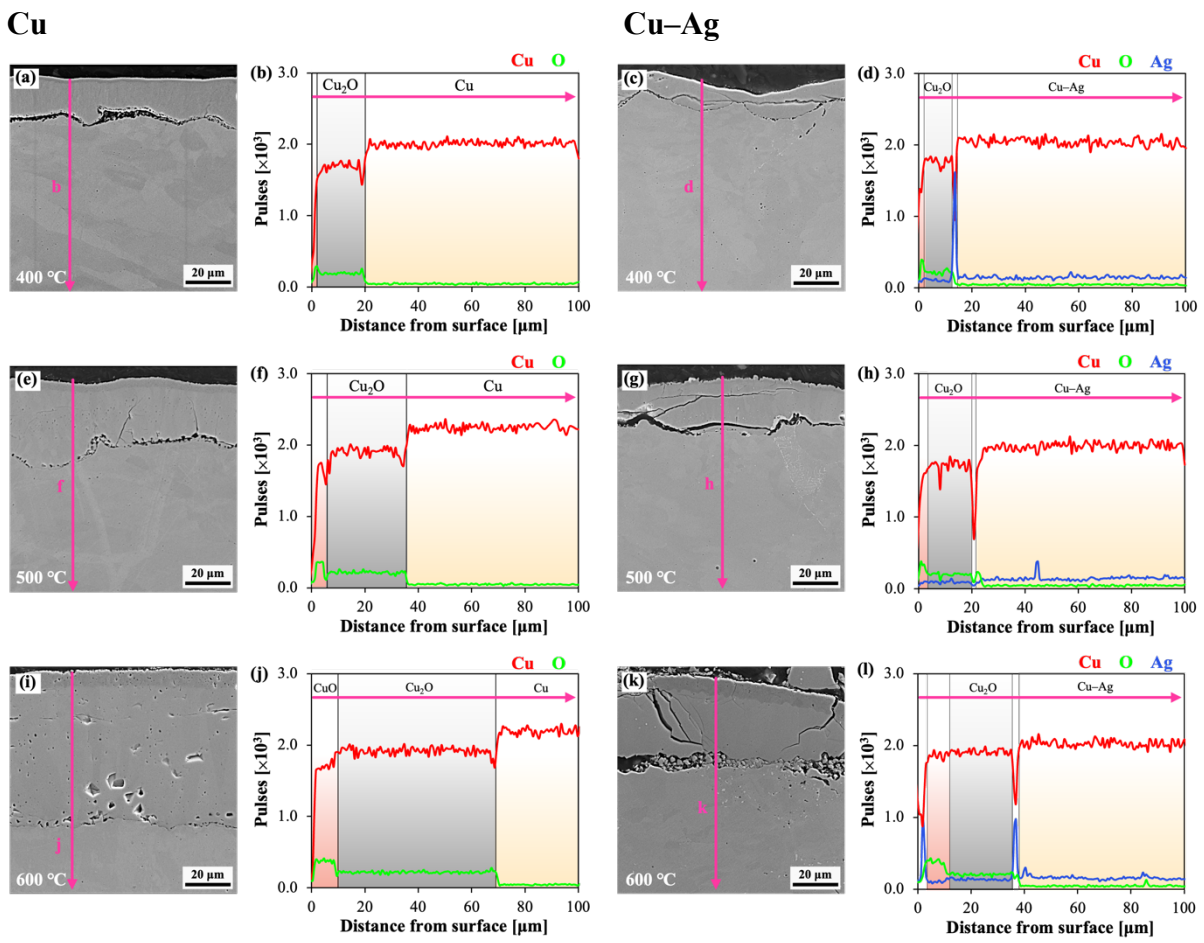


Figure 6-10 EDS line analysis of the oxide layers in Cu and Cu–2Ag at 400 °C, 500 °C, and 600 °C. The Cu and O profiles confirm the oxide layer composition, with Cu_2O as the primary oxide phase in both materials. In Cu–2Ag, Ag is detected near the oxide-metal interface, indicating possible segregation or phase separation during oxidation.

At 500 °C, the Cu_2O layer continues to grow, reaching ~30 µm in pure Cu (Figure 6-10e) and ~20 µm in Cu–2Ag (Figure 6-10g). The CuO layer also becomes more pronounced, particularly in pure Cu, where its presence is more apparent compared to Cu–2Ag. The segregation of Ag at the oxide-metal interface persists, further supporting its limited solubility in the oxide and its potential role in modifying oxidation behavior.

At 600 °C, oxidation advances significantly, with the Cu_2O layer thickening to ~60 µm in pure Cu (Figure 6-10i) and ~30 µm in Cu–2Ag (Figure 6-10k). The CuO layer also expands, measuring ~10 µm in Cu and ~7 µm in Cu–2Ag. The continued presence of Ag at the interface suggests that it influences oxidation kinetics by acting as a diffusion barrier or modifying oxide adhesion.

Interestingly, Ag is also detected at the outermost surface of the samples, raising questions about its migration behavior.

One possible explanation is that at elevated temperatures, Ag atoms diffuse through the oxide layer and accumulate at the surface due to their lower affinity for oxidation. This phenomenon could be driven by differences in oxidation potential, vacancy diffusion mechanisms, or the tendency of Ag to segregate at free surfaces rather than incorporating into the Cu_2O matrix. Further microstructural analysis, such as high-resolution TEM or XPS, would be necessary to fully understand the role of Ag in oxide scale formation and its redistribution during oxidation.

At 700 °C and 800 °C, the oxidation behavior of Cu exhibits a significant increase in oxide thickness. As shown in Figure 6-11, the Cu_2O layer becomes notably thicker, measuring ~150 μm at 700 °C (Figure 6-11a) and further increasing to ~350 μm at 800 °C (Figure 6-11e). This substantial growth reflects the fully diffusion-controlled oxidation mechanism, where Cu ions migrate outward through the Cu_2O layer while oxygen diffuses inward. The EDS line analysis further confirms this, revealing a well-defined Cu-rich and O-rich region corresponding to the Cu_2O scale, with a continuous and uniform distribution across the surface (Figure 6-11b and f).

The presence of CuO at these elevated temperatures is more likely; however, it remains a minor component, forming primarily at the outermost surface where oxygen availability is higher. The thickness of CuO is measured at ~10 μm at both 700 °C (Figure 6-11c) and 800 °C (Figure 6-11g), indicating that while its formation is thermodynamically favored at these temperatures, its growth is still limited compared to Cu_2O. This suggests that the oxidation process is predominantly governed by Cu_2O growth rather than extensive CuO formation.

The transition from grain boundary diffusion (dominant at lower temperatures) to lattice diffusion aligns with the activation energy trends observed earlier. At these temperatures, Cu oxidation is fully controlled by the diffusion of Cu ions through the Cu_2O scale rather than along grain boundaries, which was the primary pathway at lower temperatures. This shift in oxidation mechanism explains the significant increase in oxide thickness observed at 700 °C and 800 °C. Additionally, the high oxidation rate at these temperatures results in a more continuous and adherent Cu_2O layer, further reinforcing the transition to diffusion-controlled oxidation.

Cu

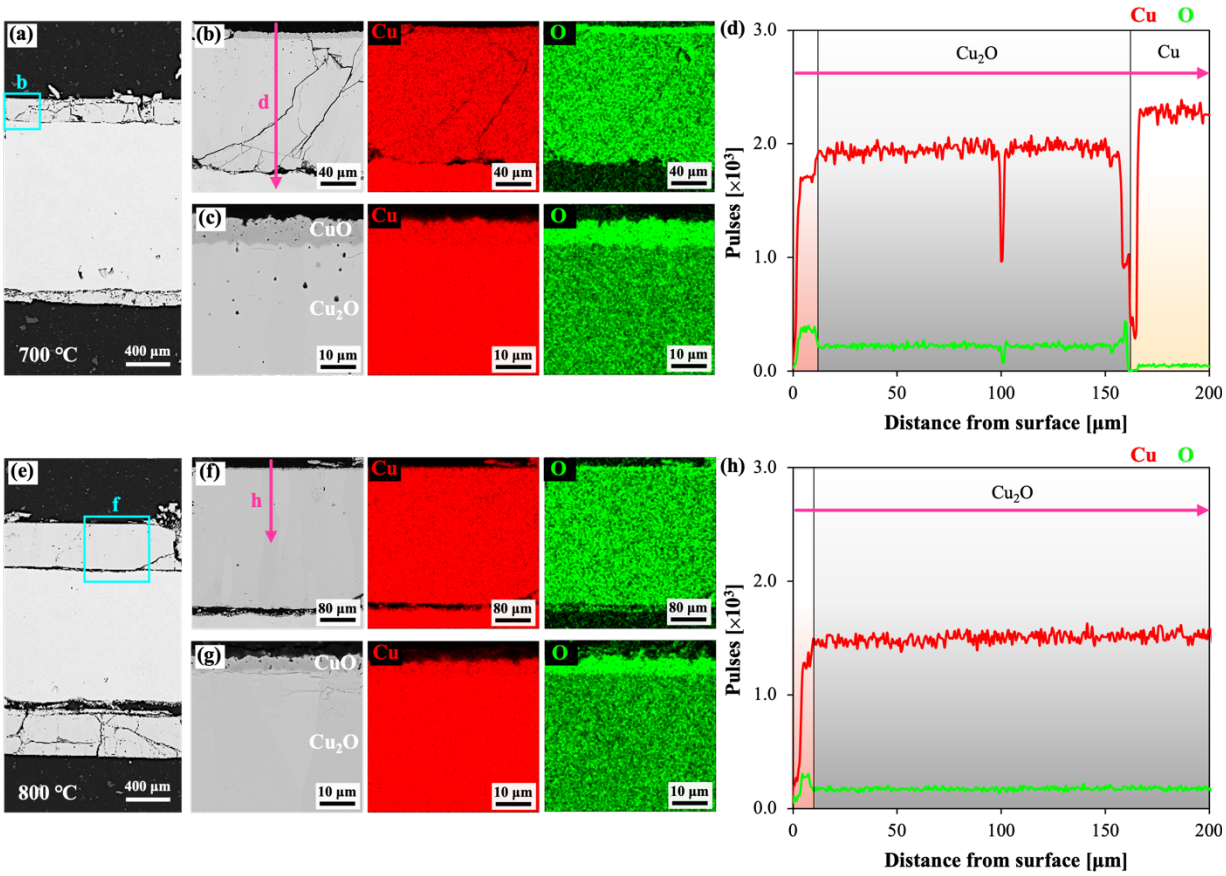


Figure 6-11 SEM images and corresponding EDS maps and line analysis showing the elemental distribution of Cu and O in Cu oxidized at (a–d) 700 °C and (e–h) 800 °C. At higher temperatures, the oxide layer continues to grow, and Cu2O remains the dominant phase.

The EBSD results presented in Figures Figure 6-12 and Figure 6-13 provide insight into the microstructural evolution of the oxide layers formed on Cu and Cu–Ag at different oxidation temperatures. In both materials, Cu_2O is the primary oxide phase, and its grain morphology is influenced by temperature and the presence of Ag.

For pure Cu (Figure 6-12), the oxide layer shows an increasing grain size with temperature, indicative of grain growth due to the enhanced mobility of Cu ions at higher temperatures. At 400 °C (Figure 6-12a) and 500 °C (Figure 6-12b), the grains within the oxide layer remain relatively small and display an elongated morphology along the growth direction, suggesting columnar grain formation driven by oxidation kinetics. As the temperature increases to 600 °C (Figure 6-12c), 700 °C (Figure 6-12d), and 800 °C (Figure 6-12e), the oxide grains become significantly coarser, reflecting the transition to a diffusion-controlled oxidation regime.

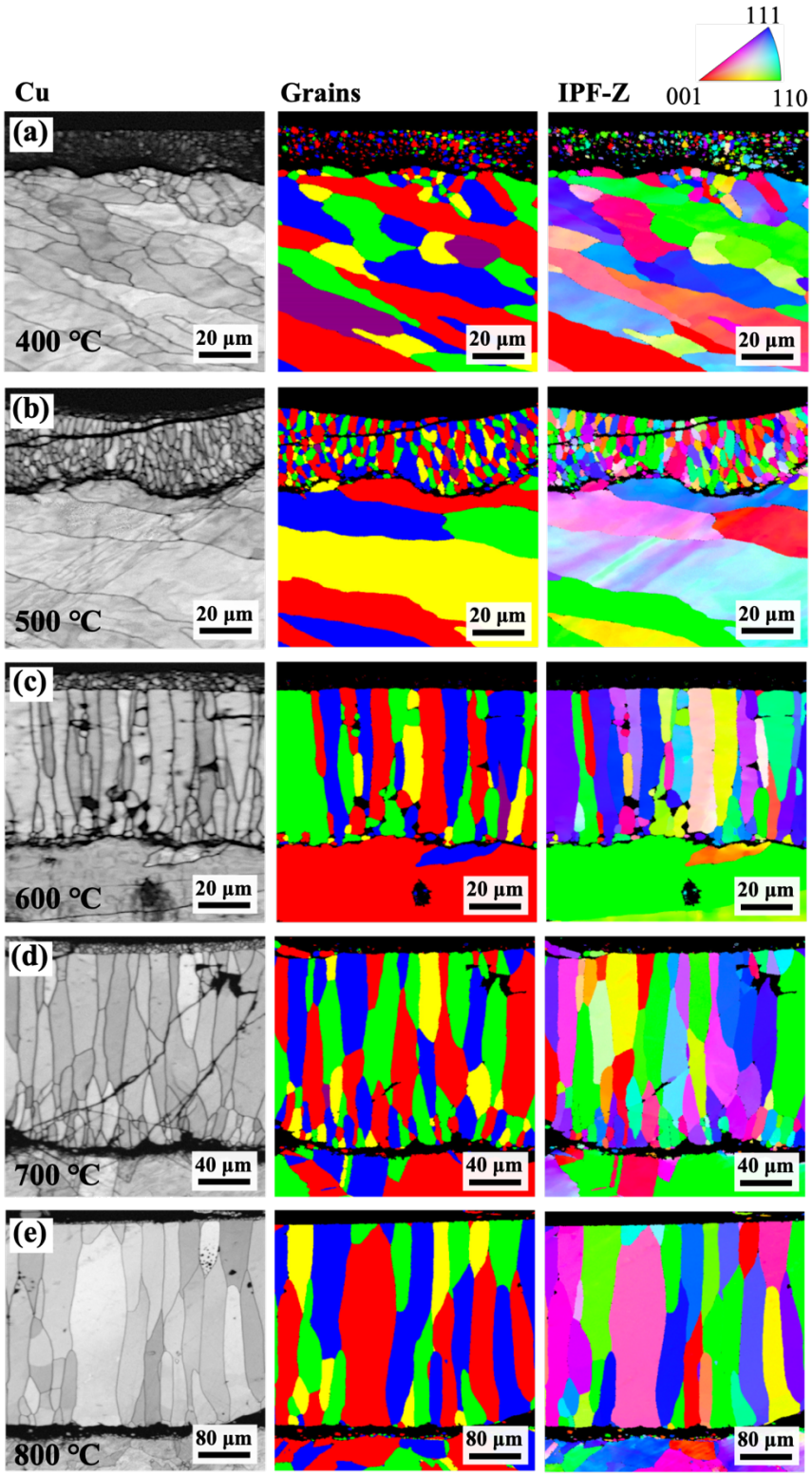


Figure 6-12 EBSD results of pure Cu oxidized in air at different temperatures, showing the oxide microstructure at (a) 400 °C, (b) 500 °C, (c) 600 °C, (d) 700 °C, and (e) 800 °C.

The EBSD inverse pole figure (IPF) maps indicate that the Cu_2O grains do not exhibit a strong preferential growth direction across all temperatures, suggesting a mostly random grain orientation. However, at higher temperatures, grain coarsening leads to a more discontinuous grain structure near the oxide-metal interface.

For Cu–Ag (Figure 6-13), the oxide layer exhibits a finer microstructure compared to pure Cu, which is particularly evident at lower temperatures (400 °C and 500 °C). The presence of Ag influences grain boundary mobility and diffusion kinetics, leading to smaller oxide grains. This refinement effect may contribute to improved oxidation resistance by modifying the diffusion pathways for Cu ions and oxygen. Additionally, the grain structure in Cu–Ag remains more homogeneous across the oxide layer, suggesting a more stable growth process compared to pure Cu. At 600 °C (Figure 6-13c), the oxide grains start coarsening, but the refinement effect of Ag is still visible, with grains remaining relatively smaller than in pure Cu.

At lower temperatures, the outer CuO layer is not detectable using the EBSD technique employed in this study, likely due to the small grain size of CuO. However, at higher temperatures, where CuO formation is more pronounced, its microstructural evolution could be further investigated using higher-resolution techniques. The elongated grain morphology observed in Cu_2O throughout the oxide thickness in both materials is a valuable observation, as it suggests a strong influence of oxidation kinetics and diffusion-driven growth along the oxide scale. The key distinction between the oxidation behavior of Cu and Cu–Ag, as observed in the EBSD results, is the grain refinement effect of Ag, which influences the stability and growth of the oxide scale.

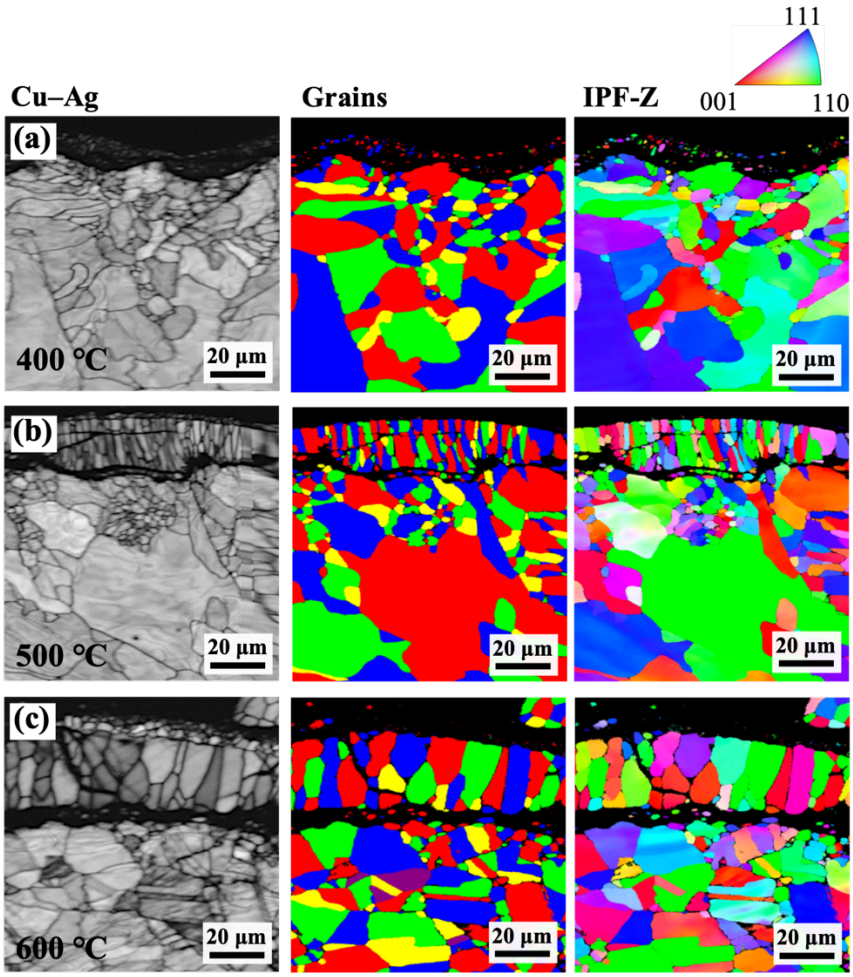


Figure 6-13 EBSD results of Cu–Ag oxidized in air at different temperatures, showing the oxide microstructure at (a) 400 °C, (b) 500 °C, and (c) 600 °C.

6.5. Summary

The high-temperature oxidation behavior of thin-walled Cu and Cu–2 wt.% Ag samples manufactured via LPBF was investigated over a temperature range of 300°C to 800°C. The oxidation kinetics were analyzed through TGA, revealing a transition from sub-parabolic to parabolic behavior as temperature increased. At lower temperatures (300 °C–600 °C), Cu–2Ag initially oxidized more rapidly than pure Cu, but its oxidation rate decreased significantly over time, leading to lower total mass gain. At higher temperatures (700 °C–800 °C), Cu–2Ag demonstrated superior oxidation resistance from the outset, exhibiting a more stable oxide scale. Activation energy (E_a) calculations confirmed two distinct oxidation regimes: grain boundary diffusion-controlled oxidation at 300 °C–500 °C and lattice diffusion-controlled oxidation at 500 °C–800 °C, with Cu–2Ag showing slightly higher activation energy in both regimes.

Microstructural analysis via SEM, EDS, and EBSD revealed that the oxide layer in Cu–2Ag was thinner and more compact than in pure Cu, suggesting that Ag influenced oxide scale morphology and stability. EBSD maps showed that Cu_2O grains were smaller and more refined in Cu–2Ag, potentially contributing to enhanced oxidation resistance. These findings demonstrate that Ag addition alters oxidation kinetics and oxide scale formation in LPBF-processed Cu, offering a pathway for improving the high-temperature durability of Cu-based components while maintaining electrical and thermal performance.

Chapter 7. Oxidation behavior of Cu–Ag alloy in-situ manufactured via laser powder bed fusion[3]

7.1. Overview

The oxidation behavior of copper-silver (Cu–Ag) alloy with the structure of triply periodic minimal surfaces (TPMS) processed by laser powder bed fusion (LPBF) was investigated at 300 °C and 600 °C. The lightweight TPMSs increase surface area, boosting measurement sensitivity in oxidation studies. The presence of silver enhances oxidation resistance of Cu–Ag alloy compared to that of pure copper by slowing down the oxidation process and thinning the oxide layer. This suggests that silver in the alloy potentially suppresses the outward diffusion of copper from the substrate to the oxide layer. This effect is evident in the oxidation rate curves, where the introduction of silver changes the oxidation kinetics from a linear rate in Cu to a parabolic rate in Cu–2 wt.% Ag at 300 °C. Moreover, at 600 °C, silver induces a slower parabolic rate in Cu–2 wt.% Ag compared to Cu.

7.2. Introduction

Copper (Cu) and its alloys have long been the focus of attention owing to their distinctive properties, including thermal and electrical conductivity, ease of fabrication, and resistance to corrosion [3]. These properties are essential across diverse sectors such as automotive, aerospace, electrical power, electronics, and nuclear waste management [104,179,180]. In numerous instances, Cu finds application in high-temperature environments, where corrosion and oxidation emerge as major concerns that negatively impact its efficacy. As temperature rises, the rate of oxidation accelerates, which reduces the material's durability and poses significant challenges.

Oxidation of pure Cu usually leads to the formation of nonconductive oxide films on its surface. The oxide films can severely degrade its electrical conductivity and radio frequency (RF) properties. The oxidation process in copper typically initiates at grain boundaries and dislocation sites with higher energy levels [65]. Therefore, to produce Cu parts that are both electrically

[3] Published in *Additive Manufacturing Letters, 2024*.

conductive and highly oxidation-resistant, it is crucial to engineer the microstructure to effectively retard oxidation at defects while minimizing the scattering effect of conducting electrons.

Enhancing the oxidation resistance of Cu by alloying often results in a dramatic decrease in electrical conductivity [65]. Hence, achieving a balance between conductivity and oxidation resistance becomes essential when designing the microstructure for use in oxidizing environments. Among the alloying elements, silver (Ag) shines as a promising option, offering minimal interference with conductivity while providing notable enhancement in the oxidation resistance of copper [67,68].

To date, numerous studies have been conducted on the conventionally manufactured Cu–Ag alloys with different Ag contents ranging from 0.1 to 24 wt.% [58,60–63,159]. Ag contents within the range of 0.1–5 wt.% tend to result in higher electrical conductivity [56,57,63,64,159], rendering the alloy more efficient and cost-effective for several applications. This includes energy savings in electrical applications and reduced downtime and maintenance in industrial settings. Environmentally, Cu–Ag alloys can also help minimize waste and resource consumption by reducing the need for frequent replacements.

Despite the potential of Cu–Ag alloys in different industrial sectors, there is a limited literature available on their oxidation behavior, especially concerning applications in oxidizing environments. Li et al. [64] examined the oxidation behavior of pre-alloyed Cu–5 wt.% Ag powder at 250 °C. Their findings show that the oxidation rate of Cu–5 wt.% Ag powder is initially very slow, whereas the oxidation rate of Cu powder accelerates more rapidly from the beginning. Additionally, as oxidation time increases, Cu–5 wt.% Ag powder exhibits minimal reduction in electrical conductivity [64]. Therefore, enhanced oxidation resistance of Cu–Ag alloys makes them suitable for diverse electrical applications such as electrical contacts, radar components, connectors, and high-temperature environments. However, the complex components composed of such the alloys often necessitate extensive and expensive manufacturing processes with conventional methods.

Additive manufacturing (AM), particularly LPBF, empowers the creation of complex designs, such as topology optimized lattice structures, offering possibilities beyond conventional manufacturing [1,69]. These lattice structures enable performance in applications such as heat exchangers, cooling fins, and thermal management systems in electronics and automotive

industries. Among lattice designs, TPMS are commonly employed in LPBF to craft lightweight, high-strength structures that boast a high surface-area-to-volume ratio crucial for efficient convective heat transfer [181,182]. In addition to these advancements, understanding the oxidation behavior of the materials processed by LPBF is critical. Recent studies have shown that the distinctive microstructures resulting from LPBF can significantly influence the oxidation resistance of the materials [170,183]. For instance, LPBF-manufactured Inconel 625 showed up to 30% faster oxidation kinetics compared to its conventionally manufactured counterpart when exposed to air at high temperatures [183].

This study aims to investigate the oxidation behavior of Cu and Cu–2 wt.% Ag with TPMS structure processed via LPBF, addressing the lack of knowledge regarding the oxidation behavior of these alloys. Incorporating lightweight TPMS structures adds dimensions to this research, as this innovative approach allows oxidation testing on lightweight samples possessing the same dimensions but featuring a larger surface area and reduced material usage. The following section provides detailed information on the materials and methods used for processing and testing these samples.

7.3. Materials and methods

Due to the absence of pre-alloyed Cu–Ag powder in the market, and recognizing the potential value of in-situ alloying of Cu–Ag alloy through LPBF, elemental gas-atomized powders of pure copper (CP Cu with purity higher than 99.95%) and pure silver (99.9% Ag) were utilized as the initial materials to print both pure Cu and Cu–2 wt.% Ag alloy coupons, aiming to yield intriguing results beneficial to both academia and industry. The particle size distribution (PSD) of Cu, sourced from AP&C, is characterized by D_{10}, D_{50}, and D_{90} values of 15.5 μm, 37.8 μm, and 63.5 μm, respectively. For Ag, supplied from Thermo Fisher, D_{10}, D_{50}, and D_{90} values are 13.1 μm, 20.7 μm, and 31.1 μm, respectively. The preparation of the powder blend for Cu–2 wt.% Ag involved mixing the elemental powders thoroughly in a tumbler mixer for a duration of 20 hours.

TPMS specimens of pure Cu and Cu–Ag were successfully 3D printed using an EOS M290 LPBF machine, which is equipped with a 1kW Ytterbium continuous fiber laser operating at a wavelength of 1060 nm and possessing a spot diameter of ~80 μm. Throughout the manufacturing process, a high purity Ar atmosphere was maintained in the process chamber, ensuring an oxygen concentration of less than 0.1%. Optimized process parameters include volume energy density

(VED) of ~130 (J/mm^3), layer thickness of 40 μm, and scanning strategy of stripe with 67º rotation in each layer. Figure 7-1a presents the computer-aided design (CAD) model alongside the printed samples intended for oxidation testing. The TPMS sample dimensions are 10 mm × 10 mm × 10 mm, resulting in a total surface area of 1296.69 mm², which is ~2.16 times larger than that of a solid cube with identical dimensions. The surface area of TPMS structure was calculated using nTop software, which employs mesh analysis to measure the complex surface geometry. This increased surface area is due to the intricate and porous nature of the TPMS lattice structure, which significantly adds to the overall surface area compared to a solid cube.

The quality of the printed samples, including relative density of higher than 99% and surface roughness of lower than 15 μm, was optimized according to requirements of an industrial application of Cu–Ag alloy. X-Ray computed tomography (CT) was conducted using a ZEISS Xradia 520 Versa to identify defect distribution in the printed parts. The resulting 3D images were generated using a beam hardening constant of 0.05 and analyzed using Dragonfly 3.1 software. Surface roughness was quantified using Keyence VK-X250 confocal microscopy equipped with non-contact laser profilometry.

To investigate the effect of Ag addition on the high temperature oxidation behavior of Cu, oxidation tests were conducted on the as-printed TPMS Cu and Cu–Ag coupons at temperatures of 300 °C and 600 °C for a duration of 30 hours. The selection of 300 °C and 600 °C for the oxidation tests is based on the distinct oxidation mechanisms observed at these temperatures for copper and its alloys [169]. Understanding these mechanisms is crucial for evaluating the performance of Cu–Ag alloys in their intended applications.

Prior to testing, the as-printed samples were cleaned using ultrasonic cleaning with anhydrous ethanol (water content <0.5%). This involved immersing the samples in ethanol and subjecting them to ultrasonic vibration for 20 minutes, repeated twice to remove any contaminants, loose powders and partially melted powder particles at the surface. A Whip Max Pro 100 Series Porcelain furnace was employed for these tests, and the mass gain of the samples was recorded every three hours. The furnace was initially evacuated to remove any potential impurities to achieve effective control over the testing environment. Then, a controlled flow of air with a specific composition of 19.5–23.5% O_2, 2.0 ppm H_2O, 0.5 ppm CO_2, 0.5 ppm CO, 0.1 ppm THC, and N_2 was introduced

to maintain a consistent atmospheric composition throughout the tests. Each experimental condition was replicated three times to ensure reliable and consistent results.

To determine the oxidation rate of the samples, the average value together with standard deviation of the data were plotted in terms of time. Linear and parabolic regression models were then applied to analyze the relationship between mass change and time.

After oxidation, the cross-sections of the oxidized samples underwent preparation for microstructural observation. The samples were initially ground using SiC papers ranging from 80 to 2500 grit sizes, followed by polishing with MD-Nap 1 μm abrasive. Subsequently, they were repolished using a Buehler VibroMet2 machine in non-crystallizing amorphous 0.02 μm Colloidal Silica suspension for 5 hours. Microstructural analysis using scanning electron microscopy (SEM), energy-dispersive X-ray spectroscopy (EDS), and electron backscatter diffraction (EBSD) was conducted by a TESCAN VEGA3 machine outfitted with a BRUKER detector. With the materials and methods thoroughly outlined, the next section presents the experimental results and discusses their implications.

7.4. Results and discussion

The results obtained from CT scans (Figure 7-1b and d) and laser profilometry measurements (Figure 7-1c and e) indicate that the relative densities of pure Cu and Cu–Ag samples are 99.06% and 99.48%, respectively with areal average surface roughness values (S_a) of 10.19 ± 1.71 μm and 11.41 ± 1.09 μm. According to the CT results, the pores within the samples are mainly concentrated within the infill regions, while areas near the surface exhibit high density. This means absence of any open pores close to the surface, which is favorable for oxidation testing. In addition, the surface roughness values fall within the specified range (lower than 15 μm), aligning with the requirements for the intended application of this alloy. It is important to note that surface roughness can influence oxidation [184]. However, both materials in this study exhibit nearly identical roughness qualities, ensuring a fair comparison of oxidation resistance of Cu and Cu–Ag.

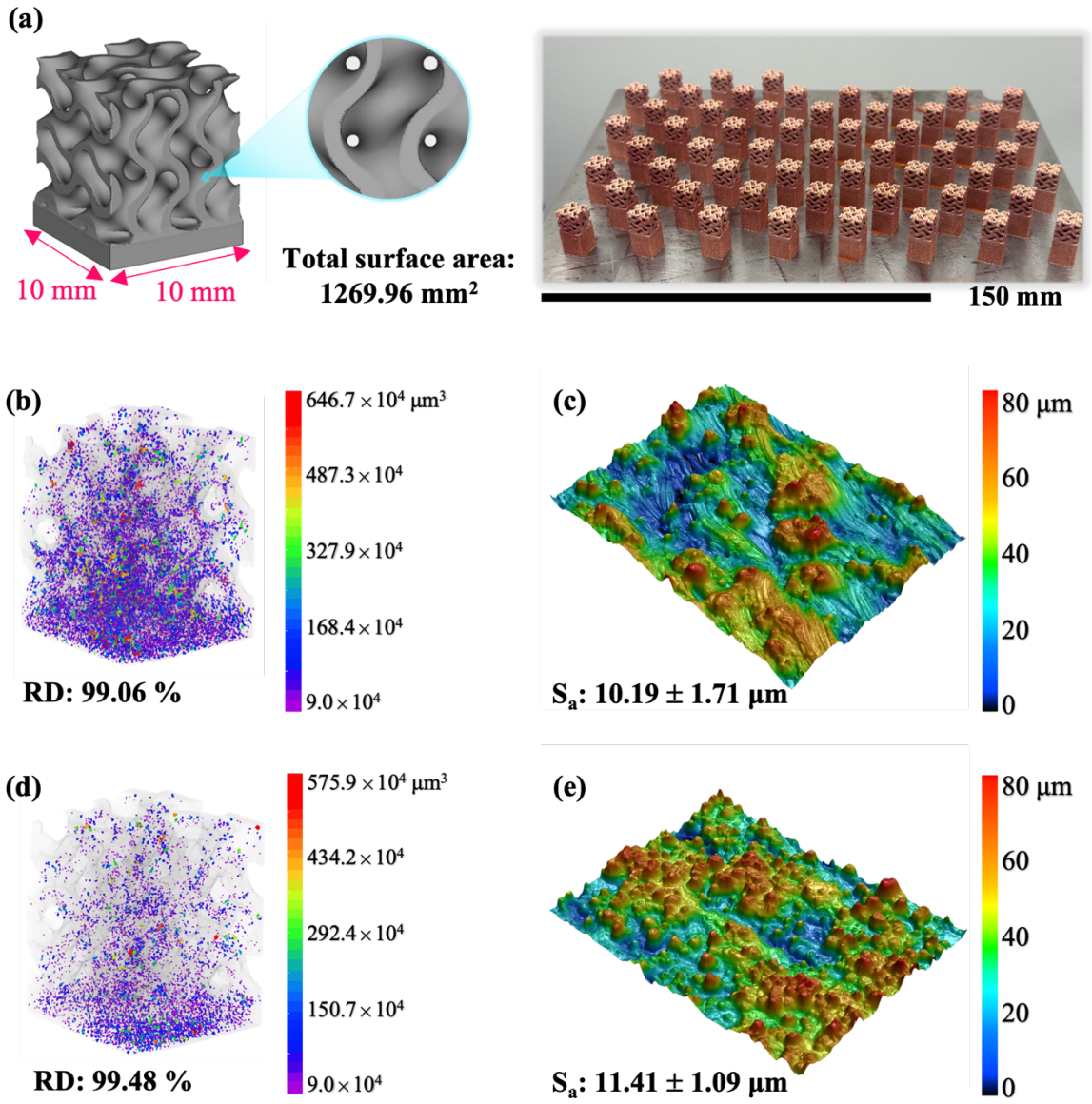


Figure 7-1 (a) CAD model of designed TPMS structure alongside with the actual printed samples used for oxidation tests, X-Ray CT images showing pores distribution in (b) Cu and (d) Cu–Ag samples, and 3D view of surface profile measurements of (c) Cu and (e) Cu–Ag, illustrating the surface roughness values.

Figure 7-2 shows SEM micrograph and EDS maps of as-printed Cu–Ag, providing insights into the distribution of Cu (Figure 7-2b) and Ag (Figure 7-2c) within the alloy. The elemental maps indicate a relatively uniform distribution of silver within the copper matrix. This could imply effective mixing of silver into the copper during the LPBF process. The homogenous distribution of silver can promote improved resistance to oxidation and corrosion of copper, enhancing the overall durability and longevity of the alloy. Moreover, the effective in-situ alloying in the LPBF process can open avenues for tailoring the microstructure and properties of additive manufactured Cu–Ag alloys to meet specific performance requirements in various applications.

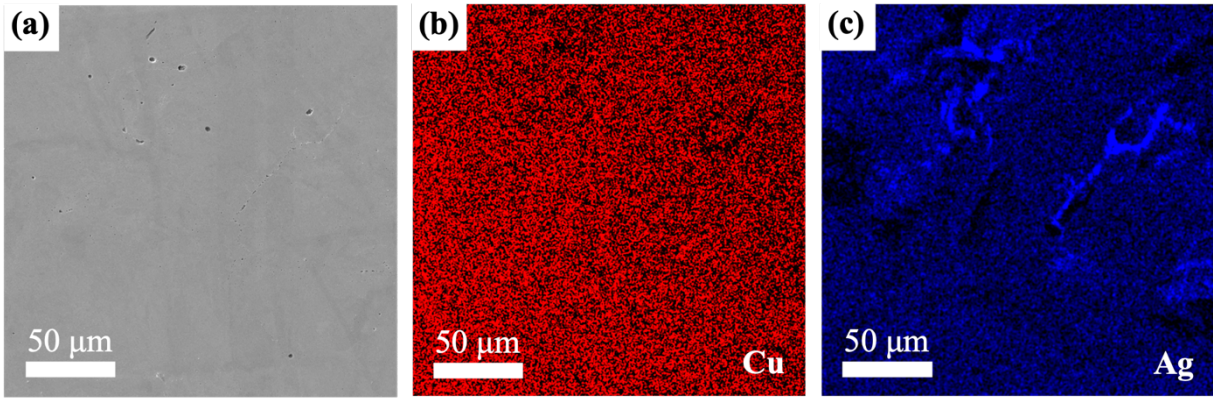


Figure 7-2 (a) SEM micrograph of as-printed Cu–Ag, with corresponding EDS maps showing the distribution of (b) Cu and (c) Ag.

Figure 7-3 indicates inverse pole figure (IPF) maps and pole figures of as-printed Cu and Cu–Ag to further explore the influence of silver on the microstructure of pure copper. The EBSD results show a reduction in grain size upon the addition of silver, with the average grain size decreasing from 39.7 ± 8.1 µm in pure copper to 28.1 ± 5.6 µm in Cu–Ag alloy. Silver can refine grain size by introducing additional heterogeneous nucleation sites during solidification or thermal processing. These extra nucleation sites can lead to grains forming in closer proximity, thereby constraining their growth and impeding the movement of grain boundaries, resulting in a reduced grain size and a finer overall microstructure.

Finer microstructures feature higher fractions of grain boundaries, which can provide more preferred sites for oxidation, especially in metals where grain boundary diffusion dominates [51,185]. This can initially speed up the oxidation process but might also result in a more stable and protective oxide layer. The incorporation of silver into the copper matrix also leads to a shift

towards more random orientation within the alloy, as evidenced in the IPF maps and pole figures. The increased color diversity observed in IPF map of Cu–Ag (Figure 7-3d) indicates a wider distribution of crystallographic orientations, implying a more randomized orientation overall. This shift is further highlighted through examination of the (100) pole figures derived from EBSD data (Figure 7-3c,f), indicating more scattered positioning of (100) planes in Cu–Ag compared to that in pure Cu.

Moreover, quantitative analysis of (100) pole figures reveals a decrease in intensity of preferred orientation from 30 in pure Cu (Figure 7-3c) to 18 in Cu–Ag alloy (Figure 7-3f). The reduction in intensity signifies a weakening of preferred orientations or texture in the alloy, indicative of a more random orientation distribution. These results reflect the structural changes induced by the presence of silver, potentially influencing the oxidation kinetics by altering grain boundary characteristics such as exposure of crystallographic planes and grain boundary mobility [186,187].

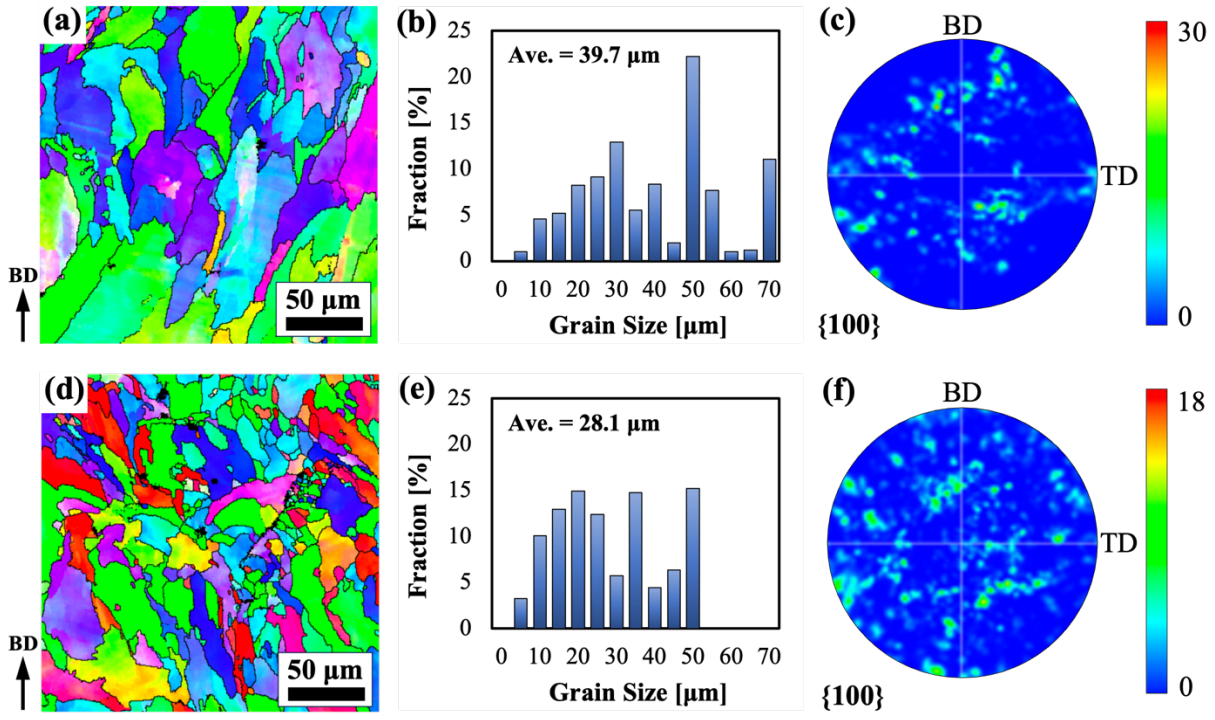


Figure 7-3 EBSD grain maps and corresponding grain size distributions and pole figures of as-printed (a,b,c) Cu and (d,e,f) Cu–Ag, captured from the build direction (BD) cross section. The color bar refers to the intensity of the pole figures.

Mass gain curves during air oxidation tests at 300 °C and 600 °C are plotted in Figure 7-4. A power law was employed to fit the curves using the equation $\Delta m = kt^n$, where Δm represents the mass gain per unit area, k is the oxidation rate constant, t is the exposure time, and n is the rate exponent. At 300 °C (Figure 7-4a), the oxidation kinetics of Cu exhibit nearly linear behavior (n ~1.14). This behavior contrasts with the parabolic oxidation kinetics typically observed for copper in the temperature range of 350 °C to 1050 °C [169].

The parabolic behavior is generally attributed to the initial rapid formation of a continuous oxide scale, after which the oxidation rate decreases as the rate of scale growth is controlled by ion outward diffusion through the oxide. Nevertheless, the thickness of the initial oxide layer is influenced by several factors, such as surface condition, microstructure, and oxygen concentration [188–190]. Rougher surfaces may tend to increase oxide thickness [190]. In this study, the surface finish of samples was characterized by roughness values of 10–12 μm (Figure 7-1c and e). This relatively high surface roughness could lead to a greater surface area and less effective adhesion of oxide layers. This might result in increased exposure to oxidizing agents and potentially affect the oxidation behavior.

Furthermore, factors such as grain size, grain boundaries, and defects influence diffusion and stress development within the material [191]. The rapid solidification and thermal cycling experienced by the samples during the LPBF process create high dislocation density [192]. The high dislocation density in Cu may promote a linear oxidation rate due to several factors [193,194]: (i) Increased diffusion pathways: dislocations provide additional pathways for oxygen and copper ion diffusion, accelerating oxidation and probably leading to linear oxide layer growth. (ii) Enhanced nucleation sites: dislocations increase the number of nucleation sites for oxide formation, resulting in more uniform and rapid initial growth. (iii) Strain energy effects: high dislocation density can introduce strain energy into the material, altering the thermodynamics of oxide formation and favoring faster growth kinetics, probably leading to a linear behavior. This linear behavior is opposed to parabolic behavior of annealed Cu reported in the literature [66,169], suggesting the critical role of the manufacturing method in determining the oxidation resistance of copper.

However, for Cu–Ag, despite undergoing the same processing route as Cu, the oxidation kinetics exhibit parabolic behavior (n ~0.49) at 300 °C (Figure 7-4a). This indicates a slower-than-linear oxidation rate, suggesting that Ag influences the oxidation resistance of the alloy. At the initial stages, it is evident that the oxidation rate of Cu–Ag exceeds that of Cu. However, after approximately 3–4 hours, the oxidation rate of Cu–Ag begins to slow down and follows a parabolic trend, while that of Cu remains linear. This divergence in oxidation resistance highlights the pivotal role of microstructure in oxygen and copper ion diffusion during the oxidation process.

The characteristics and density of grain boundaries can significantly influence the pathways of diffusion, thereby impacting the growth patterns of oxide layers. As indicated by the initial microstructure presented in Figure 7-3, Cu–Ag exhibits a finer grain microstructure compared to Cu. Consequently, Cu–Ag alloy boasts a higher fraction of grain boundaries, which initially facilitates the diffusion of oxygen atoms into the alloy, accelerating the oxidation rate. However, as the oxidation process progresses over time, a protective oxide layer begins to form on the alloy's surface, acting as a barrier and gradually slowing down the oxidation rate of the underlying material.

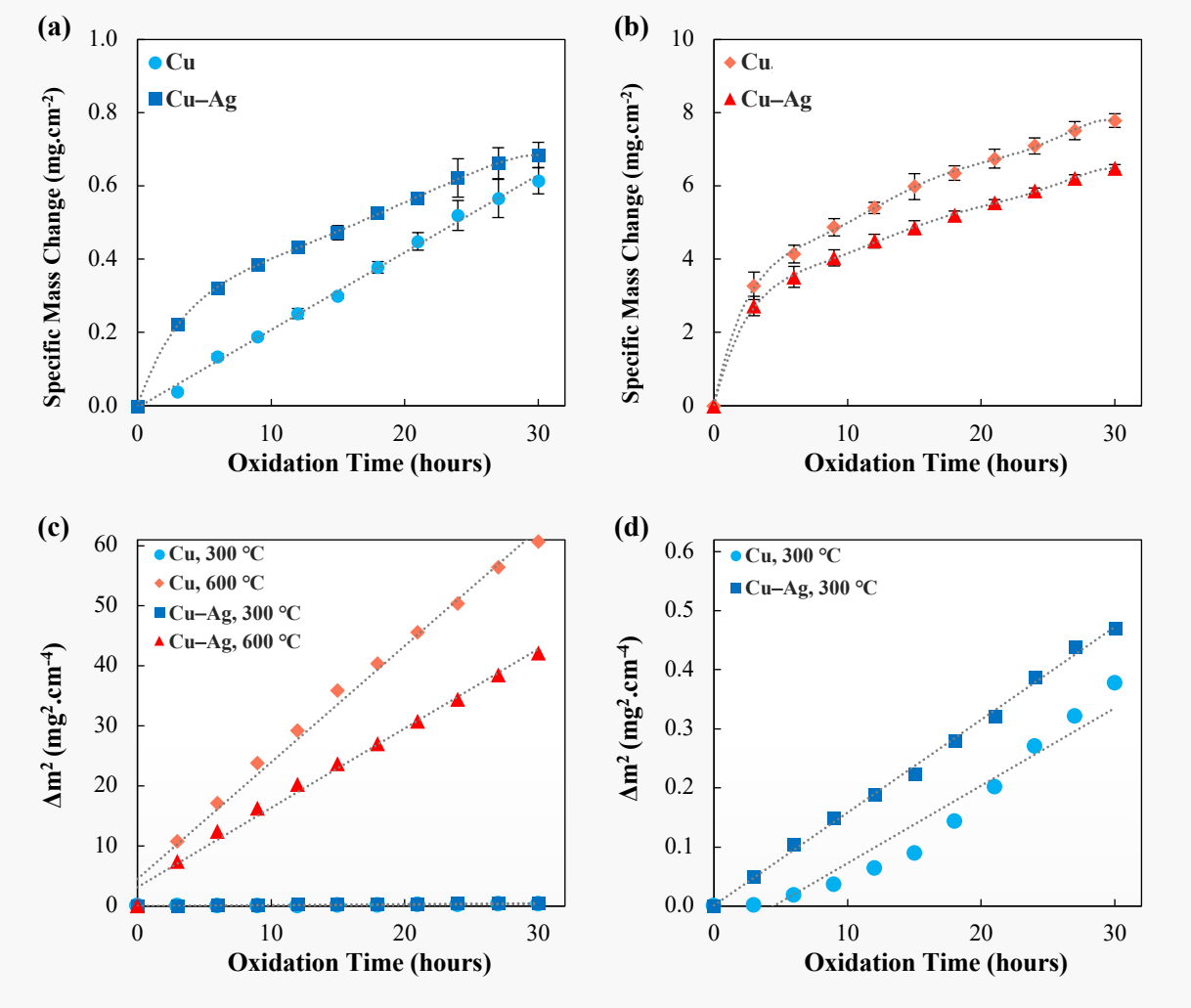


Figure 7-4 Mass change measurement of Cu and Cu–Ag during oxidation in air at temperatures of (a) 300 °C, (b) 600 °C for 30 h, and (c,d) fitted lines of square mass gain.

At 600 °C, the oxidation kinetics for both materials adhere to the parabolic law, with *n* values of ~0.38 and ~0.37 for Cu and Cu–Ag, respectively (Figure 7-4b). The initial rapid increase in mass gain suggests that oxide scales form rapidly during the early stages of exposure. Over time, the oxide scales evolve into a more protective layer, which helps limit the oxidation rate by impeding the diffusion process [66,169]. This protective mechanism slows down the oxidation rate, as evidenced by the decreasing slope of the mass gain curve over time.

Comparison between the parabolic oxidation rate constants (k_p) of both materials (Table 7-1) reveals a notable difference: while k_p for pure Cu is measured as 6×10^{-4} $mg^2.cm^{-4}.s^{-1}$, it decreases to 4×10^{-4} $mg^2.cm^{-4}.s^{-1}$ for Cu–Ag alloy. This decrease in rate constant suggests that the addition of Ag effectively retards the oxidation process of Cu, leading to improved longevity and stability of the material in oxidizing environments. However, it is noteworthy that these values still exceed those reported in the literature for pure Cu [178], emphasizing the critical role of initial microstructure and manufacturing processes.

Table 7-1 The rate exponent (***n*** in $\Delta m = kt^n$) and parabolic oxidation rate constant (**k_p** in $\Delta m^2 = k_p t$) of Cu and Cu–Ag at 300 °C and 600 °C

	300 °C		**600 °C**	
Material	*n*	k_p ($mg^2.cm^{-4}.s^{-1}$)	*n*	k_p ($mg^2.cm^{-4}.s^{-1}$)
Cu	1.14	-	0.38	6×10^{-4}
Cu–Ag	0.49	4×10^{-6}	0.37	4×10^{-4}

Figure 7-5 presents an investigation into the microstructure of Cu and Cu–Ag after 30 hours of air exposure at 300 °C. SEM micrographs and corresponding energy-dispersive X-ray spectroscopy (EDS) analyses show a high oxygen concentration at the top surface of samples, confirming the presence of an oxide layer. Furthermore, line scans (Figure 7-5b and d) conducted along specific regions marked by pink arrows in the SEM images (Figure 7-5a and c) provide insights into the distribution of elements away from the surface, revealing that the oxygen concentration is high at the surface and decreases as it moves deeper into the bulk of the material.

The atomic Cu/O ratios obtained from EDS point analysis implies that the oxide layer likely consists of cuprous oxide (Cu_2O). Other researchers have also reported the predominance of Cu_2O scale formation during copper oxidation within the temperature range of 350 °C–1050 °C [169]. It is noteworthy that the oxide layer in the Cu–Ag (4–5 μm) alloy is thinner than that of pure Cu (8–10 μm), confirming distinct oxygen responses between the two materials (Figure 7-5a and c).

The mechanism of copper oxidation typically involves the formation of cuprous (Cu_2O) and cupric (CuO) oxides layers on the surface of the copper substrate [66,168]. The oxidation process initiates with the absorption of oxygen molecules onto the copper surface, followed by inward diffusion of oxygen atoms into the copper lattice. Subsequently, copper ions are released into the lattice, giving rise to the formation of copper oxide compounds.

Copper primarily forms Cu_2O while Cu–Ag alloys can form mixed oxides such as copper-silver oxide [195,196]. The presence of silver can affect the oxidation process by modifying the diffusion pathways of oxygen atoms. Silver can impede the penetration of oxygen into the copper matrix, probably leading to the formation of a more adherent and continuous oxide layer. This enhanced oxide layer can serve as a more effective barrier, slowing further oxidation of the underlying copper and transitioning the reaction from a linear rate to a parabolic rate at 300 °C as discussed previously (Figure 7-4a).

The variations in oxide formation and behavior can have significant implications for various applications. For instance, in RF components, it is crucial to maintain high electrical conductivity and good oxidation resistance to prevent signal loss and ensure long-term reliability. The enhanced oxidation resistance of Cu–Ag alloys may make them suitable for such applications. In Figure 7-5c, silver is clearly segregated at the interface between the oxide layer and the copper substrate. This segregation could contribute to the formation of a more stable and adhesive oxide layer at 300 °C and reduce the likelihood of oxide layer delamination or spallation.

Additionally, due to the high oxidation resistance of silver, the presence of this elements at the interface may decelerate the diffusion rate of oxygen by changing the inward diffusion pathways of oxygen atoms and obstructing the penetration and reaction of oxygen atoms with the underlying copper. On the other hand, silver atoms may have occupied lattice sites within the copper matrix. This could impede the mobility of both oxygen and copper atoms, which can slow down their migration through the lattice. As a result, the rate at which copper atoms reach the surface to react with oxygen could be reduced.

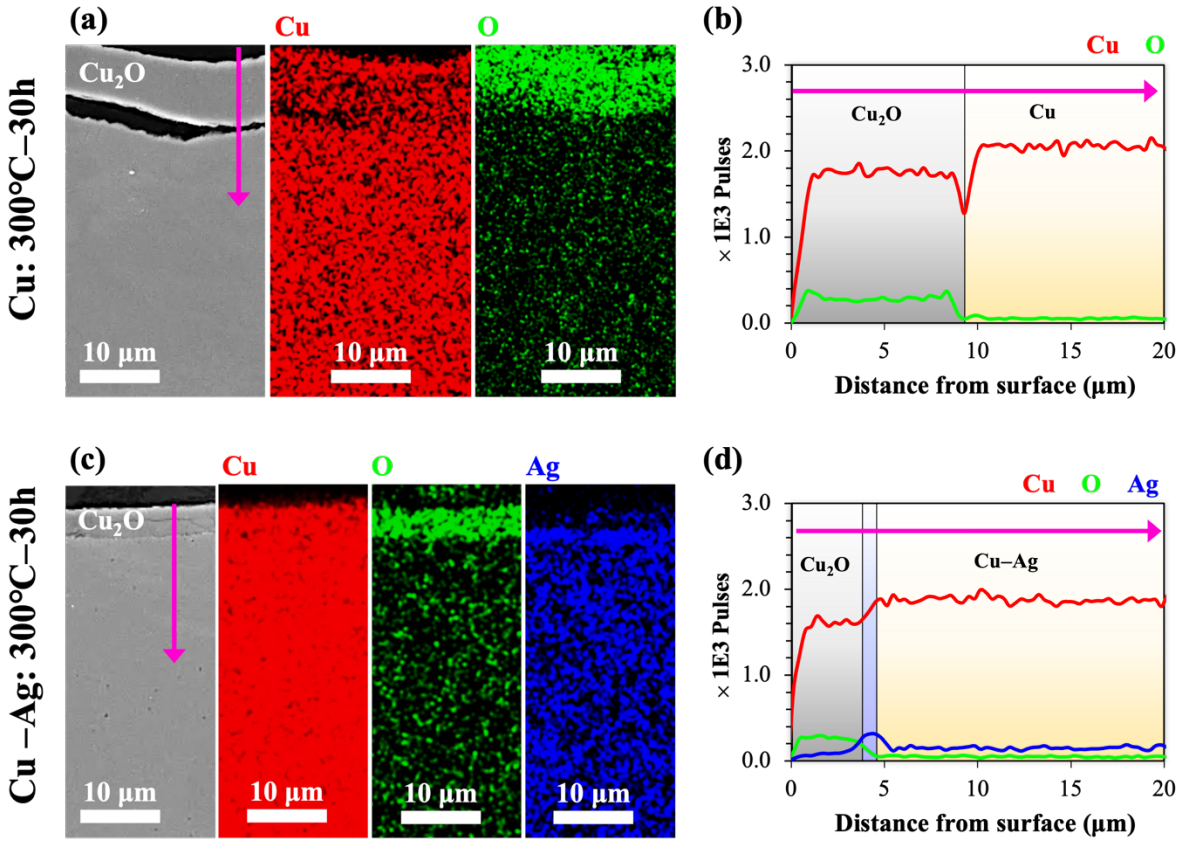


Figure 7-5 SEM micrographs with EDS map analysis for (a) Cu and (c) Cu–Ag oxidation in air at 300 °C after 30 hours, highlighting the oxide layers of Cu_2O. The plots in (b) and (d) correspond to line scans of the pink arrows shown in SEM images (a) and (c), respectively, indicating the element concentration profile away from the surface.

Figure 7-6 shows microstructure of Cu_2O and CuO oxide layers for Cu and Cu–Ag after 30 hours of exposure to air at 600 °C. EDS characterization of the cross-section (Figure 7-6a and b) reveals that the oxide layers in Cu consist of two distinct layers including an inner thicker layer and an outer thinner layer. According to the point analyses shown in Figure 7-6c, the inner layer is Cu_2O, while the outer layer is CuO. A closer examination of the SEM micrograph (Figure 7-6c) shows the presence of a thin layer of nanowires (NW) atop the oxidized Cu layer, which is likely to be CuO [166].

The CuO NWs typically form in the temperature range of 400 °C−700 °C, where the oxide layer on the Cu substrate constitutes a Cu_2O/CuO/CuO NW composite [166,167]. In this temperature range, copper predominantly forms CuO, which is a denser oxide layer compared to Cu_2O formed at lower temperatures. The denser oxide layer can effectively slow further oxidation by acting as

a barrier to oxygen diffusion. As can be seen, the fraction of Cu_2O (thickness of 110−115 μm) seems to be higher than the fraction of CuO (thickness of less than 20 μm). This can suggest that oxidation kinetics of copper at 600 °C are characterized by Cu_2O growth, driven by the outward diffusion of copper atoms, regardless of the manufacturing process.

In the case of Cu–Ag oxidation at 600 °C, the oxide layers exhibit a similar structure to that of pure Cu, comprising two distinct layers (Figure 7-6e and f). However, the outer CuO layer is significantly thinner, measuring less than 3 μm in thickness. Similarly, the inner layer of Cu_2O in Cu–Ag with thickness of 85−90 μm, is also thinner compared to that in pure Cu, proposing an improvement in oxidation resistance of Cu due to the addition of silver.

It is important to note that there is a prominent absence of NWs above the oxide layers in Cu–Ag (Figure 7-6g). This absence could be attributed to the presence of silver, which may interfere with the oxidation process, altering the growth mechanism of the oxide layer and impeding the formation of CuO NWs. The substantial presence of Ag at both the Cu/Cu_2O interface and the uppermost layer of the oxidized surface (Figure 7-6e) suggests potential interactions between silver and copper oxide which may influence the nucleation and growth of oxide phases by changing the composition of the oxide. For instance, a study on the oxidation behavior of copper and copper-aluminum alloys at temperatures between 700 °C and 1000 °C demonstrates that adding aluminum improves oxidation resistance, with up to 2 wt% forming a protective Al_2O_3 layer at lower temperatures [197].

In comparison, the presence of silver at the interface may lead to the formation of mixed oxide phases or silver-containing compounds. Further investigation using advanced electron microscopy including transmission electron microscopy (TEM) is necessary to fully comprehend the microstructural features and underlying mechanisms responsible for the impact of Ag in Cu–Ag alloy which will be pursued as part of the future research endeavors in this project. Given the relative thicknesses of the Cu_2O and CuO layers, it is likely that the primary oxidation kinetics of Cu–Ag at 600 °C predominantly involve Cu_2O growth.

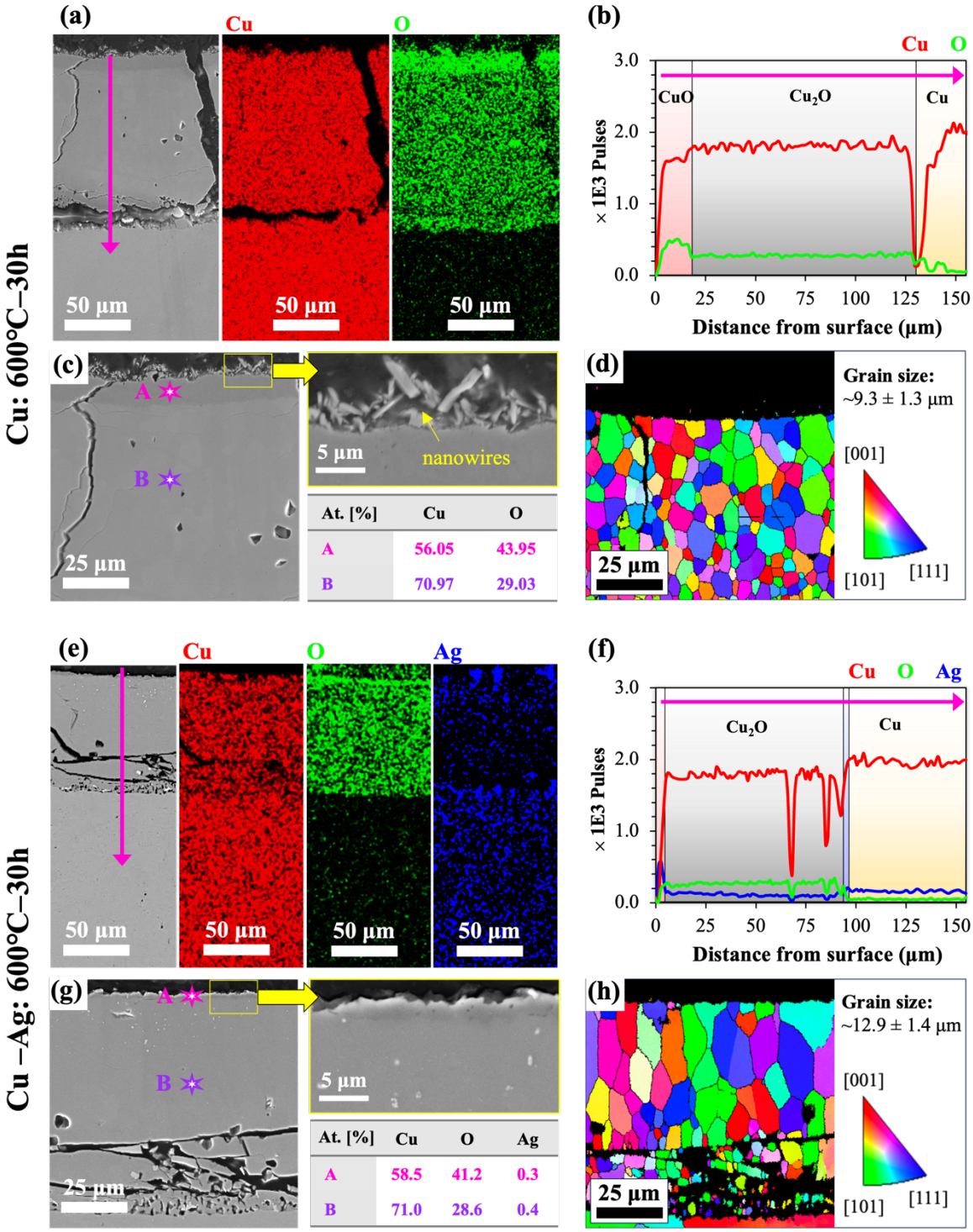


Figure 7-6 SEM micrographs with EDS map and point analysis for (a,c) Cu and (e,g) Cu–Ag oxidation in air at 600 °C after 30 hours, highlighting the oxide layers of CuO and Cu_2O. The plots in (b) and (f) correspond to line scans of the pink arrows shown in SEM images (a) and (e), respectively, indicating the element concentration profile away from the surface. The EBSD grain maps in (d) and (h) correspond to Cu_2O oxide layer shown in (c) and (g), respectively.

The microstructure of oxide layers was examined using electron backscatter diffraction (EBSD) for both Cu and Cu–Ag (Figure 7-6d and h). However, CuO was not identified through EBSD, possibly attributable to the constraints of this technique in detecting very fine grains. This suggests that the grain size within the CuO layer is exceptionally fine and evades detection by EBSD. Conversely, Cu_2O grains were successfully detected in both materials. In pure Cu, the Cu_2O grains appear to be randomly oriented and equiaxed with a grain size of ~9.3 ± 1.3 μm.

However, smaller grains, measuring around ~5.1 ± 0.9 μm, are found closer to the interface. These finer Cu_2O crystallites may serve as pathways for Cu atoms to diffuse from the copper substrate into the oxide layers. Slightly above the Cu/Cu_2O interface, the grains become somewhat larger but remains equiaxed. This hierarchical microstructure typically starts with small grains at the Cu/Cu_2O interface and transitions into elongated columnar grains [166]. This trend is more pronounced in Cu–Ag, where the grains near the surface are larger (~12.9 ± 1.4 μm) compared to pure Cu.

7.5. Summary

The present study investigates the oxidation behavior of Cu–Ag alloys produced using LPBF. The key findings are as follows:

- LPBF may elevate the oxidation rate of copper, which is likely attributed to the specific microstructure developed during LPBF.
- The addition of a small amount of silver can improve the oxidation resistance of copper.
- At 300 °C, the presence of silver changes the oxidation kinetics from linear in pure copper to parabolic in Cu–2Ag.
- At 600 °C, the presence of silver decelerates the oxidation process, leading to a slower parabolic rate compared to pure copper.
- Silver modifies the oxidation mechanism, likely by restricting diffusion pathways, ultimately resulting in the formation of thinner oxide layers of Cu_2O and CuO in Cu–2Ag.

Based on these results, Cu–Ag alloys are well-suited for high-performance electrical contacts, connectors, and electronic components like circuit boards where improved oxidation resistance and durability are essential. Future research should investigate the long-term oxidation behavior of Cu–Ag alloys at temperatures above 600 °C. It should also evaluate how varying silver concentrations influence oxidation kinetics and performance to refine alloy composition for improved oxidation resistance.

Chapter 8. Conclusions and future work

8.1. Conclusions

The present project focuses on laser powder bed fusion of two copper alloys, including Cu–Cr–Zr and Cu–Ag. Based on the obtained results, the following conclusions can be drawn:

- Optimization of Cu–Cr–Zr LPBF processing enables near-full densification and tailored microstructures. Statistical modeling identifies layer thickness, laser power, and scanning speed as the most critical parameters influencing surface roughness and relative density. The optimized conditions yield a surface roughness of 13.54 ± 2.91 μm and relative density of 98.99 ± 0.49%. Microstructural analysis reveals columnar grains aligned along the build direction, while high volumetric energy densities (VED) promote a strong <001> texture, contributing to enhanced mechanical properties.
- High strain rate testing (4400^{-1}–11300 s^{-1}) shows that Cu–Cr–Zr undergoes significant strain hardening, with ultimate compressive strength (UCS) increasing from 173 ± 8 MPa to 489 ± 14 MPa. Adiabatic shear bands (ASBs) become more pronounced at higher strain rates, leading to localized plastic deformation. Despite intense deformation, crystallographic texture remains stable, indicating that deformation is predominantly controlled by dislocation motion rather than grain reorientation.
- LPBF enables in-situ alloying of Cu–Ag, where melt pool analysis confirms that moderate scanning speeds (500 mm/s–700 mm/s) and power levels (700 W–800 W) produce stable and continuous tracks, ensuring homogenous Ag distribution. XRD analysis validates in-situ alloying, with peak shifts confirming Ag incorporation into the Cu lattice. The highest relative density (~99.49%) is achieved at 600 mm/s and 900 W, while higher speeds lead to porosity due to lack-of-fusion defects.
- Marangoni-driven convection plays a key role in in-situ alloying efficiency. Increasing energy density enhances Marangoni (Ma) numbers, promoting intense recirculating melt flow. This improves in-situ alloying by ensuring better mixing of Cu and Ag. SEM and EDS confirm that at higher energy inputs, Ag distribution is more uniform, whereas at lower energies, partially melted Ag particles remain.

- High-temperature oxidation resistance of Cu–Ag is significantly enhanced, with implications for thermal and electrical applications: Oxidation tests reveal that Ag addition refines the oxide scale, altering oxidation kinetics from a linear rate to a parabolic regime. At 300 °C –600 °C, Cu–2Ag initially oxidizes faster than pure Cu but stabilizes over time, resulting in lower total mass gain. At 700 °C –800 °C, Cu–2Ag exhibits superior oxidation resistance from the outset. Microstructural analysis shows a thinner and more compact oxide layer in Cu–2Ag, contributing to enhanced durability.

8.2. Future work

To further advance the present research, the following objectives will be pursued:

- Conducting tensile testing on Cu–Cr–Zr samples produced under varying VED conditions to evaluate the influence of processing parameters on tensile properties. This study will complement the existing high-strain-rate testing and provide a more complete understanding of the mechanical behavior relevant to practical design and qualification of LPBF-made Cu–Cr–Zr components.
- Performing TEM analysis on Cu–Cr–Zr alloy to observe precipitation behavior and microstructural evolution post-LPBF processing. This will clarify how LPBF-induced rapid solidification alters precipitation kinetics compared to conventional processes, contributing to a better understanding of strengthening mechanisms in additively manufactured Cu–Cr–Zr.
- Investigating heat treatment effects on Cu–Cr–Zr samples to optimize mechanical performance, enhance hardness, and refine microstructural features. This will help bridge the gap between LPBF-specific process optimization and application-ready mechanical performance tailored to structural applications requiring high strength and thermal stability.
- Investigating defect formation mechanisms in LPBF-made Cu–Ag, with a focus on crack minimization strategies. This includes studying the influence of process parameters (e.g., scanning strategy, laser power modulation, preheating), powder characteristics, and Ag content on the formation of solidification cracks, keyholing, or porosity. Implementing preheating or scan path optimization may help reduce thermal gradients and residual stress, improving build integrity.

- Investigating the oxidized microstructure of Cu–Ag using TEM, SEM, XRD, and XPS to determine the composition and location of oxide layers and particles and elucidate the mechanisms governing parabolic and linear oxidation kinetics. This correlation between LPBF microstructure and oxidation mechanisms will provide the first systematic dataset for LPBF-made Cu–Ag oxidation behavior, filling a significant gap in the literature.

Beyond the specific directions outlined above, the outcomes of this research have the potential to advance the broader field of AM by establishing fundamental process–structure–property relationships for challenging, high-conductivity metals. The methodologies applied in this work, from statistical process optimization to high-strain-rate mechanical testing and high-temperature oxidation studies, can serve as a framework for future alloy development and qualification in LPBF. Furthermore, this research lays the groundwork for integrating in-situ alloying strategies with targeted functional properties, accelerating the development of next-generation Cu-based materials for applications in energy, aerospace, and electronic systems.

Letter of Copyright Permission



Laser powder bed fusion: a state-of-the-art review of the technology, materials, properties & defects, and numerical modelling

Author: Sohini Chowdhury,N. Yadaiah,Chander Prakash,Seeram Ramakrishna,Saurav Dixit,Lovi Raj Gupta,Dharam Buddhi

Publication: Journal of Materials Research and Technology

Publisher: Elsevier

Date: September–October 2022

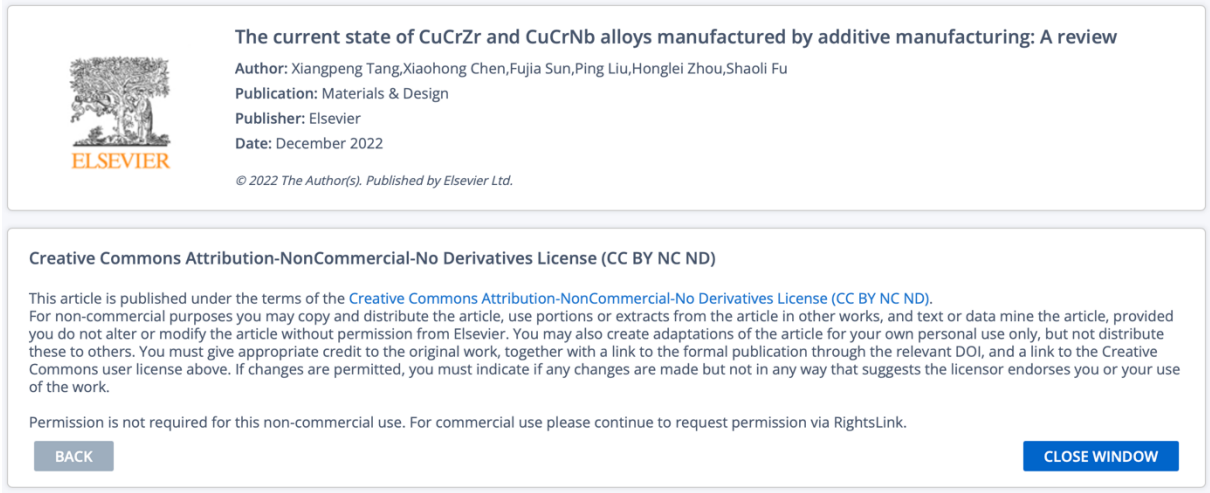
© 2022 The Author(s). Published by Elsevier B.V.

Creative Commons Attribution-NonCommercial-No Derivatives License (CC BY NC ND)

This article is published under the terms of the Creative Commons Attribution-NonCommercial-No Derivatives License (CC BY NC ND).
For non-commercial purposes you may copy and distribute the article, use portions or extracts from the article in other works, and text or data mine the article, provided you do not alter or modify the article without permission from Elsevier. You may also create adaptations of the article for your own personal use only, but not distribute these to others. You must give appropriate credit to the original work, together with a link to the formal publication through the relevant DOI, and a link to the Creative Commons user license above. If changes are permitted, you must indicate if any changes are made but not in any way that suggests the licensor endorses you or your use of the work.

Permission is not required for this non-commercial use. For commercial use please continue to request permission via RightsLink.

BACK CLOSE WINDOW



The current state of CuCrZr and CuCrNb alloys manufactured by additive manufacturing: A review

Author: Xiangpeng Tang,Xiaohong Chen,Fujia Sun,Ping Liu,Honglei Zhou,Shaoli Fu

Publication: Materials & Design

Publisher: Elsevier

Date: December 2022

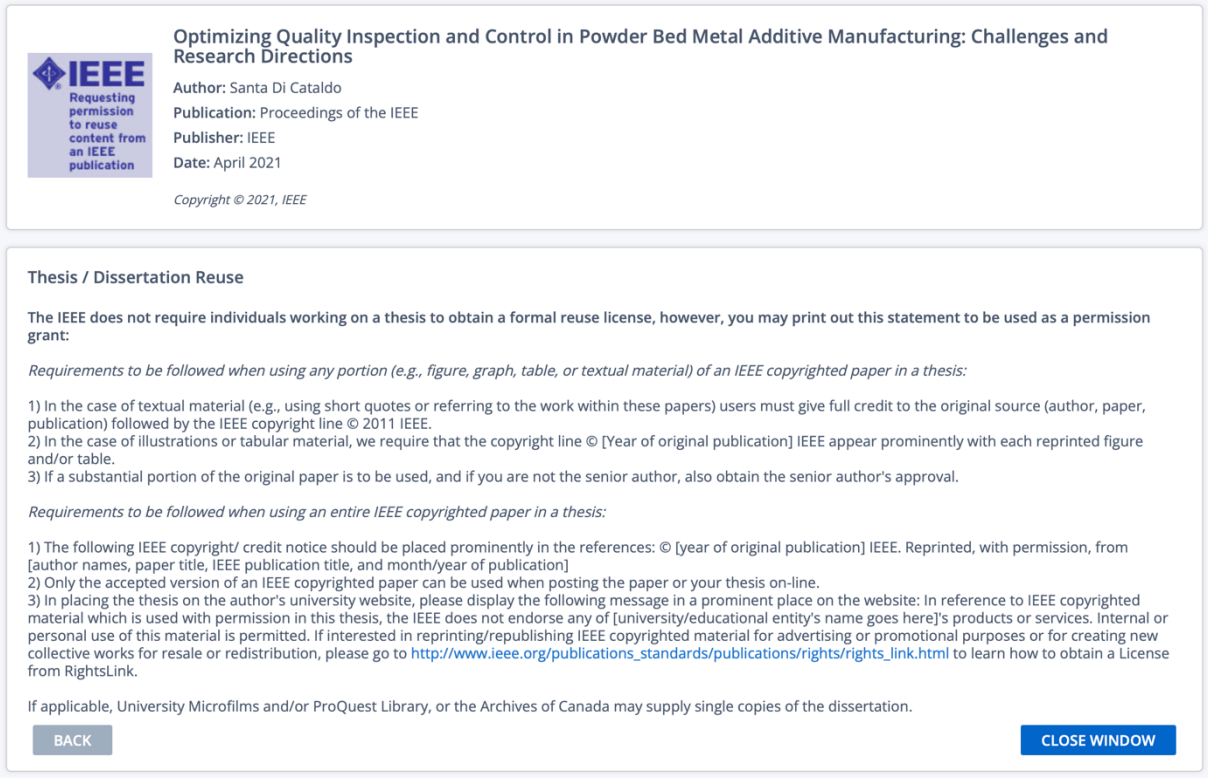
© 2022 The Author(s). Published by Elsevier Ltd.

Creative Commons Attribution-NonCommercial-No Derivatives License (CC BY NC ND)

This article is published under the terms of the Creative Commons Attribution-NonCommercial-No Derivatives License (CC BY NC ND).
For non-commercial purposes you may copy and distribute the article, use portions or extracts from the article in other works, and text or data mine the article, provided you do not alter or modify the article without permission from Elsevier. You may also create adaptations of the article for your own personal use only, but not distribute these to others. You must give appropriate credit to the original work, together with a link to the formal publication through the relevant DOI, and a link to the Creative Commons user license above. If changes are permitted, you must indicate if any changes are made but not in any way that suggests the licensor endorses you or your use of the work.

Permission is not required for this non-commercial use. For commercial use please continue to request permission via RightsLink.

BACK CLOSE WINDOW



Optimizing Quality Inspection and Control in Powder Bed Metal Additive Manufacturing: Challenges and Research Directions

Author: Santa Di Cataldo

Publication: Proceedings of the IEEE

Publisher: IEEE

Date: April 2021

Copyright © 2021, IEEE

Requesting permission to reuse content from an IEEE publication

Thesis / Dissertation Reuse

The IEEE does not require individuals working on a thesis to obtain a formal reuse license, however, you may print out this statement to be used as a permission grant:

Requirements to be followed when using any portion (e.g., figure, graph, table, or textual material) of an IEEE copyrighted paper in a thesis:

1) In the case of textual material (e.g., using short quotes or referring to the work within these papers) users must give full credit to the original source (author, paper, publication) followed by the IEEE copyright line © 2011 IEEE.
2) In the case of illustrations or tabular material, we require that the copyright line © [Year of original publication] IEEE appear prominently with each reprinted figure and/or table.
3) If a substantial portion of the original paper is to be used, and if you are not the senior author, also obtain the senior author's approval.

Requirements to be followed when using an entire IEEE copyrighted paper in a thesis:

1) The following IEEE copyright/ credit notice should be placed prominently in the references: © [year of original publication] IEEE. Reprinted, with permission, from [author names, paper title, IEEE publication title, and month/year of publication]
2) Only the accepted version of an IEEE copyrighted paper can be used when posting the paper or your thesis on-line.
3) In placing the thesis on the author's university website, please display the following message in a prominent place on the website: In reference to IEEE copyrighted material which is used with permission in this thesis, the IEEE does not endorse any of [university/educational entity's name goes here]'s products or services. Internal or personal use of this material is permitted. If interested in reprinting/republishing IEEE copyrighted material for advertising or promotional purposes or for creating new collective works for resale or redistribution, please go to http://www.ieee.org/publications_standards/publications/rights/rights_link.html to learn how to obtain a License from RightsLink.

If applicable, University Microfilms and/or ProQuest Library, or the Archives of Canada may supply single copies of the dissertation.

BACK CLOSE WINDOW

Article | Open access | Published: 22 December 2016

Ultrahigh Oxidation Resistance and High Electrical Conductivity in Copper-Silver Powder

Jiaxiang Li, Yunping Li, Zhongchang Wang, Huakang Bian, Yuhang Hou, Fenglin Wang, Guofu Xu, Bin Liu & Yong Liu

Scientific Reports **6**, Article number: 39650 (2016) | Cite this article

6720 Accesses | **50** Citations | Metrics

ELSEVIER LICENSE
TERMS AND CONDITIONS

Apr 21, 2025

This Agreement between Nadia Azizi / University of Waterloo ("You") and Elsevier ("Elsevier") consists of your license details and the terms and conditions provided by Elsevier and Copyright Clearance Center.

License Number	6013700941314
License date	Apr 21, 2025
Licensed Content Publisher	Elsevier
Licensed Content Publication	Additive Manufacturing
Licensed Content Title	Laser-based powder bed fusion additive manufacturing of pure copper
Licensed Content Author	Suraj Dinkar Jadhav,Louca Raphaël Goossens,Yannis Kinds,Brecht Van Hooreweder,Kim Vanmeensel
Licensed Content Date	Jun 1, 2021
Licensed Content Volume	42
Licensed Content Issue	n/a
Licensed Content Pages	1

ELSEVIER LICENSE
TERMS AND CONDITIONS

Apr 21, 2025

This Agreement between Nadia Azizi / University of Waterloo ("You") and Elsevier ("Elsevier") consists of your license details and the terms and conditions provided by Elsevier and Copyright Clearance Center.

License Number	6013710839148
License date	Apr 21, 2025
Licensed Content Publisher	Elsevier
Licensed Content Publication	Materials Science and Engineering: A
Licensed Content Title	CuCrZr alloy produced by laser powder bed fusion: Microstructure, nanoscale strengthening mechanisms, electrical and mechanical properties
Licensed Content Author	C. Salvan,L. Briottet,T. Baffie,L. Guetaz,C. Flament
Licensed Content Date	Oct 5, 2021
Licensed Content Volume	826
Licensed Content Issue	n/a
Licensed Content Pages	1

ELSEVIER LICENSE
TERMS AND CONDITIONS

Apr 21, 2025

This Agreement between Nadia Azizi / University of Waterloo ("You") and Elsevier ("Elsevier") consists of your license details and the terms and conditions provided by Elsevier and Copyright Clearance Center.

License Number	6013740956434
License date	Apr 21, 2025
Licensed Content Publisher	Elsevier
Licensed Content Publication	Materials Science and Engineering: A
Licensed Content Title	Microstructure evolution and properties of Cu–Ag microcomposites with different Ag content
Licensed Content Author	J.B. Liu,L. Meng,Y.W. Zeng
Licensed Content Date	Nov 5, 2006
Licensed Content Volume	435
Licensed Content Issue	n/a
Licensed Content Pages	8

ELSEVIER LICENSE
TERMS AND CONDITIONS

Apr 21, 2025

This Agreement between Nadia Azizi / University of Waterloo ("You") and Elsevier ("Elsevier") consists of your license details and the terms and conditions provided by Elsevier and Copyright Clearance Center.

License Number	6013741249653
License date	Apr 21, 2025
Licensed Content Publisher	Elsevier
Licensed Content Publication	Journal of Alloys and Compounds
Licensed Content Title	Effect of silver addition in copper-silver alloys fabricated by laser powder bed fusion in situ alloying
Licensed Content Author	John Robinson,Arun Arjunan,Mark Stanford,Iain Lyall,Craig Williams
Licensed Content Date	Mar 15, 2021
Licensed Content Volume	857
Licensed Content Issue	n/a
Licensed Content Pages	1

Materials Research Express



PAPER • OPEN ACCESS

Microstructure and properties of Cu-2Ag alloy sheet prepared by 'Upward + Thermomechanical Treatment'

Li Ming-Mao, Zhao-Xin Li, Tang Ying-Ying and Zhu Ming-Biao

Published 6 November 2020 • © 2020 The Author(s). Published by IOP Publishing Ltd

Materials Research Express, Volume 7, Number 11

Citation Li Ming-Mao *et al* 2020 *Mater. Res. Express* **7** 116505

DOI 10.1088/2053-1591/abc3f5

Article PDF

Materials Research Express



PAPER • OPEN ACCESS

Evolution of microstructure and properties of Cu-4.5 wt.% Ag alloy prepared by vacuum horizontal continuous casting in solid solution and aging treatment

Linsheng Tang, Weibin Xie, Xiangpeng Xiao, Huiming Chen, Hang Wang and Bin Yang

Published 22 December 2020 • © 2020 The Author(s). Published by IOP Publishing Ltd

Materials Research Express, Volume 7, Number 12

Citation Linsheng Tang *et al* 2020 *Mater. Res. Express* **7** 126517

DOI 10.1088/2053-1591/abd217

Article PDF

References

[1] E. Toyserkani, D. Sarker, F. Liravi, P. Russo, K. Taherkhani, Metal additive manufacturing: A comprehensive review of additive manufacturing processes for metallic structures, n.d. www.wiley.com.

[2] T.J. Horn, D. Gamzina, Additive manufacturing of copper and copper alloys, Additive Manufacturing Processes, ASM International, 2020: pp. 388–418. https://doi.org/10.31399/asm.hb.v24.a0006579.

[3] J.R. Davis, Copper and copper alloys, ASM international, 2001.

[4] T.I. El-Wardany, Y. She, V.N. Jagdale, J.K. Garofano, J.J. Liou, W.R. Schmidt, Challenges in three-dimensional printing of high-conductivity copper, Journal of Electronic Packaging, Transactions of the ASME 140 (2018). https://doi.org/10.1115/1.4039974.

[5] T. Stoll, P. Trautnitz, S. Schmiedeke, J.E. Franke, N. Travitzky, Process development for laser powder bed fusion of pure copper, in: SPIE-Intl Soc Optical Eng, 2020: p. 46. https://doi.org/10.1117/12.2563870.

[6] B. Dutta, S. Babu, B. Jared, Science, technology and applications of metals in additive manufacturing, n.d.

[7] S. Chowdhury, N. Yadaiah, C. Prakash, S. Ramakrishna, S. Dixit, L.R. Gupta, D. Buddhi, Laser powder bed fusion: a state-of-the-art review of the technology, materials, properties & defects, and numerical modelling, Journal of Materials Research and Technology 20 (2022) 2109–2172. https://doi.org/10.1016/j.jmrt.2022.07.121.

[8] S. di Cataldo, S. Vinco, G. Urgese, F. Calignano, E. Ficarra, A. MacIi, E. MacIi, Optimizing quality inspection and control in powder bed metal additive manufacturing: challenges and research directions, Proceedings of the IEEE 109 (2021) 326–346. https://doi.org/10.1109/JPROC.2021.3054628.

[9] C. Silbernagel, L. Gargalis, I. Ashcroft, R. Hague, M. Galea, P. Dickens, Electrical resistivity of pure copper processed by medium-powered laser powder bed fusion additive

manufacturing for use in electromagnetic applications, Addit Manuf 29 (2019). https://doi.org/10.1016/j.addma.2019.100831.

[10] E. Hori, Y. Sato, T. Shibata, K. Tojo, M. Tsukamoto, Development of SLM process using 200 W blue diode laser for pure copper additive manufacturing of high density structure, J Laser Appl 33 (2021) 012008. https://doi.org/10.2351/7.0000311.

[11] S.D. Jadhav, L.R. Goossens, Y. Kinds, B. van Hooreweder, K. Vanmeensel, Laser-based powder bed fusion additive manufacturing of pure copper, Addit Manuf 42 (2021). https://doi.org/10.1016/j.addma.2021.101990.

[12] A.A. Saprykin, E.A. Ibragimov, E. v. Babakova, Modeling the temperature fields of copper powder melting in the process of selective laser melting, IOP Conf Ser Mater Sci Eng, Institute of Physics Publishing, 2016. https://doi.org/10.1088/1757-899X/142/1/012061.

[13] P.A. Lykov, E. V Safonov, A.M. Akhmedianov, Selective laser melting of copper, Materials Science Forum, Trans Tech Publ, 2016: pp. 284–288.

[14] S.D. Jadhav, S. Dadbakhsh, L. Goossens, J.P. Kruth, J. Van Humbeeck, K. Vanmeensel, Influence of selective laser melting process parameters on texture evolution in pure copper, J Mater Process Technol 270 (2019) 47–58.

[15] M. Colopi, A.G. Demir, L. Caprio, B. Previtali, Limits and solutions in processing pure Cu via selective laser melting using a high-power single-mode fiber laser, International Journal of Advanced Manufacturing Technology 104 (2019) 2473–2486. https://doi.org/10.1007/s00170-019-04015-3.

[16] M. Colopi, L. Caprio, A.G. Demir, B. Previtali, Selective laser melting of pure Cu with a 1 kW single mode fiber laser, Procedia CIRP 74 (2018) 59–63.

[17] T.-T. Ikeshoji, K. Nakamura, M. Yonehara, K. Imai, H. Kyogoku, Selective laser melting of pure copper, Jom 70 (2018) 396–400.

[18] S.J. Raab, R. Guschlbauer, M.A. Lodes, C. Körner, Thermal and electrical conductivity of 99.9% pure copper processed via selective electron beam melting, Adv Eng Mater 18 (2016) 1661–1666. https://doi.org/10.1002/adem.201600078.

[19] P. Frigola, O.A. Harrysson, T.J. Horn, H.A. West, R.L. Aman, J.M. Rigsbee, D.A. Ramirez, L.E. Murr, F. Medina, R.B. Wicker, E. Rodriguez, Fabricating copper components with electron beam melting, 2014. www.arcam.com/CommonResources/Files/www.arcam.com/.

[20] M.A. Lodes, R. Guschlbauer, C. Körner, Process development for the manufacturing of 99.94% pure copper via selective electron beam melting, Mater Lett 143 (2015) 298–301. https://doi.org/10.1016/j.matlet.2014.12.105.

[21] R. Guschlbauer, S. Momeni, F. Osmanlic, C. Körner, Process development of 99.95% pure copper processed via selective electron beam melting and its mechanical and physical properties, Mater Charact 143 (2018) 163–170. https://doi.org/10.1016/j.matchar.2018.04.009.

[22] K. Asano, M. Tsukamoto, Y. Sechi, Y. Sato, S. ichiro Masuno, R. Higashino, T. Hara, M. Sengoku, M. Yoshida, Laser metal deposition of pure copper on stainless steel with blue and IR diode lasers, Opt Laser Technol 107 (2018) 291–296. https://doi.org/10.1016/j.optlastec.2018.06.012.

[23] K. Asano, M. Tsukamoto, Y. Funada, D. Tanigawa, T. Nakaaze, M. Sengoku, N. Abe, T. Yamazaki, Copper layer formation produced with 100W blue direct diode laser system, in: Laser Institute of America, 2019: p. P110. https://doi.org/10.2351/1.5118642.

[24] Y. Bai, C.B. Williams, An exploration of binder jetting of copper, Rapid Prototyp J 21 (2015) 177–185. https://doi.org/10.1108/RPJ-12-2014-0180.

[25] A. Kumar, Y. Bai, A. Eklund, C.B. Williams, Effects of hot isostatic pressing on copper parts fabricated via binder jetting, Procedia Manuf, Elsevier B.V., 2017: pp. 935–944. https://doi.org/10.1016/j.promfg.2017.07.084.

[26] S. Zhang, H. Zhu, L. Zhang, W. Zhang, H. Yang, X. Zeng, Microstructure and properties of high strength and high conductivity Cu-Cr alloy components fabricated by high power selective laser melting, Mater Lett 237 (2019) 306–309.

[27] S. Zhang, H. Zhu, L. Zhang, W. Zhang, H. Yang, X. Zeng, Microstructure and properties in QCr0.8 alloy produced by selective laser melting with different heat treatment, J Alloys Compd 800 (2019) 286–293. https://doi.org/10.1016/j.jallcom.2019.06.018.

[28] S.L. Sing, L.P. Lam, D.Q. Zhang, Z.H. Liu, C.K. Chua, Interfacial characterization of SLM parts in multi-material processing: Intermetallic phase formation between AlSi10Mg and C18400 copper alloy, Mater Charact 107 (2015) 220–227. https://doi.org/10.1016/j.matchar.2015.07.007.

[29] Z.H. Liu, D.Q. Zhang, S.L. Sing, C.K. Chua, L.E. Loh, Interfacial characterization of SLM parts in multi-material processing: Metallurgical diffusion between 316L stainless steel and C18400 copper alloy, Mater Charact 94 (2014) 116–125. https://doi.org/10.1016/j.matchar.2014.05.001.

[30] S. Uchida, T. Kimura, T. Nakamoto, T. Ozaki, T. Miki, M. Takemura, Y. Oka, R. Tsubota, Microstructures and electrical and mechanical properties of Cu-Cr alloys fabricated by selective laser melting, Mater Des 175 (2019). https://doi.org/10.1016/j.matdes.2019.107815.

[31] Y. Chen, S. Ren, Y. Zhao, X. Qu, Microstructure and properties of CuCr alloy manufactured by selective laser melting, J Alloys Compd 786 (2019) 189–197. https://doi.org/10.1016/j.jallcom.2019.01.179.

[32] S. Momeni, R. Guschlbauer, F. Osmanlic, C. Körner, Selective electron beam melting of a copper-chrome powder mixture, Mater Lett 223 (2018) 250–252. https://doi.org/10.1016/j.matlet.2018.03.194.

[33] C. Wallis, B. Buchmayr, Effect of heat treatments on microstructure and properties of CuCrZr produced by laser-powder bed fusion, Materials Science and Engineering: A 744 (2019) 215–223. https://doi.org/10.1016/j.msea.2018.12.017.

[34] K. Jahns, R. Bappert, P. Böhlke, U. Krupp, Additive manufacturing of CuCr1Zr by development of a gas atomization and laser powder bed fusion routine, International Journal of Advanced Manufacturing Technology 107 (2020) 2151–2161. https://doi.org/10.1007/s00170-020-04941-7.

[35] B. Buchmayr, G. Panzl, A. Walzl, C. Wallis, Laser powder bed fusion – materials issues and optimized processing parameters for tool steels, AlSiMg- and CuCrZr-Alloys, Adv Eng Mater 19 (2017). https://doi.org/10.1002/adem.201600667.

[36] F. Sun, P. Liu, X. Chen, H. Zhou, P. Guan, B. Zhu, Mechanical properties of high-strength cu–cr–zr alloy fabricated by selective laser melting, Materials 13 (2020) 1–16. https://doi.org/10.3390/ma13215028.

[37] A. Popovich, V. Sufiiarov, I. Polozov, E. Borisov, D. Masaylo, A. Orlov, Microstructure and mechanical properties of additive manufactured copper alloy, Mater Lett 179 (2016) 38–41. https://doi.org/10.1016/j.matlet.2016.05.064.

[38] K. Cooper, J. Lydon, Z. Jones, D. Scannapieco, D. Ellis, B. Lerch, G.C. Marshall, Three-dimensional printing GRCop-42, 2018. http://www.sti.nasa.gov.

[39] 3D printed copper rocket engine part on way to Mars, Metal Powder Report 70 (2015) 196–197. https://doi.org/10.1016/j.mprp.2015.06.021.

[40] R. Carter, S. Draper, I. Locci, B. Lerch, D. Ellis, P. Senick, M. Meyer, J. Free, K. Cooper, Z. Jones, Materials characterization of additively manufactured components for rocket propulsion, n.d.

[41] B. Onuike, A. Bandyopadhyay, Bond strength measurement for additively manufactured Inconel 718- GRCop84 copper alloy bimetallic joints, Addit Manuf 27 (2019) 576–585. https://doi.org/10.1016/j.addma.2019.04.003.

[42] J. Robinson, A. Arjunan, M. Stanford, I. Lyall, C. Williams, Effect of silver addition in copper-silver alloys fabricated by laser powder bed fusion in situ alloying, J Alloys Compd 857 (2021). https://doi.org/10.1016/j.jallcom.2020.157561.

[43] D. Tiberto, U.E. Klotz, F. Held, G. Wolf, Additive manufacturing of copper alloys: influence of process parameters and alloying elements, Materials Science and Technology (United Kingdom) 35 (2019) 969–977. https://doi.org/10.1080/02670836.2019.1600840.

[44] J. Wang, R. Zhu, Y. Liu, L. Zhang, Understanding melt pool characteristics in laser powder bed fusion: An overview of single- and multi-track melt pools for process optimization, Advanced Powder Materials 2 (2023). https://doi.org/10.1016/j.apmate.2023.100137.

[45] Q. Jiang, P. Zhang, Z. Yu, H. Shi, D. Wu, H. Yan, X. Ye, Q. Lu, Y. Tian, A review on additive manufacturing of pure copper, Coatings 11 (2021). https://doi.org/10.3390/coatings11060740.

[46] S.A. Khairallah, A.T. Anderson, A. Rubenchik, W.E. King, Laser powder-bed fusion additive manufacturing: Physics of complex melt flow and formation mechanisms of pores, spatter, and denudation zones, Acta Mater 108 (2016) 36–45. https://doi.org/10.1016/j.actamat.2016.02.014.

[47] G. Piatti, D. Boerman, Hot tensile characteristics and microstructure of a Cu-0.65Cr-0.08Zr alloy for fusion reactor applications, n.d.

[48] R. Mishnev, I. Shakhova, A. Belyakov, R. Kaibyshev, Deformation microstructures, strengthening mechanisms, and electrical conductivity in a Cu-Cr-Zr alloy, Materials Science and Engineering: A 629 (2015) 29–40. https://doi.org/10.1016/j.msea.2015.01.065.

[49] Z. Ma, K. Zhang, Z. Ren, D.Z. Zhang, G. Tao, H. Xu, Selective laser melting of Cu–Cr–Zr copper alloy: Parameter optimization, microstructure and mechanical properties, J Alloys Compd 828 (2020). https://doi.org/10.1016/j.jallcom.2020.154350.

[50] X. Tang, X. Chen, F. Sun, L. Li, P. Liu, H. Zhou, S. Fu, A. Li, A study on the mechanical and electrical properties of high-strength CuCrZr alloy fabricated using laser powder bed fusion, J Alloys Compd 924 (2022). https://doi.org/10.1016/j.jallcom.2022.166627.

[51] J. Ma, Y. He, W. Gao, J. Wang, B. Sun, The effect of micro-crystallizing on the oxidation resistance of Cu-Cr alloy in air, Materials Science and Engineering: A 488 (2008) 311–317. https://doi.org/10.1016/j.msea.2007.11.008.

[52] P. Guan, X. Chen, P. Liu, F. Sun, C. Zhu, H. Zhou, S. Fu, Z. Wu, Y. Zhu, Effect of selective laser melting process parameters and aging heat treatment on properties of CuCrZr alloy, Mater Res Express 6 (2019) 1165c1.

[53] C. Salvan, L. Briottet, T. Baffie, L. Guetaz, C. Flament, CuCrZr alloy produced by laser powder bed fusion: Microstructure, nanoscale strengthening mechanisms, electrical and mechanical properties, Materials Science and Engineering: A 826 (2021) 141915.

[54] X. Tang, X. Chen, F. Sun, P. Liu, H. Zhou, S. Fu, The current state of CuCrZr and CuCrNb alloys manufactured by additive manufacturing: A review, Mater Des 224 (2022). https://doi.org/10.1016/j.matdes.2022.111419.

[55] A. Korneva, B. Straumal, A. Kilmametov, R. Chulist, G. Cios, B. Baretzky, P. Zięba, Dissolution of Ag precipitates in the Cu-8wt.%Ag alloy deformed by high pressure torsion, Materials 12 (2019). https://doi.org/10.3390/ma12030447.

[56] L. Ming-Mao, Z.X. Li, T. Ying-Ying, Z. Ming-Biao, Microstructure and properties of Cu-2Ag alloy sheet prepared by "Upward + Thermomechanical Treatment," Mater Res Express 7 (2020). https://doi.org/10.1088/2053-1591/abc3f5.

[57] L. Tang, W. Xie, X. Xiao, H. Chen, H. Wang, B. Yang, Evolution of microstructure and properties of Cu-4.5 wt.% Ag alloy prepared by vacuum horizontal continuous casting in solid solution and aging treatment, Mater Res Express 7 (2020). https://doi.org/10.1088/2053-1591/abd217.

[58] J.B. Liu, L. Meng, Y.W. Zeng, Microstructure evolution and properties of Cu-Ag microcomposites with different Ag content, Materials Science and Engineering: A 435–436 (2006) 237–244. https://doi.org/10.1016/j.msea.2006.07.125.

[59] Z. Castro-Dettmer, M. Simmons, C. Persad, Obtainable microstructures in electrical conductors made of a copper-silver alloy, IEEE Trans Magn 39 (2003) 323–326. https://doi.org/10.1109/TMAG.2002.806372.

[60] Y. Sakai'f, H.-J. Schneider-Muntau, Ultra-high strength, high conductivity cu-ag alloy wires, Acti Metallurgica Inc, 1997.

[61] L. Zhang, L. Meng, Evolution of microstructure and electrical resistivity of Cu-12wt.%Ag filamentary microcomposite with drawing deformation, Scr Mater 52 (2005) 1187–1191. https://doi.org/10.1016/j.scriptamat.2005.03.016.

[62] J.B. Liu, L. Meng, The characteristics of Cu-12 wt.% Ag filamentary microcomposite in different isothermal process, Materials Science and Engineering: A 418 (2006) 320–325. https://doi.org/10.1016/j.msea.2005.12.001.

[63] P. Coddet, C. Verdy, C. Coddet, F. Debray, Mechanical properties of Cu-0.1Ag alloys deposited by cold spray with various powder feed rate and heat treatment, Journal of Thermal Spray Technology 24 (2014) 119–125. https://doi.org/10.1007/s11666-014-0159-1.

[64] J. Li, Y. Li, Z. Wang, H. Bian, Y. Hou, F. Wang, G. Xu, B. Liu, Y. Liu, Ultrahigh oxidation resistance and high electrical conductivity in copper-silver powder, Sci Rep 6 (2016). https://doi.org/10.1038/srep39650.

[65] A. Ul-Hamid, A microstructural study of preferential oxidation at the grain boundaries of Ni-Cr alloys, 2002.

[66] Y. Zhu, K. Mimura, M. Isshiki, Oxidation mechanism of copper at 623-1073 K *, 2002.

[67] W.H. Bowyer, The effects of impurities on the properties of ofp copper specified for the copper iron canister, (1999).

[68] Y. Sakai, K. Inoue, T. Asano, H. Wada, H. Maeda, Development of high-strength, high-conductivity Cu-Ag alloys for high-field pulsed magnet use, Appl Phys Lett 59 (1991) 2965–2967. https://doi.org/10.1063/1.105813.

[69] K. Morshed-Behbahani, A. Aliyu, D.P. Bishop, A. Nasiri, Additive manufacturing of copper-based alloys for high-temperature aerospace applications: A review, Mater Today Commun 38 (2024). https://doi.org/10.1016/j.mtcomm.2024.108395.

[70] Y. Chen, Q. Hu, L. Wang, W. Guo, J. Zhang, Study on densification and defects of Cu-Cr-Zr Alloy formed by selective laser melting, J Phys Conf Ser, Institute of Physics, 2024. https://doi.org/10.1088/1742-6596/2785/1/012139.

[71] A. Pfaff, M. Jäcklein, M. Schlager, W. Harwick, K. Hoschke, F. Balle, An empirical approach for the development of process parameters for laser powder bed fusion, Materials 13 (2020) 1–20. https://doi.org/10.3390/ma13235400.

[72] A. Paraschiv, G. Matache, M.R. Condruz, T.F. Frigioescu, L. Pambaguian, Laser powder bed fusion process parameters' optimization for fabrication of dense IN 625, Materials 15 (2022). https://doi.org/10.3390/ma15165777.

[73] Z. Hu, Z. Du, Z. Yang, L. Yu, Z. Ma, Preparation of Cu–Cr–Zr alloy by selective laser melting: Role of scanning parameters on densification, microstructure and mechanical properties, Materials Science and Engineering: A 836 (2022). https://doi.org/10.1016/j.msea.2022.142740.

[74] K. Vanaja, R.H. Shobha Rani, Design of experiments: concept and applications of Plackett Burman design, Clin Res Regul Aff 24 (2007) 1–23.

[75] L. Wang, Y. Zhang, H.Y. Chia, W. Yan, Mechanism of keyhole pore formation in metal additive manufacturing, NPJ Comput Mater 8 (2022). https://doi.org/10.1038/s41524-022-00699-6.

[76] F.C. Kiwu-Lawrence, L.C. Kiwu, D.C. Bartholomew, C.P. Obite, A.F. Chikereuba, Evaluation and comparison of three classes of central composite designs, Asian Journal of Probability and Statistics 13 (2021) 31–47.

[77] S.K. Nayak, S.K. Mishra, C.P. Paul, A.N. Jinoop, K.S. Bindra, Effect of energy density on laser powder bed fusion built single tracks and thin wall structures with 100 μm preplaced powder layer thickness, Opt Laser Technol 125 (2020). https://doi.org/10.1016/j.optlastec.2019.106016.

[78] Y. Mahmoodkhani, U. Ali, S. Imani Shahabad, A. Rani Kasinathan, R. Esmaeilizadeh, A. Keshavarzkermani, E. Marzbanrad, E. Toyserkani, On the measurement of effective powder layer thickness in laser powder-bed fusion additive manufacturing of metals, Progress in Additive Manufacturing 4 (2019) 109–116. https://doi.org/10.1007/s40964-018-0064-0.

[79] L. Cao, J. Li, J. Hu, H. Liu, Y. Wu, Q. Zhou, Optimization of surface roughness and dimensional accuracy in LPBF additive manufacturing, Opt Laser Technol 142 (2021). https://doi.org/10.1016/j.optlastec.2021.107246.

[80] B. Whip, L. Sheridan, J. Gockel, The effect of primary processing parameters on surface roughness in laser powder bed additive manufacturing, International Journal of Advanced Manufacturing Technology 103 (2019) 4411–4422. https://doi.org/10.1007/s00170-019-03716-z.

[81] M. Hasanabadi, A. Keshavarzkermani, N. Azizi, H. Asgari, A. Gerlich, E. Toyserkani, Systematic investigation into laser powder bed fusion of Ti-5553 through single-track and multi-layer studies for tailored manufacturing solutions, Journal of Materials Research and Technology 33 (2024) 4008–4022. https://doi.org/10.1016/j.jmrt.2024.10.057.

[82] S.K. Murugesan, J. Natarajan, C.H. Yang, K. Vijayananth, A synergistic impact of LPBF process parameters on attaining a defect-free Cu-Cr-Zr alloy parts: an analytical and

experimental study, International Journal of Advanced Manufacturing Technology 128 (2023) 3507–3529. https://doi.org/10.1007/s00170-023-12179-2.

[83] X. Fang, W. Xia, Q. Wei, Y. Wu, W. Lv, W. Guo, Preparation of Cu-Cr-Zr alloy by laser powder bed fusion: Parameter optimization, microstructure, mechanical and thermal properties for microelectronic applications, Metals (Basel) 11 (2021). https://doi.org/10.3390/met11091410.

[84] A. Keshavarzkermani, E. Marzbanrad, R. Esmaeilizadeh, Y. Mahmoodkhani, U. Ali, P.D. Enrique, N.Y. Zhou, A. Bonakdar, E. Toyserkani, An investigation into the effect of process parameters on melt pool geometry, cell spacing, and grain refinement during laser powder bed fusion, Opt Laser Technol 116 (2019) 83–91. https://doi.org/10.1016/j.optlastec.2019.03.012.

[85] M. Hasanabadi, S. Imani Shahabad, A. Keshavarzkermani, R. Eybel, A. Gerlich, E. Toyserkani, A numerical modelling for laser Powder-bed fusion of Ti-alloy with a hybrid heat Source: An investigation on solidification and microstructure formation, Opt Laser Technol 174 (2024). https://doi.org/10.1016/j.optlastec.2024.110647.

[86] M. Saravana Kumar, N. Jeyaprakash, C.-H. Yang, Analysis of co-relation on LPBF Process Parameter on Wear characteristics of Cu-Cr-Zr alloy, Surf Topogr (2024). https://doi.org/10.1088/2051-672x/ad76c2.

[87] H. Fan, Y. Xu, H. Li, J. Fang, M. Li, K. Dongfang, P. Liu, A novel study on microstructure and crystallographic characteristics of Cu-Cr-Zr alloy manufactured by laser powder bed fusion, Mater Today Commun 37 (2023). https://doi.org/10.1016/j.mtcomm.2023.107603.

[88] K. Deshmukh, A. Riensche, B. Bevans, R.J. Lane, K. Snyder, H. (Scott) Halliday, C.B. Williams, R. Mirzaeifar, P. Rao, Effect of processing parameters and thermal history on microstructure evolution and functional properties in laser powder bed fusion of 316L, Mater Des 244 (2024). https://doi.org/10.1016/j.matdes.2024.113136.

[89] A. Keshavarzkermani, R. Esmaeilizadeh, U. Ali, P.D. Enrique, Y. Mahmoodkhani, N.Y. Zhou, A. Bonakdar, E. Toyserkani, Controlling mechanical properties of additively manufactured hastelloy X by altering solidification pattern during laser powder-bed fusion, Materials Science and Engineering: A 762 (2019). https://doi.org/10.1016/j.msea.2019.138081.

[90] M. Hasanabadi, A. Keshavarzkermai, H. Asgari, N. Azizi, A. Gerlich, E. Toyserkani, In-situ microstructure control by laser post-exposure treatment during laser powder-bed fusion, Additive Manufacturing Letters 4 (2023). https://doi.org/10.1016/j.addlet.2022.100110.

[91] T. DebRoy, H.L. Wei, J.S. Zuback, T. Mukherjee, J.W. Elmer, J.O. Milewski, A.M. Beese, A. Wilson-Heid, A. De, W. Zhang, Additive manufacturing of metallic components – Process, structure and properties, Prog Mater Sci 92 (2018) 112–224. https://doi.org/10.1016/j.pmatsci.2017.10.001.

[92] J.P. Oliveira, A.D. LaLonde, J. Ma, Processing parameters in laser powder bed fusion metal additive manufacturing, Mater Des 193 (2020). https://doi.org/10.1016/j.matdes.2020.108762.

[93] Q. Wang, H. Shao, X. Zhang, K. Wang, S. Liu, C. Yang, W. Wang, Study of thermal behavior and microstructure formation mechanism of CuCrZr alloy melted by laser powder bed fusion, Mater Charact 198 (2023). https://doi.org/10.1016/j.matchar.2023.112721.

[94] N. Hansen, Hall-petch relation and boundary strengthening, Scr Mater 51 (2004) 801–806. https://doi.org/10.1016/j.scriptamat.2004.06.002.

[95] A. Basak, S. Das, Epitaxy and microstructure evolution in metal additive manufacturing, Annu Rev Mater Res 46 (2016) 125–149.

[96] H.L. Wei, J. Mazumder, T. DebRoy, Evolution of solidification texture during additive manufacturing, Sci Rep 5 (2015) 16446.

[97] K. Dongfang, H. Fan, S. Sui, H. Li, H. Liu, Y. Li, P. Liu, Effect of laser powder bed fusion process parameters on the microstructures, mechanical properties, and conductivity of CuCrZr alloy, J Mater Eng Perform (2024). https://doi.org/10.1007/s11665-024-10026-3.

[98] C.A. Biffi, J. Fiocchi, S. Boldrini, A. Tuissi, CuCrZr Alloy manufactured by LPBF process: correlation between microstructure, mechanical and thermal properties, Lasers in Manufacturing and Materials Processing 11 (2024) 143–153. https://doi.org/10.1007/s40516-023-00240-7.

[99] Y. Bai, C. Zhao, Y. Zhang, J. Chen, H. Wang, Additively manufactured CuCrZr alloy: Microstructure, mechanical properties and machinability, Materials Science and Engineering: A 819 (2021). https://doi.org/10.1016/j.msea.2021.141528.

[100] Í. Carneiro, S. Simões, Recent advances in EBSD characterization of metals, Metals (Basel) 10 (2020) 1–32. https://doi.org/10.3390/met10081097.

[101] X. Yang, Y. Qi, W. Zhang, Y. Wang, H. Zhu, Laser powder bed fusion of C18150 copper alloy with excellent comprehensive properties, Materials Science and Engineering: A 862 (2023). https://doi.org/10.1016/j.msea.2022.144512.

[102] W. Zhou, T. Kousaka, S. ichi Moriya, T. Kimura, T. Nakamoto, N. Nomura, Fabrication of a strong and ductile CuCrZr alloy using laser powder bed fusion, Additive Manufacturing Letters 5 (2023). https://doi.org/10.1016/j.addlet.2023.100121.

[103] S.K. Murugesan, J. Natarajan, C.H. Yang, Enhancing the wear resistance by mitigation of defect formations in laser powder bed fusion process of Cu–Cr–Zr alloy, International Journal of Advanced Manufacturing Technology 133 (2024) 1845–1864. https://doi.org/10.1007/s00170-024-13883-3.

[104] H. Lipowsky, E. Arpaci, Copper in the automotive industry, John Wiley & Sons, 2008.

[105] R.P. Minneci, E.A. Lass, J.R. Bunn, H. Choo, C.J. Rawn, Copper-based alloys for structural high-heat-flux applications: a review of development, properties, and performance of Cu-rich Cu–Cr–Nb alloys, International Materials Reviews 66 (2021) 394–425. https://doi.org/10.1080/09506608.2020.1821485.

[106] I.S. Batra, G.K. Dey, U.D. Kulkarni, S. Banerjee, Microstructure and properties of a Cu–Cr–Zr alloy, n.d. www.elsevier.com/locate/jnucmat.

[107] S. Huang, W. Huang, W. Xie, H. Chen, H. Wang, B. Yang, Microstructure and strengthening mechanisms of CuCrZr alloy by two-step thermomechanical treatment, Journal of Materials Science: Materials in Electronics 31 (2020) 17798–17809. https://doi.org/10.1007/s10854-020-04333-3.

[108] R. Ihira, H. Gwon, R. Kasada, S. Konishi, Improvement of tensile properties of pure Cu and CuCrZr alloy by cryo-rolling process, Fusion Engineering and Design 109–111 (2016) 485–488. https://doi.org/10.1016/j.fusengdes.2016.02.070.

[109] L. Gong, Y. Huang, Z. Han, S. Song, H. Feng, Z. Chen, X. Liu, W. Huang, Texture evolution and strengthening mechanism of CuCrZr alloys during cold rolling, Vacuum 221 (2024). https://doi.org/10.1016/j.vacuum.2023.112908.

[110] U. Holzwarth, H. Stamm, M. Pisoni, A. Volcan, R. Scholz, The recovery of tensile properties of CuCrZr alloy after hot isostatic pressing, 2000. www.elsevier.com/locate/fusengdes.

[111] P.E. Frayssines, J.M. Gentzbittel, A. Guilloud, P. Bucci, T. Soreau, N. Francois, F. Primaux, S. Heikkinen, F. Zacchia, R. Eaton, V. Barabash, R. Mitteau, CuCrZr alloy microstructure and mechanical properties after hot isostatic pressing bonding cycles, Phys Scr, Institute of Physics Publishing, 2014. https://doi.org/10.1088/0031-8949/2014/T159/014018.

[112] S.F. Nabavi, H. Dalir, A. Farshidianfar, A comprehensive review of recent advances in laser powder bed fusion characteristics modeling: metallurgical and defects, International Journal of Advanced Manufacturing Technology 132 (2024) 2233–2269. https://doi.org/10.1007/s00170-024-13491-1.

[113] M. Masoomi, J.W. Pegues, S.M. Thompson, N. Shamsaei, A numerical and experimental investigation of convective heat transfer during laser-powder bed fusion, Addit Manuf 22 (2018) 729–745. https://doi.org/10.1016/j.addma.2018.06.021.

[114] X. Zhang, Y. Yuan, S. Zhao, J. Zhang, Q. Yan, Microstructure stability, softening temperature and strengthening mechanism of pure copper, CuCrZr and Cu-Al2O3 up to 1000 ℃, Nuclear Materials and Energy 30 (2022). https://doi.org/10.1016/j.nme.2022.101123.

[115] J. Chen, J. Wang, X. Xiao, H. Wang, H. Chen, B. Yang, Contribution of Zr to strength and grain refinement in Cu–Cr–Zr alloy, Materials Science and Engineering: A 756 (2019) 464–473. https://doi.org/10.1016/j.msea.2019.04.053.

[116] Z. Li, M. Zhou, K. Jing, Y. Liu, G. Xin, H. Hu, J. Zou, B. Tian, Y. Zhang, X. Li, A.A. Volinsky, Effects of different Cr contents on microstructure, mechanical and electrical properties of Cu-Zr-Cr alloy, Mater Today Commun 38 (2024). https://doi.org/10.1016/j.mtcomm.2024.108408.

[117] J. Zhou, Y. Huang, Z. Li, X. Tong, D. You, J. Yang, Q. Zhang, W. Li, X. Wang, Effect of heat treatments on microstructure, mechanical and electrical properties of Cu–Cr–Zr alloy manufactured by laser powder bed fusion, Mater Chem Phys 296 (2023). https://doi.org/10.1016/j.matchemphys.2022.127249.

[118] S. Rahman, P.J. Schilling, P.D. Herrington, U.K. Chakravarty, Thermal behavior and melt-pool dynamics of cu-cr-zr alloy in powder-bed selective laser melting process, 2019. http://asmedigitalcollection.asme.org/IMECE/proceedings-pdf/IMECE2019/59360/V001T03A023/6512473/v001t03a023-imece2019-11087.pdf.

[119] X. Qian, X. Peng, Y. Song, J. Huang, Y. Wei, P. Liu, X. Mao, J. Zhang, L. Wang, Dynamic constitutive relationship of CuCrZr alloy based on Johnson-Cook model, Nuclear Materials and Energy 24 (2020). https://doi.org/10.1016/j.nme.2020.100768.

[120] D. Cortis, E. Mancini, S. Nisi, D. Orlandi, P. Di Stefano, M. Utzeri, M. Sasso, Compression tests at high strain rate on 3D-printed CuCrZr alloy specimens - material model calibration, J Phys Conf Ser, Institute of Physics, 2023. https://doi.org/10.1088/1742-6596/2444/1/012001.

[121] S. Dehgahi, R. Alaghmandfard, J. Tallon, A. Odeshi, M. Mohammadi, Microstructural evolution and high strain rate compressive behavior of as-built and heat-treated additively manufactured maraging steels, Materials Science and Engineering: A 815 (2021). https://doi.org/10.1016/j.msea.2021.141183.

[122] Introduction to high strain rate testing, Mechanical Testing and Evaluation, ASM International, 2018: pp. 427–428. https://doi.org/10.31399/asm.hb.v08.a0003293.

[123] K.T. Ramesh, High rates and impact experiments, Springer Handbook of Experimental Solid Mechanics (2008) 929–960.

[124] O. Engler, V. Randle, Introduction to texture analysis: macrotexture, microtexture, and orientation mapping, CRC Press, 2003.

[125] S. Zhang, H. Zhu, Z. Hu, X. Zeng, F. Zhong, Selective laser melting of Cu–10Zn alloy powder using high laser power, Powder Technol 342 (2019) 613–620. https://doi.org/10.1016/j.powtec.2018.10.002.

[126] L. Zhang, P. Dong, Y. Zeng, H. Yao, J. Chen, Additive manufacturing of Inconel 718/CuCrZr multi-metallic materials fabricated by laser powder bed fusion, Addit Manuf 92 (2024). https://doi.org/10.1016/j.addma.2024.104377.

[127] H. Asgari, M. Salarian, H. Ma, A. Olubamiji, M. Vlasea, On thermal expansion behavior of invar alloy fabricated by modulated laser powder bed fusion, Mater Des 160 (2018) 895–905. https://doi.org/10.1016/j.matdes.2018.10.025.

[128] Z. Kuai, Z. Li, B. Liu, Y. Chen, S. Lu, X. Tang, T. Liu, Selective laser melting of CuCrZr alloy: processing optimisation, microstructure and mechanical properties, Journal of Materials Research and Technology 19 (2022) 4915–4931. https://doi.org/10.1016/j.jmrt.2022.06.158.

[129] S. Shrestha, Y.K. Chou, A numerical study on the keyhole formation during laser powder bed fusion process, J Manuf Sci Eng 141 (2019). https://doi.org/10.1115/1.4044100.

[130] J. Yang, L.M. Schlenger, M.H. Nasab, S. Van Petegem, F. Marone, R.E. Logé, C. Leinenbach, Experimental quantification of inward Marangoni convection and its impact on keyhole threshold in laser powder bed fusion of stainless steel, Addit Manuf 84 (2024). https://doi.org/10.1016/j.addma.2024.104092.

[131] N. Ramachandiran, H. Asgari, F. Dibia, R. Eybel, A. Gerlich, E. Toyserkani, Effect of non-lamellar α precipitate morphology on the mechanical properties of Ti5553 parts made by laser powder-bed fusion at high laser scan speeds, Materials Science and Engineering: A 841 (2022). https://doi.org/10.1016/j.msea.2022.143039.

[132] X. Yang, Y. Wang, W. Zhang, Y. Qi, B. Zhang, H. Zhang, H. Zhu, Laser powder bed fusion fabricated Cu-1.8Cr-1.0Nb-2.0Fe alloy with in-situ precipitation strengthening, Materials Science and Engineering: A 878 (2023). https://doi.org/10.1016/j.msea.2023.145222.

[133] N. Ordás, L. Portolés, M. Azpeleta, A. Gómez, J.R. Blasco, M. Martinez, J. Ureña, I. Iturriza, Development of CuCrZr via electron beam powder bed fusion (EB-PBF), Journal of Nuclear Materials 548 (2021). https://doi.org/10.1016/j.jnucmat.2021.152841.

[134] P.H.F. Oliveira, D.C.C. Magalhães, M.T. Izumi, O.M. Cintho, A.M. Kliauga, V.L. Sordi, Evolution of dislocation and stacking-fault densities for a Cu-0.7Cr-0.07Zr alloy during cryogenic tensile test: An in-situ synchrotron X-ray diffraction analysis, Materials Science and Engineering: A 813 (2021). https://doi.org/10.1016/j.msea.2021.141154.

[135] A. Hadadzadeh, C. Baxter, B.S. Amirkhiz, M. Mohammadi, Strengthening mechanisms in direct metal laser sintered AlSi10Mg: Comparison between virgin and recycled powders, Addit Manuf 23 (2018) 108–120.

[136] K. Song, Y. Geng, Y. Ban, Y. Zhang, Z. Li, X. Mi, J. Cao, Y. Zhou, X. Zhang, Effects of strain rates on dynamic deformation behavior of Cu-20Ag alloy, J Mater Sci Technol 79 (2021) 75–87. https://doi.org/10.1016/j.jmst.2020.11.043.

[137] Y. Xu, J. Zhang, Y. Bai, M.A. Meyers, Shear localization in dynamic deformation: microstructural evolution, Metallurgical and Materials Transactions A 39 (2008) 811–843.

[138] K.D. Karantza, D.E. Manolakos, A review on the adiabatic shear banding mechanism in metals and alloys considering microstructural characteristics, morphology and fracture, Metals (Basel) 13 (2023). https://doi.org/10.3390/met13121988.

[139] R. Alaghmandfard, C. Dharmendra, A.G. Odeshi, M. Mohammadi, Dynamic mechanical properties and failure characteristics of electron beam melted Ti-6Al-4V under high strain rate impact loadings, Materials Science and Engineering: A 793 (2020) 139794.

[140] Q. lin Xiong, Z. Li, T. Shimada, T. Kitamura, Atomistic investigation on the conversion of plastic work to heat in high-rate shear deformation, Int J Plast 149 (2022). https://doi.org/10.1016/j.ijplas.2021.103158.

[141] W. An, C. zhi Liu, Q. lin Xiong, Z. Li, X. Huang, T. Suo, Shear localization in polycrystalline metal at high-strain rates with dynamic recrystallization: Crystal plasticity modeling and texture effect, Int J Plast 165 (2023). https://doi.org/10.1016/j.ijplas.2023.103616.

[142] A. Kundu, P.C. Chakraborti, Effect of strain rate on quasistatic tensile flow behaviour of solution annealed 304 austenitic stainless steel at room temperature, J Mater Sci 45 (2010) 5482–5489.

[143] T.D. Truong, G. Asala, O.T. Ola, O.A. Ojo, A.G. Odeshi, Texture and damage evolution in additively manufactured 18 %Ni-M350 maraging steel under dynamic impact loading: Processing parameters and heat treatment effects, Materialia (Oxf) 32 (2023). https://doi.org/10.1016/j.mtla.2023.101961.

[144] W.-S. Lee, C.-F. Lin, Comparative study of the impact response and microstructure of 304L stainless steel with and without prestrain, Metallurgical and Materials Transactions A 33 (2002) 2801–2810.

[145] A.A. Tiamiyu, J.A. Szpunar, A.G. Odeshi, Strain rate sensitivity and activation volume of AISI 321 stainless steel under dynamic impact loading: Grain size effect, Mater Charact 154 (2019) 7–19. https://doi.org/10.1016/j.matchar.2019.05.027.

[146] N. Yan, Z. Li, Y. Xu, M.A. Meyers, Shear localization in metallic materials at high strain rates, Prog Mater Sci 119 (2021). https://doi.org/10.1016/j.pmatsci.2020.100755.

[147] I. V. Alexandrov, R.G. Chembarisova, V.D. Sitdikov, Analysis of the deformation mechanisms in bulk ultrafine grained metallic materials, Materials Science and Engineering: A 463 (2007) 27–35. https://doi.org/10.1016/j.msea.2006.07.155.

[148] Y. Zhang, S. Huili, A.A. Volinsky, B. Tian, Z. Chai, P. Liu, Y. Liu, Hot deformation and dynamic recrystallization behavior of the Cu-Cr-Zr-Y alloy, J Mater Eng Perform 25 (2016) 1150–1156. https://doi.org/10.1007/s11665-016-1914-x.

[149] U. Andrade, M.A. Meyers, K.S. Vecchio, A.H. Chokshi, Dynamic recrystallization in high-strain, high-strain-rate plastic deformation of copper, 1994.

[150] Y.B. Xu', Y.L. Bai, Q. Xue, L.T. Shen, Formation, microstructure and development of the localized shear deformation in low-carbon steels, 1996.

[151] A.R. Vishnu, J.C. Nieto-Fuentes, J.A. Rodríguez-Martínez, Shear band formation in porous thin-walled tubes subjected to dynamic torsion, Int J Solids Struct 252 (2022). https://doi.org/10.1016/j.ijsolstr.2022.111837.

[152] M. Marvi-Mashhadi, A. Vaz-Romero, F. Sket, J.A. Rodríguez-Martínez, Finite element analysis to determine the role of porosity in dynamic localization and fragmentation: Application to porous microstructures obtained from additively manufactured materials, Int J Plast 143 (2021). https://doi.org/10.1016/j.ijplas.2021.102999.

[153] H.L. Dorothy, P. Longère, Unified modelling of adiabatic shear banding and subsequent micro-voiding driven dynamic failure of viscoplastic solids, Int J Impact Eng 132 (2019). https://doi.org/10.1016/j.ijimpeng.2019.103322.

[154] J.W. Kysar, Y. Saito, M.S. Oztop, D. Lee, W.T. Huh, Experimental lower bounds on geometrically necessary dislocation density, Int J Plast 26 (2010) 1097–1123. https://doi.org/10.1016/j.ijplas.2010.03.009.

[155] R. Yuan, Establishing a quantitative relationship between strain gradient and hetero-deformation-induced stress in gradient-structured metals, Acta Mech 233 (2022) 961–989. https://doi.org/10.1007/s00707-021-03141-y.

[156] R. Alaghmandfard, P. Seraj, M. Sanjari, H. Pirgazi, C. Dharmendra, A.G. Odeshi, B. Shalchi Amirkhiz, M. Mohammadi, High strain rate deformation behavior, texture and microstructural evolution, characterization of adiabatic shear bands, and constitutive models in electron beam melted Ti-6Al-4V under dynamic compression loadings, Journal of Materials Research and Technology 21 (2022) 4093–4114. https://doi.org/10.1016/j.jmrt.2022.11.016.

[157] M.E. Kassner, Taylor hardening in five-power-law creep of metals and Class M alloys, Acta Mater 52 (2004) 1–9. https://doi.org/10.1016/j.actamat.2003.08.019.

[158] Y. Guo, Q. Ruan, S. Zhu, Q. Wei, J. Lu, B. Hu, X. Wu, Y. Li, Dynamic failure of titanium: Temperature rise and adiabatic shear band formation, J Mech Phys Solids 135 (2020). https://doi.org/10.1016/j.jmps.2019.103811.

[159] X. Zhu, Z. Xiao, J. An, H. Jiang, Y. Jiang, Z. Li, Microstructure and properties of Cu-Ag alloy prepared by continuously directional solidification, J Alloys Compd 883 (2021). https://doi.org/10.1016/j.jallcom.2021.160769.

[160] T. Mukherjee, V. Manvatkar, A. De, T. DebRoy, Dimensionless numbers in additive manufacturing, J Appl Phys 121 (2017). https://doi.org/10.1063/1.4976006.

[161] L. Ladani, J. Romano, W. Brindley, S. Burlatsky, Effective liquid conductivity for improved simulation of thermal transport in laser beam melting powder bed technology, Addit Manuf 14 (2017) 13–23. https://doi.org/10.1016/j.addma.2016.12.004.

[162] L. Gargalis, J. Ye, M. Strantza, A. Rubenchik, J. Murray, A. Clare, I. Ashcroft, R. Hague, M. Matthews, Determining processing behaviour of pure Cu in laser powder bed fusion using direct micro-calorimetry, 2022.

[163] G.K. White, M.L. Minges, R.B. Castanet, S.J. Collocott, P.D. Desai, C.Y. Ho, J.G. Hust, R.B. Roberts, C.A. Swenson, Thermophysical properties of some key solids, 1997.

[164] J.J. Valencia, Thermophysical properties sources and availability of reliable data, (2008). https://doi.org/10.1361/asmhba0005240.

[165] L. Zhang, S. Li, Empirical atom model of Vegard's law, Physica B Condens Matter 434 (2014) 38–43. https://doi.org/10.1016/j.physb.2013.10.066.

[166] M. Košiček, J. Zavašnik, O. Baranov, B. Šetina Batič, U. Cvelbar, Understanding the growth of copper oxide nanowires and layers by thermal oxidation over a broad temperature range at atmospheric pressure, Cryst Growth Des 22 (2022) 6656–6666. https://doi.org/10.1021/acs.cgd.2c00863.

[167] L. Yuan, Y. Wang, R. Mema, G. Zhou, Driving force and growth mechanism for spontaneous oxide nanowire formation during the thermal oxidation of metals, Acta Mater 59 (2011) 2491–2500. https://doi.org/10.1016/j.actamat.2010.12.052.

[168] Z. Grzesik, M. Migdalska, Oxidation mechanism of Cu_2O and defect structure of CuO at high temperatures, High Temperature Materials and Processes 30 (2011) 277–287. https://doi.org/10.1515/HTMP.2011.046.

[169] Y. Zhu, K. Mimura, J.-W. Lim, Q. Jiang, Brief review of oxidation kinetics of copper at 350 °C to 1050 °C, n.d.

[170] C. Juillet, A. Oudriss, J. Balmain, X. Feaugas, F. Pedraza, Characterization and oxidation resistance of additive manufactured and forged IN718 Ni-based superalloys, Corros Sci 142 (2018) 266–276. https://doi.org/10.1016/j.corsci.2018.07.032.

[171] X. Xu, C. Tang, H. Wang, Y. An, Y. Zhao, Microstructure evolution and grain refinement mechanism of rapidly solidified single-phase copper based alloys, J Mater Sci Technol 128 (2022) 160–179. https://doi.org/10.1016/j.jmst.2022.04.025.

[172] A. Baumard, D. Ayrault, O. Fandeur, C. Bordreuil, F. Deschaux-Beaume, Numerical prediction of grain structure formation during laser powder bed fusion of 316 L stainless steel, Mater Des 199 (2021). https://doi.org/10.1016/j.matdes.2020.109434.

[173] M. Zheng, G. Wang, W. Zhou, L. Wei, X. Lin, W. Huang, Understanding grain evolution in laser powder bed fusion process through a real-time coupled Lattice Boltzmann model-Cellular Automaton simulation, J Mater Process Technol 321 (2023). https://doi.org/10.1016/j.jmatprotec.2023.118126.

[174] R. Wróbel, P. Scheel, X. Maeder, E. Hosseini, C. Leinenbach, Microstructure formation in micron-scale thin-walled Hastelloy X samples fabricated with laser powder bed fusion, Progress in Additive Manufacturing 9 (2024) 361–373. https://doi.org/10.1007/s40964-023-00458-z.

[175] S.I. Shahabad, U. Ali, Z. Zhang, A. Keshavarzkermani, R. Esmaeilizadeh, A. Bonakdar, E. Toyserkani, On the effect of thin-wall thickness on melt pool dimensions in laser powder-bed fusion of Hastelloy X: Numerical modeling and experimental validation, J Manuf Process 75 (2022) 435–449. https://doi.org/10.1016/j.jmapro.2022.01.029.

[176] Y. Geng, Y. Ban, B. Wang, X. Li, K. Song, Y. Zhang, Y. Jia, B. Tian, Y. Liu, A.A. Volinsky, A review of microstructure and texture evolution with nanoscale precipitates for copper alloys, Journal of Materials Research and Technology 9 (2020) 11918–11934. https://doi.org/10.1016/j.jmrt.2020.08.055.

[177] T.J. Pan, J. Chen, Y.X. He, W. Wei, J. Hu, Influence of Grain Refinement on Oxidation Behavior of Two-Phase Cu-Cr Alloys at 973-1,073 K in Air, High Temperature Materials and Processes 35 (2016) 1005–1011. https://doi.org/10.1515/htmp-2015-0138.

[178] L. Ogbuji, D.L. Humphrey, Comparison of the oxidation rates of some new copper alloys, n.d.

[179] F. King, C. Lilja, K. Pedersen, P. Pitkänen, M. Vähänen, An update of the state-of-the-art report on the corrosion of copper under expected conditions in a deep geologic repository, Swedish Nuclear Fuel and Waste Management Co., 2010.

[180] J. Aromaa, M. Kekkonen, M. Mousapour, A. Jokilaakso, M. Lundström, The oxidation of copper in air at temperatures up to 100 C, Corrosion and Materials Degradation 2 (2021) 625–640.

[181] S. Catchpole-Smith, R.R.J. Sélo, A.W. Davis, I.A. Ashcroft, C.J. Tuck, A. Clare, Thermal conductivity of TPMS lattice structures manufactured via laser powder bed fusion, Addit Manuf 30 (2019). https://doi.org/10.1016/j.addma.2019.100846.

[182] M. Jin, Q. Feng, X. Fan, Z. Luo, Q. Tang, J. Song, S. Ma, Y. Nie, P. Jin, M. Zhao, Investigation on the mechanical properties of TPMS porous structures fabricated by laser powder bed fusion, J Manuf Process 76 (2022) 559–574. https://doi.org/10.1016/j.jmapro.2022.02.035.

[183] A. Chyrkin, K.O. Gunduz, I. Fedorova, M. Sattari, A. Visibile, M. Halvarsson, J. Froitzheim, K. Stiller, High-temperature oxidation behavior of additively manufactured IN625: Effect of microstructure and grain size, Corros Sci 205 (2022). https://doi.org/10.1016/j.corsci.2022.110382.

[184] L. Yuan, G. Zhou, Enhanced CuO Nanowire Formation by Thermal Oxidation of Roughened Copper, J Electrochem Soc 159 (2012) C205–C209. https://doi.org/10.1149/2.102204jes.

[185] J.H. Kim, D.I. Kim, S. Suwas, E. Fleury, K.W. Yi, Grain-size effects on the high-temperature oxidation of modified 304 austenitic stainless steel, in: Oxidation of Metals, 2013: pp. 239–247. https://doi.org/10.1007/s11085-012-9347-x.

[186] E. Martinez-Lombardia, Y. Gonzalez-Garcia, L. Lapeire, I. De Graeve, K. Verbeken, L. Kestens, J.M.C. Mol, H. Terryn, Scanning electrochemical microscopy to study the effect of crystallographic orientation on the electrochemical activity of pure copper, Electrochim Acta 116 (2014) 89–96. https://doi.org/10.1016/j.electacta.2013.11.048.

[187] M.P. Phaniraj, D.I. Kim, Y.W. Cho, Effect of grain boundary characteristics on the oxidation behavior of ferritic stainless steel, Corros Sci 53 (2011) 4124–4130. https://doi.org/10.1016/j.corsci.2011.08.020.

[188] I.G. Wright, R.B. Dooley, A review of the oxidation behaviour of structural alloys in steam, International Materials Reviews 55 (2010) 129–167. https://doi.org/10.1179/095066010X12646898728165.

[189] G.Y. Fu, Y. Niu, F. Gesmundo, Microstructural effects on the high temperature oxidation of two-phase Cu-Cr alloys in 1 atm O 2, n.d. www.elsevier.com/locate/corsciCorrosionScience45.

[190] P. Platt, V. Allen, M. Fenwick, M. Gass, M. Preuss, Observation of the effect of surface roughness on the oxidation of Zircaloy-4, Corros Sci 98 (2015) 1–5. https://doi.org/10.1016/j.corsci.2015.05.013.

[191] K.T. Young, S.S. Phillips, J.T.T. Coley, C.J. Perini, D.A. Hitchcock, S.M. Serkiz, E.M. Vogel, The impact of defect density, grain size, and Cu orientation on thermal oxidation of graphene-coated Cu, Appl Surf Sci 478 (2019) 959–968. https://doi.org/10.1016/j.apsusc.2019.02.053.

[192] A. Mehta, L. Zhou, H. Hyer, T. Huynh, B. Lu, K. Graydon, E.J. Drobner, S.H. Park, Y. Sohn, Microstructural characteristics and mechanical properties of additively manufactured Cu–10Sn alloys by laser powder bed fusion, Materials Science and Engineering: A 838 (2022). https://doi.org/10.1016/j.msea.2022.142775.

[193] N.J. Peter, D. Zander, X. Cao, C. Tian, S. Zhang, K. Du, C. Scheu, G. Dehm, Preferred corrosion pathways for oxygen in Al2Ca – twin boundaries and dislocations, J Alloys Compd 936 (2023). https://doi.org/10.1016/j.jallcom.2022.168296.

[194] A.J. Mayne, F. Rose, G. E Erald Dujardin, An STM study of the growth behaviour of the oxidation of the Geð1 1 1Þ surface, n.d. www.elsevier.com/locate/susc.

[195] P. Gómez-Romero, E.M. Tejada-Rosales, M.R. Palacín, Ag2Cu2O3: The first silver copper oxide, Angewandte Chemie - International Edition 38 (1999) 524–525. https://doi.org/10.1002/(SICI)1521-3773(19990215)38:4<524::AID-ANIE524>3.0.CO;2-F.

[196] F. Sauvage, D. Muñoz-Rojas, K.R. Poeppelmeier, N. Casañ-Pastor, Transport properties and lithium insertion study in the p-type semi-conductors AgCuO2 and AgCu0.5Mn0.5O2, J Solid State Chem 182 (2009) 374–380. https://doi.org/10.1016/j.jssc.2008.10.038.

[197] N.J. Tannyan, G. Plascencia, T.A. Utigard, High temperature oxidation of copper and copper aluminum alloys, Canadian Metallurgical Quarterly, Metallurgical Society of CIM, 2002: pp. 213–217. https://doi.org/10.1179/cmq.2002.41.2.213.

Appendices

Appendix A:

Table A1 PBD matrix for screening of 23 process parameters in LPBF where "+" and "-" symbols represent high and low parameter values, respectively.

Run	A	B	C	D	E	F	G	H	J	K	L	M	N	O	P	Q	R	S	T	U	V	W	X
1	+	-	-	-	-	+	-	+	-	-	+	+	-	-	+	+	-	+	-	+	+	+	+
2	+	+	-	-	-	-	+	-	+	-	-	+	+	-	-	+	+	-	+	-	+	+	+
3	+	+	+	-	-	-	-	+	-	+	-	-	+	+	-	-	+	+	-	+	-	+	+
4	+	+	+	+	-	-	-	-	+	-	+	-	-	+	+	-	-	+	+	-	+	-	+
5	+	+	+	+	+	-	-	-	-	+	-	+	-	-	+	+	-	-	+	+	-	+	-
6	-	+	+	+	+	+	-	-	-	-	+	-	+	-	-	+	+	-	-	+	+	-	+
7	+	-	+	+	+	+	+	-	-	-	-	+	-	+	-	-	+	+	-	-	+	+	-
8	-	+	-	+	+	+	+	+	-	-	-	-	+	-	+	-	-	+	+	-	-	+	+
9	+	-	+	-	+	+	+	+	+	-	-	-	-	+	-	+	-	-	+	+	-	-	+
10	+	+	-	+	-	+	+	+	+	+	-	-	-	-	+	-	+	-	-	+	+	-	-
11	-	+	+	-	+	-	+	+	+	+	+	-	-	-	-	+	-	+	-	-	+	+	-
12	-	-	+	+	-	+	-	+	+	+	+	+	-	-	-	-	+	-	+	-	-	+	+
13	+	-	-	+	+	-	+	-	+	+	+	+	+	-	-	-	-	+	-	+	-	-	+
14	+	+	-	-	+	+	-	+	-	+	+	+	+	+	-	-	-	-	+	-	+	-	-
15	-	+	+	-	-	+	+	-	+	-	+	+	+	+	+	-	-	-	-	+	-	+	-
16	-	-	+	+	-	-	+	+	-	+	-	+	+	+	+	+	-	-	-	-	+	-	+
17	+	-	-	+	+	-	-	+	+	-	+	-	+	+	+	+	+	-	-	-	-	+	-
18	-	+	-	-	+	+	-	-	+	+	-	+	-	+	+	+	+	+	-	-	-	-	+
19	+	-	+	-	-	+	+	-	-	+	+	-	+	-	+	+	+	+	+	-	-	-	-
20	-	+	-	+	-	-	+	+	-	-	+	+	-	+	-	+	+	+	+	+	-	-	-
21	-	-	+	-	+	-	-	+	+	-	-	+	+	-	+	-	+	+	+	+	+	-	-
22	-	-	-	+	-	+	-	-	+	+	-	-	+	+	-	+	-	+	+	+	+	+	-
23	-	-	-	-	+	-	+	-	-	+	+	-	-	+	+	-	+	-	+	+	+	+	+
24	-	-	-	-	-	-	-	-	-	-	-	-	-	-	-	-	-	-	-	-	-	-	-
25	0	0	0	0	0	0	0	0	0	0	0	0	0	0	0	0	0	0	0	0	0	-	-
26	0	0	0	0	0	0	0	0	0	0	0	0	0	0	0	0	0	0	0	0	0	+	-
27	0	0	0	0	0	0	0	0	0	0	0	0	0	0	0	0	0	0	0	0	0	-	+
28	0	0	0	0	0	0	0	0	0	0	0	0	0	0	0	0	0	0	0	0	0	+	+

Appendix B:

Table B1 Parameter codes corresponding to Figure 3-4, where each code (a_i–p_i, #i = 1–16) represents the process parameters for samples printed in the CCD experiment.

Core exposure					**Skin exposure**				
X	Laser power [W]	Scanning speed [mm/s]	Hatch distance [µm]	Stripe overlap [µm]	Y	Laser power [W]	Scanning speed [mm/s]	Hatch distance [µm]	Contour power [W]
a	700	800	160	10	1	300	600	75	300
b	700	800	160	110	2	300	600	75	500
c	700	800	200	10	3	300	600	125	300
d	700	800	200	110	4	300	600	125	500
e	700	1000	160	10	5	300	800	75	300
f	700	1000	160	110	6	300	800	75	500
g	700	1000	200	10	7	300	800	125	300
h	700	1000	200	110	8	300	800	125	500
i	900	800	160	10	9	500	600	75	300
j	900	800	160	110	10	500	600	75	500
k	900	800	200	10	11	500	600	125	300
l	900	800	200	110	12	500	600	125	500
m	900	1000	160	10	13	500	800	75	300
n	900	1000	160	110	14	500	800	75	500
o	900	1000	200	10	15	500	800	125	300
p	900	1000	200	110	16	500	800	125	500

Appendix C:

$$RD\ [\%] = 79.22 + 0.01788\ A + 0.00092\ B + 0.02615\ C + 5.01\ D + 0.001427E + 0.00515\ F - 1.34\ G + 89.4\ H + 8.8\ J - 0.000015AB - 0.000012\ AC - 0.0291\ AD - 0.000007\ BC + 0.000010\ BF - 0.000006\ CF - 0.0773\ CH + 0.0788\ CJ + 266.0\ DJ - 0.0895\ EJ - 0.0637\ FH \quad \text{(C1)}$$

$$S_a\ [\mu m] = 52.4 - 0.0696\ A - 0.0278\ B + 0.0865\ C - 372.4\ D - 0.04381\ E + 0.04637\ F - 68.1\ G - 154.2\ H + 437\ J + 0.000105\ AC + 0.000027\ AE + 0.1145\ AG - 0.4748\ AJ - 0.000063\ BC + 0.3037\ BD + 0.1374\ BH - 0.1748\ BJ - 0.2545\ CD - 0.000054\ CF - 0.3309\ CJ + 0.1942\ DE + 540\ DH + 0.4061\ EJ - 0.2532\ FJ \quad \text{(C2)}$$

Table C1 List of parameters and their coded variables used in the regression Equations (C1) and (C2)

Category	#	Code	Parameter
Post-exposure	1	A	Contour power [W]
Skin-exposure	3	B	Scanning speed [mm/s]
	4	C	Power [W]
	5	D	Hatch distance [mm]
Core-exposure	5	E	Scanning speed [mm/s]
	6	F	Power [W]
	7	G	Hatch distance [mm]
	8	H	Stripe overlap [mm]
Additional	9	J	Layer thickness [mm]